ORIGIN OF CHEMICAL HETEROGENEITIES IN THE SUBCONTINENTAL LITHOSPHERIC MANTLE

INSIGHTS FROM THE WESTERNMOST MEDITERRANEAN OROGENIC PERIDOTITES AND ALLIED CRUSTAL ROCKS

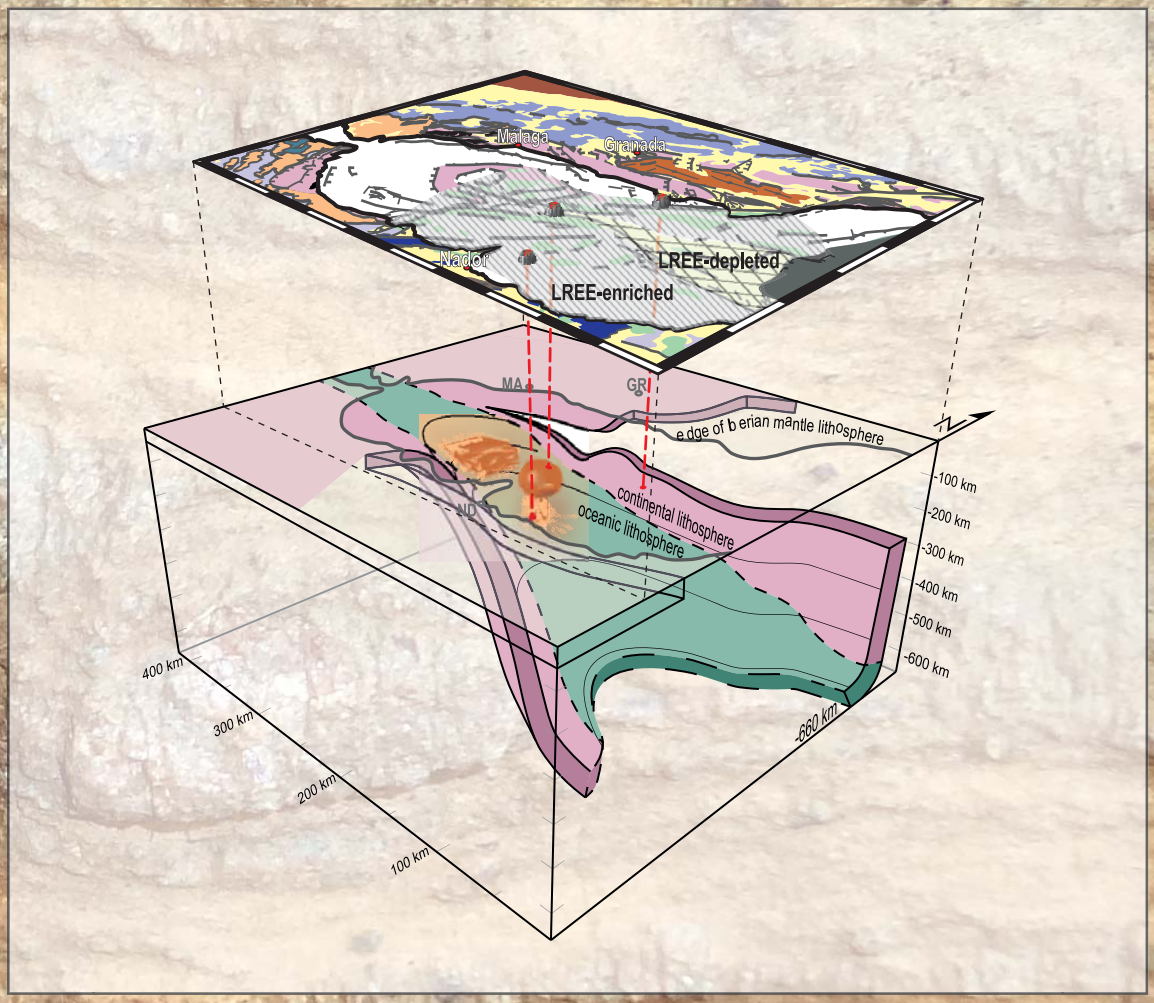

María Isabel Varas Reus

CSIC
IACT INSTITUTO ANDALUZ DE CIENCIAS DE LA TIERRA
ugr Universidad de Granada
Programa Doctorado Ciencias de la Tierra

Tesis Doctoral, 2016

Editor: Universidad de Granada. Tesis Doctorales
Autora: María Isabel Vara Reus
ISBN: 978-84-9163-042-5
URI:http://hdl.handle.net/10481/45854

ORIGIN OF CHEMICAL HETEROGENEITIES IN THE SUBCONTINENTAL LITHOSPHERIC MANTLE

INSIGHTS FROM THE WESTERNMOST MEDITERRANEAN OROGENIC PERIDOTITES AND ALLIED CRUSTAL ROCKS

MARÍA ISABEL VARAS REUS

Ph.D. Thesis – Tesis Doctoral

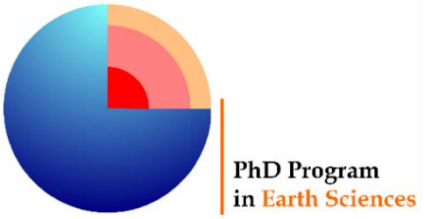

Memoria de Tesis Doctoral presentada por la Licenciada en Geología
María Isabel Varas Reus para optar al grado de
Doctora por la Universidad de Granada

Esta Tesis Doctoral ha sido dirigida por el Dr. Carlos J. Garrido Marín, del Instituto Andaluz de Ciencias de la Tierra (CSIC-UGR),
y el Dr. Claudio Marchesi, del Departamento de Mineralogía y Petrología de la Universidad de Granada.

En Granada, 25 de noviembre de 2016

La doctoranda **María Isabel Varas Reus** y los directores de la tesis **Carlos J. Garrido Marín** y **Claudio Marchesi** garantizamos, al firmar esta tesis doctoral, que el trabajo ha sido realizado por la doctoranda bajo la dirección de los directores de la tesis y hasta donde nuestro conocimiento alcanza, en la realización del trabajo, se han respetado los derechos de otros autores a ser citados, cuando se han utilizado sus resultados o publicaciones.

En Granada, 25 de noviembre de 2016

Directores de la Tesis

Fdo.: Carlos J. Garrido Marín

Fdo.: Claudio Marchesi

Doctoranda

Fdo.: María Isabel Varas Reus

Research leading to these results has been funded by a CSIC JAE-Predoc Fellowship to M.I.V.R. This work has also been supported by the “Spanish Ministry of Economic and Competitiveness” (MINECO) grants CGL2013-42349-P-14848, CGL2016-81085-R, and the Junta de Andalucía research group RNM-131 and grant P12-RNM-3141. This research has benefited from EU Cohesion Policy funds from the European Regional Development Fund (ERDF) and the European Social Fund (ESF) in support of human resources, innovation and research capacities, and research infrastructures.

A mís padres,

por ser siempre el viento bajo mís alas.

Let's descend to that blind world below.

I'll go first, and you can follow.

Dante

Resumen

Comprender los mecanismos y procesos responsables de la formación de las heterogeneidades del manto es crucial para poder avanzar en nuestro conocimiento sobre la composición y diferenciación de la Tierra a diferentes escalas. Los macizos peridotíticos orogénicos ofrecen una oportunidad excepcional para investigar *in situ* la naturaleza y escala de las heterogeneidades composicionales del manto. Esta tesis doctoral tiene como objetivo principal arrojar luz sobre el papel que juegan los procesos de reacción fundido-roca y el reciclaje de corteza oceánica y continental en la generación de las heterogeneidades químicas del manto. Con este fin, presentamos en esta tesis un estudio geoquímico detallado —incluyendo elementos mayores y trazas e isótopos radiogénicos de Sr-Nd-Pb-Hf— de rocas mantélicas que afloran en los macizos peridotíticos de Ronda (sur de España, Cordillera Bética) y Beni Bousera (norte de Marruecos, Cordillera Rifeña) en el Mediterráneo occidental, y de rocas corticales espacialmente asociadas al macizo de Ronda (Complejo Alpujárride occidental y sedimentos pre-miocénicos del Flysch en la Cordillera Bética). En esta tesis doctoral se han investigado dos procesos relacionados con la formación de heterogeneidades químicas en el manto terrestre: (i) la formación de lherzolitas secundarias por procesos de reacción de fundidos con peridotitas residuales del manto, y (ii) la formación de piroxenitas con granate de ultra-alta presión y su relación con el reciclaje de corteza oceánica subducida en el manto terrestre. La evolución Alpina del Mediterráneo occidental registra una historia compleja de subducción y extensión que acabó formando la cuenca del Mar de Alborán y el estrecho de Gibraltar. Las rocas mantélicas de la Cordillera Bético-Rifeña —y rocas corticales asociadas— constituyen, por tanto, un laboratorio natural ideal para investigar a gran escala los procesos de reciclaje de corteza en el manto terrestre.

Algunas de las preguntas a tratar en esta tesis son: ¿Cuál es la causa principal de las composiciones generalmente fértiles de las peridotitas derivadas del manto litosférico subcontinental (MLSC)? ¿Cómo la corteza oceánica y continental reciclada se mezclan en el MLSC muestreado por peridotitas orogénicas? ¿Son "exóticos" los componentes corticales registrados en la composición de rocas magmáticas, es decir, se incorporaron por subducción en el manto convectivo antes de la formación del MLSC, o están genéticamente relacionados con la sección cortical litosférica asociada a las peridotitas orogénicas?

***Palabras claves**: manto terrestre; macizos de peridotitas orogénicas; Ronda; Beni Bousera; Mediterráneo occidental; reciclaje de corteza; isótopos radiogénicos de Sr-Nd-Pb-Hf; lherzolitas secundarias; piroxenitas con granate.*

Extended abstract

Understanding the mechanisms and processes responsible for the generation of mantle heterogeneities is crucial for improving our knowledge about the composition and differentiation of the Earth at different scales. Orogenic peridotite massifs provide an exceptional opportunity to investigate *in situ* the nature and scale of compositional mantle heterogeneities. This Ph.D. thesis aims to shed new light on the role of melt-rock reaction processes and recycling of oceanic and continental crustal material in creating chemical heterogeneities in the mantle. To achieve this objective, this study focuses on mantle rocks exposed in orogenic peridotites from the Betic-Rif Cordillera in the westernmost Mediterranean, and their allied crustal rocks. Two processes related to the development of geochemical heterogeneities in the Earth's upper mantle are addressed in this work: (i) the formation of secondary lherzolites by melt-rock reaction processes, and (ii) the genesis of ultra-high pressure garnet pyroxenites and its implications for crustal recycling into the mantle. Furthermore, this thesis explores (iii) to what extent Betic crustal rocks were involved in the geochemical signature of magmatism recorded in the subcontinental lithospheric mantle (SCLM), and in the Miocene Alborán Sea basin volcanism. The westernmost Mediterranean records an Alpine history of subduction and slab roll-back that resulted in the creation of the Alborán Sea basin. Mantle rocks and their allied crustal rocks in the Betic-Rif belt hence provide a unique natural laboratory for studying large scale recycling of crustal components in the SCLM.

In order to address how melt-rock reaction processes are recorded in the SCLM, a large geochemical database of peridotites from the four tectono-metamorphic domains of the Beni Bousera orogenic massif (Rif Belt, N. Morocco) was processed. This study reveals that variations in bulk rock major and minor elements, Mg-no. and modal proportions of lherzolites, as well as their clinopyroxene trace element compositions, are inconsistent with simple partial melting and mainly resulted from different reactions between melts and depleted peridotites. On the other hand, up to 30% melting at < 3 GPa and cryptic metasomatism can account for the geochemical variations of most harzburgites. In garnet-spinel mylonites, melting and melt-rock reactions are masked by tectonic mixing with garnet pyroxenites and subsolidus re-

equilibration. In the rest of the massif, lherzolites were mostly produced by refertilization of a refractory protolith (Mg-no. ~ 91, olivine ~ 70%, clinopyroxene/orthopyroxene = 0.4) via two distinct near solidus, melt-rock reactions: (1) clinopyroxene and orthopyroxene precipitation and olivine consumption at melt/rock ratios < 0.75 and variable mass ratio between crystallized minerals and infiltrated melt (*R*), which are recorded quite homogeneously throughout the massif; and (2) dissolution of orthopyroxene and precipitation of clinopyroxene and olivine at melt/rock ratios ≤ 1 and $R = 0.2 - 0.3$, which affected mainly the Ariègite-Seiland and Seiland domains. The distribution of secondary lherzolites in the massif suggests that the first refertilization reaction occurred prior to the differentiation of the Beni Bousera mantle section into petro-structural zones, whereas the second reaction was associated to the development of the tectono-metamorphic domains during exhumation. These data support a secondary, refertilization-related, origin for most lherzolites in orogenic peridotite massifs.

The genesis of ultra-high pressure garnet pyroxenites and its implications for crustal recycling into the mantle were investigated through a detailed major and trace element and Sr-Nd-Pb-Hf isotopic study of garnet pyroxenites from the Ronda and Beni Bousera massifs (Betic-Rif Belt, westernmost Mediterranean). The results obtained show that the analyzed garnet pyroxenites not only derived from recycled oceanic crust, but also from recycled lower continental crust spatially associated with the orogenic massifs. Recycled continental crust is often invoked as the source of the Enriched Mantle (EM) isotopic component sampled by some oceanic basalts. This new isotopic evidence lends further support to the hypothesis that ultra-high pressure garnet pyroxenites can be a proxy for the study of the Earth's mantle sampled by oceanic and continental basalts. The existence of exotic recycled oceanic and co-lithospheric continental crust components in the subcontinental lithospheric mantle requires new recipes for the generation of the Earth's Marble Cake Mantle.

To evaluate the role of the Betic crustal rocks (southern Spain) in the geochemical signature of the magmatism recorded in the SCLM of the westernmost Mediterranean, and in the Miocene Alborán Sea basin volcanism, this thesis presents a detailed trace element and Sr-Nd-Pb isotope study of the western Alpujárride metamorphic basement and the pre-Miocene Flysch sediments. The results indicate that Nd model ages are consistent with an increasing detrital input from the Alborán domain to the Flysch Trough in the western Mediterranean during the late Oligocene. The Alpujárride metamorphic crustal rocks derived from Archean-Paleoproterozoic terranes located along the northern margin of Gondwana in the Neoproterozoic. The heterogeneous isotopic signatures of the Alpujárride units indicate that

they have different sedimentary protoliths and underwent contrasted Variscan and pre-Variscan tectono-magmatic evolutions. Melts/fluids derived from the western Alpujárride gneisses contaminated the mantle source of the Ronda high-Mg pyroxenite dykes, implying that the Alpujárride lower crust underthrusted the subcontinental lithospheric mantle of the Alborán domain generating subduction-like magmatism in the late Oligocene. The western Alpujárride upper crust is involved in the Neogene volcanism of the Alborán Sea basin, but only contaminated some LREE-enriched calc-alkaline lavas during their ascent close to the continental margins. On the other hand, tholeiitic lavas in the centre of the basin show no isotopic evidence of crustal assimilation. This indicates that most of the crust in the central Alborán Sea accreted by Miocene tholeiitic magmatism and that Alpujárride lower crust is absent and likely foundered close to the continental margins of the basin.

***Keywords**: Beni Bousera; garnet pyroxenites; geochemical modelling; lherzolite; mantle refertilization; Nd model age; orogenic peridotite massifs; recycled crust; Ronda; Sr-Nd-Pb-Hf radiogenic isotopes; westernmost Mediterranean.*

Resumen extendido

Comprender los mecanismos y procesos responsables de la formación de las heterogeneidades del manto es crucial para poder avanzar en nuestro conocimiento sobre la composición y diferenciación de la Tierra a diferentes escalas. Los macizos peridotíticos orogénicos ofrecen una oportunidad excepcional para investigar *in situ* la naturaleza y escala de las heterogeneidades composicionales del manto. Esta tesis doctoral tiene como objetivo principal arrojar luz sobre el papel que juegan los procesos de reacción fundido-roca y el reciclaje de corteza oceánica y continental en la generación de las heterogeneidades químicas del manto. Con este objetivo, este trabajo investiga la composición de las rocas mantélicas que afloran en los macizos peridotíticos de la Cordillera Bético-Rifeña en el Mediterráneo occidental y de las rocas corticales asociadas. En esta tesis doctoral se han investigado dos procesos potenciales para la formación de heterogeneidades químicas en el manto terrestre: (i) la formación de lherzolitas secundarias por procesos de reacción de fundidos con peridotitas residuales del manto, y (ii) la formación de piroxenitas con granate de ultra-alta presión y su relación con el reciclaje de corteza oceánica subducida en el manto terrestre. Finalmente, la evolución Alpina del Mediterráneo occidental registra una historia compleja de subducción y extensión que acabó formando la cuenca del Mar de Alborán y el estrecho de Gibraltar. Las rocas mantélicas de la Cordillera Bético-Rifeña —y rocas corticales asociadas— constituyen, por tanto, un laboratorio natural ideal para investigar a gran escala los procesos de reciclaje de corteza en el manto terrestre. Con este objetivo, en esta tesis doctoral se ha investigado el papel potencial del reciclaje de rocas corticales de la Cordillera Bética en la signatura geoquímica del magmatismo registrado en el manto litosférico subcontinental (MLSC) y del volcanismo Mioceno de la cuenca del Mar de Alborán.

Los resultados de la investigación de los procesos de reacción fundido-roca en el MLSC presentados en esta tesis se sustentan en una extensa base de datos geoquímicos de muestras de peridotitas provenientes de los cuatro dominios tectono-metamórficos del macizo orogénico de Beni Bousera (Cordillera Rifeña, norte de Marruecos). Este estudio revela que en las muestras de lherzolitas las variaciones de las proporciones modales, del número de magnesio (Mg-no.), de la composición de los elementos mayores y menores en roca total, y de los elementos trazas

en clinopiroxenos, son inconsistentes con un simple proceso de fusión parcial. Estas variaciones indican que las lherzolitas son peridotitas secundarias que se formaron por procesos de refertilización magmática en el manto mediante reacción de fundidos basálticos con peridotitas residuales. Por otra parte, las variaciones composicionales de la mayoría de las muestras de harzburgitas se pueden explicar por tasas de fusión parcial de hasta un 30% a presiones < 3 GPa y por metasomatismo críptico. En el dominio de las milonitas con granate y espinela, los procesos de fusión y reacción entre fundidos y peridotitas han sido enmascarados por la mezcla tectónica entre peridotitas y piroxenitas con granate y por transformaciones metamórficas. En el resto del macizo, las lherzolitas fueron principalmente producidas por reacciones magmáticas de refertilización a partir de un protolito de peridotita refractaria (Mg-no. ~ 91, olivino ~ 70%, clinopiroxeno/ortopiroxeno = 0.4). Estos procesos magmáticos de refertilización y formación de lherzolitas secundarias tuvieron lugar mediante dos tipos contrastados de reacciones entre rocas residuales y fundidos basálticos. Un primer tipo de reacción —que afectó a todas las peridotitas del macizo— fue de cristalización de clinopiroxeno y ortopiroxeno, y disolución de olivino. Esta reacción implicó razones de fundido/roca < 0.75 y una tasa variable de minerales cristalizados y fundido (R). El segundo tipo de reacción —que afectó principalmente a los dominios de Ariegita-Seiland y Seiland del macizo— tuvo lugar mediante la disolución de ortopiroxeno de las peridotitas residuales y la cristalización de clinopiroxeno y olivino secundarios. Esta reacción implicó razones fundido/roca ≤ 1 y $R = 0.2 – 0.3$. La distribución de lherzolitas secundarias en el macizo sugiere que la primera reacción de refertilización ocurrió antes de la individualización de los dominios tectono-metamórficos que ahora se observan en el macizo de Beni Bousera. Por otro lado, la segunda reacción de formación de peridotitas secundarias está probablemente asociada a procesos magmáticos de erosión del MLSC que condujeron a la formación de los dominios y la final exhumación del macizo en la corteza. Nuestro estudio demuestra que la mayoría de las lherzolitas de macizos de peridotitas orogénicas son secundarias y se formaron en el manto por procesos de refertilización magmática de peridotitas residuales.

La segunda parte de esta tesis investiga la génesis de las piroxenitas con granate de ultra-alta presión, y su relación con el componente cortical reciclado que se observa en los basaltos oceánicos. Esta investigación se ha realizado mediante un estudio geoquímico detallado de elementos mayores y trazas, e isótopos radiogénicos (Sr-Nd-Pb-Hf) en piroxenitas con granate de los macizos peridotíticos de Ronda y Beni Bousera (Cordillera Bético-Rifeña). Los resultados obtenidos muestran que las piroxenitas con granate analizadas no sólo derivan de

corteza oceánica reciclada, sino también de corteza continental inferior reciclada. Desde el punto de vista isotópico, este componente reciclado de corteza inferior está genéticamente relacionado con la corteza inferior espacialmente asociada a los macizos peridotíticos. Se cree que la corteza continental reciclada es la fuente del componente isotópico del manto enriquecido (EM) muestreado por algunos basaltos oceánicos. Esta nueva evidencia isotópica respalda aún más la hipótesis de que las piroxenitas con granate de ultra-alta presión podrían ser el mejor indicador natural de las heterogeneidades mantélicas muestreadas por los basaltos oceánicos y continentales. La existencia de una mezcla de componentes reciclados oceánicos y continentales en el MLSC requiere de una nueva receta para la formación de un manto heterogéneo tipo "Marble-Cake".

Por último, hemos investigado el papel que juegan las rocas corticales de la Cordillera Bética (sur de España) en la signatura geoquímica del magmatismo registrado en el MLSC del Mediterráneo occidental, y en el volcanismo Mioceno de la cuenca del Mar de Alborán. Este estudio se ha hecho mediante el análisis de los elementos traza e isótopos radiogénicos (Sr-Nd-Pb) de rocas corticales del Complejo Alpujárride occidental y de sedimentos pre-miocénicos del Flysch. Los resultados indican que las edades modelo de Nd de los sedimentos del Flysch son consistentes con un creciente aporte detrítico —derivado del dominio del Alborán— durante el Oligoceno tardío. Las rocas metamórficas corticales del Complejo Alpujárride derivan de terrenos Arcaicos-Paleoproterozoicos situados a lo largo del margen septentrional de Gondwana durante el Neoproterozoico. Las signaturas isotópicas heterogéneas de las unidades Alpújarride indican proveniencias sedimentarias diferentes y evoluciones tectono-magmáticas contrastantes durante y antes de la orogenia Varisca. Nuestros resultados también revelan que los fundidos/fluidos derivados de los gneises del Complejo Alpujárride occidental contaminaron la fuente mantélica de diques de piroxenitas, ricos en Mg, del macizo de Ronda. Esto implica que la corteza inferior del Complejo Alpujárride subdujo bajo el MLSC del dominio del Alborán, dando lugar en el Oligoceno tardío a un magmatismo similar al generado en una zona de arco. Finalmente, este estudio demuestra que lavas calco-alcalinas y enriquecidas en tierras raras ligeras, extruidas durante el Mioceno cerca de los márgenes continentales de la cuenca del Mar de Alborán, fueron contaminadas durante su ascenso por la corteza superior del Complejo Alpujárride occidental. Por otra parte, lavas toleíticas extruidas en el centro de la cuenca no muestran evidencia isotópica de asimilación cortical. Esto indica que la mayoría de la corteza en el centro de la cuenca del Mar de Alborán se formó por magmatismo toleítico durante el Mioceno, y que existe una ausencia de corteza inferior del

Complejo Alpujárride alrededor de los márgenes continentales de la cuenca, implicando una posible delaminación de la corteza inferior.

***Palabras claves**: manto terrestre; macizos de peridotitas orogénicas; Ronda; Beni Bousera; Mediterráneo occidental; reciclaje de corteza; isótopos radiogénicos de Sr-Nd-Pb-Hf; lherzolitas secundarias; modelización geoquímica; piroxenitas con granate; refertilización del manto.*

AGRADECIMIENTOS — ACKNOWLEDGEMENTS

En primer lugar, quisiera agradecer a mis directores de tesis, **Carlos J. Garrido Marín** y **Claudio Marchesi**. Mucho de lo que hoy sé (y las dudas que me quedan) sobre el manto, y sobre el lío de las Béticas se los debo a ustedes. Gracias por la infinidad de horas dedicadas, la paciencia, y sobre todo por creer en mí. Siempre he podido contar con ustedes, tanto a nivel profesional como personal, y eso ha marcado toda la diferencia. **Carlos,** te agradezco el haber confiado en mí para este proyecto, por compartir tus conocimientos y manera de trabajar, y, sobre todo, por darme la posibilidad de ser parte de este gran equipo. Dicen que "*la tarea de un líder es llevar a su gente de donde está hasta donde no haya llegado jamás*" —Henry Kissinger— y yo termino este proceso con la certeza de haber logrado lo inimaginable. Por eso y por mucho más, gracias. **Claudio**, a ti quiero agradecerte por tu apoyo y guía constante en este viaje. Gracias por tu tiempo, tus enseñanzas, y por aguantarme en todos estos años. ¿Qué voy a hacer ahora sin mi compañero de revisión de papers? ¿Con quién pasaré horas frente al computador revisando que todo este perfecto? Sin duda, he tenido mucha suerte por tenerte como director. Nuevamente, infinitas gracias a los dos.

I would also like to thank **Delphine Bosch,** who showed me the amazing world of the clean lab. This thesis would not have been possible without your constant guidance. Thank you so much for welcoming me with open arms when I arrived to Montpellier, for having taught me how to work in the clean lab and about the isotope world, something that I now love, and for all your support during these years. You are a truly wonderful person and I got the joy of having learnt from you.

Agradezco también a **Vicente López Sánchez-Vizcaino**, **Fernando Gervilla**, **Alessandra Montanini** y **Theodoros Ntaflos** por aceptar participar como tribunal de esta tesis y por su interés en este trabajo.

Esta tesis no hubiera sido posible sin la gran ayuda de **Károly**, **Amel, Alpi, Antonio** y **Chari**. Gracias chicos por toda la ayuda que me han brindado, por sacarme de tantos apuros y por simplemente ser como son. **Inma**, aunque llegaste más tarde al grupo, haces que venir a trabajar siempre sea más ameno. Muchas gracias por tu apoyo en este tiempo y por tu sonrisa constante. Termino esta etapa con el corazón llenito por haber podido trabajar y compartir con ustedes.

No podría haber llegado a este punto sin el apoyo de mis amigos *granainos*, que de *granainos* poco y nada tienen. Gracias **Ari, Patricia**, **Chiara, Mapi** (María Pilar miles de gracias por ayudarme con **Nono** a moler rocas en esos días de tensión, sin su ayuda no hubiera terminado nunca!)**, Marga, Jp, Enric, Muntsa** y **Lluis** por todas las juntaciones, las cervecitas compartidas y la petanca ♥. Mención especial se llevan mis coachings **Marga** y **JP**, siempre dispuestos a entregar sus palabras de sabiduría a este "proyecto de investigadora". Gracias a todos por compartir sus días conmigo.

Siempre tuve un pedacito de Chile conmigo gracias a **Mauri**, **Miguel** y el ya retornado **Juan**. Nos conocimos muy lejos de nuestra tierra natal, pero desde que los conocí siempre he podido contar con ustedes. No sé cómo agradecerles todo lo vivido, más que mis amigos, hoy son mi familia. Gracias chicos por estar ahí.

A **Inma Marquez**, gracias por abrirme las puertas de tu casa cuando lo necesite; a **Maribel** por toda la increíble ayuda que me has prestado, siempre con el corazón abierto y sin esperar nada a cambio; a **Mar**, por ser como eres, esa intensa y hermosa mujer que no dudo un segundo en darme su amistad al poco de conocernos; a **Carmina**, por todas las conversaciones de pasillo y los momentos compartidos. Infinitas gracias.

A mis queridísimos compañeros de comidas en estos años. Las repetidas **Ari, Marga, Enric y Carmina; Nieves**, **Claudia**, **Luis**, **Alberto**, **Adrián**, **Nicole**, **Manuel**, **Rubén**, **Zita, Rita, Annika** y **Marta.** Gracias por hacerme olvidar por una hora diariamente del trabajo, por compartir historias, recetas, viajes, ideas, alegrías y tristezas. Gracias por alegrar mis días, espero también yo haberles aportado un granito de arena.

Dear **Laure** and **Anais**, you were my light in the dark. I can never thank you enough for all your support during my stay in Montpellier. If it wasn't for you guys, I will have been a lonely soul in that university, but you were always friendly to me, since day one…and that will stay with me forever. Today I can say I have two amazing and young friends in that land called France. Thank you so much for all what you gave me and you know you can always count on me.

Queridísimas **Ani** y **María**, aun doy gracias al universo por ponerlas en mi camino al poco de tiempo de haber llegado a Granada. Antes de venir a España, pensaba lo difícil que sería tener a mi familia lejos, pero gracias a ustedes, mis hermanas del alma, hoy tengo una segunda familia. Gracias por todos los momentos compartidos, por las risas y los llantos, sin duda son uno de mis tesoros *granainos* más grandes.

Quisiera también agradecer a mi hermosa familia por su apoyo y amor incondicional. En especial, a mis padres, **Jaime y Marcia**, por siempre creer en mí y alentarme a seguir mis sueños, aunque eso significara estar separados. Gracias por ser mi refugio, sin ustedes hoy no estaría aquí. A mis hermanos **Alejandra y Jaime**, a mi cuñado **Francisco** y a mis sobris **Diego e Isabel (**que han tenido que crecer con una tía virtual), miles de gracias por siempre estar presentes, por darse el tiempo de conectarse (mención especial a Skype) y por contarme de sus días. Aunque nos separen unos cuantos kilómetros, yo siempre los siento cerca.

Finalmente, a **Daniel**. Gracias por aparecer en mi vida y quedarte; por toda tu paciencia, apoyo y amor en estos años. Gracias por quererme tal como soy, por soportar mis conversaciones geológicas, por sacarme una sonrisa aun en esos días en que parece que todo va mal, por ser mi traductor personal y simplemente por acompañarme en este camino. Nunca terminaré de agradecer tenerte a mi lado. Tú eres, sin duda, el mejor regalo que me ha dado esta tesis.

Este viaje que comenzó hace 5 años parece mentira que hoy termina. Ha sido un viaje intenso, aventurero, agotador, pero lo mejor de todo ha sido la compañía. Agradezco a la vida por haberme dado la oportunidad de conocer a gente tan increíble y maravillosa durante estos años. Perdonen si dejo a alguien en el tintero, pero que sepan que los llevo a todos en mi corazón.

Con cariño,

María Isabel Varas Reus

Granada, diciembre 2016

Gracias por todas las noches que se hicieron mañanas, por esos amigos que se hicieron familia y por todos aquellos sueños que se hicieron realidad

Anónimo

TABLE OF CONTENTS

Part I

Introduction, Aims and Thesis Structure, and Methodology

1 Introduction

1.1 General considerations

Unraveling the composition and evolution of the mantle of terrestrial planets is critical for our understanding of their origin and differentiation. Plate tectonics makes Earth a unique planet in our Solar System (Schubert *et al.*, 2001) and leads to important physical and chemical differences between continents and seafloors. With the recognition that new crust is being continually created at ocean ridges and destroyed and recycled by subduction into the Earth's mantle at convergent margins, plate tectonics theory has led to the realization that the Earth's interior must be highly heterogeneous in composition. Therefore, understanding the mechanisms and processes responsible for mantle heterogeneities is crucial for improving our knowledge about the composition and differentiation of the planet at different scales.

Orogenic peridotite massifs —large pieces of subcontinental lithospheric mantle (SCLM) tectonically emplaced into the crust (Bodinier & Godard, 2014)— provide an exceptional opportunity to investigate *in situ* the nature and scale of compositional heterogeneities in the Earth's mantle. This Ph.D. thesis aims to constrain the nature and origin of mantle heterogeneities through a detailed elemental and Sr-Nd-Pb-Hf isotopic study of peridotites and pyroxenites from the Beni Bousera (northern Morocco) and Ronda (southern Spain) peridotite massifs (Fig. 1.1), as well as of the crustal section spatially-associated with the Ronda massif (i.e., the western Alpujárride complex and the pre-Miocene Flysch Trough units of the Betic Cordillera) (c.f. Sec. 1.4). This thesis focuses on two processes that have been invoked as those responsible for the generation of compositional heterogeneities in the mantle: melt-rock reactions (e.g., Becker, 1996a; Lenoir *et al.*, 2001; Müntener *et al.*, 2004; Niu, 2004; Rampone *et al.*, 2004; Ionov *et al.*, 2005; Le Roux *et al.*, 2007) and recycling of oceanic and continental crust (e.g., Hofmann & White, 1982; Chauvel *et al.*, 1992; Hart *et al.*, 1992; Helffrich & Wood, 2001; Davies, 2002; Workman *et al.*, 2008; Willbold & Stracke, 2010; Hofmann, 2014; van Keken *et al.*, 2014).

Some of the questions addressed in this work are: *What is the main cause of the generally fertile compositions of SCLM peridotites? How recycled oceanic and continental*

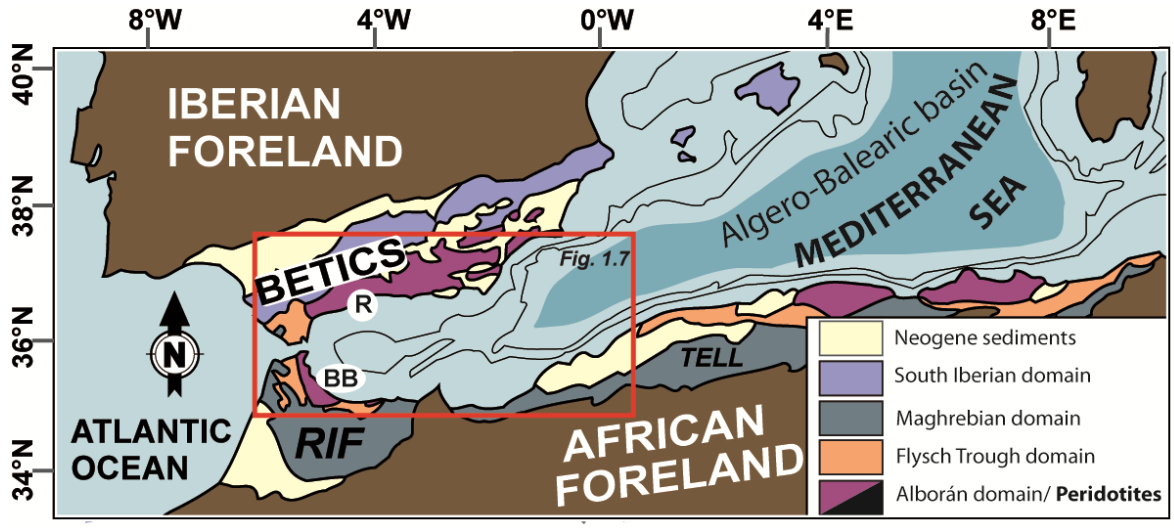

Figure 1.1 *Simplified geological map of the westernmost Mediterranean termination of the circum-Mediterranean Alpine belt showing the location of the Ronda (R) and Beni Bousera (BB) peridotites. Inset shows the location of Fig. 1.7a.*

crust gets intimately mixed in the mantle sampled by orogenic peridotite massifs? Are crustal components recorded in the composition of magmatic rocks "exotic" or genetically related to the lithospheric section associated with orogenic peridotites?

1.2 Origin and differentiation of the Earth's interior

Before discussing the origin and evolution of compositional heterogeneities in the SCLM, it is necessary to have a general understanding of the internal structure and composition of the Earth's interior. This information provides a general framework for interpreting the geochemical messages from orogenic peridotite massifs.

Seismological data have shown that the Earth's interior is differentiated into three main layers: the crust, the mantle and the core (Fig. 1.2). This layered structure is the result of two fundamental processes: (1) the formation of a metal core very early in the history of the Earth, which ended at ~30 million years after the beginning of the solar system, and (2) the formation of the continental crust by partial melting of the silicate mantle, a process that occurred with variable intensity throughout the Earth's history (Bina & Helffrich, 2014, and references therein).

The mantle is about 2900 km thick, constitutes over 80% of the Earth's volume and 65% of its mass, and comprises virtually all the silicate part of the Earth (Helffrich & Wood, 2001).

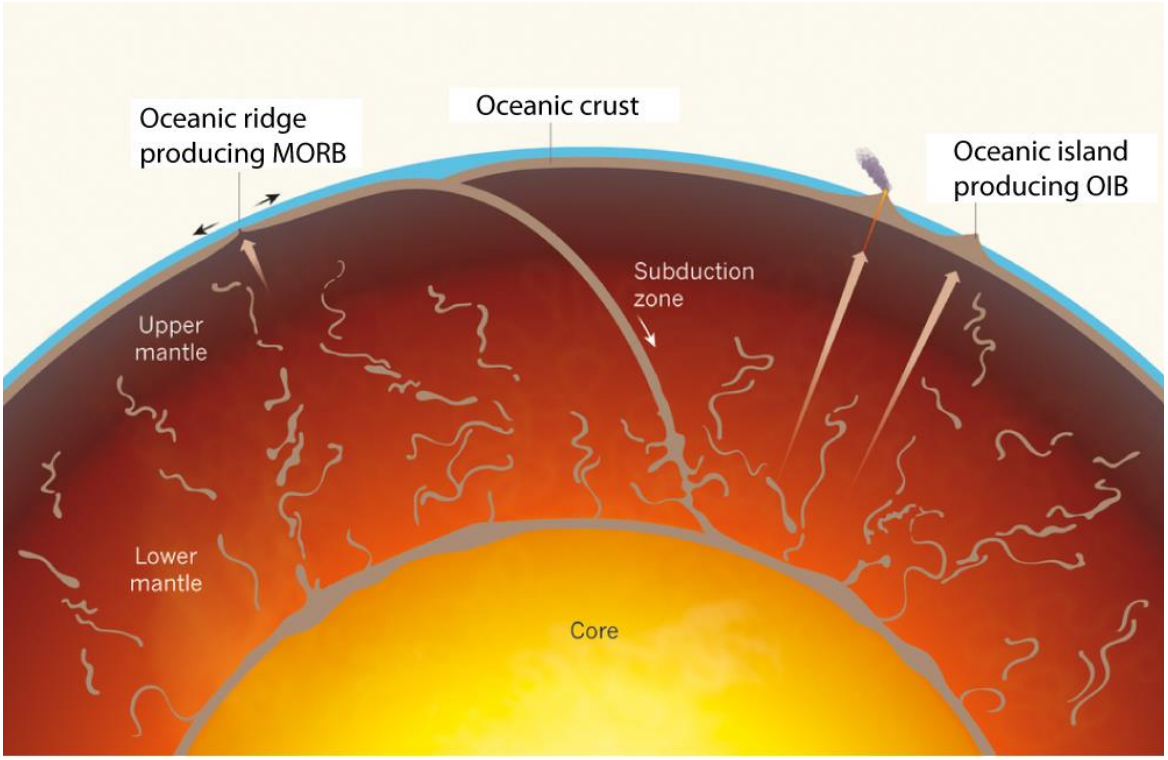

Figure 1.2 *Oceanic crust (brown) is 'recycled' into the Earth's mantle at convergent plate boundaries (subduction zones). Over time, this crustal-recycling process and melt-rock reactions formed a chemically heterogeneous mantle. Generation of mid-ocean-ridge basalts (MORBs) is represented by a short brown arrow and that of ocean island basalts (OIBs) by long brown arrows. Image from Woodhead (2015).*

Several distinct seismic discontinuities identify different domains in the mantle (McDonough & Sun, 1995; Helffrich & Wood, 2001), which are, from the crust to the core (Fig. 1.3):

a) The upper mantle. This is the most studied and best understood part of the mantle. It is separated from the Earth's crust by the Mohorovicic discontinuity ("Moho"), and includes the mantle up to the 410 km deep seismic discontinuity.

b) The transition zone. It is located between the 410 and 660 km seismic discontinuities. This domain has a distinct mineralogy, a stronger seismic velocity gradient and different physical characteristics compared to the upper mantle.

c) The lower mantle. Most of our knowledge of this layer is generally restricted to information derived from seismology, mineral physics and fluid dynamic experiments (McDonough & Sun, 1995). This domain is located below the 660 km discontinuity and its seismic velocities increase monotonically with depth up to the D´´ region (~ 2700 km deep) (Helffrich & Wood, 2001).

d) The D´´ region, which comprises the mantle region about 200 km above the core-mantle boundary and it is denser than the other mantle layers (Davies, 2011, and references therein).

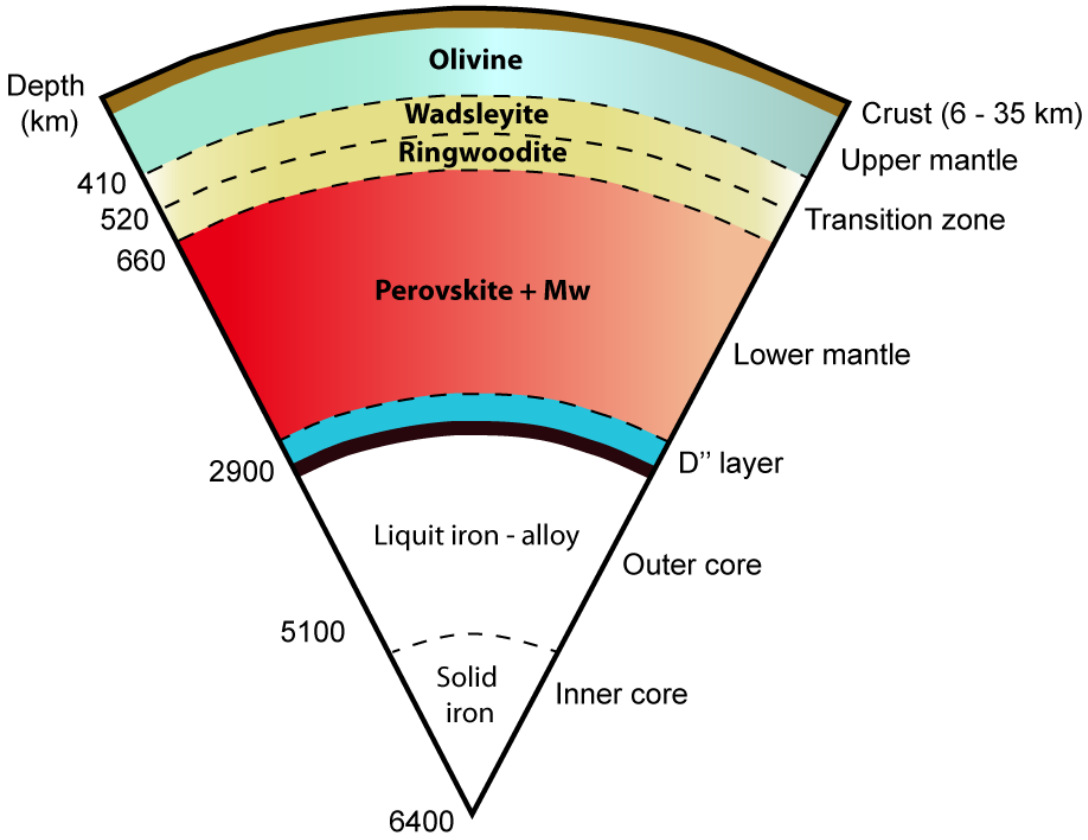

Figure 1.3 *Cartoon representing the Earth's internal structure and changes of mineral assemblage with depth. The seismological boundaries are delineated in the solid Earth. Modified from Yuen et al. (2007).*

1.2.1 The upper mantle

1.2.1.1 Upper mantle composition

Most of the information used for estimating the composition of the mantle derives from seismology, cosmochemical data, and mantle-derived rocks (Helffrich & Wood, 2001; Schubert *et al.*, 2001; Davies, 2011; Bina & Helffrich, 2014; Bodinier & Godard, 2014; Hofmann, 2014). The latter are mainly rocks from the upper mantle, which are predominantly peridotites, and, to a lesser extent, mafic rocks generally identified as pyroxenites and eclogites (McDonough & Frey, 1989; McDonough & Sun, 1995). Direct sampling of upper mantle rocks is limited to tectonically emplaced mantle portions, including orogenic, ophiolitic and abyssal peridotites (Bodinier & Godard, 2014), and xenoliths transported to the surface by magmas (Pearson *et al.*, 2014). On the other hand, samples of the transition zone and lower mantle have been recognized as inclusions in diamonds and polymineralic fragments in kimberlites (McDonough & Sun, 1995, and references therein).

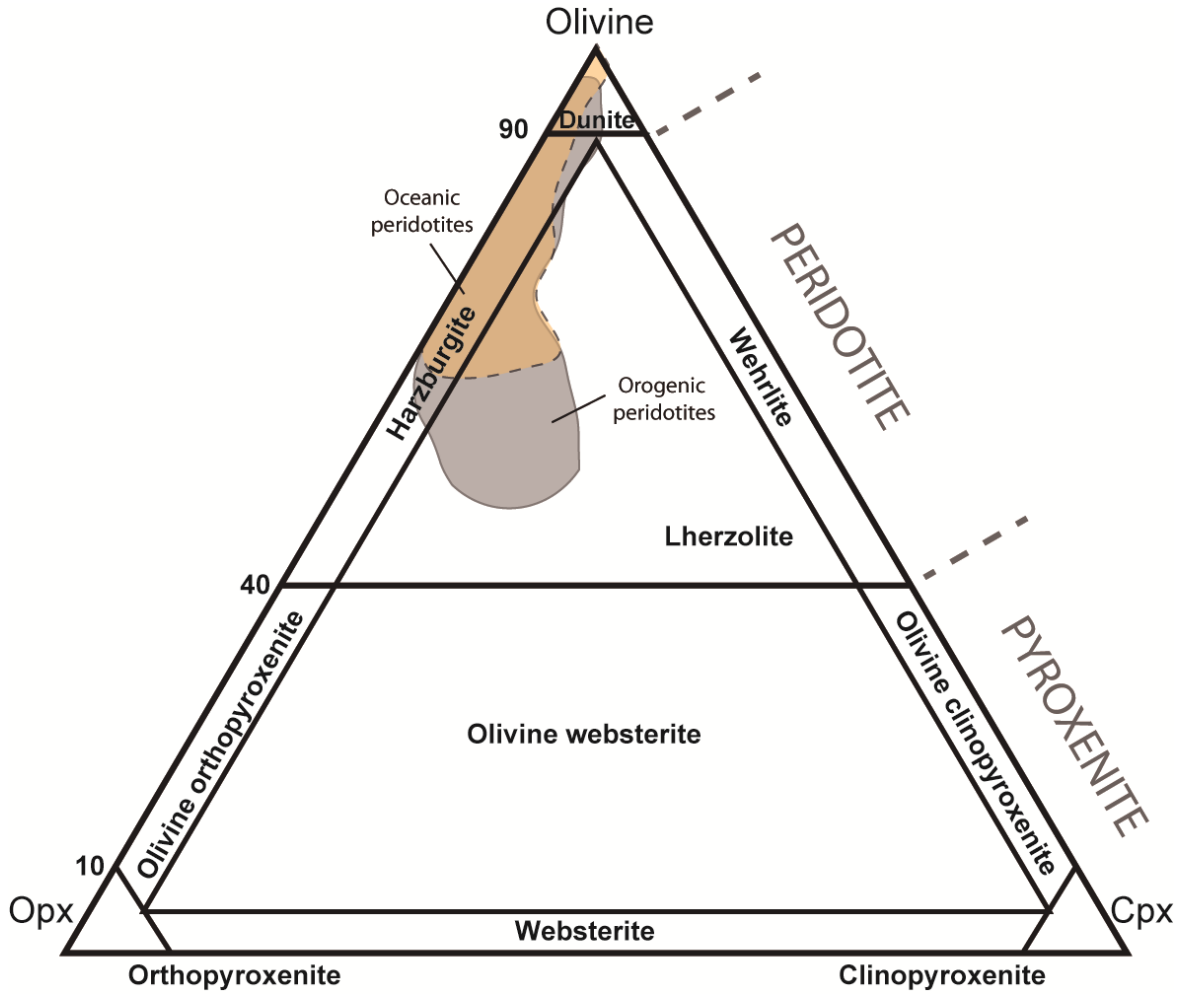

Figure 1.4 *Modal classification diagram for peridotites and pyroxenites, based on proportions of olivine and pyroxene. The grey area encompasses the most common compositions of orogenic peridotites and the orange area those of oceanic peridotites (modified after Bodinier & Godard, 2014).*

Typical mantle peridotites contain more than 50% olivine, variable amounts of pyroxenes (Fig. 1.4), and an aluminous phase that is dependent on the pressure at which the peridotite equilibrated (plagioclase at less than ~ 1 GPa, spinel at ~ 1 – 2.5 GPa and garnet at > 2.5 GPa) (Bodinier & Godard, 2014). Olivine also undergoes successive pressure-dependent transformations and is replaced by its polymorphs wadsleyite (also called "modified spinel") at 13 – 14 GPa and 410 km depth, ringwoodite (also called "silicate spinel") at 18 GPa and 520 km depth, and ultimately, at 23 GPa and 660 km depth, it breaks down to form a mixture of silicate perovskite and magnesiowüstite (Fig. 1.3) (Helffrich & Wood, 2001).

1.2.1.2 Upper mantle structure and mantle convection

Two layers are distinguished in the upper mantle according to their rheological behavior: the lithosphere, formed by the relatively rigid uppermost mantle plus the overlying crust, and the

asthenosphere, which is the highly viscous, mechanically weak and ductile region underlying the lithosphere (e.g., Hofmann, 1997). The lithosphere is subdivided into tectonic plates that can sustain long-term stresses, while the asthenosphere flows readily at much lower stress levels due to higher pressure-temperature conditions (Anderson, 1995). Mantle convection stirs the Earth's interior, including recycled material, and is the driving mechanism for plate tectonics and associated geological activity on the Earth's surface, including continental drift, earthquakes, volcanoes and mountain building. The slow motion of plates and the mantle is powered by radiogenic heating and by the slow cooling of the Earth over its 4.5 billion-year history (Tackley, 2000).

Different models have been proposed for mantle convection (see for example Hofmann, 1997 and Tackley, 2000). Geochemical constraints have favored models in which the mantle is chemically and dynamically layered, with the upper mantle being depleted in incompatible elements and the lower mantle being primitive and identical to the bulk silicate earth (BSE), i.e., the bulk Earth composition minus that of the core (e.g., van Keken *et al.*, 2014). However, this model is compromised by geophysical and geodynamic observations that indicate that significant mass-transfer occurs through the Earth's transition zone (e.g., Davies, 1998) and that seismic discontinuities are best explained by pressure-induced phase transformations (Fig. 1.3) —at least for the 410 and 660 km discontinuities— rather than by changes in mantle composition (Helffrich & Wood, 2001; Davies, 2011). These features favor whole-mantle instead of layered mantle convection. In addition, tomographic images evidence the existence of subducted lithosphere extending through the transition zone and deep into the lower mantle (Grand *et al.*, 1997; Zhao, 2004) (e.g., subducted oceanic crust in Fig. 1.2), implying that convection operates in a single layer.

1.2.1.3 Upper mantle heterogeneities

In the layered model of mantle convection (c.f. Sec. 1.2.1.2), mid-ocean ridge basalts (MORBs) are derived from a relatively homogeneous depleted upper mantle, which resulted by extraction of parental melts of the continental crust, whereas ocean island basalts (OIBs) are formed from reservoirs derived by mixing of the MORB source with more enriched sources (e.g., Hofmann, 1988). However, it is well known that the upper depleted mantle is continuously re-enriched in incompatible elements, which leads to an overall compositional heterogeneous upper mantle (e.g., Stracke, 2012).

The processes commonly invoked to explain the re-enrichment of the mantle in incompatible elements are: recycling of oceanic and continental crust (e.g., Hofmann & White, 1982; Chauvel *et al.*, 1992; Hart *et al.*, 1992; Helffrich & Wood, 2001; Davies, 2002; Workman *et al.*, 2008; Willbold & Stracke, 2010; Hofmann, 2014; van Keken *et al.*, 2014), delamination and foundering of the subcontinental lithosphere (e.g., McKenzie & O'Nions, 1983; Kay & Mahlburg Kay, 1993; Lustrino, 2005), and various types of metasomatism/refertilization induced by melt-rock reactions (e.g., Hart, 1988; Bodinier *et al.*, 1990; Garrido & Bodinier, 1999; Bodinier *et al.*, 2004; Marchesi *et al.*, 2013). Independent of the process, it has become clear that, with the exception of intra-mantle metasomatism, re-enrichment of the mantle principally occurs by large-scale chemical exchanges between the different silicate reservoirs of the Earth: the continental and oceanic crust and associated lithospheres, and the deep Earth's mantle (Stracke, 2012).

Due to the limited access to direct sampling, the composition of the mantle has been firstly studied through the investigation of oceanic basalts. Numerous chemical and isotopic analyses of these rocks have evidenced the Earth's mantle heterogeneity (e.g., Hauri & Hart, 1993; Hanan & Graham, 1996; Eisele *et al.*, 2002; Workman & Hart, 2005; Hofmann, 2014; Iwamori & Nakamura, 2015). The higher concentrations of incompatible elements in OIBs compared to MORBs, led Hofmann & White (1982) to argue that OIBs contain a component of old oceanic crust recycled in the mantle by subduction and subsequently incorporated in a mantle plume. MORBs and OIBs show a large isotopic variability (e.g., Hart, 1988; Hart *et al.*, 1992; Hofmann, 1997; Stracke *et al.*, 2005), which was used by Zindler & Hart (1986) to classify the Earth's mantle into a restricted number of large-scale reservoirs: DMM (depleted MORB mantle), HIMU (high μ; $\mu = {}^{238}U/{}^{204}Pb$), EM-1 and EM-2 (EM = enriched mantle) (Fig. 1.5). These authors proposed that mixing between these reservoirs explains most of the isotopic variability observed in oceanic basalts. However, several studies have shown that the mantle isotopic heterogeneity occurs at all spatial scales, from global (several thousands of kilometers) to μm-scale (Stracke, 2012, and references therein), implying that the mantle does not consist of separate kilometric reservoirs and that rather than represent a unique mixture between these end-member compositions, oceanic basalt sources have their own unique composition (Stracke *et al.*, 2003; Davies, 2011). These four mantle-reservoirs, however, remain useful to elucidate processes and types of basalt sources, rather than to individuate the specific composition of a melt source (Davies, 2011).

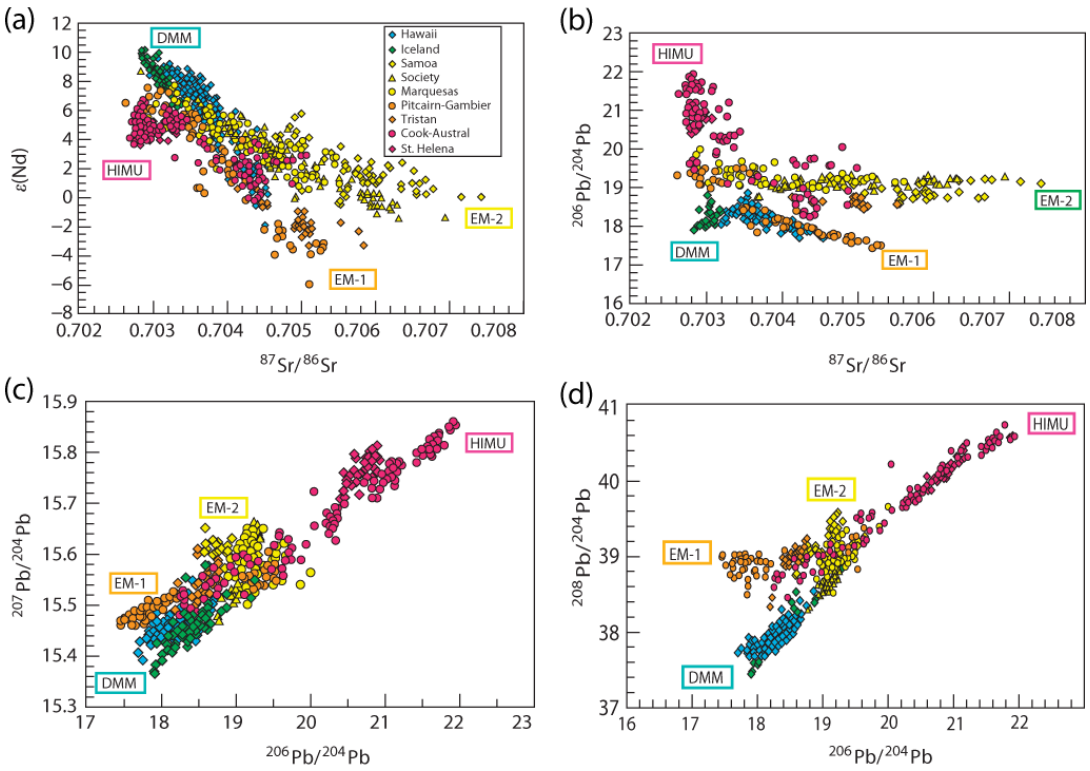

Figure 1.5 *a)* $^{87}Sr/^{86}Sr$ *vs* ε_{Nd}*; b)* $^{87}Sr/^{86}Sr$ *vs* $^{206}Pb/^{204}Pb$*; c)* $^{206}Pb/^{204}Pb$ *vs* $^{207}Pb/^{204}Pb$ *and d)* $^{206}Pb/^{204}Pb$ *vs* $^{208}Pb/^{204}Pb$ *for OIBs. The selected islands are chosen to represent extreme isotopic compositions. These basalts are from the "type localities" of HIMU (Cook-Austral Islands and St. Helena), EM-1 (Pitcairn-Gambier and Tristan) and EM-2 (Society Islands, Samoa and Marquesas) components (Hofmann, 2014).*

1.3 Orogenic peridotite massifs and the record of mantle heterogeneities

Orogenic peridotite massifs provide insights into upper mantle compositions and processes such as vein injection, melt-rock reaction and deformation. Several massifs are sufficiently well preserved to allow the observation of structural relationships between mantle lithologies, from cm– to km scales, and to evaluate the extent, scale and nature of mantle heterogeneities (Downes, 2001; Bodinier & Godard, 2014). Generally, these massifs are associated to continental crustal rocks recording extreme metamorphic conditions, from high temperature (HT) at intermediate or low pressure (LP) to high or ultra-high pressure (UHP) at variable temperature conditions (Bodinier & Godard, 2014). The Beni Bousera (Morocco), Ronda (Spain), Lanzo (Italy) and Lherz (France) massifs are some examples of orogenic peridotite outcrops in the world (Downes, 2001; Bodinier & Godard, 2014).

Orogenic peridotite massifs are mainly composed of lherzolites (equilibrated in the garnet-, spinel- or plagioclase-peridotite facies), harzburgites, and minor dunites (Fig. 1.4)

(Bodinier & Godard, 2014). These peridotites are commonly associated to layers —irregular bodies and dykes of mafic rocks— that are mainly pyroxenites (e.g., Garrido & Bodinier, 1999). Alike oceanic basalts (c.f. Sec. 1.2.1.3), orogenic peridotites are highly heterogeneous in composition, showing a large range of major and trace element and isotopic variability (Bodinier & Godard, 2014). Their chemical variations have been classically attributed to variable degrees of partial melting and melt extraction from the upper mantle. In this scenario, the most fertile lherzolites (> 10% modal clinopyroxene; Fig. 1.4) are interpreted as relatively pristine mantle weakly affected by partial melting, and harzburgites as products of high-degrees of melt extraction (Bodinier, 1988; Walter, 2014). However, several studies have shown that some orogenic fertile peridotites are the result of igneous refertilization rather than slightly melted pristine mantle (e.g., Lenoir *et al.*, 2001; Beyer *et al.*, 2006; Le Roux *et al.*, 2007, 2009). In order to elucidate how melt extraction and melt-rock reaction processes, involving mineral dissolution and/or precipitation and leading to depletion or refertilization, are recorded in the SCLM, I processed a large geochemical database of peridotites from the Beni Bousera orogenic massif (Fig. 1.1). The results, presented in Chapter 4, show that the Beni Bousera lherzolites have peculiar modal variations normally not observed in a unique orogenic massif, which were induced by two different melt-rock reactions causing pyroxene addition to a refractory mantle protolith. These data support a secondary, refertilization-related, origin for most lherzolites in orogenic peridotite massifs and provide general insights into melt-rock reactions in the mantle.

1.3.1 Pyroxenite layers: lithological evidence of mantle heterogeneity

Pyroxenite layers within orogenic peridotite massifs provide direct evidence of mantle compositional heterogeneity. They may constitute 2 to 5% of the Earth's upper mantle and locally up to 10% (Allègre & Turcotte, 1986). In detail, the origin of these pyroxenites is diverse (Pearson *et al.*, 1993; Becker, 1996b; Blichert-Toft *et al.*, 1999; Garrido & Bodinier, 1999; Downes, 2007; Gysi *et al.*, 2011; Bodinier & Godard, 2014; Montanini & Tribuzio, 2015), but a group of UHP (diamond-bearing) garnet pyroxenites shows isotopic and major element compositional variations similar to the "oceanic recycled crust" component observed in oceanic basalts (c.f. Sec. 1.2.1.3) (Pearson *et al.*, 1989; Davies *et al.*, 1993; Pearson *et al.*, 1993; Morishita *et al.*, 2003; Pearson & Nowell, 2004).

In the Beni Bousera massif (Fig. 1.1), highly-stretched UHP garnet pyroxenites are tectonically mixed with peridotites at different length-scales (Kornprobst, 1969; Pearson *et al.*, 1989; El Atrassi *et al.*, 2011; Gysi *et al.*, 2011; Frets *et al.*, 2014). Such outcrops inspired the

"Marble Cake Mantle" model (Allègre & Turcotte, 1986), which interprets the mantle source of oceanic basalts like a "marble cake" of intermixed peridotite-pyroxenite components, where pyroxenites constitute subducted old oceanic crust mixed with the Earth's peridotitic mantle by convection processes (Fig. 1.6). The Sr-Nd-Pb-Hf isotopic compositions and old Re-Os depletion ages (1.1 – 1.4 Ga) of UHP garnet pyroxenite layers from the Beni Bousera and Ronda peridotite massifs (Fig. 1.1) (Reisberg *et al.*, 1991; Pearson & Nowell, 2004; Downes, 2007) are consistent with the expected isotopic variability and timescale for oceanic crustal recycling in the Earth's mantle.

New geochemical evidence in mantle pyroxenites indicates, however, that they may not derive only from recycled oceanic crust, but also from recycled lower continental crust (e.g., Santos *et al.*, 2002; Xu, 2002; Svojtka *et al.*, 2016). Recycled continental crust is often invoked as the source of the enriched mantle isotopic component sampled by some oceanic basalts (e.g., McKenzie & O'Nions, 1983; Kay & Mahlburg Kay, 1993; Helffrich & Wood, 2001; Lustrino, 2005; Workman *et al.*, 2008; Willbold & Stracke, 2010; Hofmann, 2014). These new data provide further support to the hypothesis that orogenic pyroxenites, which are preferentially melted owing to lower solidus temperature and higher melt productivities compared to their host peridotites (e.g., Hirschmann & Stolper, 1996; Pertermann & Hirschmann, 2003, Lambart *et al.*, 2009), are a proxy of the mantle enriched component sampled by oceanic and continental basalts (Hirschmann & Stolper, 1996; Hirschmann *et al.*, 2003; Kogiso *et al.*, 2003; Pertermann

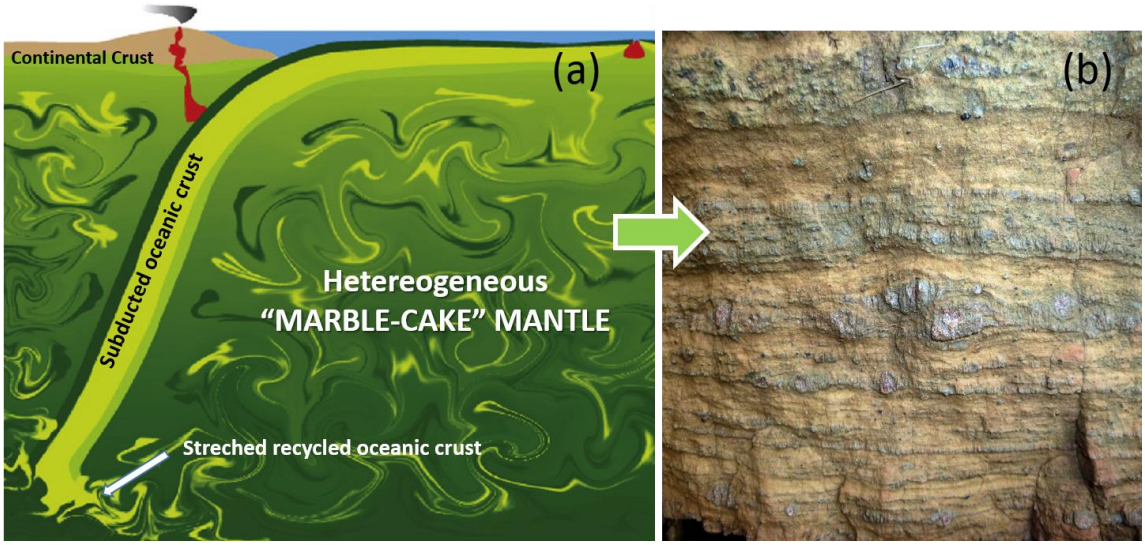

Figure 1.6 *a) Cartoon of the "Marble Cake Mantle" model where the Earth mantle is composed of a mixture of peridotite (dark green) and stretched recycled oceanic crust (light green) (modified from Xu et al., 2008); (b) boudins and layers of highly stretched ultra-high pressure garnet pyroxenites (red=garnet; dark greenish= pyroxene rich layers) in a matrix of peridotite (light brown).*

& Hirschmann, 2003; Kogiso *et al.*, 2004; Lambart *et al.*, 2009, 2012; Marchesi *et al*., 2013; Montanini & Tribuzio, 2015; Lambart *et al.*, 2016). Therefore, the study of orogenic mantle pyroxenites and their allied crustal units is key to unravel the petrogenesis of mantle rocks and basalts, and the chemical and geodynamical evolutions of the Earth's mantle-crust system.

To provide further constraints on how compositional heterogeneities are produced and crustal components are introduced into the mantle, Chapter 5 presents the results of bulk rock major and trace element and Sr-Nd-Pb-Hf isotopic analyses of garnet pyroxenites from the Ronda and Beni Bousera peridotite massifs (Fig. 1.1). The results show that the protoliths of orogenic garnet pyroxenites derived from recycled oceanic and continental sources, implying the need of a new "recipe" to stir the Earth's Marble Cake Mantle. On the other hand, Chapter 6 provides the results of a trace element and Sr-Nd-Pb isotopic study of the western Alpujárride metamorphic basement and the pre-Miocene Flysch sediments of the Betic Cordillera (southern Spain) (Fig. 1.1). These data are used to discuss the recycling of continental crustal units spatially-associated to orogenic peridotite massifs and its influence in the composition of mantle-derived rocks. In addition, these data allow constraining the provenance and evolution of these crustal units.

1.4 Geological setting

1.4.1 The Betic-Rif belt

The western Mediterranean underwent a complex Alpine tectonic evolution that mainly consisted of oceanic subduction initiation, slab fragmentation, and slab rollback during convergence between Africa and Europe (Royden, 1993; Chalouan & Michard, 2004; Faccenna *et al.*, 2004; Mauffret *et al.*, 2007; Platt *et al.*, 2013; van Hinsbergen *et al.*, 2014). In the westernmost Mediterranean, the Alpine orogeny shaped the Gibraltar tight arc, which is bounded by the Betic and Rif belts that surround the Alborán basin (Figs. 1.1 & 1.7a). The rocks of the Betic-Rif belt have been divided into three main tectonic-paleogeographic domains: the External Zones, the Flysch Trough units and the Internal Zones (Figs. 1.1 & 1.7a) (Platt *et al.*, 2013, and references therein). The latter are mostly included in an allochthonous lithospheric domain (the Alborán domain) that collided and overthrusted Mesozoic and Tertiary sedimentary rocks of the South Iberian (Betics) and Maghrebian (Rif) continental paleomargins (Figs. 1.1 & 1.7a). As result of this evolution, portions of the SCLM accreted into the internal crustal units of the Betic and Rif belts, and are exposed in the Ronda (S. Spain) and Beni

Bousera (N. Morocco) peridotite massifs (Fig. 1.7a) (Reuber *et al.*, 1982; Leblanc & Temagoult, 1989; Bruguier *et al.*, 2009; Afiri *et al.*, 2011; Garrido *et al.*, 2011; Hidas *et al.*, 2013; Frets *et al.*, 2014).

1.4.2 The Betic orogenic belt

1.4.2.1 The External Zones

The External Zones consist of a thin-skinned fold-and thrust belt oriented towards SW in the Betics, the S across the Strait of Gibraltar and in the northern Rif, and towards SE in the southern Rif (Fig. 1.1). In the Betics, the External Zones are composed of non-metamorphic Triassic to Miocene sedimentary rocks derived from the south Iberian paleomargin (Figs. 1.1 & 1.7). Presently, the External Betics are divided in the Prebetic and Subbetic domains (Lonergan & White, 1997; Platt *et al.*, 2013, and references therein).

1.4.2.2 The Flysch Trough units

The Flysch Trough units derived from sediments deposited in an oceanic basin underlain by a thinned continental or oceanic crust (Durand-Delga *et al.*, 2000; Guerrera *et al.*, 2005). These units expand from the NW African margin and can be followed across the Strait of Gibraltar into the westernmost Betics, where they crop out below the Alborán domain and above the South Iberian paleomargin units (Fig. 1.7).

In the Betics, the Flysch units comprise Cretaceous to Miocene siliciclastic and calcareous turbidites. These sedimentary sequences are commonly subdivided into the Aljibe, Algeciras (both Late Cretaceous to late Burdigalian), and Bolonia (Late Cretaceous to Aquitanian) units (Guerrera *et al.*, 2005; Luján *et al.*, 2006; Crespo-Blanc *et al.*, 2012). The Late Cretaceous to Paleogene material is mainly composed of quartz-rich sediments with a detrital input derived from African sources, whereas the detrital components of the late Oligocene to early Miocene sequence have been ascribed to the African craton for the Aljibe unit, the erosion of the Alborán domain upper crust for the Algeciras unit, and to Alborán and/or African sources for the Bolonia unit (Guerrera *et al.*, 2005; Luján *et al.*, 2006).

1.4.2.3 The Internal Zones: the Alborán domain

Traditionally, the Betic Internal Zones, which are divided (from top to bottom) into the Maláguide, Alpujárride and Nevado-Filábride complexes (Fig. 1.7a), have been included in the allochthonous lithospheric Alborán domain (Balanyá *et al.*, 1997; Hidas *et al.*, 2013; Platt *et*

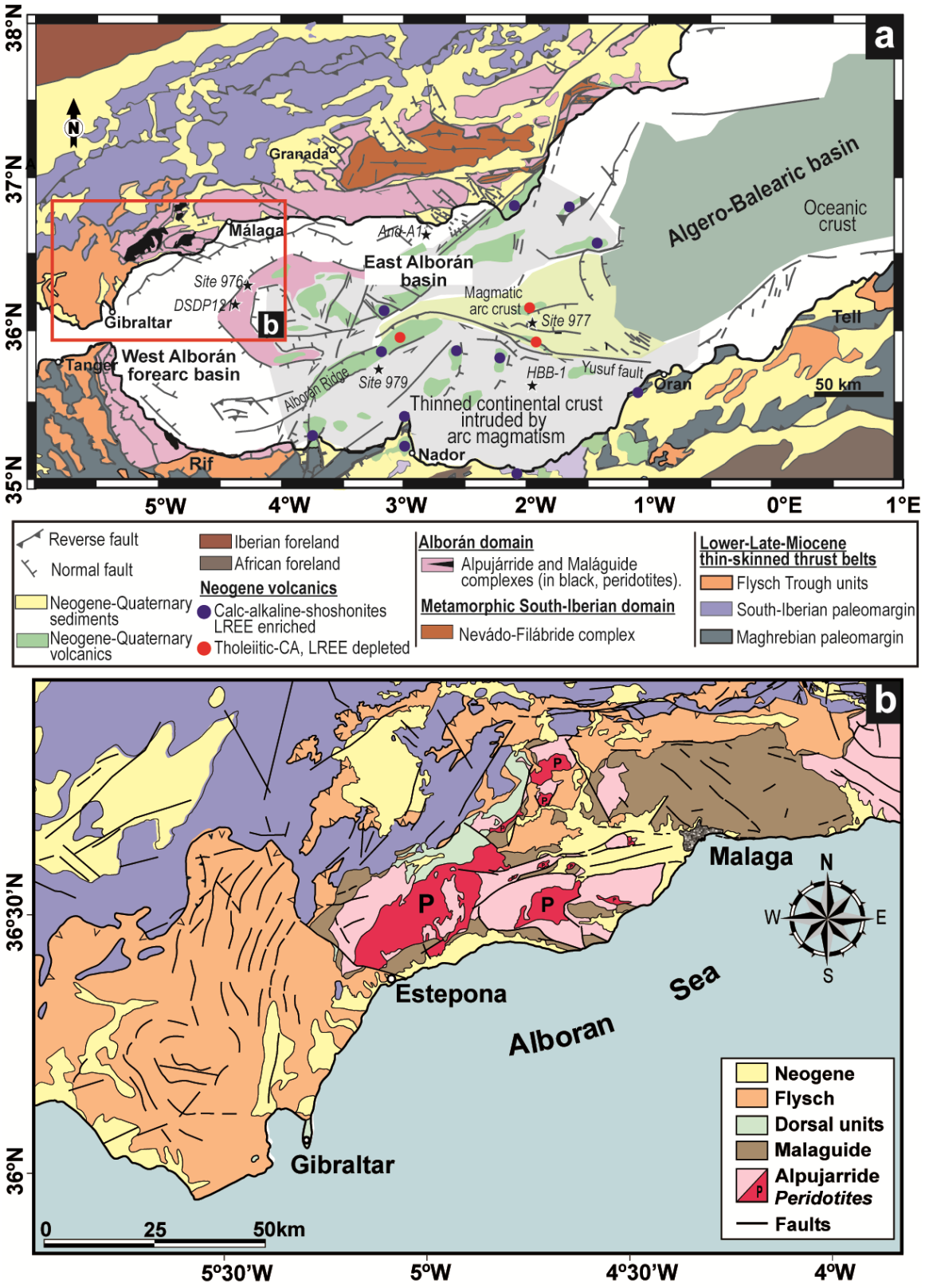

Figure 1.7 *(a) Simplified geological map of the westernmost Mediterranean showing the main tectonic-paleogeographic domains of the Betic-Rif belt and the areas of oceanic crust, magmatic arc, and thin continental crust in the Alborán basin (modified after Booth-Rea et al., 2007, and references therein). Inset shows the location of the area enlarged in (b).*

al., 2013). However, other studies have concluded that the Nevado-Filábride complex, which is absent in the Rif and only exposed in the central and eastern sectors of the Betics (Fig. 1.7a), is formed by rocks of the Iberian paleomargin subducted to HP beneath the Alborán domain, including a Paleozoic basement and part of its Mesozoic cover (Booth-Rea *et al.*, 2005, 2015, Mancilla *et al.*, 2015). Therefore, in this work only the Maláguide and Alpujárride complexes, and the equivalent Ghomaride and Sebtide complexes in the Rif, are considered part of the Alborán domain.

1.4.2.3.1 The Maláguide complex

The Maláguide complex crops out at the top of the Alborán domain (Fig. 1.7) and includes the most complete and tectonically least disturbed stratigraphic sections in the Alborán domain (Platt *et al.*, 2013). It is composed of very low-grade Paleozoic metamorphic rocks and a Mesozoic-Cenozoic sedimentary cover that shows no indication of pervasive deformation or metamorphism (Martín‐Algarra *et al.*, 2000; Chalouan & Michard, 2004).

1.4.2.3.2 The Alpujárride complex

The Alpujárride complex constitutes the intermediate tectonic unit of the Betic Internal Zones, which is sandwiched between the upper Maláguide and the lower Nevado-Filábride complexes (Fig. 1.7). The western Alpujárride complex includes the Jubrique and Blanca crustal units that overlie and underlie the Ronda peridotite massif, respectively (Fig. 1.7) (Balanyá *et al.*, 1997; Tubía *et al.*, 1997). The Jubrique unit represents a highly attenuated (≤ 5 km) continental crustal section composed of non-metamorphic to greenschist-facies Triassic carbonates, which overlie a metamorphic sequence of increasing metamorphic grade towards the contact with the Ronda peridotites. From top to bottom, this sequence is composed of Permo-Triassic low-grade phyllites and quartzites with relics of HP-LT assemblages, graphitic micaschists with garnet, staurolite, kyanite and late andalusite, a crystalline basement of kyanite-, sillimanite- and garnet-bearing porphyroblastic gneisses and, near the contact with the underlying peridotites, garnet-rich mylonitic gneisses. The schists and gneisses are of assumed Paleozoic age (Balanyá *et al.*, 1997; Platt *et al.*, 2013).

A high temperature ductile shear zone separates the Jubrique unit from the underlying Ronda peridotite massif, the largest outcrop of SCLM in the westernmost Mediterranean (Figs. 1.1 & 1.7). The Ronda peridotite, and the equivalent Beni Bousera peridotite in the Rif, are included in the Alpujárride (Sebtide in the Rif) complex, but here they are described separately (c.f. Sec. 1.4.3). The Ronda peridotite slab rests on the Blanca Unit (Fig. 1.7), which has an

uncertain provenance (Esteban *et al.*, 2011; Platt *et al.*, 2013). This unit is composed of variably deformed, HT-LP schists, marbles, and migmatitic gneisses (Tubía *et al.*, 1997; Acosta-Vigil *et al.*, 2014), and rare eclogite bodies that yield U-Pb zircon ages indicating a Jurassic protolith affected by early Miocene metamorphism (Sánchez-Rodriguez & Gebauer, 2000).

1.4.3 The Betic and Rif orogenic peridotites

The peridotite bodies in the Internal Zones of the Betic-Rif belt are mantle slices several kilometers thick, which are tectonically interlayered with high-grade metamorphic crustal rocks of the Alpujárride/Sebtide complex (Figs. 1.1 & 1.7a). They are composed mainly of spinel (± garnet) lherzolites, harzburgites, minor dunites and subordinate pyroxenite layers (< 10% in volume), which are generally parallel to the foliation of their host peridotites (Kornprobst, 1969; Obata, 1980; Reuber *et al.*, 1982; Reisberg, 1988; Pearson *et al.*, 1993; Garrido & Bodinier, 1999; Lenoir *et al.*, 2001; Pearson & Nowell, 2004; Garrido *et al.*, 2011). The Ronda peridotite massif in the Betics is not only the largest (c. 300 km^2) of several peridotite bodies in the westernmost Mediterranean, but it is also the largest outcrop of SCLM peridotite worldwide, whereas the Beni Bousera peridotite in the Rif has a more restricted area of c. 65 km^2 (Fig. 1.7a). These massifs have similar compositions and tectonic evolutions, suggesting that they derived from similar portions of SCLM. In particular, there is a consensus that both massifs show an extended record from early exhumation at the roots of thick continental lithosphere in the diamond facies (> 45 Kbar) (Pearson *et al.*, 1989; Davies *et al.*, 1993; Pearson *et al.*, 1993; Pearson & Nowell, 2004; El Atrassi *et al.*, 2011) to final Miocene emplacement in an extremely attenuated shallow continental lithosphere at around 23 – 19 Ma (Van der Wal & Vissers, 1993; Blichert-Toft *et al.*, 1999; Platt *et al.*, 2005; Garrido *et al.*, 2011; Hidas *et al.*, 2013; Frets *et al.*, 2014).

1.4.3.1 The Ronda peridotite

The western Ronda peridotite massif forms a coherent lithospheric mantle section with a peculiar kilometer-scale petrological, geochemical and structural zoning (Obata, 1980; Van der Wal & Vissers, 1993, 1996; Lenoir *et al.*, 2001; Précigout *et al.*, 2007; Soustelle *et al.*, 2009; Garrido *et al.*, 2011; Hidas *et al.*, 2013).

Three main domains have been distinguished in the Ronda massif on the basis of their petrology and thermal and structural evolutions (Obata, 1980; Van der Wal & Vissers, 1993),

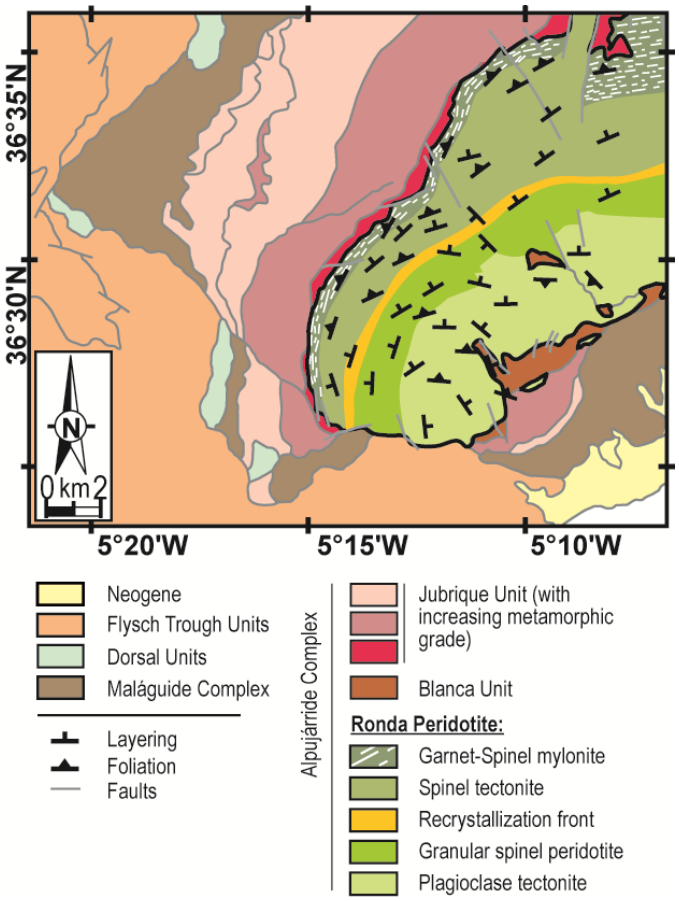

Figure 1.8 *Simplified geological map of the westernmost Alborán domain in the Betics with indication of the tectono-metamorphic domains and internal structures of the western Ronda peridotite (modified after Hidas et al., 2013).*

which are from top to bottom (from NNW to SSE), and from the oldest to the youngest (Fig. 1.8):

1- The spinel (± garnet) tectonite domain. It is divided into two sub-domains: the garnet-spinel (Grt-Sp) mylonites and the foliated spinel tectonites (Fig. 1.8) (Precigout *et al.*, 2007), with subordinated amounts of garnet-bearing granulite and pyroxenite layers (Garrido & Bodinier, 1999).

2- The granular spinel peridotite domain. It is made up of coarse granular spinel peridotites, formed at the expense of spinel tectonites by partial melting and annealing (Van der Wal & Bodinier, 1996; Van der Wal & Vissers, 1996; Lenoir *et al.*, 2001; Vauchez & Garrido, 2001), and of subordinate spinel pyroxenite layers devoid of garnet (Garrido & Bodinier, 1999). This domain is separated from the spinel tectonites by a narrow (*c.* 200 – 400 m wide) and continuous (*c.* 20 km long) transitional zone referred to as the *recrystallization front* (Fig. 1.8) (Van der Wal & Bodinier, 1996; Lenoir *et al.*, 2001).

3- The plagioclase tectonite domain. This is the largest and youngest portion of the massif. It overprints the previous domains and attests for partial equilibrium in the plagioclase lherzolite facies (Van der Wal & Vissers, 1996; Lenoir *et al.*, 2001; Hidas *et al.*, 2013).

1.4.3.2 The Beni Bousera peridotite

The Beni Bousera peridotite massif (Figs. 1.9 & 1.10) crops out at the bottom of the Sebtides unit —the lowermost crustal unit exposed in the Rif internal zones (Fig. 1.9). The Sebtides crust records the polymetamorphic evolution of an original Variscan HP-HT basement, overprinted

by a late LP-HT Alpine event related to the exhumation of mantle peridotites (Goffe *et al.*, 1996; Michard *et al.*, 1997; Bouybaouene *et al.*, 1998; Janots *et al.*, 2006; Michard *et al.*, 2006; Rossetti *et al.*, 2010). These crustal rocks have ductile foliations and lineations coherent with the internal ductile structures of the peridotite massif (Figs. 1.9 & 1.10) (Reuber *et al.*, 1982; Saddiqi *et al.*, 1988; Janots *et al.*, 2006; Afiri *et al.*, 2011; Frets *et al.*, 2014), and record a strong metamorphic gradient from 500 – 550 ºC at 0.7 – 0.8 GPa in the Filali schists to 800 – 850 ºC at 1.0 – 1.3 GPa in the garnet granulites (¨kinzigites¨) (Fig. 1.9; Chalouan and Michard, 2004, and references therein).

Several studies have revealed the polybaric and polythermal evolution of the massif (Saddiqi *et al.*, 1988; Targuisti, 1994; Afiri *et al.*, 2011; Frets *et al.*, 2014). Recently, Frets *et al.* (2014) distinguished four main tectono-metamorphic domains in Beni Bousera, which show gradual variations of olivine grain size, microstructures, and peridotite and pyroxenite mineral

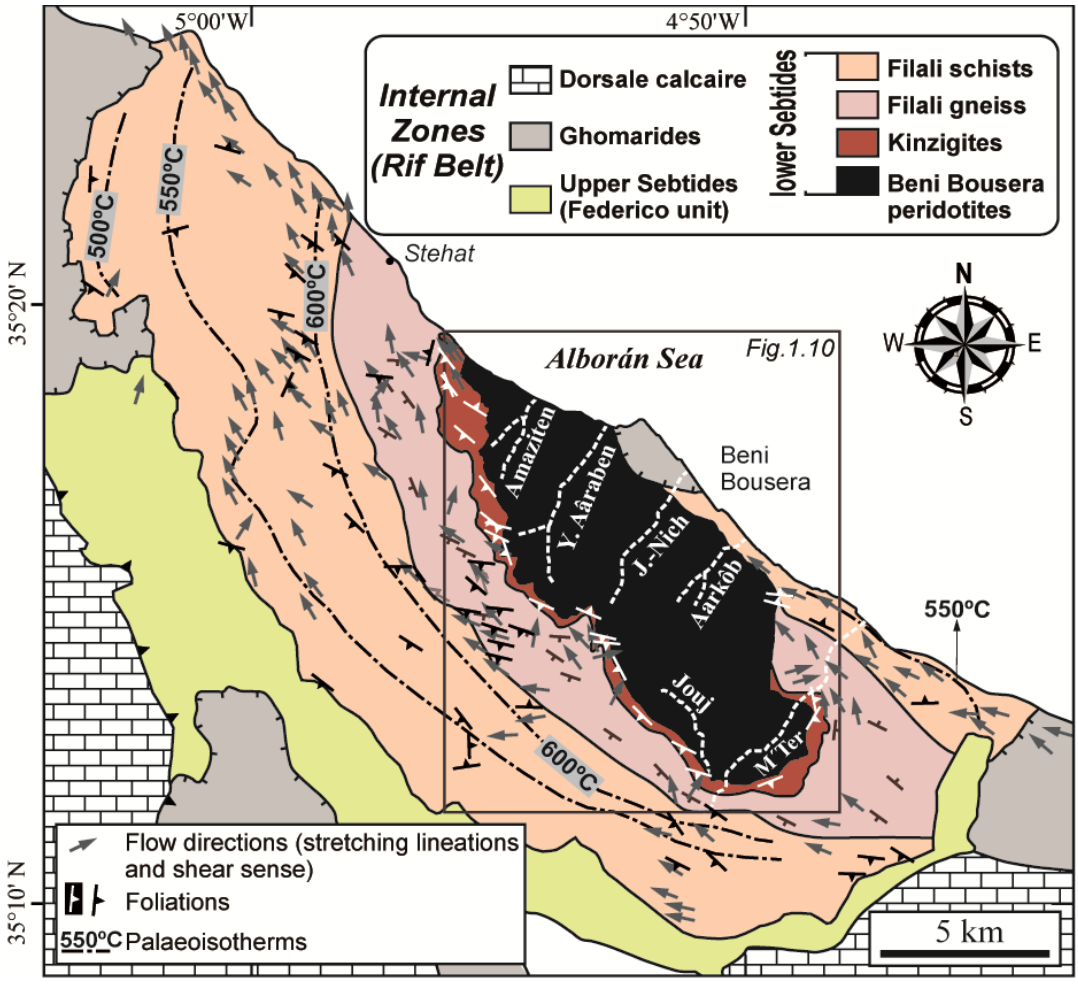

Figure 1.9 *Simplified geological and structural setting of the Beni Bousera peridotite in the Internal Zones of the Rif belt. Location of the Beni Bousera peridotite is depicted (enlarged in Fig. 1.11). Flow directions and foliations are from Kornprobst (1969), Saddiqi et al. (1988) and Negro et al. (2006). Paleo-isotherms are from Negro et al. (2006).*

assemblages. From SW to NE and from top to bottom these domains are: (i) the garnet and spinel mylonite domain ("Grt-Sp mylonites"); (ii) the Ariègite subfacies domain ("Ar domain"); (iii) the Ariègite to Seiland transitional domain ("Ar-Se domain"); and (iv) the Seiland subfacies domain ("Se domain") (Fig. 1.10).

Grt-Sp mylonites (100 – 200 m thick) crop out below the overlying crustal kinzigites (Figs. 1.9 & 1.10) and consist of mylonitic Grt-Sp peridotites enclosing stretched and boudinaged (corundum) garnet pyroxenite layers (1 – 10 cm thick) (Chetouani *et al., in press*;

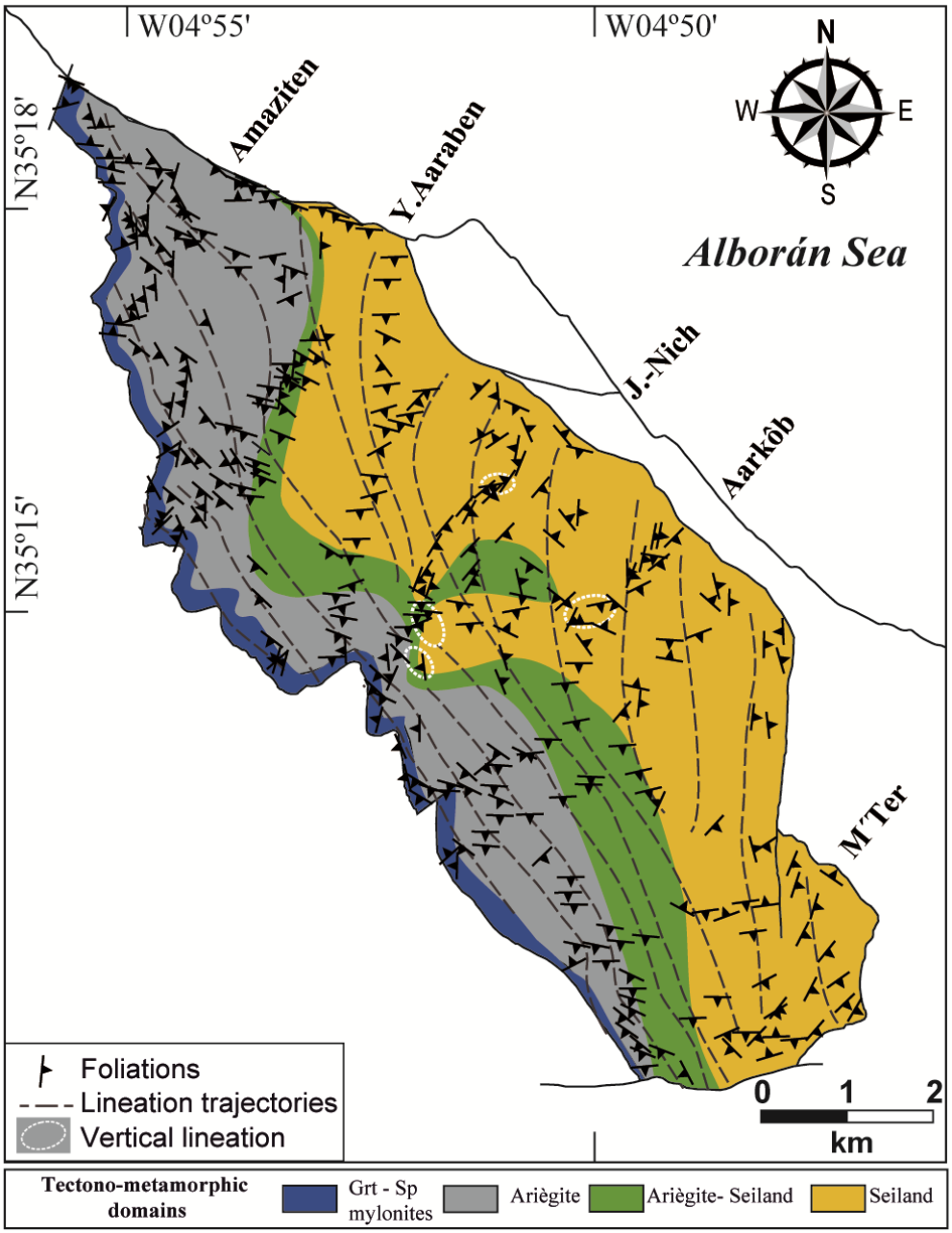

Figure 1.10 *Map of the structure of the Beni Bousera peridotite showing the orientations of foliation and lineation. The four tectono-metamorphic domains defined by Frets et al. (2014) are represented in the background. Foliation and lineation are from Frets et al. (2014), and references therein.*

Tabit *et al.*, 1997; Afiri *et al.*, 2011; Frets *et al.*, 2012). The Ar domain is composed of fine-grained porphyroclastic spinel peridotites with penetrative foliation and lineation, and boudinaged, isoclinally folded or layered concordant garnet pyroxenites with sharp contacts with the peridotites. Garnet pyroxenites at the transition between the Grt-Sp mylonites and Ar domain include graphite pseudomorphs after diamond (Pearson *et al.*, 1989; El Atrassi *et al.*, 2011). The Ar-Se domain has variable thickness and is composed of medium to coarse-grained porphyroclastic spinel peridotites, with pyroxenite layers containing kelyphite aggregates after garnet, and coarse spinel. These layers are commonly composite, showing a transition from spinel websterites to garnet-spinel websterites. The lowermost exposed domain of the massif is the Se domain, which consists of coarse- to very coarse-grained porphyroclastic and granular peridotites, and spinel pyroxenite layers. At places, this domain contains centimetric to metric diffuse dunite-harzburgite-lherzolite layering and areas with abundant dunites and wehrlites, particularly close to coarse granular peridotites with vertical olivine lineations (Fig. 1.10) interpreted as diapiric instabilities (Frets *et al.*, 2014). This petro-structural zoning has been considered the record of a low-angle transtensional shear zone, which accommodated exhumation at the base of the lithosphere from ~90 to ~60 km depth (Frets *et al.*, 2014). Slow thermal diffusion relative to deformation-induced exhumation rates explains the strong thermal gradient across the Beni Bousera massif (Frets *et al.*, 2014).

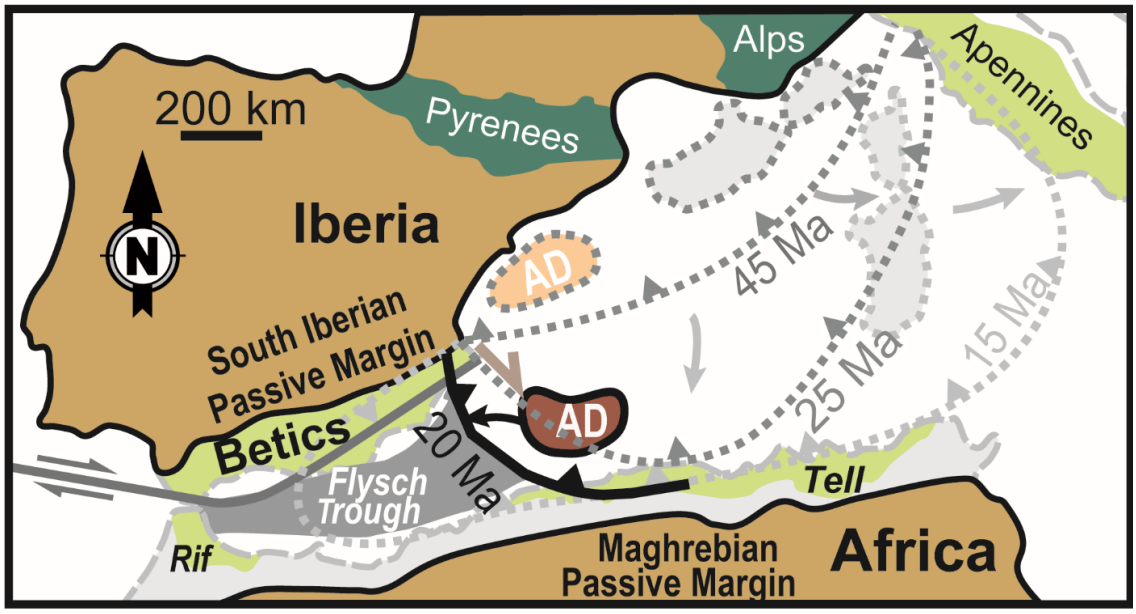

Figure 1.11 *Cartoon of the tectonic scenario proposed for the Eocene to Miocene geodynamic evolution of the westernmost Mediterranean and the formation of the Betic-Rif belt by rollback of the Alpine Tethys (after Marchesi et al., 2012). AD: Alborán domain.*

1.4.4 Alpine geological evolution of the westernmost Mediterranean

The ancestor of the Alborán domain is the allochthonous AlKaPeCa micro-continent, a group of east-west trending continental domains originally located in a north-easternmost position in the current western Mediterranean (Fig. 1.11) (Royden, 1993; Faccenna *et al.*, 2004; Booth-Rea *et al.*, 2007; Mauffret *et al.*, 2007; Platt *et al.*, 2013; van Hinsbergen *et al.*, 2014). From the Late Jurassic to the Cretaceous, a deep oceanic basin —floored by oceanic crust or thinned continental crust— separated the southern AlKaPeCa continental margin from the Maghrebian passive paleomargin (Martín-Algarra, 1987; Durand-Delga *et al.*, 2000; Guerrera *et al.*, 2005; Luján *et al.*, 2006). This oceanic basin constituted the NW branch of the western Tethys and connected the central Atlantic to the Piemonte-Ligurian oceans (Guerrera *et al.*, 2005; Luján *et al.*, 2006). During the Late Cretaceous-Eocene a subduction zone was initiated in this basin. The lateral extent, location and single or double vergence of this subduction is a current matter of debate (Faccenna *et al.*, 2004; Booth-Rea *et al.*, 2007; Mauffret *et al.*, 2007; Vergés & Fernàndez, 2012; Platt *et al.*, 2013; van Hinsbergen *et al.*, 2014). The most widely accepted hypothesis is that the basement of the Flysch Trough and its sedimentary cover subducted northward beneath the AlKaPeCa continental domain (Fig. 1.11). In the westernmost part of this convergent margin, subduction caused the crustal stacking of the Alpujárride/Sebtide complex under the Maláguide/Ghomaride complex, and the Eocene HP-LT metamorphism of the Alpujárride/Sebtide complex (Azañon *et al.*, 1997; Platt *et al.*, 2005). In the Oligocene, outward directed rollback of the Tethyan slab formed a continental back-arc located in a position likely corresponding to the current eastern Algero-Balearic basin (Fig. 1.1). This continental back-arc was bounded to the west by the Flysch Trough and to the south by the arc and forearc regions of AlKaPeCa (Fig. 1.11). In the Alborán domain, the basement of the back-arc was formed by the extensional collapse of the Alpujárride/Sebtide-Maláguide/Ghomaride orogenic wedge (Balanyá *et al.*, 1997; Booth-Rea *et al.*, 2005, 2007; Garrido *et al.*, 2011).

Contractive tectonic inversion of this back-arc initiated in the late Oligocene-early Miocene and led to the intracrustal emplacement of the Ronda and Beni Bousera peridotites and thrusting of the Alborán crustal basement (Balanyá *et al.*, 1997; Booth-Rea *et al.*, 2005; Hidas *et al.*, 2013; Platt *et al.*, 2013). This shortening probably initiated eastward-northeastward underthrusting of the Flysch basin beneath the Alborán back-arc domain, favoring its south-westward migration driven by slab rollback. During its westward migration, the Alborán thrust wedge consumed the Tethys oceanic lithosphere in the central area of the arc and collided laterally with the Maghrebian and South Iberian paleomargins in the early to late Miocene (Fig.

1.11) (Platt *et al.*, 2013). Thrusting of the Flysch units occurred since the late Burdigalian (~ 17 Ma) and was followed by the complete detachment of these units from their subducted basement (Luján *et al.*, 2006). At that time, the Betic and Rif continental allochthonous terrains formed a N/NE-S/SW trending orogenic arc above the eastward subducting Tethys oceanic lithosphere and were bounded to the N and S by the Iberian and Maghrebian margins.

Since the Burdigalian, further extension of this orogenic wedge formed the western Alborán Sea basin floored by thinned Alpujárride continental crust (Booth-Rea *et al.*, 2007). Middle Miocene to Pleistocene volcanism in the Alborán region occurred in the central and mostly eastern Alborán Sea basin, and in the SE Iberian and NW Africa continental margins (Figs. 1.1 & 1.7a) (Turner *et al.*, 1999; Duggen *et al.*, 2004; Gill *et al.*, 2004; Duggen *et al.*, 2008). LREE-depleted tholeiitic lavas extruded in the central part of the Alborán Sea basin, surrounded by LREE-enriched calc-alkaline lavas near the continental margins (Fig. 1.7a) (Duggen *et al.*, 2008). This volcanism was ascribed by Duggen *et al.* (2008) to the eastward subduction of the Alpine Tethys oceanic lithosphere. Afterward, Late Miocene to Pliocene Si-K-rich and Quaternary alkali magmatism was caused by subcontinental-edge lithospheric delamination followed by asthenospheric mantle upwelling (Duggen *et al*., 2004, 2005, 2008; Gill *et al.*, 2004).

2 Aims and thesis structure

2.1 Synthesis of the state-of-the-art

The geochemical and isotopic heterogeneities found in mantle-derived basalts imply the existence of heterogeneities in their mantle source regions (Hofmann, 2014). Geochemical studies of basalt composition and melting experiments on peridotites and pyroxenites provide indirect information on the geochemistry and partial melting behavior of the heterogeneous mantle (e.g., Hirschmann & Stolper, 1996; Hirschmann *et al.*, 2003; Hofmann, 2014; Lambart *et al.*, 2016). Orogenic peridotite massifs offer a unique opportunity to directly characterize the nature and length scale of upper mantle heterogeneities from centimeters to tens of kilometers (Menzies & Dupuy, 1991; Downes, 2001; Bodinier & Godard, 2014).

Several models have been proposed for producing compositional and lithological heterogeneities in the upper mantle. Classically, partial melting and melt extraction from a fertile mantle source have been invoked to explain a large proportion of depleted or enriched bulk compositions recognized in orogenic peridotites as well as in mantle xenoliths (e.g., Bodinier, 1988; McDonough & Frey, 1989; Herzberg, 2004). However, numerous studies in orogenic, ophiolitic and oceanic peridotites have provided evidence that these compositions could also be caused by melt-rock reaction processes acting in an ancient refractory mantle (e.g., Becker, 1996a; Lenoir *et al.*, 2001; Müntener *et al.*, 2004; Niu, 2004; Rampone *et al.*, 2004; Ionov *et al.*, 2005; Le Roux *et al.*, 2007). In addition, recycling of oceanic and continental crust has been invoked as the main cause of the enriched isotopic composition of OIB (e.g., Hofmann & White, 1982; Chauvel *et al.*, 1992; Hart *et al.*, 1992; Helffrich & Wood, 2001; Davies, 2002; Workman *et al.*, 2008; Willbold & Stracke, 2010; Hofmann, 2014; van Keken *et al.*, 2014) but how this recycling component manifests itself in the chemical composition of the mantle is still a highly debated issue.

2.2 Thesis aims

The main aim of this thesis is to **shed new light on the role of melt-rock reaction processes and recycling of oceanic and continental crustal material in creating chemical**

heterogeneities in the Earth's mantle. We will first focus on the investigation of two processes related to the development of geochemical heterogeneities in the Earth's upper mantle: **(i) the formation of secondary lherzolites by melt-rock reaction processes**, and **(ii) the genesis of ultra-high pressure garnet pyroxenites and its implications for crustal recycling into the Earth's mantle**. We will use as case studies mantle rocks exposed in orogenic peridotites from the Betic-Rif Cordillera in the westernmost Mediterranean. Furthermore, in this thesis we will explore (iii) **to what extent Betic crustal rocks were involved in the geochemical signature of magmatism recorded in the subcontinental lithospheric mantle (SCLM), and in the Miocene Alborán Sea basin volcanism**. The westernmost Mediterranean records an Alpine history of subduction and slab roll-back that resulted in the creation of the Alborán sea basin. Hence, mantle rocks and their allied crustal rocks in this belt provide a unique natural laboratory for studying large scale recycling of crustal components in the SCLM.

To achieve the first aim —**formation of secondary lherzolites by melt-rock reaction processes**— we have carried out a detailed study of the major and trace element compositional variability of peridotites from the Beni Bousera massif (Rif Belt, N. Morocco). This study will elucidate how melt extraction and melt-rock reaction processes —leading to depletion or refertilization— operated in the SCLM. We will constrain different melt-rock reactions involved in the formation of secondary lherzolites at length scales that have not yet been fully investigated in the literature. To address the second aim —**genesis of ultra-high pressure garnet pyroxenites and its implications for crustal recycling into the Earth's mantle—** We have performed analyses on major and trace element compositions, and, for the first time, an integrated Sr-Nd-Pb-Hf isotopic study of garnet pyroxenites from the Ronda (Betic belt, S. Spain) and Beni Bousera peridotite massifs. This rather unique dataset will be used to constrain the genesis of these enigmatic pyroxenites, and evaluate the role of recycling of oceanic and continental crust in their provenance. Finally, **to investigate to what extent Betic crustal rocks were involved in the geochemical signature of magmatism observed in the subcontinental lithospheric mantle rocks, and in the Miocene Alborán sea basin volcanism**, we conducted a detailed bulk rock trace element and Sr-Nd-Pb isotopic study of crustal rocks from the Internal Zones of the Betics. This study focuses on crustal rocks associated to the Ronda massif, particularly from the western Alpujárride metamorphic basement and the pre-Miocene Flysch sediments of the Betic Cordillera.

By meeting these goals, this thesis will shed new light on the role of melt-rock reaction processes and recycling of oceanic and continental crustal material in creating chemical heterogeneities in the Earth's mantle at different length scales.

2.3 Thesis structure

The thesis is divided into five parts: I – Introduction, aims and methodology; II – Results; III – Conclusions; IV – References; and, V – Appendixes.

PART I introduces the research topic and provides an overview of the current state-of- the-art; outlines the main sections of this work and the applied methodology. This part is subdivided into three main chapters:

- Chapter 1: *Introduction*. This chapter introduces the problem and motivation of the present study. It first reviews the current knowledge about the Earth's interior and our knowledge of mantle heterogeneities, and some key open questions that still need to be addressed. This chapter also presents the geological setting of the case studies in the Betic-Rif belt.
- Chapter 2: *Aims and thesis structure*. This is the current chapter, which outlines the purposes and specific objectives of this work. In addition, it briefly describes the structure and contents of the thesis and each of its chapters.
- Chapter 3: *Methodology.* This chapter describes the methodology followed to obtain the data presented in this thesis, including sampling and sample preparation, and analytical methods such as X-Ray Fluorescence (XRF), Electron Probe Micro-Analyses (EPMA), Inductively Coupled Plasma Mass Spectrometry (ICP-MS), Laser Ablation (LA) and Multi-Collector (MC) ICP-MS, and Thermal Ionization Mass Spectrometry (TIMS).

PART II includes the results of this work and consists of three chapters:

- Chapter 4: *Refertilization processes in the subcontinental lithospheric mantle: The record of the Beni Bousera orogenic peridotite (Rif Belt, N. Morocco).* This chapter presents an extensive and detailed geochemical dataset of peridotites from the four tectono-metamorphic domains of the Beni Bousera orogenic massif. The results support a secondary, refertilization-related, origin for most lherzolites in orogenic peridotite massifs and provide general insights into melt-rock reactions in the mantle. This chapter is accepted in the JCR *Journal of Petrology*. In addition, these results have been presented in several international conferences: a talk at the 2015 2nd European Mantle Workshop (Wroclaw, Poland), an invited talk at the Goldschmidt 2015 Conference (Prague, Czech Republic),

and a solicited talk at the European Geosciences Union General Assembly 2016 (Vienna, Austria).

- Chapter 5: *Genesis of ultra-high pressure garnet pyroxenites in the subcontinental lithospheric mantle—Constraints from the Ronda and Beni Bousera orogenic peridotite massifs.* This chapter presents the bulk rock major and trace element compositions, and the Sr-Nd-Pb-Hf isotopic signatures of garnet pyroxenites from the Ronda and Beni Bousera peridotite massifs. The source of these rocks has been largely debated and it has been generally associated with subducted oceanic crust, which is the basis of the "marble-cake" model of Allègre & Turcotte (1986). However, these data show that in addition to oceanic crust, the source of garnet pyroxenites should also involve lower continental crust. The way recycled oceanic and continental components occur intimately mixed in orogenic peridotites is highly enigmatic and its understanding is paramount for our knowledge on how compositional heterogeneities are formed in the mantle. This chapter is a draft of a manuscript that will be submitted to the JCR journal *Geochimica et Cosmochimica Acta*.
- Chapter 6: *Sr-Nd-Pb isotopic systematics of crustal rocks from the western Betics (S. Spain): Implications for crustal recycling in the lithospheric mantle beneath the westernmost Mediterranean*. This chapter provides new trace element and Sr-Nd-Pb isotopic data of the Flysch sediments and metamorphic rocks from the internal Betics (western Alpujárride complex). It discusses the provenance and evolution of these crustal units, and it shows how the lower continental crust, associated to the Ronda peridotite massif, played a major role on the composition of orogenic pyroxenites and calc-alkaline lavas of the westernmost Mediterranean. This chapter has been published in *Lithos*[1] and presented in several international conferences such as the 2015 2nd European Mantle Workshop (Wroclaw, Poland), the 2015 Congreso Geológico Chileno (La Serena, Chile), several European Geosciences Union General Assemblies (from 2013 to 2015) (Vienna, Austria) and the 2014 Sixth International Orogenic Lherzolite Conference (Marrakech, Morocco).

[1] Varas-Reus, M. I., Garrido, C. J., Marchesi, C., Bosch, D., Acosta-Vigil, A., Hidas, K., Barich, A. & Booth-Rea, G. Sr-Nd-Pb isotopic systematics of crustal rocks from the western Betics (S. Spain): Implications for crustal recycling in the lithospheric mantle beneath the westernmost Mediterranean. *Lithos*. http://dx.doi.org/10.1016/j.lithos.2016.10.003

Finally, PART III includes Chapter 7 (*Conclusions*) that summarizes the main conclusions drawn from this study; PART IV contains the *References* cited in this thesis; and PART V presents the appendixes with geochemical data obtained from this study.

3 Methodology

3.1 Sampling and sample preparation

3.1.1 Sampling

This thesis presents a geochemical study (major and trace elements, and Sr-Nd-Pb-Hf radiogenic isotopes) of peridotites and pyroxenites from the Ronda and Beni Bousera orogenic massifs, as well as of the western Alpujárride crustal rocks and the pre-Miocene Flysch sediments of the Betic Cordillera. Most of the samples analyzed in this work were collected during field campaigns carried out prior to the start of the thesis. In the Beni Bousera massif, these campaigns were performed by a group of international researchers and students from several institutions: IACT (Granada, Spain), University of Montpellier (France), University of Tetuan and University of Rabat (both in Morocco). In the Ronda massif, field work was undertaken by the Research Group on Petrology, Geochemistry and Geochronology of the IACT. Two additional campaigns were conducted in 2012 and 2013 to collect sediments from the Algeciras Flysch unit and to complete the sampling of the Jubrique metamorphic rocks (Fig. 3.1). Geochemical analyses require large volumes of rock, thus ~ 8 to 10 kg of material per sample was collected in the field. Chapters 4, 5 and 6 give details on the lithological, mineralogical and microstructural features of the samples selected for this study.

Figure 3.1 *Sampling a) Flysch sediments and b) Jubrique crustal metamorphic rocks*

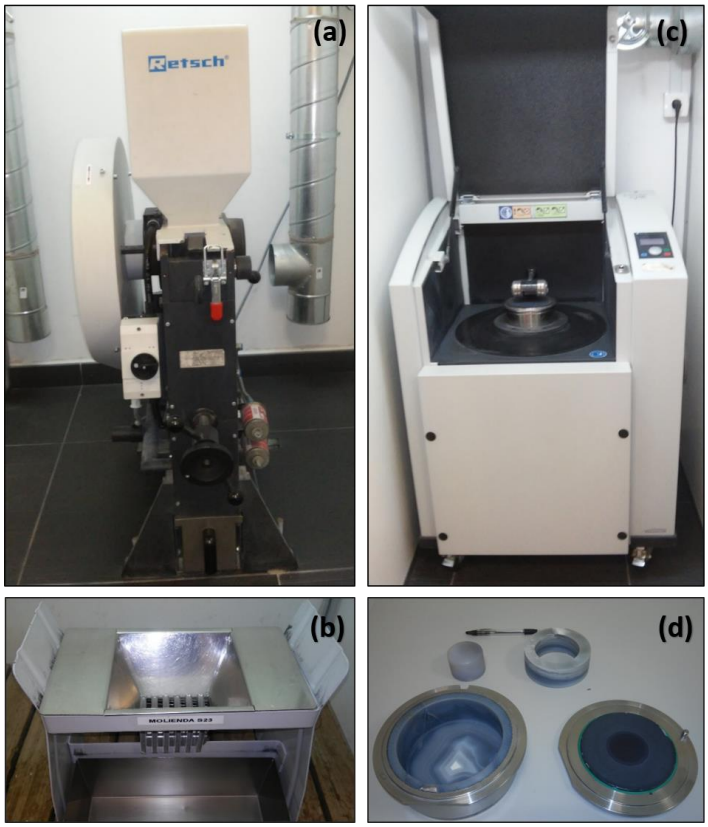

Figure 3.2 *Equipment used for sample preparation at the IACT: a) steel jaw crusher, b) riffle-splitter, c) Vibratory Disc Mill RS 200 and (d) agate grinding set.*

3.1.2 Sample preparation

Samples were prepared at the analytical facilities of the IACT. Secondary veins and alteration rims were carefully removed using a diamond saw, and large samples were then cut into smaller cubic slices. These slices were ultrasonicated in distilled water for 30 minutes in order to remove superficial dust, clays and metal particles. A representative slice of each sample was stored for subsequent preparation of thin sections. Dried samples were then crushed in a steel jaw crusher (Fig. 3.2a) and representative aliquots of crushates were obtained using a riffle-splitter (Fig. 3.2b). One batch of crushates was reserved for mineral separation and the other aliquot was used to prepare bulk rock powders.

3.1.2.1 Preparation of thin sections

For each sample slice (see above), a thin sliver of rock (~ 3 mm thick) was cut by a diamond saw. The specimen "chip" was ground on one side to produce a flat, smooth surface, followed by polishing with a 3 µm diamond grit using Buehler™ polishing pads. The chip was then thoroughly cleaned to remove all loose abrasive and other residues, and was subsequently attached to a glass slide (26 x 46 mm) using epoxy resin of two-components. Mounted sections were further ground by progressively finer abrasive grits, and polished until the sample reached 100 – 150 µm thickness for LA-ICP-MS analyses (c.f. Sec. 3.2.4) or the standard thickness of 30 µm for conventional petrographic study. This procedure was conducted at the "Thin Section Lab" of the IACT.

3.1.2.2 Preparation of bulk rock powders

Sample powders (mesh size ≤ 25 μm) were obtained by powdering representative crushates in an agate disc mill at the facilities of the IACT (Fig. 3.2c, d). The grinding time to obtain the required mesh size varied between 45 minutes and 2 hours, depending on the nature of the sample. To avoid sample contamination, quartz chips were crushed and milled between each sample. In addition, the jaw crusher and the agate disc mill were carefully washed after processing each sample (several alcohol wash cycles, then cleaning using abundant distilled water and drying by compressed air). The powders obtained were stored into three PVC vials, previously rinsed using distilled water and dried with compressed air, for bulk rock major and trace element, and isotopic analyses.

3.2 Analytical methods

3.2.1 X-Ray Fluorescence (XRF)

Bulk rock major and minor transition elements of Beni Bousera peridotites (Ch. 4) and Ronda and Beni Bousera pyroxenites (Ch. 5) were analyzed by X-Ray Fluorescence (XRF) in fused beads and pellets at IACT. Fused beads were made by weighing rock powders (~ 1 g) with di-lithium tetraborate flux, and fusing the mixture at 1000 °C for 15 minutes. The analyses were performed using a BRUKER D8 Advance XRF instrument equipped with six analyzers (LiF200, LiF220, Ge, PE, PX1, PX2). Within-run precision (% RSD), measured by repeated analyses of USGS reference materials as external standards, is better than 0.5% for all elements except Na, for which it is 1.5%. The entire dataset of bulk rock major and minor transition elements of Beni Bousera peridotites is reported in Appendix A, whereas the Ronda and Beni Bousera pyroxenites data are reported in Chapter 5 (Table 5.1).

3.2.2 Electron Probe Micro-Analyses (EPMA)

Major element compositions of minerals (olivine, orthopyroxene, clinopyroxene and spinel) in Beni Bousera peridotites (Ch. 4) have been analysed by Frets *et al.* (2014). These data were acquired using the CAMECA SX-100 Electron Probe Micro-Analysers (EPMA) of the Centro de Instrumentación Científica (CIC) of the University of Granada (Spain) and the Service Microsonde Sud-Géosciences Montpellier (CNRS-Université Montpellier, France). EPMA analyses were performed using accelerating voltage and beam current of 20 kV and 10 nA,

respectively, and counting times were 20 – 30 s. A summary of Mg-numbers (Mg-no.) variations in minerals is listed in Appendix B.

3.2.3 Inductively Coupled Plasma Mass Spectrometry (ICP-MS)

Bulk rock trace element compositions of Flysch sediments and Jubrique and Blanca metasedimentary rocks (Ch. 6) were analyzed at CIC (University of Granada, Spain). The trace element data of samples from the Blanca unit were obtained by Acosta-Vigil (1998), whereas Flysch sediments and Jubrique metasedimentary rocks were analyzed in this study. About 100 mg of bulk rock powder were digested by HNO_3-HF in Teflon-lined vessels at 180°C and ~ $1.38*10^6$ Pa during 30 minutes using a Milestone™ Microwave system. Solutions were then evaporated to dryness and dissolved in 4 vol. % HNO_3. Solutions of Flysch sediments and Jubrique metamorphic rocks were analyzed using a PE NEXION 300D Inductively Coupled Plasma Mass Spectrometer (ICP-MS), whereas the Blanca samples were analyzed by a Perkin-Elmer SCIEX-ELAN 500 ICP-MS. Element concentrations were determined by external calibration and data were corrected for procedural blanks and isobaric interferences. International standards UB-N, PMS, WSE, BE-N, BR, AGV-1, DRN, GSN and GA were run as unknowns during the analytical sessions to check for accuracy. Our results (Table 3.1) show good agreement with certified values for these international standards (Govindaraju, 1994 and GeoReM preferred values – http://georem.mpch-mainz.gwdg.de/; Jochum *et al.,* 2016). Bulk rock trace element data of Flysch sediments, Jubrique and Blanca metamorphic rocks are reported in Chapter 6 (Table 6.1).

Bulk rock trace element compositions of Ronda and Beni Bousera pyroxenites (Ch. 5) were analysed in solution using an Agilent 7700 ICP-MS at the AETE technical platform of Géosciences Montpellier (University of Montpellier-CNRS, Montpellier, France). About 100 mg of powder were digested following the HF-$HCLO_4$ procedure described in Ionov *et al.* (1992) and Godard *et al.* (2000). The precision and the accuracy of the results were estimated by measurements of well characterized international standards UB-N and BE-N. Our results (Table 3.2) show good agreement with certified values for these international standards (Govindaraju, 1994 and GeoReM preferred values – http://georem.mpch-mainz.gwdg.de/; Jochum *et al.,* 2016). Bulk rock trace element abundances of the Ronda and Beni Bousera pyroxenites are reported in Chapter 5 (Table 5.1).

Table 3.1 ICP-MS reference standards used at the Centro de Instrumentación Científica (University of Granada, Spain).

Standards	UB-N		PMS		WSE		BE-N		BR		AGV-1		DRN		GSN		GA	
Trace elements (ppm)	This study	Preferred values[1]	This study	Preferred values[2]	This study	Preferred values[2]	This study	Preferred values[2]	This study	Preferred values[1]	This study	Preferred values[2]	This study	Preferred values[1]	This study	Preferred values[1]	This study	Preferred values[1]
Rb	4.0	4.0	0.50	0.98	25	26	47	48	48	47	68	68	73	73	187	185	175	175
Sr	8.6	9.0	282	279	412	408	1369	1392	1332	1320	661	661	403	400	577	570	309	310
Y	2.6	2.5	11.3	11	31	32	30	29	29	30	20	20	27	26	18	16	21	21
Zr	4.2	4.0	37	38	200	204	261	273	260	260	222	232	38	125	116	235	98	150
Nb	0.40	0.050	2.3	2.4	18	18	105	113	99.7	98	14.7	14.53	6.9	7.0	20.6	21	11	12
Cs	10	10	0.40	0.37	0.60	0.48	0.80	0.73	0.80	0.80	1.3	1.3	6.1	6.3	5.5	5.4	6.0	6.0
Ba	26	27	147	148	339	335	1029	1039	1062	1050	1210	1218	383	385	1396	1400	795	840
La	0.36	0.35	3.1	2.7	28	27	84	83	84	82	39	38	22	22	70	75	40	40
Ce	0.82	0.80	7.5	6.9	61	60	154	153	153	151	70	69	46	46	129	135	76	76
Pr	0.12	0.12	1.1	1.1	7.9	7.7	17	17	17	17	8.3	8.3	5.7	5.7	14	15	8.0	8.3
Nd	0.67	0.60	5.7	5.5	33	33	66	66	65	65	32	32	24	24	47	49	28	27
Sm	0.26	0.20	1.8	1.8	8.8	8.7	12	12	12	12	5.9	5.8	5.4	5.4	7.3	7.5	5.2	5.0
Eu	0.090	0.080	1.1	1.1	2.3	2.2	3.7	3.7	3.7	3.7	1.6	1.7	1.5	1.5	1.5	1.7	1.0	1.1
Gd	0.33	0.30	2.1	2.0	7.0	7.2	9.7	10	9.6	9.5	4.9	4.9	5.0	4.7	5.0	5.2	4.0	3.8
Tb	0.070	0.060	0.35	0.34	1.0	1.1	1.3	1.3	1.3	1.3	0.67	0.67	0.77	0.77	0.68	0.60	0.59	0.60
Dy	0.47	0.38	2.1	2.1	6.0	6.1	6.4	6.5	6.4	6.4	3.6	3.6	4.6	4.6	3.0	3.1	3.2	3.3
Ho	0.11	0.090	0.46	0.43	1.2	1.2	1.1	1.1	1.1	1.1	0.71	0.68	0.96	1.0	0.59	0.60	0.65	0.70
Er	0.30	0.28	1.2	1.1	2.9	3.1	2.6	2.6	2.6	2.5	1.7	1.8	2.6	2.5	1.5	1.5	1.7	1.9
Tm	0.050	0.045	0.19	0.17	0.43	0.42	0.35	0.32	0.35	0.30	0.29	0.27	0.40	0.39	0.24	0.22	0.30	0.30
Yb	0.32	0.28	1.0	0.997	2.5	2.5	1.9	1.8	1.9	1.9	1.6	1.7	2.5	2.5	1.4	1.4	1.8	2.00
Lu	0.050	0.045	0.15	0.15	0.39	0.36	0.27	0.25	0.27	0.25	0.25	0.25	0.38	0.40	0.22	0.22	0.28	0.30
Hf	0.20	0.100	1.1	1.1	5.2	5.2	5.9	5.7	6.0	5.6	5.1	5.1	0.90	3.5	2.1	6.2	2.7	4.0
Ta	0.20	0.020	0.30	0.19	1.2	1.1	6.2	5.6	6.2	6.2	0.90	0.87	0.70	0.60	2.5	2.6	1.3	1.3
Pb	13	13	2.5	2.5	13	12	4.2	4.1	5.1	5.00	38	36	55	55	53	53	29	30
Th	0.070	0.070	0.050	0.053	3.0	3.0	11	11	11	11	6.4	6.4	4.8	5.0	41	41	17	17
U	0.050	0.070	0.020	0.019	0.64	0.62	2.5	2.4	2.5	2.5	1.9	1.9	1.5	1.5	7.7	7.5	4.8	5.0

Preferred values after 1-Govindaraju (1994) and 2-GeoReM (http://georem.mpch-mainz.gwdg.de/; Jochum et al., 2016)

3.2.4 Laser Ablation ICP-MS (LA-ICP-MS)

Trace element analyses of clinopyroxene in Beni Bousera peridotites (Ch. 4) were performed by Laser Ablation (LA) ICP-MS in 72 thin sections. 59 of these samples were analysed at Géosciences Montpellier using a ThermoFinnigan ELEMENT XR high-resolution ICP-MS, coupled with a Geolas (Microlas) automated platform housing a 193-nm wavelength Complex 102 laser from LambdaPhysik. Signals were acquired in time-resolved acquisition, devoting 2 minutes for the blank and 1 minute for measurement of the sample. The laser was fired at energy density of 15 J/cm^2, frequency of 8 Hz and using a spot size of 100 – 120 μm. The remaining 13 samples were analysed at IACT (Granada, Spain) using an Agilent 8800 QQQ ICP-MS instrument, coupled with a Photon Machine Analyte G2 system equipped with a 193-nm wavelength excimer laser. The signals of the background blank and samples were measured for 1 minute each, and the laser was fired at energy density of 11 J/cm^2, frequency of 10 Hz and a spot size of 100 – 110 μm. Data were reduced using Glitter (Van Achterberg *et al.*, 2001) and Iolite (Paton *et al.*, 2011) software at Montpellier and Granada, respectively. Calcium, measured by electron microprobe, was used as internal standard, and concentrations were calibrated against the NIST glass 612 according to the values of (Pearce *et al.*, 1997). In both institutions, the reference sample BIR-1G was analysed as an external reference material in all analytical runs, and its averages (Table 3.3) are in good agreement with working values of this international standard (Gao *et al.*, 2002). Typical within-run 1σ uncertainties are < 5% for Light Rare Earth Elements (LREE: La, Ce, Pr, Nd, Sm), < 7% for Large Ion Lithophile

Table 3.2 ICP-MS reference standards used at the AETE technical platform of Géosciences Montpellier

Standards	**UB-N**		**BE-N**	
Trace elements (ppm)	This study	Preferred values[1]	This study	Preferred values[2]
Rb	3.4	4.0	48	48
Sr	8.0	9.0	1399	1392
Y	2.8	2.5	30	29
Zr	3.3	4.0	254	273
Nb	0.085	0.050	105	113
Cs	11	10.0	0.76	0.73
Ba	27	27	998	1039
La	0.34	0.35	82	83
Ce	0.83	0.80	154	153
Pr	0.12	0.12	17	17
Nd	0.63	0.60	67	66
Sm	0.21	0.20	12	12
Eu	0.081	0.080	3.6	3.7
Gd	0.33	0.30	9.5	10.1
Tb	0.060	0.060	1.2	1.3
Dy	0.45	0.38	6.4	6.5
Ho	0.10	0.090	1.0	1.1
Er	0.30	0.28	2.5	2.6
Tm	0.046	0.045	0.31	0.32
Yb	0.30	0.28	1.7	1.8
Lu	0.051	0.045	0.26	0.25
Hf	0.13	0.10	5.6	5.7
Ta	0.054	0.020	5.7	5.6
Pb	13	13	4.1	4.1
Th	0.063	0.070	10.6	10.6
U	0.047	0.070	2.2	2.4

Preferred values after 1-Govindaraju (1994) and 2-GeoReM (http://georem.mpch-mainz.gwdg.de/; Jochum et al., 2016)

Elements (LILE: Rb, Sr, Cs, Ba, Pb), < 11% for High Field Strength Elements (HFSE: Ti, Zr, Nb, Hf, Ta), Th, U, Middle REE (MREE: Eu, Gd, Tb, Dy) and Heavy REE (HREE: Ho, Er, Tm, Yb, Lu). Compositional variations between ablation spots in the same sample were only observed in some Grt-Sp mylonites. LA-ICP-MS analyses of clinopyroxene in Beni Bousera peridotites are given in Appendix B.

3.2.5 Multi-Collector (MC)-ICP-MS and Thermal Ionization Mass Spectrometry (TIMS)

Sample digestion and chromatographic separation of Sr-Nd-Pb-Hf in Ronda and Beni Bousera pyroxenites (Ch. 5) and of Sr-Nd-Pb in Flysch sediments and Jubrique and Blanca metasedimentary rocks (Ch. 6) were carried out at the clean lab facilities of Géosciences Montpellier (Fig. 3.3) following the procedure described in Bosch *et al.* (2008).

3.2.5.1 Sample preparation

In order to obtain c. 100 to 300 ng of Sr, Nd, Pb and Hf in the final solutions, 100 to 500 mg of bulk rock powders were weighed (Fig. 3.3b) according to their elemental concentrations, which were measured previously by ICP-MS (c.f. Sec. 3.2.3). Two aliquots of powders were placed into two Teflon beakers with screw cap. One aliquot was used for Sr, Nd and Pb separations, and the other was used for Hf separation.

Table 3.3 LA-ICP-MS reference standards used at Géosciences Montpellier and IACT

Standards	**BIR-1G**	**RSD (%)**	**BIR-1G**	**RSD (%)**	**BIR-1G**
Trace elements (ppm)	**IACT** (n = 13)		**Montpellier** (n = 35)		**Gao et al. (2002)**
Cs	0.0038	9.9	0.0059	17	0.0069
Rb	0.18	9.2	0.22	6.3	0.26
Ba	6.3	9.2	6.5	5.4	6.3
Th	0.029	11	0.030	8.2	0.028
U	0.018	11	0.021	9.8	0.032
Nb	0.51	7.4	0.52	4.3	0.48
Ta	0.036	5.6	0.039	11	0.032
La	0.60	6.9	0.63	4.4	0.60
Ce	1.8	5.7	2.1	4.4	1.9
Pb	3.2	6.6	4.5	8.5	3.6
Pr	0.36	8.5	0.39	4.9	0.36
Sr	107	5.1	105	3.7	104
Nd	2.4	8.2	2.5	4.6	2.3
Zr	14	4.2	12	5.5	13
Hf	0.55	7.4	0.53	7.2	0.53
Sm	1.1	4.4	1.1	5.2	1.1
Eu	0.51	3.2	0.53	4.6	0.51
Gd	1.7	3.0	1.7	6.4	1.6
Ti	6090	7.1	6145	8.4	5532
Tb	0.33	3.7	0.34	5.4	0.32
Dy	2.5	3.9	2.5	4.7	2.3
Y	14	4.9	13	4.0	13
Ho	0.55	2.9	0.56	5.5	0.51
Er	1.7	3.1	1.6	5.2	1.5
Tm	0.24	3.2	0.25	6.0	0.22
Yb	1.6	4.7	1.7	5.5	1.5
Lu	0.24	4.3	0.25	6.2	0.23

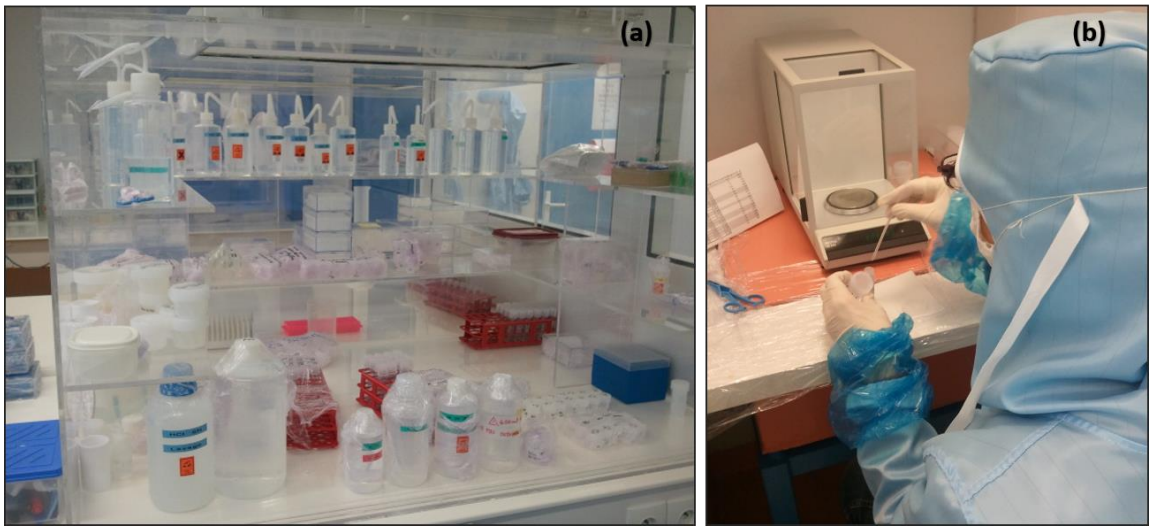

Figure 3.3 *a) Overview of the room used for the storage of acids and b) sample weighing at the clean lab facilities in Géosciences Montpellier.*

3.2.5.2 Leaching and acid attack

Leaching was performed by adding 2 cc of HCl 6N to each sample, except to the carbonate-bearing Flysch sediments (Ch. 6), and heating them on the hot plate (Fig. 3.4) for 45 to 60 minutes at 110 ºC. Afterwards, samples were homogenized in an ultrasonic bath for 5 minutes and were transferred to tubes for centrifugation (10 minutes) (Fig. 3.5a). Leachates were discarded and leached residues were rinsed three times by Milli-Q ultra-pure water. Powders were then transferred to clean Teflon beakers and digested during 36 – 48 h on the hotplate at 140 ºC using a mixture of HNO_3, HF, and $HClO_4$. After evaporation to dryness, 2 cc of HNO_3 13N was added to the residues, followed by homogenization in an ultrasonic bath. Closed beakers were then put on the hot plate at 95 ºC for 72 h, before a second evaporation to dryness. Finally, 1.5 cc of HNO_3 13N was added to each residue, which was then ultrasonicated and put at 95 ºC during 4 h on the hotplate, followed by complete evaporation.

3.2.5.3 Chromatographic separation of elements

3.2.5.3.1 Separation of Pb

After leaching and acid attack (c.f. Sec. 3.2.5.2), 0.5 cc of HBr 8N was added to the residues, which were then heated at 110 º C on the hot plate for 2 – 3 h and opened for evaporation. Subsequently, 1 cc of HBr 0.5N was added to the samples that were then transferred to tubes (Fig. 3.5a) for centrifugation (10 minutes). The Teflon columns utilized for Pb separation (Fig. 3.5b) were firstly cleaned through three washing cycles introducing 1 cc of HCl 6N followed

by 1 cc of ultra-pure water. The 200-400 mesh AG1X8^{TM} anion exchange resin, conditioned in ultra-pure water, was then introduced into each column and washed in the same way than the Teflon columns. Afterwards, 0.8 cc of HBr 0.5N was added and, once the acid percolated, a clean beaker was placed below the columns. Then, sample solutions were loaded into the columns and leached three times by 1 cc of HBr 0.5N. The residues of centrifugation were remobilized in the tubes by 1 cc of HCl 6N and centrifuged again for 10 minutes. These leachates were then added to the sample solutions previously recovered in the beakers, which were then put on the hot plate for evaporation and subsequent pre-concentrations of Sr and REE. Afterwards, clean recovery beakers were placed below the columns and Pb was eluted by 1 cc of HCl 6N. Before putting the samples on the hot plate for evaporation, aliquots (25 µl) were taken to determine the Pb concentrations previously to the isotopic analyses (c.f. Sec. 3.2.5.4). Pb total procedural blanks were less than 60 pg.

Figure 3.4 *Hot-plate for sample dissolution and open beaker dry-down in closed system evaporation cabinets at the clean lab facilities in Géosciences Montpellier.*

3.2.5.3.2 Pre-concentration of rare earth elements (REE) and Sr

Prior to the Nd and Sr individual separations, the 200-400 mesh AG50X8 ^{TM} cation exchange resin was used for REE and Sr pre-concentrations. Firstly, the resin in the Teflon columns was washed three times alternating 12 cc of HCl 6N and 12 cc of ultra-pure water (Fig. 3.6). Samples were retaken by 0.3 cc of HCl 6N and heated on the hot plate for 1 hour, followed by evaporation to dryness. Subsequently, 1.9 cc of HCl 1.5N was added to the samples, which were then transferred to tubes for centrifugation (10 minutes). After washing, the resin was pre-conditioned by adding 3 cc of HCl 1.5N. Once the acid percolated, the solutions from the centrifuged tubes were introduced and major elements were eluted in 6 cc of HCl 1.5N and 10 cc of HCl 2.5N. Then, Sr, Rb and other alkali and alkaline earth metals were recovered by leaching with 5 cc of HCl 4N and samples were heated on the hot plate for complete

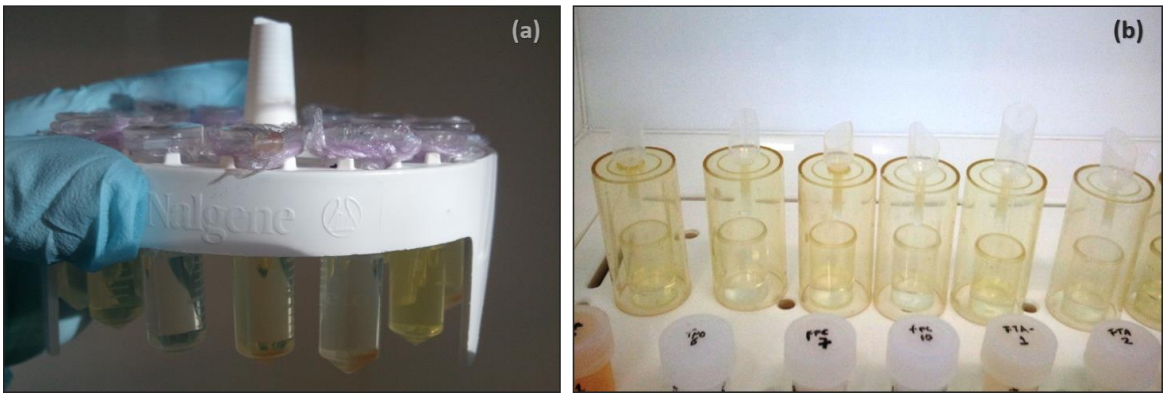

Figure 3.5 *a) Tubes for centrifugation. B) Columns and beakers used during Pb separation.*

evaporation. REE were recovered by elution of 8 cc of HCl 6N and solutions were put on the hot plate for evaporation. Before storage, the resin in the columns was washed three times by alternating 12 cc of HCl 6N and 12 cc of ultra-pure water.

3.2.5.3.3 Separation of Nd

Nd was extracted from the other REE by using organic acid HDEHP fixed on the surface of microscopic Teflon balls (diameter ~ tens μm) mounted on silica columns. Samples of pre-concentrated REE were retaken by 0.5 cc of HCl 0.3N and columns were pre-conditioned by 3 cc of HCl 0.3N. After careful introduction of the samples, LREE (La, Ce, Pr) were eluted by a calibrated volume of HCl 0.3N. Once the acid percolated, Nd was recovered in new beakers by introducing a second calibrated volume of HCl 0.3N. Beakers were then put on the hot plate for evaporation. The balls in the columns were washed by 8 cc of HCl 6N and then pre-conditioned by 3 cc of HCl 0.3N before storage. Typically, Nd total procedural blanks in the Géosciences Montpellier clean lab are lower than 10 pg (e.g., Fernandez *et al.*, 2016).

3.2.5.3.4 Separation of Sr

Sr was separated using the Eichrom™ chromatographic resin following an extraction method modified from Pin *et al.* (1994). Before being introduced into the columns, the resin, conditioned by HNO_3 0.05N, was rinsed with HCl 6N and air-dried. Afterwards, the columns were washed four times alternating 10 cc of HCl 6N and 10 cc of HNO_3 0.05N. Samples were retaken in 0.2 cc of HNO_3 7N, heated on the hot plate at 80 ºC for 2 hours and later evaporated. 2 cc of HNO_3 2N was then added to the samples, which were transferred to tubes for centrifugation (10 minutes). The resin was pre-conditioned by 3 cc of HNO_3 2N before the introduction of the samples. 0.5 cc of HNO_3 2N (twice), 3 cc of HNO_3 7N and 0.5 cc of HNO_3 3N were successively added to the columns to elute K, Rb and Ba. Then, Sr was recovered by elution of 7 cc of HNO_3 0.05N. Solutions were finally evaporated on the hot plate after the

extraction of aliquots (25 µl) to determine the Sr concentrations for isotopic analyses (c.f. Sec. 3.2.5.5). Sr total procedural blanks were less than 30 pg.

3.2.5.3.5 Separation of Hf

The purification of Hf followed the method of Blichert-Toft *et al.* (1997). Separation was done in two steps: first, High Field Strength Elements (HFSE) were separated using the 200-400 mesh AG50X8 ^{TM} cation exchange resin, and then Hf was eluted using different columns filled with the TODGA resin. In the first purification step, samples were retaken by 2 cc of HNO_3 13N and the beakers were put closed on the hot plate for 24 hours, followed by evaporation. Afterwards, 1 cc of HCl 6N was added to the samples, which were heated on the hot plate for 30 minutes and then transferred to tubes for centrifugation (10 minutes). After centrifugation, the solutions were transferred to new beakers. The residues of centrifugation were remobilized by 0.2 cc of HNO_3 3.5M – H_3BO_4 0.45 M and centrifuged again for 10 minutes. 0.4 cc of HCl 8N was then added to the residues of this second centrifugation, which were centrifuged once more for 10 minutes. All these leachates were added to the solutions in the beakers that were then put on the hot plate at 110 ºC for evaporation to dryness. Samples were retaken in 1 cc of HCl 0.5N, put on the hot plate for 7 minutes (to dissolve any solid residue) and then transferred to tubes for centrifugation (10 minutes). Columns were firstly cleaned by 3 cc of HCl 6N and the resin was pre-conditioned by 3 cc of HCl 0.5N before the introduction of the samples. Afterwards, HFSE (Nb, Ta, Zr, Hf, Ti) were recovered in new beakers by adding 9 cc of HCl 0.5M/HF 0.22M. These beakers were then put on the hot plate for evaporation and columns were cleaned by four cycles of 10 cc of HCl 6N and 10 cc of ultra-pure water.

For the second purification step, 0.85 cc of HNO_3 3.5M–H_3BO_3 0.06M was added to the residues after evaporation (see above) and samples were then transferred to tubes for centrifugation (10 minutes). The TODGA resin was cleaned by elution of 2 cc of HNO_3 10.5M, 6 cc of HNO_3 1M–HF 0.35M, 3 cc of HCl 0.05M and 1 cc of HNO_3

Figure 3.6 *Cleaning of the Teflon columns utilized for pre-concentrations of rare earth elements and Sr.*

3.5M–H_3BO_3 0.45 M. Then, the resin was pre-conditioned by 2 cc of HNO_3 3.5M. After the acid percolated, the solutions from the centrifuged tubes were introduced into the columns, followed by the addition of 3.5 cc of HNO_3 3.5N. Hf was then eluted in 6 cc of HNO_3 1M–HF 0.35M. Finally, the beakers were put on the hot plate for evaporation to dryness. Typically, Hf total procedural blanks in the Géosciences Montpellier clean lab are lower than 20 pg (e.g., Fernandez *et al.*, 2016).

3.2.5.4 MC-ICP-MS analyses of Pb, Nd and Hf radiogenic isotopes

Pb, Nd and Hf isotopes were measured either by a Nu Plasma 500™ (Fig. 3.7) or a Neptune Plus™ MC-ICP-MS at the École Normale Supérieure (ENS) of Lyon (France). Two rinsing solutions of 3% vol. HNO_3 and HNO_3 0.05N were used at the end of every measurement. Pb isotopes were analysed using the Tl normalization method described by White *et al.* (2000). First, Pb was dissolved in 2 cc of HNO_3 0.05N containing 30 ppb of Tl and kept some minutes on the hot plate. Then, solutions were homogenized in an ultrasonic bath and transferred to tubes to be analysed. Each batch of two samples was bracketed between NBS 981 standard splits and an external correction was applied according to the Tl normalization values of Thirlwall (2002). All the $^{206}Pb/^{204}Pb$, $^{207}Pb/^{204}Pb$ and $^{208}Pb/^{204}Pb$ ratios measured in the NBS 981 standard during the analytical sessions are listed in Table 3.4.

Nd was dissolved in 1 cc of HNO_3 0.05N and solutions were then ultrasonicated. Afterwards, the solutions were transferred to tubes to be analysed. Mass dependent fractionation was corrected using a $^{146}Nd/^{144}Nd$ ratio of 0.7219. The "Rennes" in-house Nd

Figure 3.7 *Nu Plasma 500™ MC-ICP-MS at the ENS of Lyon (France).*

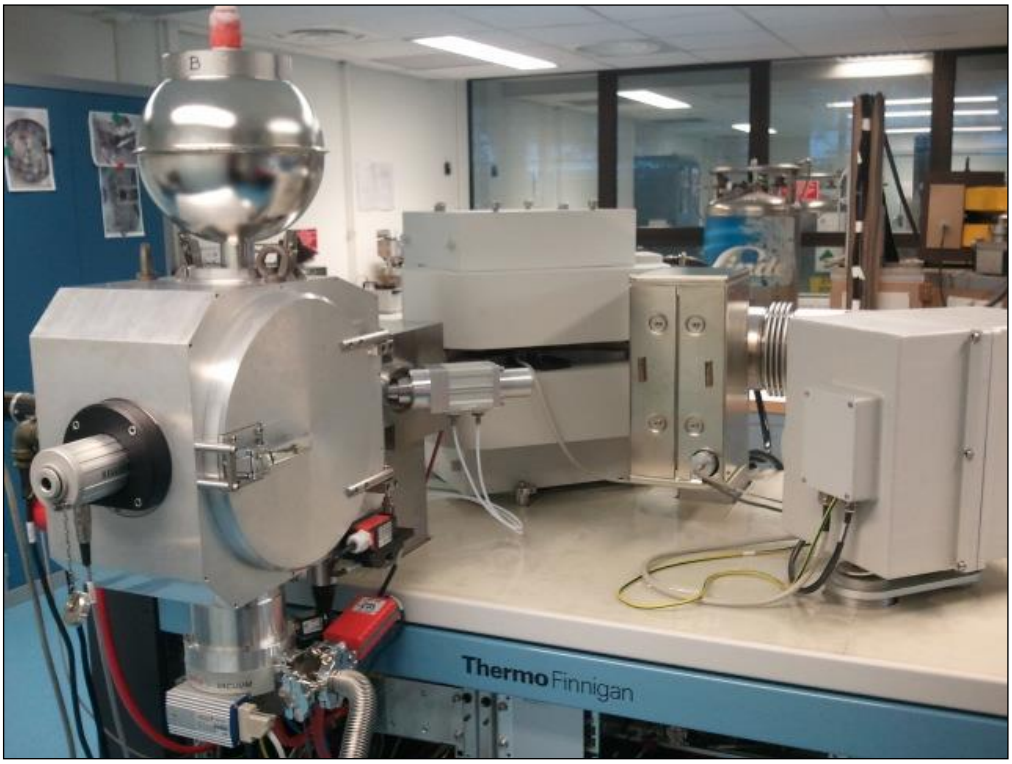

Figure 3.8 *ThermoFinnigan T1-Triton TIMS at LABOGIS (University of Nîmes, France).*

standard (Chauvel & Blichert-Toft, 2001) was measured repeatedly during the course of the Nd analyses. The values of $^{143}Nd/^{144}Nd$ ratios measured in the standard during the analytical sessions of the crustal rocks analyses are listed in Table 3.4.

Hf was diluted in 0.8 cc of HNO_3 0.05N and solutions were homogenized in an ultrasonic bath. Afterwards, the solutions were transferred to tubes for analysis. The JMC-475 Hf standard (Blichert-Toft *et al.*, 1997) was measured every two samples. Mass dependent fractionation was corrected using a $^{179}Hf/^{177}Hf$ ratio of 0.7325. The values of $^{176}Hf/^{177}Hf$ ratios measured in the standard during the analytical sessions of the pyroxenite analyses are listed in Table 3.4. The Nd-Pb-Hf isotopic ratios of the Ronda and Beni Bousera pyroxenites are reported in Chapter 5 (Table 5.2), and the Nd and Pb isotopic ratios of the Flysch sediments and Jubrique and Blanca metasedimentary rocks are listed in Chapter 6 (Table 6.2).

3.2.5.5 TIMS analyses of Sr radiogenic isotopic ratios

Sr isotopic ratios were measured by a ThermoFinnigan T1-Triton Thermal Ionization Mass Spectrometer (TIMS) at LABOGIS (University of Nîmes, France) (Fig. 3.8). Sr was dissolved in 2.5 µl of HNO_3 0.1N and loaded onto previously degassed Rhenium (Re) filaments. The loading procedure was done using a power supply device, which allowed loading 5 filaments

Table 3.4 Analytical measurements during isotope analyses

Elements	Instrument	Laboratory	Standards	n	Normalisation ratio	Standard results	References
Pb	MC-ICPMS (Nu Plasma 500)	École Normale Supérieure, Lyon	NBS-981	13*	$^{205}Tl/^{203}Tl$= 2.4336**	***Crustal rocks analyses***	(White *et al*., 2000)
						$^{208}Pb/^{204}Pb$ = 36.694 ± 0.001(2s)	(Thirlwall, 2002)
						$^{207}Pb/^{204}Pb$ = 15.4928 ± 0.0004 (2s)	
						$^{206}Pb/^{204}Pb$ = 16.9381 ± 0.0004 (2s)	
						$^{207}Pb/^{206}Pb$ = 0.91466 ± 0.00001(2s)	
						$^{208}Pb/^{206}Pb$ = 2.16642 ± 0.00002 (2s)	
	MC-ICPMS (Nu Plasma 1700)	École Normale Supérieure, Lyon	NBS-981	9*	$^{205}Tl/^{203}Tl$= 2.4336**	***Crustal rocks analyses***	(White *et al*., 2000)
						$^{208}Pb/^{204}Pb$ = 36.6546 ± 0.0006 (2s)	(Thirlwall, 2002)
						$^{207}Pb/^{204}Pb$ = 15.4766 ± 0.0002 (2s)	
						$^{206}Pb/^{204}Pb$ = 16.9282 ± 0.0002 (2s)	
						$^{207}Pb/^{206}Pb$ = 0.91426 ± 0.00006 (2s)	
						$^{208}Pb/^{206}Pb$ = 2.16531 ± 0.00002 (2s)	
	MC-ICPMS (Nu Plasma 500)	École Normale Supérieure, Lyon	NBS-981	10*	$^{205}Tl/^{203}Tl$= 2.4336**	***Pyroxenite analyses***	(White *et al*., 2000)
						$^{208}Pb/^{204}Pb$ = 36.709 ± 0.007 (2s)	(Thirlwall, 2002)
						$^{207}Pb/^{204}Pb$ = 15.496 ± 0.002 (2s)	
						$^{206}Pb/^{204}Pb$ = 16.9402 ± 0.0009 (2s)	
						$^{207}Pb/^{206}Pb$ = 0.91468 ± 0.00001(2s)	
						$^{208}Pb/^{206}Pb$ = 2.1669 ± 0.0001 (2s)	
Nd	MC-ICPMS (Nu Plasma 500)	École Normale Supérieure, Lyon	JMC	14*	$^{146}Nd/^{144}Nd$= 0.7219	***Crustal rocks analyses***	Standard AMES Rennes
						$^{143}Nd/^{144}Nd$ = 0.511964±0.000003 (2s)	
						$^{145}Nd/^{144}Nd$= 0.348422±0.000006 (2s)	(Chauvel and Blichert-Toft, 2001)
	MC-ICPMS (Nu Plasma 1700)	École Normale Supérieure, Lyon	JMC	11*	$^{146}Nd/^{144}Nd$= 0.7219	***Crustal rocks analyses***	Standard AMES Rennes
						$^{143}Nd/^{144}Nd$ = 0.511921±0.000005 (2s)	
						$^{145}Nd/^{144}Nd$= 0.348422±0.000006 (2s)	(Chauvel and Blichert-Toft, 2001)
Hf	MC-ICPMS (Nu Plasma 500)	École Normale Supérieure, Lyon	JMC-475	6*	$^{179}Hf/^{177}Hf$ = 0.7325	***Pyroxenite analyses***	
						$^{176}Hf/^{177}Hf$ = 0.282145 ± 0.000003 (2s)	(Blichert-Toft *et al*., 1997)
Sr	ThermoFinnigan Triton T1 TIMS	LABOGIS (Nîmes)	NBS-987	3	$^{88}Sr/^{86}Sr$=0.1194	***Crustal rocks analyses***	
						$^{86}Sr/^{87}Sr$ = 0.710252±0.000004 (2s)	
	ThermoFinnigan Triton T1 TIMS	LABOGIS (Nîmes)	NBS-987	2	$^{88}Sr/^{86}Sr$=0.1194	***Pyroxenite analyses***	
						$^{86}Sr/^{87}Sr$ = 0.710253 ± 0.000005 (2s)	

**standard compilation for one session of analyses with standards regularly analysed every two samples*

*** internal mass bias correction using exponential correction to $^{205}Tl/^{203}Tl$*

simultaneously applying a current of 0.5 A. Loading consisted on deposition of 1 µl of sample solution between two aliquots of 1 µl of $TaCl_5$. After drying, the current was gradually increased (usually up to 1.5 A) until the filaments shone. Then the current was turned off d uring the analytical sessions, the filaments were heated in 3 steps up to ~ 1400 ºC before the onset of the analysis that consisted of 5 cycles of 15 runs each. The NBS 987 standard was run at the beginning of each analytical session. Mass dependent fractionation was corrected using $^{86}Sr/^{88}Sr = 0.1194$. Further details on analytical measurements, including values of the measured international standards, are listed in Table 3.4. The Sr isotopic ratios of the Ronda and Beni Bousera pyroxenites are reported in Chapter 5 (Table 5.2), whereas those of the Flysch sediments and Jubrique and Blanca metasedimentary rocks are listed in Chapter 6 (Table 6.2).

Part II

Results

4 Refertilization processes in the subcontinental lithospheric mantle: The record of the Beni Bousera orogenic peridotite (Rif belt, N. Morocco)[1]

4.1 Introduction

Orogenic peridotite massifs play an important role in our understanding of the structural and chemical evolution of the subcontinental lithospheric mantle. These large peridotite bodies offer the opportunity to characterize the compositional variations induced by partial melting, melt transport and melt-rock reactions in the mantle over scales ranging from centimeters to tens of kilometers (e.g., Bodinier & Godard, 2014).

Classically, covariations of modal, major and trace element compositions in orogenic peridotites have been ascribed to variable degrees of melt extraction from a fertile mantle source (Bodinier, 1988; McDonough & Frey, 1989; Herzberg, 2004). However, several studies in orogenic, ophiolitic and oceanic peridotites have provided evidence that similar trends are caused by melt-rock reaction processes (involving mineral dissolution and/or precipitation and leading to depletion or refertilization), which are associated with major events of thinning and/or rejuvenation of the lithospheric mantle (e.g., Becker, 1996; Lenoir *et al.*, 2001; Müntener *et al.*, 2004; Niu, 2004; Rampone *et al.*, 2004; Ionov *et al.*, 2005; Le Roux *et al.*, 2007). These processes are particularly well-documented in the Lherz (W. Pyrenees, S. France) and Ronda peridotite massifs (Betic Cordillera, S. Spain), which show modal, chemical and textural variations resulting from partial melting, melt-rock reaction, annealing of deformation microstructures and crystallization of secondary minerals (Van der Wal & Bodinier, 1996; Garrido & Bodinier, 1999; Lenoir *et al.*, 2001; Le Roux *et al.*, 2007; Bodinier *et al.*, 2008; Marchesi *et al.*, 2013). In Ronda, structural and compositional variations at km-scale are associated with a recrystallization front that separates a partially molten granular peridotite domain from its precursor lithospheric tectonite domain (Fig. 1.8, Ch. 1) (Van der Wal &

[1] *This chapter is accepted in the JCR Journal of Petrology*

Bodinier, 1996; Garrido & Bodinier, 1999; Lenoir *et al.*, 2001; Soustelle *et al.*, 2009). Lenoir *et al.* (2001) concluded that a strong thermal gradient existed across the Ronda mantle section during the formation of the recrystallization front, allowing small melt fractions to percolate up to 1.5 km ahead of the front and form a meter-scale layering of harzburgites and lherzolites produced by reactive melt percolation (Soustelle *et al.*, 2009). In Lherz, the boundary between the spinel lherzolite-websterite and harzburgite units constitutes an extremely convoluted refertilization front, formed by the coalescence of relatively narrow melt infiltration channels (Le Roux *et al.*, 2007, 2008). These refertilization and melting fronts are considered the upper and lower boundaries of transient, moving asthenosphere-lithosphere transition zones generated by the thermo-mechanical erosion of the lithospheric mantle by upwelling asthenosphere (Le Roux *et al.*, 2007; Soustelle *et al.*, 2009).

The Beni Bousera orogenic peridotite massif (Figs. 1.9 & 1.10, Ch. 1; Rif Belt, N. Morocco) has chemical and structural features similar to those observed in Lherz and Ronda (Frets *et al.*, 2014), and it is dominated by fertile spinel (± garnet) lherzolite compositions (Pearson *et al.*, 1989; Kornprobst *et al.*, 1990). Here we present an extensive and detailed geochemical dataset of peridotites from the Beni Bousera massif, which includes major element abundances in bulk rock and minerals, and trace element abundances in clinopyroxene. Our results show that the Beni Bousera lherzolites have peculiar modal variations normally not observed in a unique orogenic massif, which were induced by two different melt-rock reactions causing pyroxene addition to a refractory mantle protolith. These data support a secondary, refertilization-related, origin for most lherzolites in orogenic peridotite massifs and provide general insights into melt-rock reactions in the mantle.

4.2 Sampling

For this study we selected 238 peridotites collected mainly along river valleys roughly perpendicular to the NW-SE orientation of the Beni Bousera massif and at varying distances from the contact with the overlying crustal kinzigites (Fig. 4.1). The sampling spans the four tectono-metamorphic domains defined by Frets *et al.* (2014). We sampled 46 peridotites from the Grt-Sp mylonites, 52 from the Ar domain, 30 from the Ar-Se domain, and 110 from the Se domain, focusing on harzburgite and lherzolite lithologies. Peridotites near pyroxenite layers were not sampled in order to minimize the effects of subsolidus equilibration between different lithologies, except in Grt-Sp mylonites where, based on microstructural data, peridotite and pyroxenite are mixed at centimetric scale (Frets *et al.*, 2012).

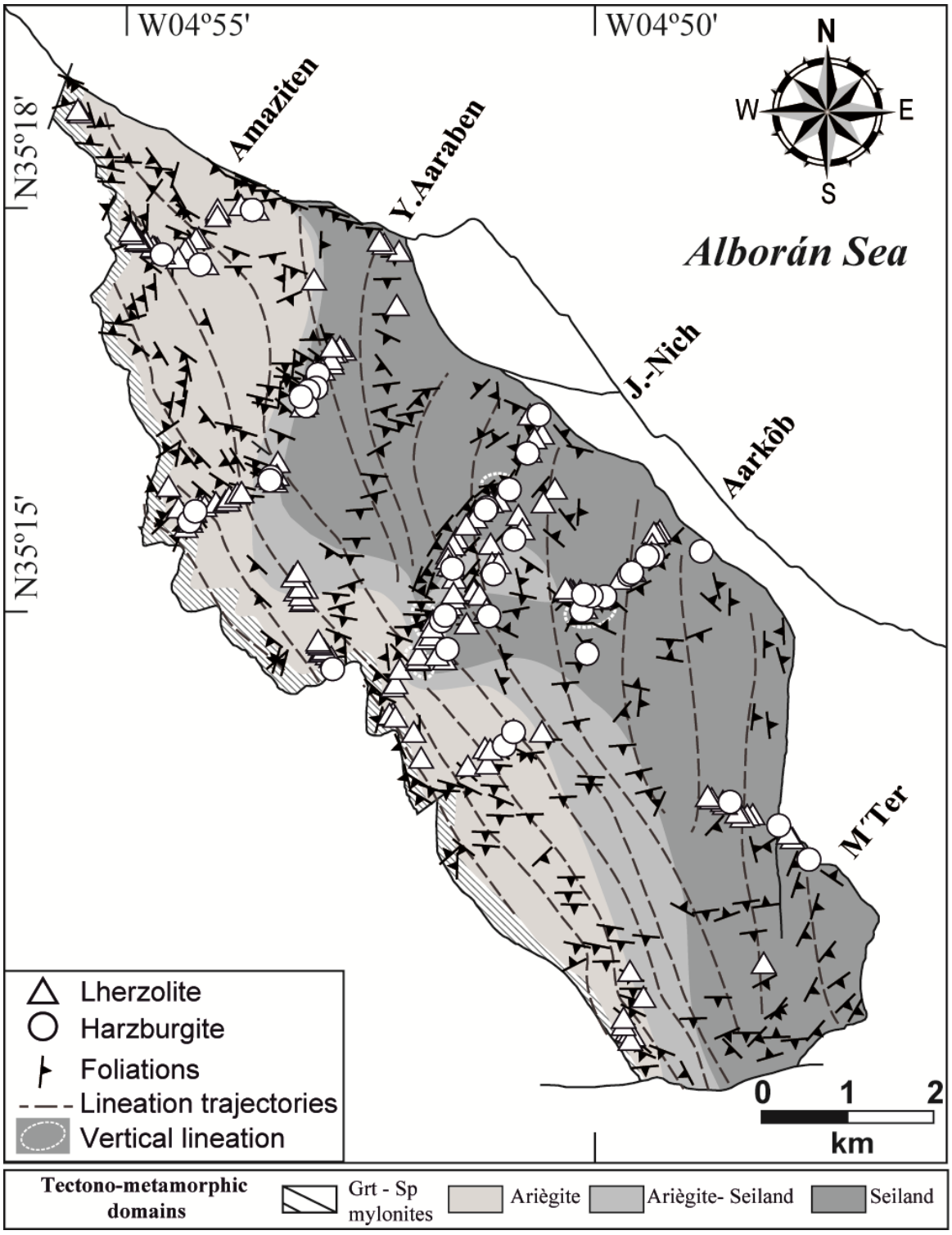

Figure 4.1 *Map of the structure of the Beni Bousera peridotite showing the sample localities, foliation and lineation trajectories. The four tectono-metamorphic domains defined by Frets et al. (2014) are represented in the background. Lherzolite samples are shown as open triangles and harzburgite samples as open circles. Foliation and lineation trajectories based on data collected by Frets et al. (2014, and references therein).*

Grt-Sp peridotite mylonites have porphyroclastic texture defined by mm-sized garnet and pyroxene porphyroclasts embedded in a fine-grained (< 1 mm) recrystallized matrix of

olivine, pyroxene and spinel neoblasts, whose elongated shapes define the mylonitic foliation. Garnet, which occurs only in peridotites from this domain, forms rounded porphyroclasts usually partly transformed to kelyphite (pyroxene-spinel symplectites) and occasionally containing inclusions of spinel, pyroxene and olivine. Garnet is concentrated in clinopyroxene-rich lenses parallel to the mylonitic foliation and has irregular grain boundaries with embayments filled with pyroxene. The porphyroclasts of orthopyroxene are larger and more elongated than those of clinopyroxene and their embayments are generally filled with olivine. From the Grt-Sp mylonites to the Se domain, the Beni Bousera peridotites are characterized by an increase in the average grain size of olivine and a decrease of the volume fractions of recrystallized grains. Ar peridotites have porphyroclastic texture consisting of mm-sized olivine and pyroxene porphyroclasts enclosed by fine-grained (~ 175 – 250 μm) recrystallized olivine and pyroxenes. Both porphyroclasts and matrix minerals have undulose extinction and serrated and/or irregular grain boundaries. Orthopyroxene porphyroclasts show pervasive clinopyroxene exsolution and grain boundaries embayments filled with olivine, and spinel is coarser (0.5 – 2 mm) than in Grt-Sp mylonites. Ar-Se peridotites have (mm-sized) pyroxene and (up to 1 cm) olivine porphyroclasts, and an olivine-rich (~ 250 – 350 μm) matrix coarser than in the Ar domain. Porphyroclasts and olivine neoblasts display undulose extinction. Orthopyroxene porphyroclasts have grain boundary embayments filled with olivine and clinopyroxene occurs mainly as aggregates, in places associated with orthopyroxene. Spinel occurs either as holly-leaf-shaped crystals or as small rounded grains, usually included in olivine. Se peridotites have coarse-grained porphyroclastic to coarse-granular textures. Olivine shows very sinuous grain boundaries and undulose extinction. Orthopyroxene is coarse (up to 8 mm), has irregular shapes and grain boundary embayments or fractures filled with olivine. It usually shows fine clinopyroxene exsolution lamellae and undulose extinction. Clinopyroxene occurs as irregularly shaped, isolated crystals with exsolution lamellae of orthopyroxene and undulose extinction. Further details on the petrographic and microstructural features of the studied samples are reported by Frets *et al.* (2014).

4.3 Results

4.3.1 Rock types

The lithological classification of peridotites was done based on their mineral modes of olivine (Ol), orthopyroxene (Opx) and clinopyroxene (Cpx) obtained by mass-balance calculations

between anhydrous bulk rock and mineral compositions (see caption of Fig. 4.2 for more details).

This classification resulted in the following lithological distribution of samples: 5 harzburgites and 41 lherzolites in the Grt-Sp mylonites; 8 harzburgites and 44 lherzolites in the Ar domain; 8 harzburgites and 22 lherzolites in the Ar-Se domain; and 25 harzburgites and 85 lherzolites in the Se domain. On average, this sampling distribution reflects the lithological compositions of the structural domains and it is proportional to their areal extents (Fig. 4.1), except for a slight oversampling of Grt-Sp mylonites and undersampling of the Ar domain.

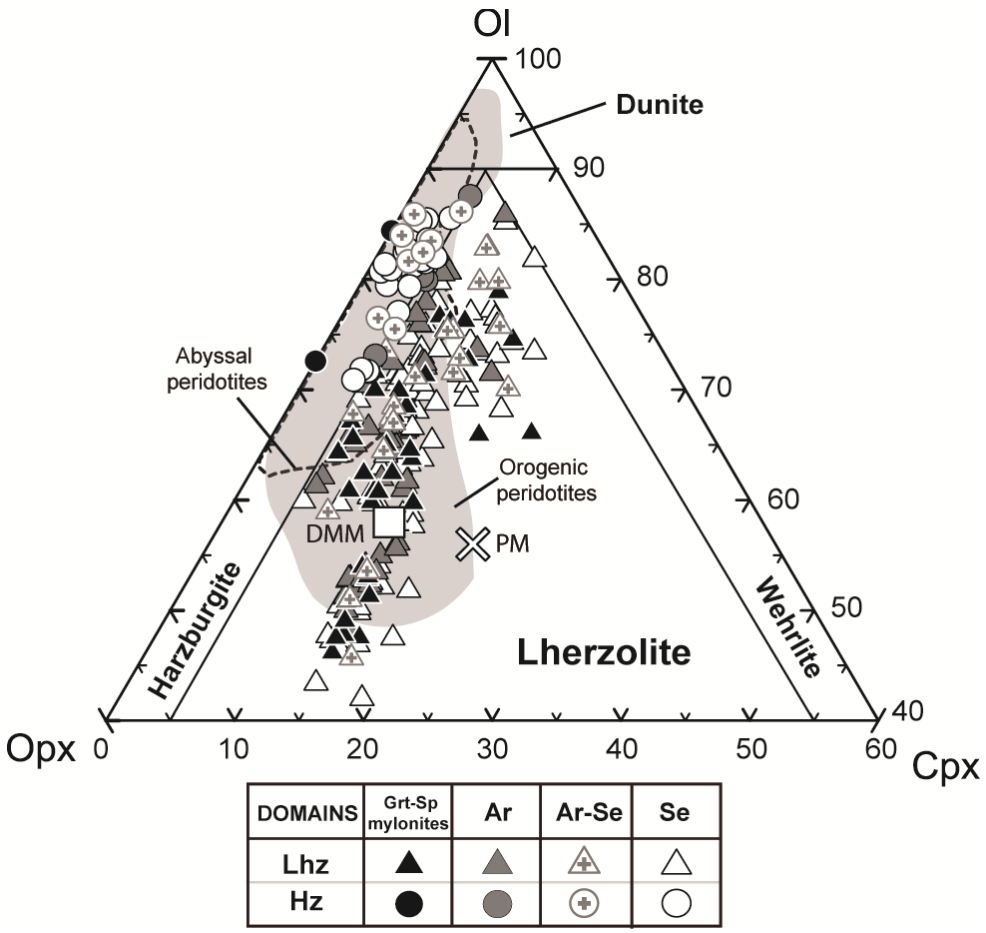

Figure 4.2 *Peridotite modal compositions from the different tectono-metamorphic domains of the Beni Bousera massif (Frets et al., 2014). The mineral modes were calculated by mass balance, plotting onto the peridotite field of olivine (Ol)– orthopyroxene (Opx)– clinopyroxene (Cpx) diagram (Streckeisen, 1976). The calculation method employed uses an inversion procedure combining the major element data for bulk rock and minerals. Among the 238 samples studied, 192 correspond to lherzolite (Lhz) and 46 to harzburgite (Hz). Orogenic (grey area) and abyssal peridotite (dashed line) fields are taken from Bodinier & Godard (2014, and references therein). The estimates of Depleted MORB Mantle (DMM; open square) from Workman & Hart (2005) and of Primitive Mantle (PM; open X) from McDonough & Sun (1995) are also shown.*

4.3.2 Bulk rock chemistry

The entire dataset of bulk rock major and minor element composition of the Beni Bousera peridotites can be found in Appendix A. Peridotites from the different Beni Bousera structural domains overlap in terms of bulk major and minor element compositions (Figs. 4.3 & 4.4). In general, their anhydrous silica contents (41.8 – 47.4 wt. %) slightly decrease in conjunction with Al_2O_3 (0.1 – 5.4 wt. %) from fertile lherzolites to refractory harzburgites (Fig. 4.3a). Some samples, particularly those from the Grt-Sp mylonite and Se domains, have rather high SiO_2 (46.2 – 47.4 wt. %) relative to their Al_2O_3 abundances, whereas three highly refractory harzburgites from the Se domain have especially low SiO_2 contents (< 42.5 wt. %) (Fig. 4.3a).

Similar to common mantle peridotites (e.g., Bodinier & Godard, 2014), the Beni Bousera samples show coherent covariation trends of anhydrous MgO and CaO against Al_2O_3 (Fig. 4.3b, c), with a slight dispersion between MgO and Al_2O_3 in some samples from the Grt-Sp mylonite and Se domains (Fig. 4.3b). These compositional trends range between fertile — comparable to the primitive mantle (PM)— and refractory end members. Anhydrous MgO spans from 35.9 to 47.5 wt. %, and is particularly low (< 36.3 wt. %) in a few lherzolites from the Grt-Sp mylonite, Ar-Se and Se domains (Fig. 4.3b). Anhydrous CaO varies between 0.3 and 4.2 wt. %, and is especially high (> 3.8 wt.%) in one Grt-Sp mylonite and three Se lherzolites (Fig. 4.3c), which also have MgO values lower than the PM (Fig. 4.3b).

Anhydrous FeO does not show significant covariation with Al_2O_3 and spans from 7.4 to 9.7 wt. % (Fig. 4.3d). Grt-Sp mylonites have a more restricted range of FeO than peridotites from the other domains. Some Se harzburgites are particularly rich in FeO (> 8.5 wt. %), whereas some Ar, Ar-Se and Se peridotites have especially low FeO content (< 7.7 wt. %; Fig. 4.3d).

Ni (1742 – 2424 ppm) and V (15 – 99 ppm) display negative and positive correlations with Al_2O_3, respectively (Fig. 4.4), which are in agreement with the common control of olivine abundances on Ni and of pyroxenes on V in spinel peridotites (Canil, 2004). Some lherzolites from the Se domain are particularly rich in Ni, whereas three Grt-Sp mylonitic lherzolites and one Ar lherzolite have low V compared to rocks with similar Al_2O_3 (Fig. 4.4).

4.3.3 Mineral major element composition

Mg-no. of minerals and LA-ICP-MS analyses of clinopyroxene are given in Appendix B.

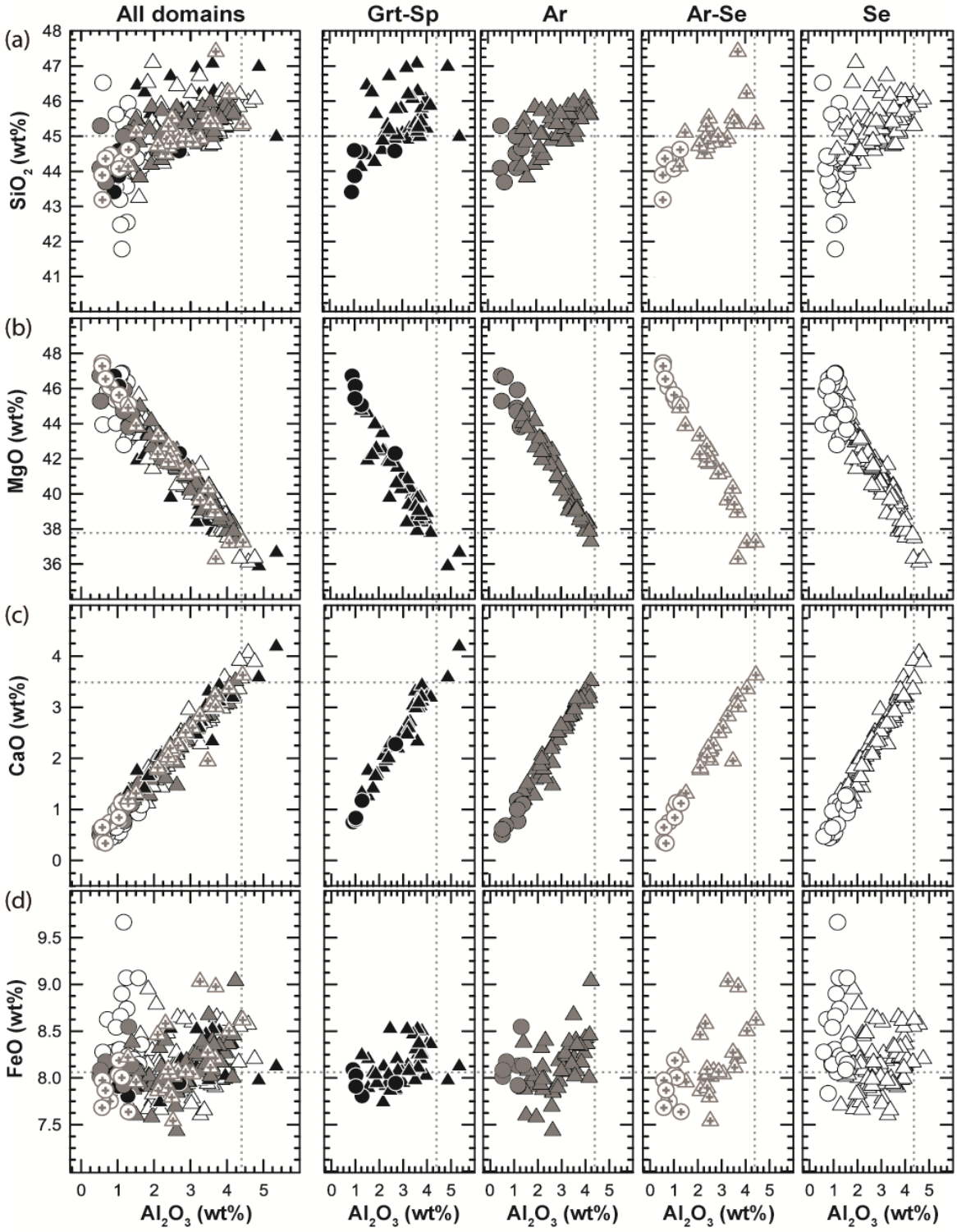

Figure 4.3 *Bulk rock Al_2O_3 vs (a) SiO_2, (b) MgO, (c) CaO and (d) FeO of harzburgites and lherzolites from the Beni Bousera massif. Covariation diagrams per domain are also shown. Data are in wt. % and on anhydrous basis. Symbols as in Figure 4.2. Dashed lines represent the estimates of PM after McDonough & Sun (1995).*

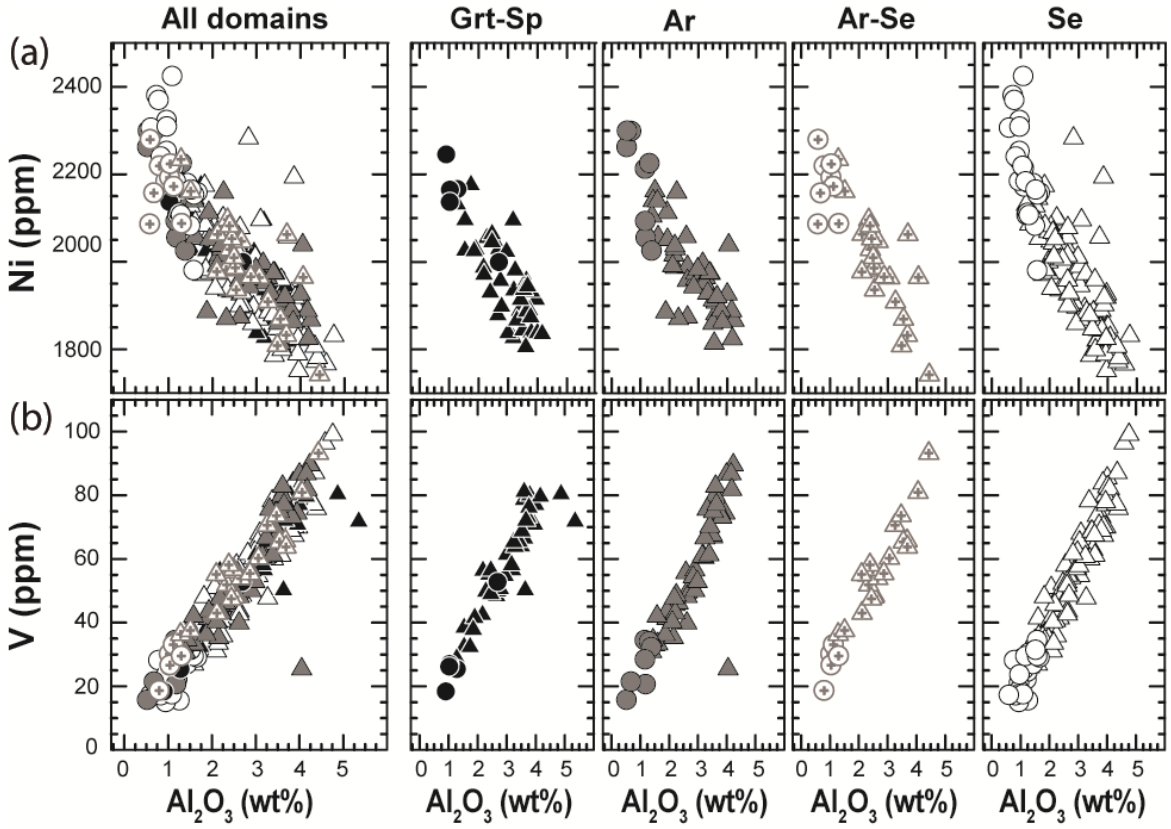

Figure 4.4 *Bulk rock Al_2O_3 (wt. %) vs (a) Ni (ppm) and (b) V (ppm) of harzburgites and lherzolites from the Beni Bousera massif. Covariation diagrams per domain are also shown. Data are in wt. % and on anhydrous basis. Symbols as in Figure 4.2.*

4.3.3.1 Olivine

The major element composition of olivine is related to the fertility of the samples, with lherzolites having slightly lower forsterite content (Fo = 88.2 – 90.4) than harzburgites (89.4 – 91.2) (Fig. 4.5a). Focusing on lherzolites (Fig. 4.5b), the average Fo in olivine is very similar for the Ar, Ar-Se and Se domains (c. 89.6) —excluding two Ar-Se (Fo = 88.2) and Se (Fo = 88.1) outliers— but it is lower in the Grt-Sp mylonites (c. 89.3) (Fig. 4.5b).

4.3.3.2 Spinel

Similar to Fo in olivine, the Cr-no. in spinel reflects the lithology of the rocks, as harzburgites have higher Cr-no. (10.2 – 57.1) than lherzolites (7.5 – 22.9) (Fig. 4.5a). In the Ar, Ar-Se and Se domains, the Cr-no. in spinel increases with increasing Fo in olivine within the olivine-spinel mantle array (OSMA) of Arai (1994), partially overlapping the field of abyssal peridotites, whereas in the Grt-Sp mylonites no clear correlation is observed (Fig. 4.5a). Contrary to Fo in olivine, the lherzolites from Grt-Sp mylonites have, on average, a higher Cr-no. in spinel (18.3)

than lherzolites from the other domains, especially compared to those from the Se domain (11.7) (Fig. 4.5c).

4.3.3.3 Pyroxenes

The Mg-no. in orthopyroxene varies similar to Fo in olivine, with lherzolites having in general slightly lower Mg-no. (88.5 – 90.6) than harzburgites (89.4 – 91.2) (Fig.4.6a). Rough negative correlations between Al_2O_3 (2.0 – 6.2 wt. %) and Mg-no. in orthopyroxene (Fig.4.6a), and between Al_2O_3 in orthopyroxene and Fo in olivine (Fig.4.6b) are shown by lherzolites from the Ar, Ar-Se and Se domains, but are absent in Grt-Sp mylonites (Fig.4.6).

The Mg-no. in clinopyroxene ranges from 88.6 to 92.8 in lherzolites and from 90.6 to 93.3 in harzburgites (Appendix B) and, in general, it is negatively correlated with Ti (704 – 4457 ppm) and Na_2O (0.5 – 2.2 wt.%) in clinopyroxene (not shown).

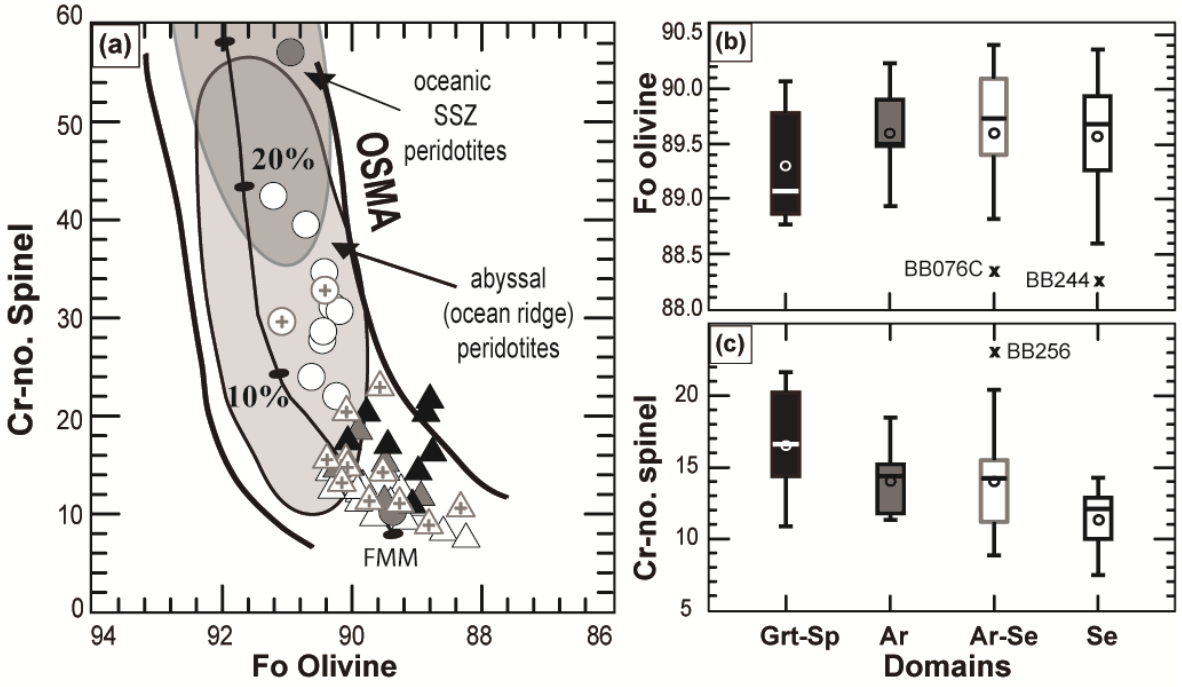

Figure 4.5 *(a) Fo [(100*Mg/(Mg + Fe^{2+})] in olivine vs Cr-no. [100*(Cr/(Cr + Al)] in spinel for 13 harzburgites and 44 lherzolites of the Beni Bousera massif (Appendix B). Trend of partial melting of the Fertile MORB Mantle (FMM), "Olivine-spinel mantle array" (OSMA), abyssal (light grey area) and supra-subduction zone (SSZ) (dark grey area) are taken from Arai (1994). Symbols as in Figure 4.2. Box plots show the variation of (b) Fo in olivine and (c) Cr-no. in spinel of lherzolites from the four domains of the massif. Each box extends from the 25th percentile to the 75th percentile of the data distribution, the 50th percentile ("median") corresponds to the line across the box, and the average value is represented by an open circle. Lines extending from the box correspond to the values between the 10th and 90th percentile. Individual samples outside these distribution bounds are called outliers and are symbolized by an "X" with their respective sample names. Box plots were done using olivine and spinel major element data of 46 lherzolite samples: 10 Grt-Sp mylonites (one sample not analysed for olivine), 6 lherzolites from the Ar domain (one sample not analysed for olivine), 11 from the Ar-Se domain and 19 from the Se domain.*

4.3.4 Clinopyroxene trace element composition

The PM-normalized extended patterns and the chondrite-normalized REE patterns of clinopyroxene in peridotites are differentiated in Figures 4.7, 4.8, and 4.9 according to the petrological domains of the massif.

Clinopyroxene in almost all the samples shows enrichment of Cs relative to Rb and of U relative to Th, and negative anomalies of Ba, Nb, Pb, Zr and Ti (Figs. 4.7a & 4.8). Some exceptions are clinopyroxene enriched in Rb relative to Cs —in BB183, BB187, BB191 from the Ar domain, and in BB138 and BB246A from the Se domain—; clinopyroxene with a positive anomaly in Ba and Nb —in BB026 from the Ar domain—; and clinopyroxene relatively rich in Pb —in BB102 and BB205 from the Ar-Se domain— (Fig. 4.8).

4.3.4.1 Rare earth elements

4.3.4.1.1 Grt-Sp mylonites

Clinopyroxene in lherzolites from this domain has varied REE patterns (Fig. 4.7b). In samples BB088B and BB165, clinopyroxene has convex-upward MORB-like patterns depleted in LREE and MREE relative to HREE (Ce_N/Sm_N = 0.4 – 0.5; Sm_N/Yb_N = 0.6 – 0.9). Clinopyroxene in BB006, BB083 and BB171 is enriched in MREE relative to LREE and HREE, displaying a bell-shaped pattern (Ce_N/Sm_N = 0.5 – 0.7; Sm_N/Yb_N = 6.5 – 11.9). In sample BB201, clinopyroxene is depleted in REE and presents three S-shaped patterns (Ce_N/Sm_N = 0.5 – 0.9; Sm_N/Yb_N = 0.9 – 5.3) that mainly differ in their HREE concentrations (Fig. 4.7b).

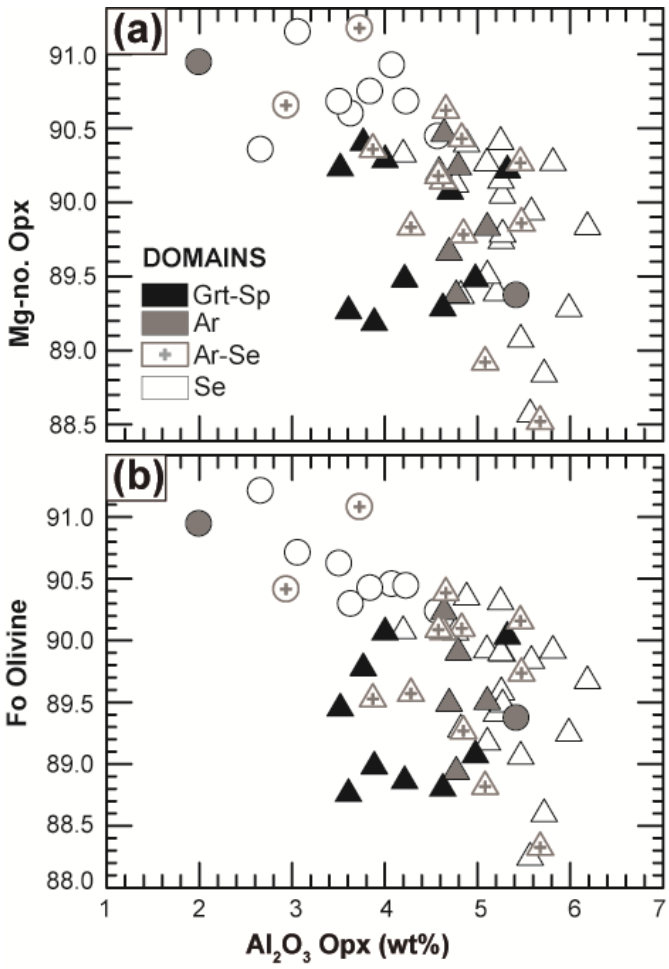

Figure 4.6 *Al_2O_3 in Opx (wt. %) vs (a) Mg-no. [(100*Mg/(Mg + Fe^{2+})] of Opx and (b) Fo in olivine of harzburgites (circles) and lherzolites (triangles) from the Beni Bousera massif (mineral data taken from Frets et al., 2014, Appendix B).*

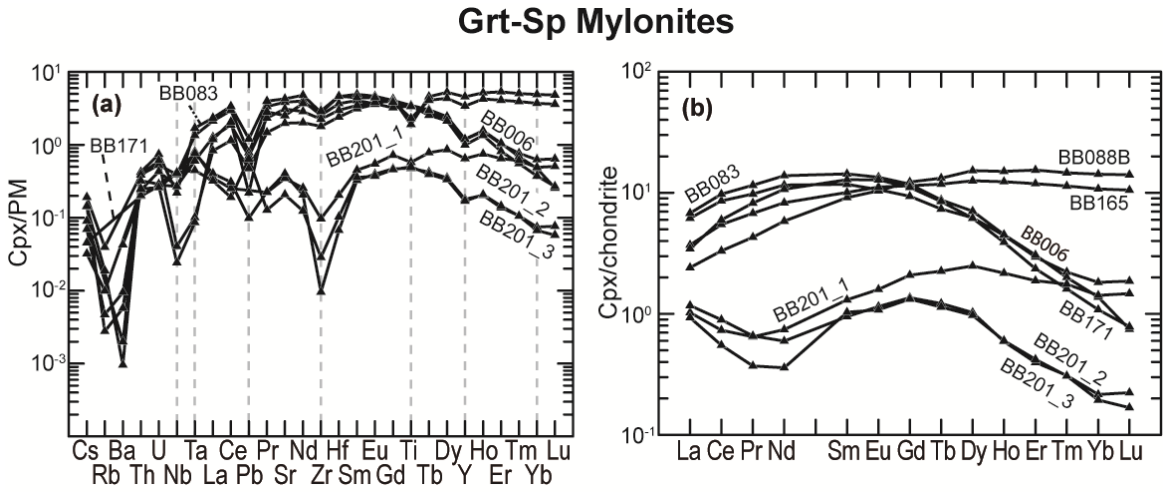

Figure 4.7 *(a) PM-normalized trace element patterns and (b) chondrite-normalized REE patterns of clinopyroxene from the Grt-Sp mylonites lherzolites. Normalizing values are from Sun & McDonough (1989). Mineral data listed in Appendix B.*

4.3.4.1.2 Ar domain

Most of the lherzolites in this domain have clinopyroxene depleted in LREE and MREE relative to HREE (Ce_N/Sm_N = 0.1 – 0.8; Sm_N/Yb_N = 0.2 – 0.8), especially in sample BB026 (Fig. 4.9a). Exceptions are lherzolites BB187, BB098 and BB143 that have clinopyroxene patterns which differ from the general convex-upward shape as they are enriched in LREE relative to HREE (Fig. 4.9a). Concerning the harzburgites, clinopyroxene in sample BB108 displays a convex-upward REE pattern (Ce_N/Sm_N = 0.5; Sm_N/Yb_N = 0.9) that is very similar to the general trend of lherzolites, whereas clinopyroxene in BB035D is enriched in LREE and MREE relative to HREE (Ce_N/Sm_N =2.0; Sm_N/Yb_N = 2.2) (Fig. 4.9b).

4.3.4.1.3 Ar-Se domain

Clinopyroxene in lherzolites from this domain also displays the convex-upward MORB-like pattern (Ce_N/Sm_N = 0.5 – 0.7; Sm_N/Yb_N = 0.6 – 0.9) described for lherzolites from the other domains (Figs. 4.7a & 4.9). Exceptions to this trend are clinopyroxene in samples BB207, with a spoon-shaped pattern, in BB130, BB205 and BB256, in which it displays a bell-shaped pattern; and in BB216, with an almost unfractionated clinopyroxene pattern (Fig. 4.9c). Focusing on harzburgites, clinopyroxene in BB076A has the general convex-upward REE pattern of lherzolites (Ce_N/Sm_N = 0.7; Sm_N/Yb_N = 0.8), whereas in BB070 it is mildly fractionated and in BB259 shows a bell-shaped pattern (Fig. 4.9d).

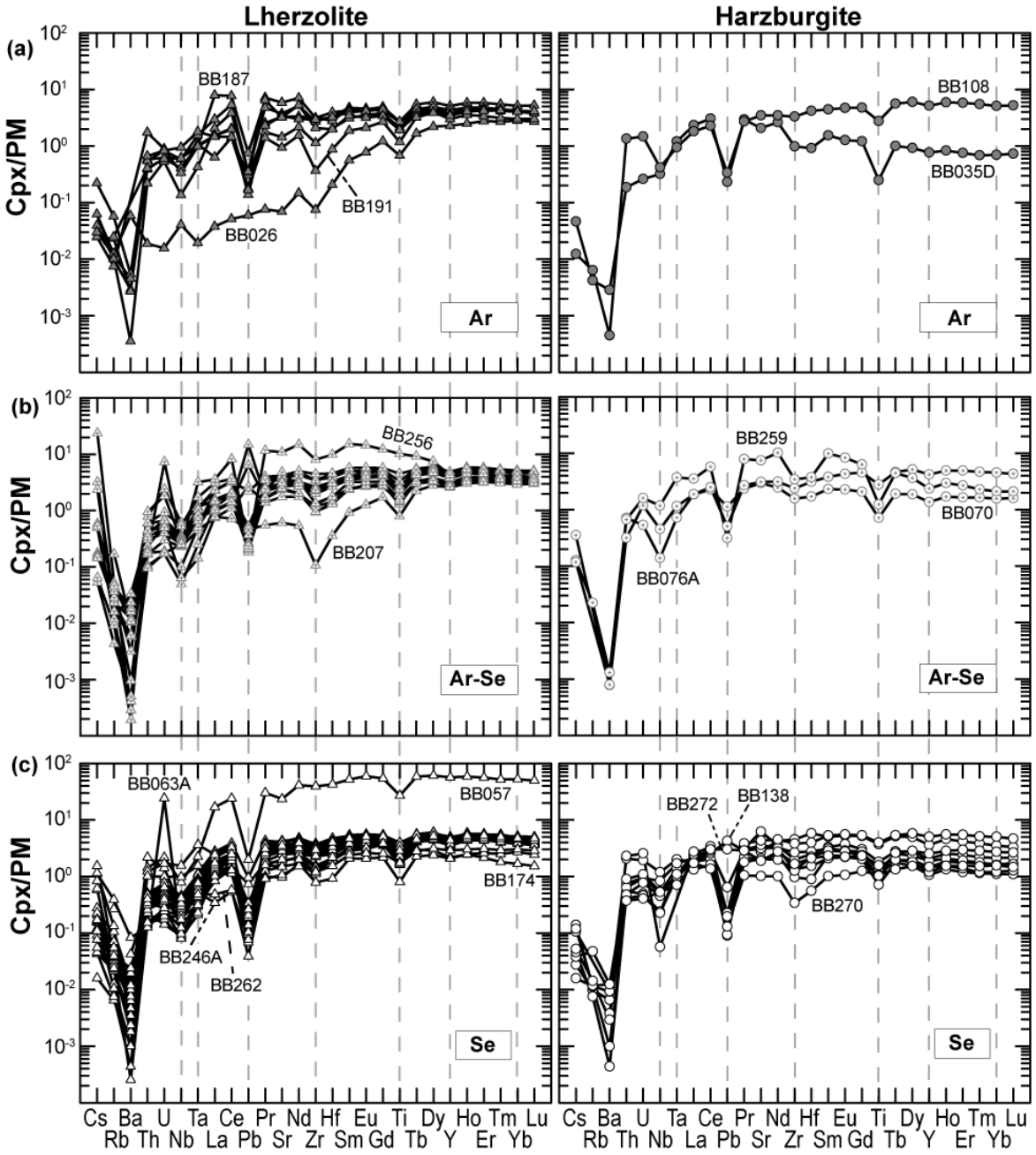

Figure 4.8 *PM-normalized trace elements patterns of clinopyroxene from lherzolites and harzburgites from the (a) Ar domain, (b) Ar-Se domain and (c) Se domain, respectively. Normalizing values are from Sun & McDonough (1989). Mineral data listed in Appendix B.*

4.3.4.1.4 Se domain

Clinopyroxene in Se lherzolites (Fig. 4.9e) is very homogeneous in terms of REE compositions and shows the typical convex-upward pattern (Ce_N/Sm_N = 0.4 – 1.0; Sm_N/Yb_N = 0.7 – 1.1) generally described in the massif. Clinopyroxene is particularly LREE-depleted in lherzolites BB246A and BB262 (Ce_N/Sm_N = 0.2; Sm_N/Yb_N = 0.6 – 0.7), and it is especially rich in REE in BB057. Lherzolite BB174 has clinopyroxene with a bell-shaped pattern (Ce_N/Sm_N = 0.8; Sm_N/Yb_N = 2.4; Fig. 4.9e), similar to most harzburgites from this domain (Ce_N/Sm_N = 0.5 – 1.0;

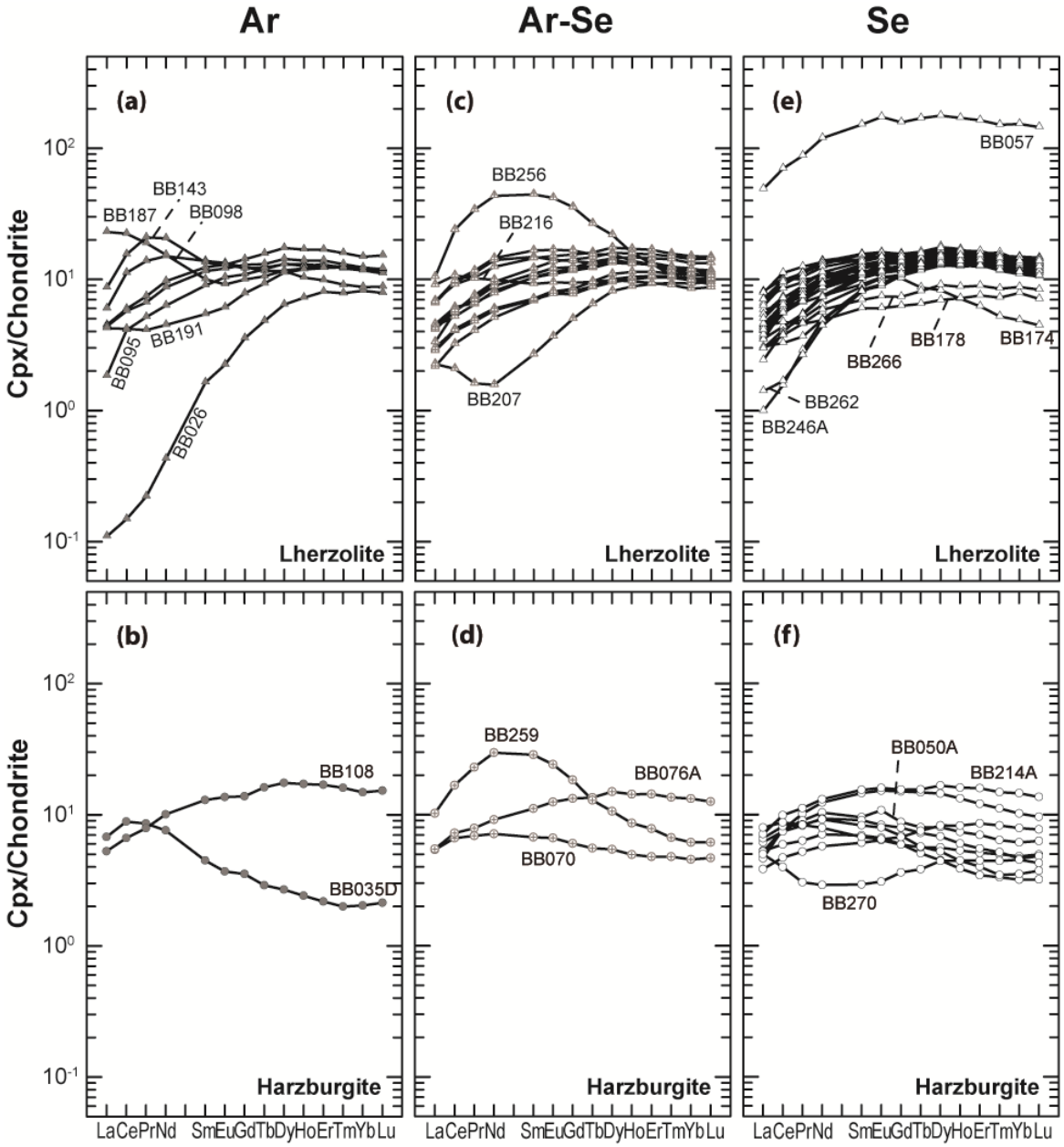

Figure 4.9 *Chondrite-normalized REE patterns of clinopyroxene from lherzolites and harzburgites from the Ar (a, b), Ar-Se (c, d) and Se (e, f) domains. Normalizing values are from Sun & McDonough (1989). Mineral data listed in Appendix B.*

Sm_N/Yb_N = 1.4 – 3.9; Fig. 4.9f). Clinopyroxene in harzburgites BB050A and BB214A has positive Eu anomaly, and in harzburgite BB270 it shows a spoon-shaped pattern (Fig. 4.9f).

4.4 Discussion

4.4.1 The role of tectonic mixing and subsolidus equilibration

Tectonic mixing between peridotites and garnet pyroxenites has been reported in mylonites from the Lherz, Ronda and Beni Bousera orogenic massifs (e.g., Schubert, 1977; Obata, 1980;

Fabriès & Conquéré, 1983; Pearson *et al.*, 1993; Garrido *et al.*, 2011), and, to some extent, constitutes the observational foundation of the two-component marble-cake mantle hypothesis (Allegre & Turcotte, 1986). The Beni Bousera Grt-Sp mylonites experienced strong shearing under lithospheric conditions that resulted in stretching and transposition of the pyroxenite layers leading to local mechanical mixing between garnet pyroxenites and host peridotites (Reuber *et al.*, 1982; Saddiqi *et al.*, 1988; Pearson *et al.*, 1993; Frets *et al.*, 2012, 2014). Therefore, it is important to assess to what extent syntectonic grain size reduction and increasing contact surface between peridotites and pyroxenites (Kornprobst, 1969; Pearson *et al.*, 1993; Tabit *et al.*, 1997; Frets *et al.*, 2012, 2014) influenced the bulk rock (Figs. 4.3 & 4.4) and mineral major (Figs. 4.5 & 4.6) and trace element variability (Fig. 4.7) in this domain.

The anomalously high bulk SiO_2 and low MgO of some Grt-Sp mylonites compared to other Beni Bousera peridotites with similar Al_2O_3 (Fig. 4.3a, b) and their CaO and Al_2O_3 contents higher than the PM (Fig. 4.3c) cannot be explained by melting processes. These data point instead to tectonic mixing with mafic layers. Furthermore, subsolidus re-equilibration with garnet pyroxenites is supported by the relatively low Fo content in olivine (Fig. 4.5b), high Cr no. in spinel due to preferential incorporation of Al_2O_3 in garnet (Fig. 4.5c) (Arai, 1994), and the lack of correlation between Al_2O_3 and Mg-no. in orthopyroxene (Fig.4.6a) and between Al_2O_3 in orthopyroxene and Fo in olivine (Fig.4.6b). Re-equilibration with garnet is also confirmed by the trace element patterns of clinopyroxene in some Grt-Sp mylonites, which are depleted in HREE, Zr and Y, and are locally in disequilibrium at thin section scale (Fig. 4.7) similar to hybrid peridotites from lower Austria (Becker, 1996a). These compositional features are in agreement with other geochemical and structural evidence of tectonic mixing and subsolidus equilibration between peridotites and garnet pyroxenites at the garnet to spinel lherzolite transition (Kornprobst *et al.*, 1990; Pearson *et al.*, 1993; Pearson & Nowell, 2004). Therefore, we exclude this domain from the following discussion about the igneous evolution of the massif because its bulk rock and mineral compositions are significantly influenced by subsolidus re-equilibration.

4.4.2 Relationships between peridotite modes and the petro-structural zoning of the massif

Similar to other orogenic massifs, the Beni Bousera peridotites mostly consist of fertile spinel lherzolites (Fig. 4.2). In the spatially-associated Ronda massif, the fertility of peridotites is related to their petro-structural domains, as granular peridotites are on average more depleted

in major and trace elements than spinel tectonites and transitional peridotites at the recrystallization front (Lenoir *et al.*, 2001). In contrast, the Beni Bousera peridotites do not show clear variations of bulk rock and mineral compositions related to the tectono-metamorphic zoning of the massif (Figs. 4.3 to 4.9), but some correspondence exists between the petro-structural domains and different trends of mineral modes in lherzolites. According to their modal compositions, we distinguish three types of lherzolites (Fig. 4.10):

i. *Group I.* Lherzolites with Ol ≥ 60%, Ol/Opx ratios higher than the DMM and variable Cpx/Opx ratios generally lower than 0.8. They mostly occur in the Ar (c. 50% of the domain) and Se (c. 45%) domains, and are slightly less abundant in the Ar-Se domain (c. 36%) (Fig. 4.11).

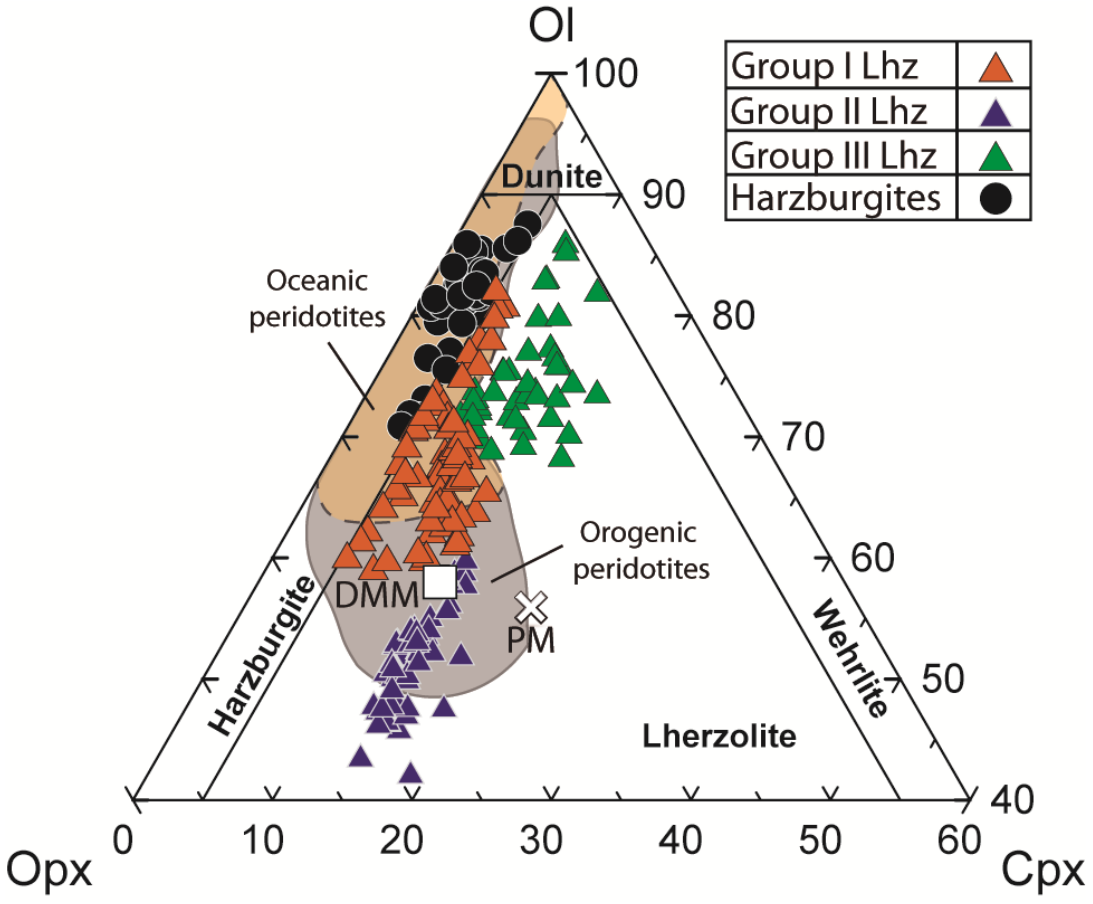

Figure 4.10 *Peridotite modal compositions from the Beni Bousera massif, excluding Grt-Sp mylonites. Lherzolites are divided into three groups: Group I with Ol ≥ 60%, and variable abundance of pyroxenes (orange triangles), Group II with Ol <60%, Cpx >11% and Opx >28% (blue triangles), and Group III with Ol >65%, Opx <21% and Cpx >7 % (green triangles). Mineral modes were calculated by mass balance as described in the caption of Figure 4.2. Fields of orogenic (grey area) and abyssal peridotites (yellow area) are taken from Bodinier & Godard (2014, and references therein). DMM, open square (Workman & Hart, 2005) and PM, open X (McDonough & Sun, 1995).*

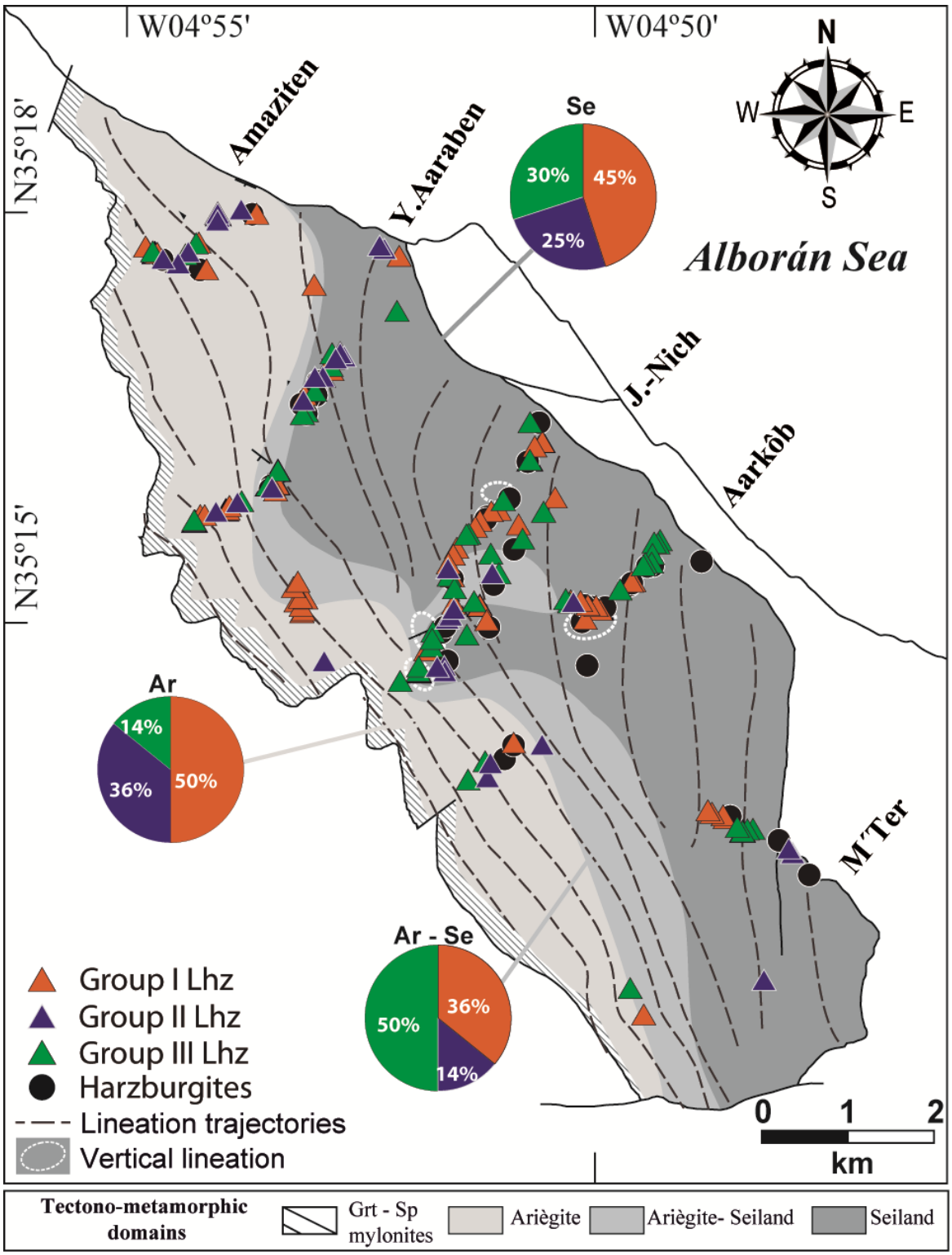

Figure 4.11 *Map of the structure of the Beni Bousera peridotite massif showing the field distribution of harzburgites and lherzolites from the Ar, Ar-Se and Se domains grouped according to the mode-classification of Figure 4.10. The four tectono-metamorphic domains defined by Frets et al. (2014) are represented in the background. Circular diagrams show the percentage of each group of lherzolite in each tectono-metamorphic domain. Lineation trajectories based on data collected by Frets et al. (2014, and references therein). Ar – Ariègite, Ar-Se – Ariègite-Seiland and Se – Seiland domains.*

ii. *Group II*. Lherzolites with Ol < 60%, Ol/Opx generally lower than the DMM, and Cpx/Opx ratios rather constant. These lherzolites are heterogeneously distributed, but they are mostly found in the Ar (c. 36%) and Se domains (c. 25%), and are less common in the Ar-Se domain (c. 14%) (Fig. 4.11).

iii. *Group III.* Lherzolites with Ol > 65%, Opx < 21% and Cpx > 7%, showing a dispersion toward the wehrlite field normally not observed in orogenic massifs. Cpx/Opx ratios are highly variable, generally higher than in Groups I and II lherzolites and the DMM. These samples mostly occur in the Ar-Se (c. 50%) and Se domains (c. 30%), and are rarer in the Ar domain (c. 14%) (Fig. 4.11).

Henceforth, we will use this new mode-based classification to evaluate in detail the igneous processes that generated the compositional variability of the Beni Bousera peridotites.

4.4.3 Assessment of the role of partial melting and melt extraction

In order to account for the variability of major elements in mantle peridotites, different experiments have been conceived to model melting of fertile mantle sources at different pressures and melt fractions (e.g., Herzberg, 2004). The main drawbacks of this approach are the uncertainties in the source composition and melting regime (e.g., batch, fractional or incremental melting), and the similarity between the compositions of residues of simple melt extraction and those of secondary peridotites affected by refertilization processes (Bodinier & Godard, 2014, and references therein). However, this approximation remains useful to assess the major element variation induced by partial melting in peridotite suites.

Figure 4.12 shows the average major element compositions of the Beni Bousera harzburgites and lherzolites —grouped according to the classification defined in the previous section— compared with the fractional melting residues modeled by Herzberg (2004). The covariations of MgO-FeO and MgO-Al_2O_3 in Groups I and III lherzolites are consistent with initial melting pressures of 3 – 2 GPa, final melting pressures of 2 – 1 GPa, and melting degrees between 10% and 20% (Fig. 4.12a, b). However, in the MgO-SiO_2 diagram (Fig. 4.12c), the initial (7 – 5 GPa) and final (5 – 4 GPa) melting pressures inferred for these rocks are much higher. The average composition of Group II lherzolites plots outside the predictions of all melting models due to its high FeO and SiO_2 and low MgO contents (Fig. 4.12), indicating that this group cannot result from simple fractional melting. Concerning the harzburgites of the massif (except from the Grt-Sp mylonite domain, as explained above), their average composition coincides with those of residues of initial melting at 3 – 2 GPa, final melting at 2

– 1 GPa and high degrees of melt extraction (up to 30%). Similar to Groups I and III lherzolites, the ranges of melting pressures inferred for harzburgites in the MgO-Al_2O_3 and MgO-FeO diagrams (Fig. 4.12a, b) differ from those derived from the MgO-SiO_2 diagram (Fig. 4.12c). These inconsistencies support that the geochemical variability of the Beni Bousera peridotites is not primarily controlled by fractional melting processes. This conclusion is independent on the composition of the fertile source and the melting regime (batch, fractional or incremental melting) considered in the modelling (see below).

4.4.4 Further evidence against a simple residual origin for lherzolites and harzburgites

The variations of bulk rock Mg-no. and mineral modes in peridotites can be used to assess the record of partial melting and refertilization processes. Walter (1998, 2014) parameterized the bulk rock Mg-no. and modal variations in batch melting experiments of a fertile peridotite source in the garnet and spinel lherzolite facies. The trends calculated in these experiments are illustrated in Figures 4.13a and 4.14a, together with the compositions of the Beni Bousera peridotites plotted for comparison. In the garnet peridotite stability field (5 – 3 GPa), the melting curves predict bulk rock Mg-no. much higher at a given olivine proportion than those of the Beni Bousera peridotites, except for few lherzolites of Group I (Fig. 4.13a). On the other hand, several lherzolites of Groups I and III and most harzburgites have modal olivine and bulk rock Mg-no. consistent with melting of spinel lherzolite at pressures of 2 – 0.5 GPa, and melting degrees that range from 10% to 20% for lherzolites and higher than 20% for harzburgites (Fig. 4.13a). Batch melting at these low pressure conditions can also explain the bulk rock Mg-no.-Cpx/Opx variations of many harzburgites but is at odds with most lherzolites of Groups I and III (Fig. 4.14a). On the other hand, Group II lherzolites plot outside the curves modeled for melting at low and high pressure due to their low bulk rock Mg-no. and modal olivine content (Fig. 4.13a), and their rather constant Cpx/Opx (Fig. 4.14a). These results indicate that batch melting processes cannot explain the general modal and bulk rock Mg-no. variations of the Beni Bousera lherzolites. However, melting may account for the composition of most harzburgites, which are similar to old refractory lithospheric mantle rocks preserved in the Lherz massif (Le Roux *et al.*, 2007).

Further evidence that partial melting cannot account for the geochemical features of the Beni Bousera lherzolites is given by their clinopyroxene REE compositions. Figure 4.15a displays the curves calculated for fractional, incremental and batch melting of the PM in the

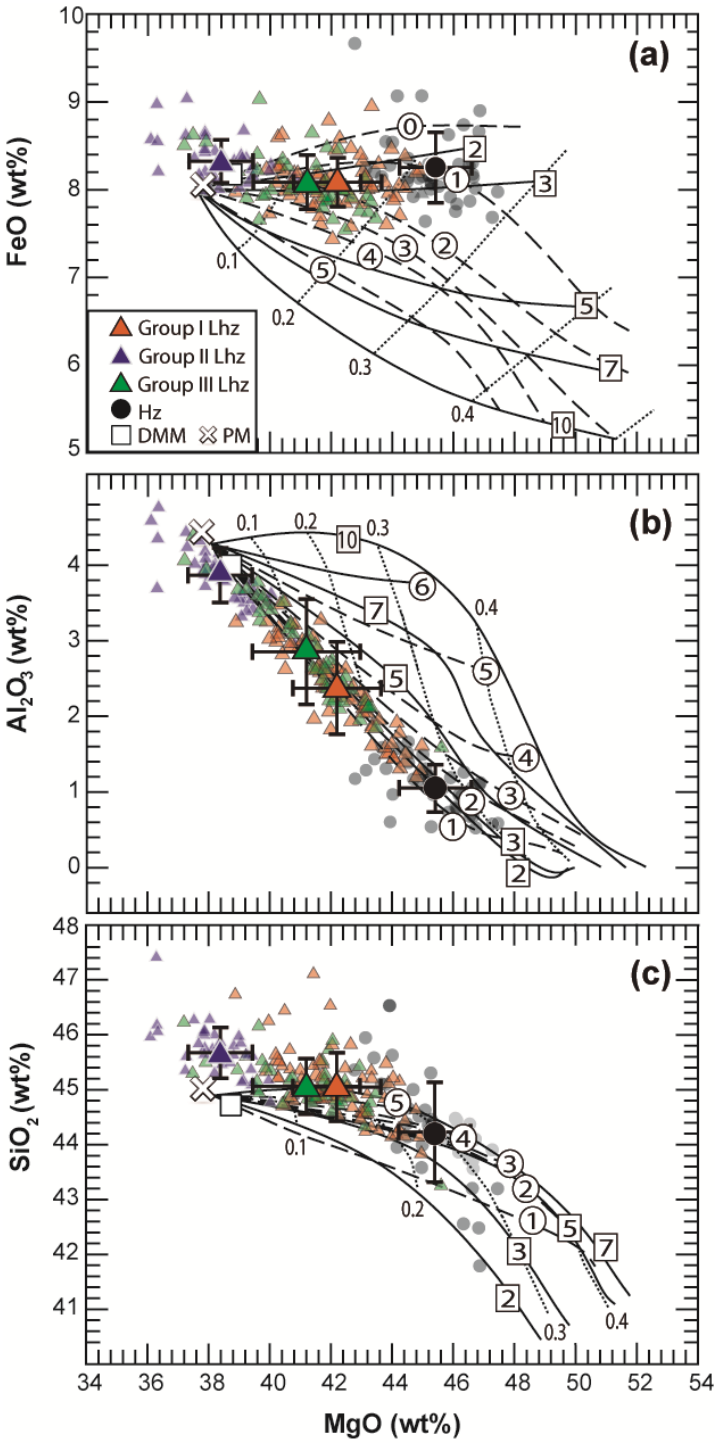

Figure 4.12 *Bulk rock MgO vs (a) FeO, (b) Al_2O_3 and (c) SiO_2 of harzburgites and lherzolites from the Ar, Ar-Se and Se domains grouped according to the classification of Fig. 4.10. Bulk rock data are in wt. % and on anhydrous basis. The modelled residues of Herzberg (2004), resultant from fractional melting of a fertile peridotite (KR4003; Walter, 1998) at different initial (numbers enclosed in squares) and final (numbers circled), pressures (GPa), are plotted for comparison. Decimals indicate the melt extraction degrees.*

spinel stability field, together with the clinopyroxene compositions of the Beni Bousera lherzolites. Moderate to high degrees of fractional and incremental melting predict a strong fractionation of LREE, which is at odds with the relatively restricted range of Ce_N/Nd_N (~ 0.6 – 0.8) in clinopyroxene of most Beni Bousera lherzolites. This general low LREE fractionation is more consistent with the trends produced by batch melting, but this model does not explain the relatively large Sm_N/Yb_N variability of clinopyroxene in these rocks (Fig. 4.15a). These features hence indicate that the Beni Bousera lherzolite compositions cannot simply be accounted by fractional, incremental or batch melting of a PM source.

The resemblance of clinopyroxene trace element compositions in lherzolites and harzburgites (Fig. 4.8) suggests that the latter underwent post-melting (metasomatic) processes similar to lherzolites but to a lesser extent. Clinopyroxene in

several harzburgites (e.g., BB108, BB014, BB272) is variably enriched in Th, U, Nb and Ta relative to neighboring elements in the PM-normalized patterns (Fig. 4.8a, c), it is slightly fractionated in LREE relative to HREE (Fig. 4.9b, d, f), and in some samples (e.g., BB035D, BB070, BB259) it is enriched in LREE and MREE relative to HREE (Fig. 4.9b, d). These

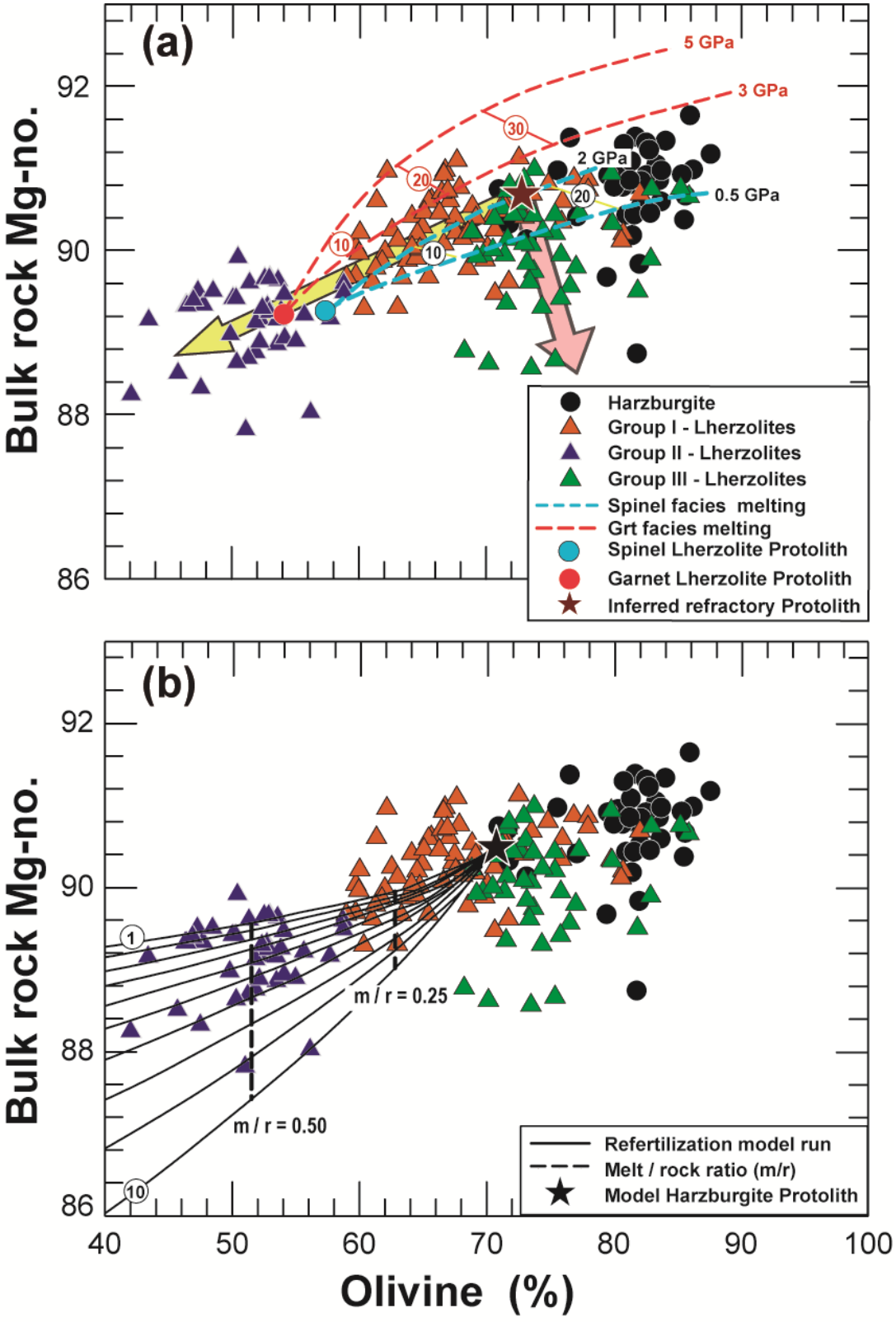

characteristics suggest that harzburgites likely experienced cryptic metasomatism by chromatographic interaction with migrating melts (e.g., Vernières et al., 1997), which mainly influenced their trace element budgets but not their modal and major element compositions (e.g., Ackerman et al., 2007).

4.4.5 Formation of secondary lherzolites by refertilization reactions

Alternatively to partial melting of a fertile mantle source, the compositional variability of Beni Bousera lherzolites can be explained by refertilization of an original refractory protolith, such as a harzburgite or depleted lherzolite. Variations of bulk rock Mg-no. versus modal proportions of olivine (Fig. 4.13a) and pyroxenes (Fig. 4.14a) converge towards a depleted lherzolite composition (dark red star: Mg-no. ~ 91, Ol ~ 70%, Cpx/Opx = 0.4) that may resemble those of refractory peridotite domains later modified by refertilization. Decreasing bulk rock Mg-no. with decreasing modal olivine in Groups I and II (Fig. 4.13a, yellow arrow) and the rather constant Cpx/Opx of these rocks (Fig. 4.14a, yellow arrow) may be accounted by near-solidus, melt-consuming reaction involving olivine dissolution and pyroxene precipitation. Petrographic evidence of this reaction is obscure, possibly owing to obliteration of melt-rock reaction textures in strongly deformed peridotites (Frets *et al.*, 2014). On the other hand, Group III lherzolites show increasing modal olivine contents (Fig. 4.13a, pink arrow) and Cpx/Opx ratios (Fig. 4.14a, pink arrow) with decreasing bulk rock Mg-no., which may be explained by orthopyroxene dissolution and precipitation of clinopyroxene and olivine at near constant or decreasing melt-mass. This conclusion is consistent with petrographic observations, which show that orthopyroxene embayments are filled with olivine in less deformed peridotites (Frets *et al.*, 2014).

Figure 4.13 *Modal olivine vs bulk rock Mg-no. of harzburgites and lherzolites from the Ar, Ar-Se and Se domains grouped according to the classification of Fig. 4.10, compared with the results of modelling of (a) batch partial melting and (b) refertilization reactions. (a) The residual trends for batch melting of a fertile peridotite (KR4003; Walter, 1998) are shown at 5 – 3 GPa (red dashed lines) and 2 – 0.5 GPa (light blue dashed lines) (after Walter, 1998, 2014). The yellow arrow represents the main trend of Groups I and II lherzolites, whereas the pink arrow represents that of Group III lherzolites. Their intersection is represented by a dark red star. (b) Modeled bulk rock Mg-no. variations produced by interaction of a refractory protolith (black star: Mg-no. = 90.5; olivine = 70.8%, taken from Ionov et al., 2005) with different types of incoming melts, involving clinopyroxene + orthopyroxene forming reactions at the expense of olivine in the spinel stability field (adapted model of Bodinier et al., 2008). The composition of the infiltrated melt of stage n+1 is calculated by mixing reacted melt from stage n with melt in equilibrium with the harzburgite protolith (i.e., the infiltrated melt of stage 1 with Mg-no. = 74.5). The numbers on the curves refer to the consecutive nth runs, and the m/r values close to vertical lines indicate the melt/rock ratio.*

Clinopyroxene in most lherzolites shows variably negative HFSE anomalies (Nb, Ta, Zr, Hf and Ti) in the PM-normalized patterns (Fig. 4.8). These low HFSE concentrations may be generated by reactions between depleted peridotites and carbonatitic melts, which normally causes dissolution of orthopyroxene and precipitation of clinopyroxene and olivine (e.g., Yaxley *et al.*, 1991). However, this reaction is inconsistent with the clinopyroxene and

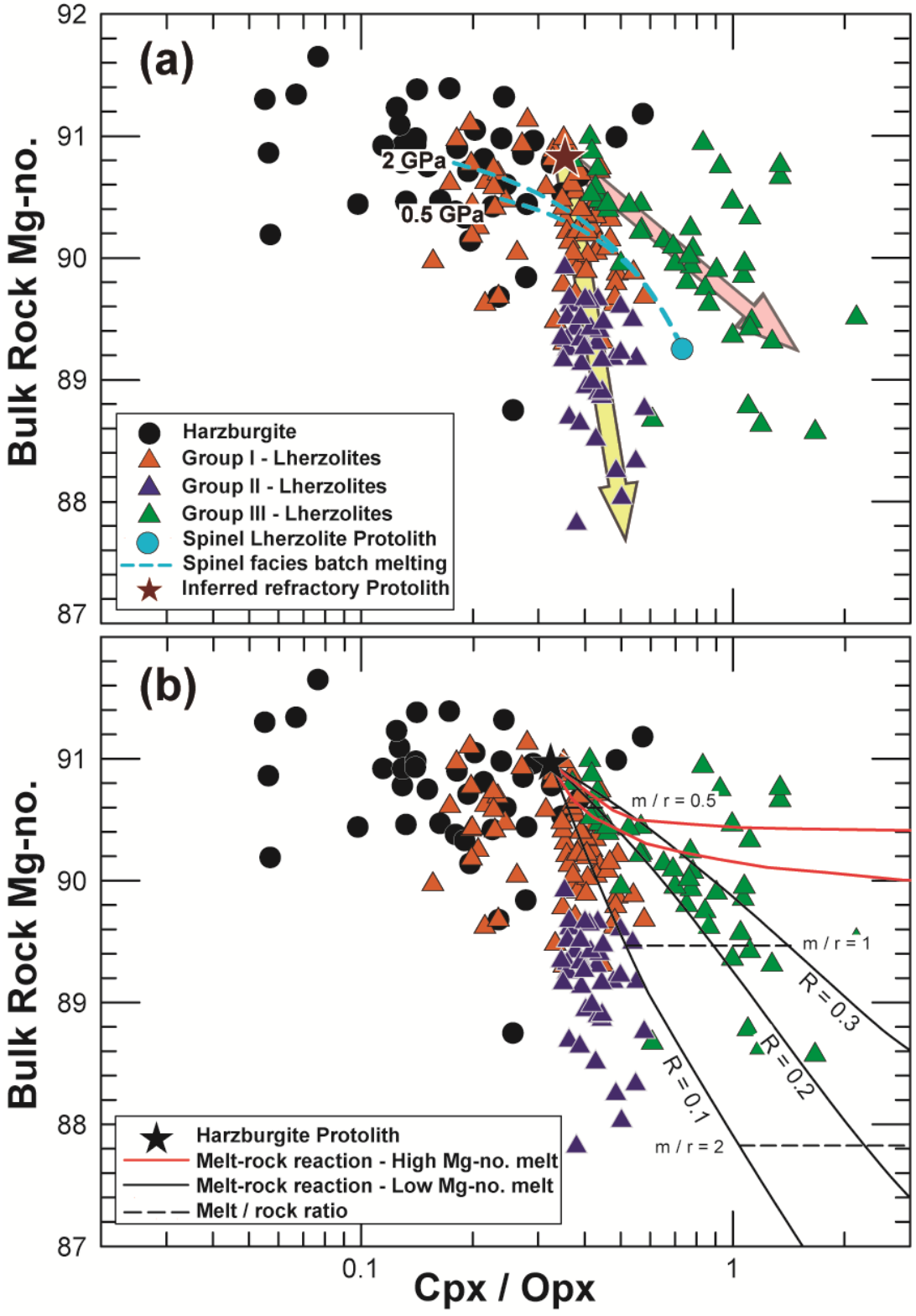

orthopyroxene enrichment in Group I and II lherzolites (Figs. 4.13 & 4.14, yellow arrow) that are prevalent in the Beni Bousera massif. On the other hand, this reaction may account for Group III lherzolites (Figs. 4.13 & 4.14, pink arrow) but carbonatite metasomatism also produces clinopyroxene with low Al_2O_3 and high Zr/Hf and Nb/Ta ratios (Rudnick *et al.*, 1993), which is not observed in any Beni Bousera lherzolite (Fig. 4.8). These clinopyroxene compositions thus point to a silicate basaltic melt slightly fractionated in REE, instead of a highly fractionated carbonatitic melt, as the metasomatic agent that reacted with peridotites.

4.4.5.1 Formation of Groups I and II secondary lherzolites

Figure 4.13b shows the variation of bulk rock Mg-no. and modal olivine in the Beni Bousera lherzolites, together with the curves modeled for the precipitation of clinopyroxene + orthopyroxene at the expense of melt + olivine in the spinel stability field (adapted model of Bodinier *et al.*, 2008). The initial depleted source (black star) is taken from Ionov *et al.* (2005) and is in agreement with the composition of the inferred protolith of the Beni Bousera lherzolites (dark red star in Fig. 4.13a). The model involves a first continuous infiltration of a 'primitive' melt (Mg-no. = 74.5) in equilibrium with the refractory protolith (stage 1; Fig. 4.13b), followed by infiltration of more evolved melts. The composition of the infiltrated melt of stage *n+1* is calculated by mixing the reacted melt from stage *n* with the melt of stage 1 (Bodinier *et al.*, 2008). The variations of bulk rock Mg-no. and modal olivine predicted by this model are similar to those of Group II and part of Group I lherzolites at melt/rock ratios ranging from ~ 0.30 to 0.75 and < 0.30, respectively. The higher bulk rock Mg-no. and higher modal olivine of some lherzolites of Group I could be accounted by similar reactions if the source has higher bulk rock Mg-no. and higher modal olivine than that used in Figure 4.13b (e.g., a

Figure 4.14 *Clinopyroxene/orthopyroxene (Cpx/Opx) ratio vs bulk rock Mg-no. of harzburgites and lherzolites from the Ar, Ar-Se and Se domains grouped according to the classification of Fig. 4.10, compared with the results of modelling of (a) batch partial melting and (b) refertilization reactions. (a) The predicted residual trends for batch melting of a fertile peridotite (KR4003; Walter, 1998) are shown at 2 – 0.5 GPa (light blue dashed lines) (after Walter, 1998, 2014). The yellow arrow represents the main trend of Groups I and II lherzolites, whereas the pink arrow represents the trend of Group III lherzolites. Their intersection is marked by a dark red star. (b) Modeled bulk rock Mg-no. variations produced by interaction of a refractory protolith (black star; Mg-no. = 90.5; Cpx/Opx = 0.32) with percolating melts involving clinopyroxene + olivine forming reactions at the expense of orthopyroxene (adapted model of Ionov et al., 2005). The modelling was run for two different infiltrated melts: (1) a primitive, high Mg-no. (76) melt in equilibrium with the protolith (red lines) and (2) an evolved, lower Mg-no. (63) melt (grey lines). For the evolved melt experiments, values of R (crystallized mineral/infiltrated melt mass ratio) are shown. The m/r values close to the horizontal dashed lines indicate the melt/rock ratio (for more details on the model see Ionov et al., 2005).*

harzburgite). These results support that most of Groups I and II lherzolites were formed by reactions with melts that were already differentiated in previous reaction stages.

The REE compositions of clinopyroxene in Groups I and II lherzolites are also consistent with predictions of pyroxene forming, melt-consuming reactions in the spinel stability field (Fig. 4.15b). To reproduce these variations, we used the 'Plate Model' of Vernières *et al.* (1997), in which the infiltrated melts percolate through —and react with— a peridotite column composed of discrete 'reaction cells'. The curves in Figure 4.15b are associated with different values of *R* (crystallized mineral/infiltrated melt mass ratio) and the arrows indicate the bottom-to-top cell evolution of melts in the reaction column. In each case, the reacted peridotite tends to be more fertile than the protolith and the fertility degree increases with the value of *R*. The infiltrated melt used in this model is produced by 15% batch melting of PM and is in equilibrium with clinopyroxene in the reactant refractory peridotite (black star, Fig. 4.15b). For runs with low values of *R* (0.02 – 0.07, Fig. 4.15b), clinopyroxene in the uppermost cells of the reaction column tends to have refractory compositions similar to that of clinopyroxene in the peridotite protolith (black star, Fig. 4.15b). This derives, for a given *R* ratio, in trends characterized by a backward loop in the reaction path (Fig. 4.15b). For experimental runs with *R* between 0.13 and 1.20, the refertilization model results in clinopyroxene REE patterns ranging from convex-upward in the middle-bottom to LREE and MREE-enriched in the top of the column (Fig. 4.15b). These modeled patterns, especially those produced in the middle-bottom cells, reproduce the clinopyroxene REE compositions of most Groups I and II lherzolites (Fig. 4.15b), which are especially controlled by the infiltrated melt.

As lherzolites from Groups I and II represent ~ 50% – 85% of the Ar, Ar-Se and Se domains (Fig. 4.11), the envisaged melt-rock reaction —precipitation of clinopyroxene + orthopyroxene at the expense of melt + olivine— should have affected the entire Beni Bousera massif previously to the development of the Beni Bousera tectono-metamorphic domains. This conclusion is consistent with petro-structural data, which indicate that most pyroxenites in the Ar and Ar-Se domains have been deformed under solid-state conditions (Frets *et al.*, 2012, 2014).

4.4.5.2 Formation of Group III secondary lherzolites

Figure 4.14b shows the covariation of bulk rock Mg-no. and Cpx/Opx ratios in the Beni Bousera lherzolites, together with the predicted curves of a numerical modelling involving precipitation of clinopyroxene ± olivine at the expense of orthopyroxene in the spinel stability field (adapted

model of Ionov *et al.*, 2005). The initial refractory peridotite (black star, Ionov *et al.,* 2005) is coincident with the inferred protolith of the Beni Bousera lherzolites (dark red star in Fig. 4.14a). The applied numerical modelling considers two different compositions for the infiltrated melt: (1) a primitive, high Mg-no. (76) melt in equilibrium with the refractory protolith (red curves), and (2) a more evolved, low Mg-no. (63) melt (black curves). The bulk rock variations modeled using the evolved melt at *R* values between 0.2 and 0.3 and melt/rock ratios ≤ 1 are very similar to the compositions of most Group III lherzolites (Fig. 4.14 b). However, a few Group III lherzolites with high bulk rock Mg-no. are better explained by refertilization through primitive melts (Fig. 4.14b).

Further evidence that Group III lherzolites represent secondary peridotites formed by melt-rock reaction is given by their clinopyroxene REE fractionation. In Figure 4.15c, we compare the clinopyroxene trace element compositions of the Beni Bousera lherzolites with the results of an olivine-forming reaction modeled using the 'Plate Model' of Vernières *et al.* (1997). In spite of not producing clinopyroxene, the latter reaction resembles the process envisaged for Group III lherzolites and implies dissolution of orthopyroxene and precipitation of olivine. This model considers two infiltrated melts reacting at different values of *R*: a primitive, high Mg-no. (76) melt (grey lines), and an evolved, low Mg-no. (63) melt (red lines) derived by fractional crystallization from the primitive one. The grey star indicates the trace element composition of clinopyroxene in the refractory protolith, calculated by 15% batch melting of PM, which is in equilibrium with the primitive melt; whereas, the red star marks the composition of clinopyroxene in equilibrium with the evolved melt (Fig. 4.15c).

The modeled reactions predict counter-clockwise curved paths in the Sm_N/Yb_N *vs* Ce_N/Nd_N diagram (Fig. 4.15c). In the bottom cells of the reaction column, the clinopyroxene Ce_N/Nd_N ratio is buffered by the composition of the melt and remains almost constant, whereas the Sm_N/Yb_N ratio decreases rapidly, resulting in relatively flat paths. On the other hand, in the upper part of the reaction column, clinopyroxene depletion in LREE at rather constant Sm_N/Yb_N produces nearly vertical paths (Fig. 4.15c). The model considering the evolved melt reproduces the composition of clinopyroxene in most Group III lherzolites at the lower part of the reaction column, where clinopyroxene abundance remains constant.

Group III lherzolites are mostly present in the Ar-Se and Se domains (Fig. 4.11), suggesting that this type of refertilization, involving clinopyroxene ± olivine precipitation and orthopyroxene dissolution, took place during the development of the Beni Bousera tectono-

metamorphic domains. This conclusion is consistent with petrographic observations of this

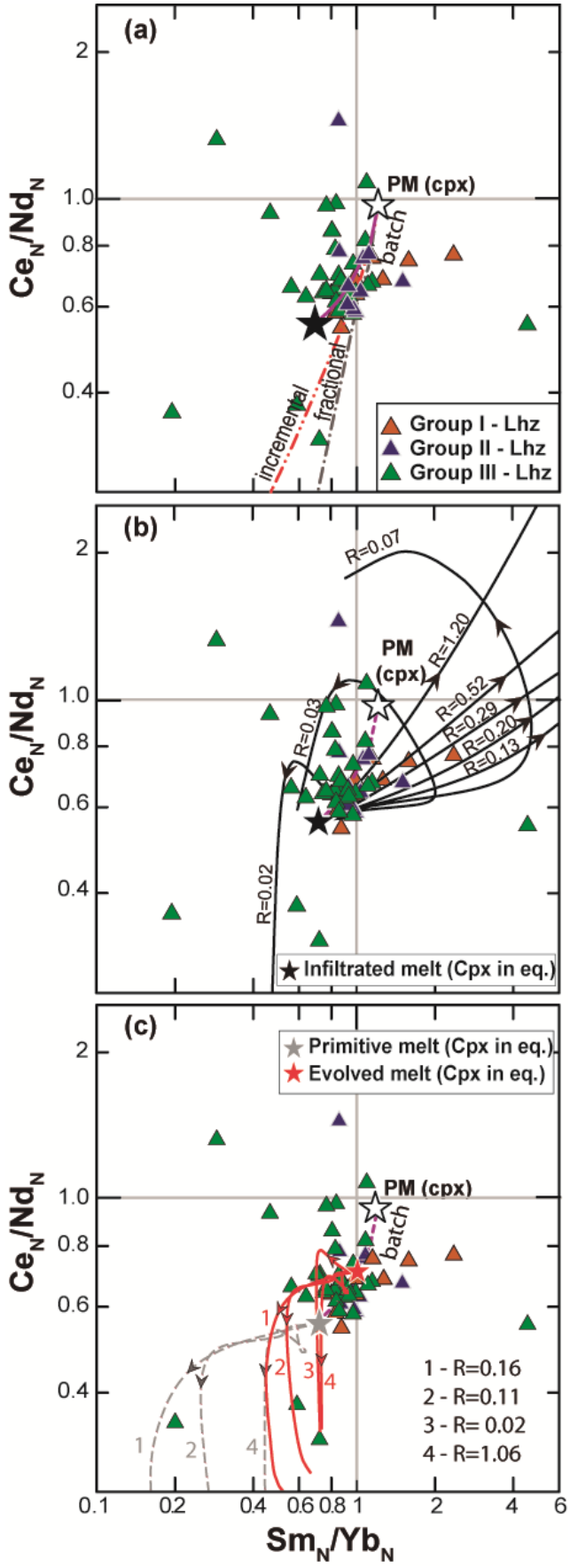

Figure 4.15 *Sm_N/Yb_N vs Ce_N/Nd_N of clinopyroxene from lherzolites of the Ar, Ar-Se and Se domains grouped according to the classification of Fig. 4.10. These compositions are compared to modeled clinopyroxene REE fractionation caused by (a) partial melting, (b) precipitation of clinopyroxene + orthopyroxene at the expense of melt + olivine, and (c) precipitation of olivine at the expense of orthopyroxene. Normalizing values are from Sun & McDonough (1989). (a) Three different models of partial melting in the spinel stability field are represented: batch (bold purple line), fractional (black dotted line), and incremental melting (red dashed line), all with a starting PM composition (Sun & McDonough, 1989). The refertilization models in (b) and (c) are executed based on the 'Plate Model' of Vernières et al. (1997). The curves are calculated using different values of R (see text for further details) and their arrows indicate the bottom-to-top cell evolution of melts in the reaction column. In all the runs the initial porosity ($\phi 0$) is 0.1, and the melt/rock ratio decreases from bottom to top of the column. The composition of clinopyroxene in the reactant refractory peridotite in (b) (black star) is in equilibrium with a melt (Mg-no. = 74.5, Sm_N/Yb_N = 0.72, Ce_N/Nd_N = 0.55) produced by 15% batch melting of the PM (white star). The olivine-forming model applied in (c) uses two infiltrated melts: (1) a primitive, high-Mg-no. (76) melt with Sm_N/Yb_N = 0.72 and Ce_N/Nd_N = 0.55 (grey lines) produced by 15% batch melting of the PM, and (2) an evolved, low Mg-no. (63) melt (red lines), derived by fractional crystallization from the primitive melt in (1). The grey and red stars show the compositions of clinopyroxene in equilibrium with the primitive and evolved melts, respectively. Porosity in the base of the column is higher than the initial value, and it decreases in the upper part of the column.*

reaction in less deformed Ar-Se and Se peridotites (Frets *et al*., 2014). The possible late formation of Group III lherzolites suggests that their protolith may have been different from that of Groups I and II. In this scenario, Group III lherzolites may have formed from a previously-refertilized Group I lherzolite with a composition similar to the source assumed in Figs. 4.13a and 4.14a (red star). On the other hand, older Group I and II lherzolites may derive from an original harzburgite with a highly refractory composition (~ Mg-no. = 91, Ol = 83%, Cpx/Opx = 0.2).

5 Genesis of ultra-high pressure garnet pyroxenites in the subcontinental lithospheric mantle—Constraints from the Ronda and Beni Bousera orogenic peridotite massifs [1]

5.1 Introduction

Unraveling the composition and evolution of the mantle of terrestrial planets is critical for our understanding of their origin and differentiation. With the recognition that new crust is being continually created at ocean ridges and destroyed and recycled back into the deep mantle at convergent margins, Plate Tectonics theory has led to the realization that the Earth's mantle composition is heterogeneous. The extreme isotopic compositional variability of oceanic basalts demonstrates the presence of recycled oceanic and continental crust in the Earth's mantle (Stracke, 2012, and references therein; Hofmann, 2014). However, despite robust isotopic evidence for the presence of recycled crustal lithologies in the mantle, the nature, mechanisms, length scales and extent to which different recycled crustal components are mixed in the Earth's mantle are still not fully understood (Kogiso *et al.*, 2004b; Stracke, 2012; Lambart *et al.*, 2016).

Orogenic peridotite massifs provide an exceptional opportunity to investigate *in situ* the nature and scale of the Earth's mantle compositional heterogeneities (Bodinier & Godard, 2014, and references therein). Orogenic peridotites contain a great diversity of pyroxene- and garnet-rich rich layers that are commonly termed garnet pyroxenites (Garrido & Bodinier, 1999; Downes, 2007; Bodinier *et al.*, 2008). In particular, some ultra-high pressure (UHP) garnet pyroxenites have isotopic compositional variations similar to the recycled oceanic crustal component commonly observed in oceanic basalts (Blichert-Toft *et al.*, 1999; Pearson & Nowell, 2004). Some of these pyroxenites also display trace elements signatures, such as positive Eu anomalies, that are analogous to those found in the lower oceanic crust (Kornprobst *et al.*, 1990; Garrido & Bodinier, 1999; Morishita *et al.*, 2003; Montanini *et al.*, 2012; Marchesi

[1] *This chapter is a draft of a manuscript to be submitted to the JCR journal "Geochimica et Cosmochimica Acta".*

et al., 2013; Montanini & Tribuzio, 2015). In orogenic peridotites, like the Beni Bousera massif (N. Morocco), UHP garnet pyroxenites are highly-stretched and tectonically mixed with peridotites at different length scales (Frets *et al.*, 2012). Such outcrops of garnet pyroxenites inspired the Allègre and Turcotte's "Marble Cake Mantle" model for a heterogeneous Earth's mantle (Allègre & Turcotte, 1986). This model envisions that, similarly to orogenic peridotites, the mantle source of oceanic basalts would resemble a "marble cake" of subducted, ancient oceanic crust —represented by garnet pyroxenites— intimately mixed with peridotites by mantle convection. Despite they constitute a minor mantle component, the contribution of garnet pyroxenites to the genesis of primary mantle melts may be disproportionally high because of its lower solidus and higher melt productivity at high-pressure than surrounding peridotites (Hirschmann & Stolper, 1996; Yaxley & Green, 1998; Pertermann & Hirschmann, 2003; Kogiso *et al.*, 2004a; Kogiso & Hirschmann, 2006; Lambart *et al.*, 2009, 2012, 2016).

The Sr-Nd-Hf isotopic composition and old Re-Os depletion ages (1.1–1.4 Ga) found in UHP garnet pyroxenites from the Beni Bousera and Ronda (S. Spain) peridotite massifs are consistent with the expected isotopic variability and time scale for oceanic crustal recycling in the Earth's mantle (Blichert-Toft *et al.*, 1999; Pearson & Nowell, 2004; Marchesi *et al.*, 2014), lending support to the marble cake mantle hypothesis. However, the genesis of UHP garnet pyroxenites in orogenic peridotite massifs and its implications on the formation of chemical heterogeneities in the Earth's mantle and mantle basalt petrogenesis are still poorly understood: How recycled oceanic crust with such an isotopically diverse composition gets intimately mixed in the subcontinental lithospheric mantle (SCLM) sampled by orogenic peridotites? Are these recycled components exotic —i.e., incorporated by subduction in the convective mantle before the formation of the SCLM— or are they genetically related to the crustal lithospheric section associated with orogenic peridotites? What is the absolute timing of the recycling and melting events recorded in these lithological heterogeneities and its bearing in the formation of the SCLM? To clarify some of these issues, we present an integrated geochemical study of UHP garnet pyroxenites from the Ronda and Beni Bousera peridotite massifs. This investigation encompasses, in the same sample, bulk rock major and trace elements, as well as Sr-Nd-Pb-Hf isotopic analyses. This unique geochemical dataset will shed new light into the marble cake hypothesis for the genesis of UHP garnet pyroxenites and its implications for the formation of chemical heterogeneities in the Earth's mantle.

5.2 Sampling

For this study, we selected 13 garnet pyroxenite samples from the HP tectono-metamorphic domains of the Ronda and Beni Bousera peridotite massifs (Obata, 1980; Garrido & Bodinier, 1999; Frets *et al.*, 2014) (c.f. Ch. 1). Geographical coordinates, host tectono-metamorphic domains, and lithologies of the selected garnet pyroxenites are provided in Table 5.1. In these massifs, garnet pyroxenites occur as cm- to meter-scale layers with generally sharp contacts to the host peridotite, isoclinally folded and/or boudinaged and parallel to the peridotite foliation. To warrant length scales large enough to preserve primary isotopic signatures (Kogiso *et al.*, 2004b), garnet pyroxenite portions were sampled from the center of thick pyroxenite layers (c. 1 – 4 m in thickness).

Detailed descriptions of field outcrops, mineralogy, petrology and microstructures have been reported in previous studies (Garrido & Bodinier, 1999; Frets *et al.*, 2012; Chetouani *et al.*, in press). In addition to common garnet pyroxenites, samples include two garnet pyroxenites with graphite-pseudomorphs after diamond from the Ronda (RO-DIA) and Beni Bousera (BB-DIA) massifs, and two corundum-bearing garnet pyroxenites (RO-175 and BB-COR from Ronda and Beni Bousera, respectively). The petrology and geochemistry of these pyroxenites have been the subject of numerous studies (Obata, 1980; Pearson *et al.*, 1989; Kornprobst *et al.*, 1990; Pearson *et al.*, 1991; Davies *et al.*, 1993; Pearson *et al.*, 1993; Blichert-Toft & Albarède, 1997; Morishita *et al.*, 2001; El Atrassi *et al.*, 2011; Gysi *et al.*, 2011; El Atrassi *et al.*, 2013). The primary UHP mineralogy has generally been overprinted by ductile deformation and metamorphism leading to the formation of different tectono-metamorphic domains in the corresponding massifs (Obata, 1980; Garrido & Bodinier, 1999; Garrido *et al.*, 2011; Frets *et al.*, 2012; Hidas *et al.*, 2013; Frets *et al.*, 2014). Their present mineral assemblage is made up of porphyroclastic clinopyroxene and garnet, subordinate amounts of orthopyroxene, plagioclase, spinel, amphibole and olivine, and minor corundum, sapphirine, ilmenite, quartz, rutile and graphite.

5.3 Results

5.3.1 Bulk rock major elements

The bulk rock major element composition of garnet pyroxenites is given in Table 5.1. Figure 5.1 shows selected plots of the concentration of oxides — in anhydrous basis —plotted against MgO (wt. %).

Table 5.1 Bulk rock major element data of garnet pyroxenites

	Group A					
Sample	RP7-1	RP7-8	RP7-11	RP7-17	RO-175	BB-COR
Massif	Ronda	Ronda	Ronda	Ronda	Ronda	B. Bousera
Domain (1)	Sp	Sp	Sp	Sp	Sp	Grt-Sp
Lithology	Grt pxt	Grt pxt	Grt pxt	Grt pxt	Cor-Grt pxt	Co-Grt pxt
UTM E (2)	299669	304504	301590	305187	304857	327268
UTM N	4038065	4043690	4042523	4047498	4048307	3902707
SiO_2 (wt.%)	46.33	47.27	48.31	47.29	47.98	45.67
TiO_2	0.53	0.32	0.70	0.57	0.31	0.20
Al_2O_3	15.46	17.26	16.07	15.17	14.75	17.11
Fe_2O_3	11.37	7.69	9.63	10.19	7.39	6.53
MnO	0.22	0.13	0.16	0.16	0.090	0.15
MgO	12.21	11.81	9.46	11.33	14.31	14.45
CaO	12.78	13.26	13.12	13.09	13.37	14.78
Na_2O	1.23	1.09	1.68	1.36	1.08	0.97
K_2O	*b.d.l.*	0.010	0.010	*b.d.l.*	0.040	0.010
P_2O_5	0.026	0.022	0.038	0.029	0.040	0.010
L.O.I.	0.00	0.15	0.00	0.00	0.00	0.13
Total	100.15	99.01	99.18	99.19	99.36	100.01
Mg-no.	*68.0*	*75.3*	*66.1*	*68.8*	*79.3*	*81.4*
CaTs	*51.4*	*53.5*	*56.6*	*53.1*	*49.8*	*55.3*
Qz (wt.%)	*15.8*	*18.9*	*19.4*	*17.6*	*17.6*	*13*
Fo (wt.%)	*32.8*	*27.6*	*24*	*29.3*	*32.6*	*31.7*
Cs (ppm)	*n.a.*	0.19	0.094	0.25	*n.a.*	0.18
Rb	1.9	2.1	0.61	1.6	1.5	0.68
Ba	12	2.0	3.0	11	3.1	1.2
Th	0.024	0.0076	0.0045	0.0027	0.015	0.052
U	0.0043	0.0034	0.0037	0.0017	0.0053	0.016
Nb	0.11	0.20	0.017	0.037	0.18	1.3
Ta	0.0059	0.044	0.018	0.020	0.0096	0.100
La	0.67	0.41	0.71	0.15	0.58	0.50
Ce	2.3	1.7	5.1	1.2	1.8	0.92
Pb	0.71	0.18	0.18	0.14	0.30	0.15
Pr	0.49	0.33	1.435	0.32	0.34	0.10
Sr	35	42	84	72	69	54
Nd	3.1	2.1	7.4	2.4	1.9	0.50
Zr	24	16	34	18	13	3.2
Hf	0.86	0.52	1.2	0.67	0.44	0.12
Sm	1.5	0.74	1.6	1.0	0.73	0.21
Eu	0.62	0.38	0.75	0.51	0.35	0.15
Gd	2.6	1.1	2.4	2.1	1.1	0.38
Tb	0.52	0.19	0.44	0.39	0.20	0.073
Dy	3.8	1.3	3.1	2.9	1.4	0.54
Y	*n.a.*	7.0	18	16	*n.a.*	2.7
Ho	0.86	0.27	0.65	0.59	0.29	0.11
Er	2.7	0.77	1.9	1.8	0.79	0.32
Tm	0.40	0.11	0.28	0.26	0.12	0.046
Yb	2.6	0.69	1.7	1.6	0.73	0.29
Lu	0.42	0.11	0.28	0.27	0.12	0.047

n.a.: not analyzed; b.d.l.: below detection limit; L.O.I: Loss on ignition

(1) Sp: Spinel tectonite domain; Ar: Ariègite domain; Grt-Sp: Garnet-Spinel mylonites.

(2) UTM coordinates zone 30S.

Table 5.1 (continued)

	Group B					*Group C*	
Sample	RP7-2	RP7-3	RO-DIA	BB-DIA	10BB42-B	RP7-12	10BB60-G
Massif	Ronda	Ronda	Ronda	B. Bousera	B. Bousera	Ronda	B. Bousera
Domain (1)	Grt-Sp	Sp	Sp	Ar	Grt-Sp	Sp	Grt-Sp
Lithology	Grt pxt	Grt pxt	Gp-Grt pxt	Gp-Grt pxt	Grt pxt	Grt pxt	Grt-Sp pxt
UTM E (2)	299026	300092	300572	332007	327547	301590	328460
UTM N	4038265	4038025	4037243	3897404	3902488	4042524	3902424
SiO_2 (wt.%)	46.97	46.62	47.45	47.79	47.22	46.23	47.23
TiO_2	0.78	0.57	0.25	0.68	0.39	0.53	0.29
Al_2O_3	12.75	13.63	12.57	12.33	11.20	14.01	14.80
Fe_2O_3	12.08	13.69	10.38	13.85	9.53	10.12	6.62
MnO	0.21	0.23	0.21	0.44	0.18	0.19	0.13
MgO	14.60	12.87	13.81	14.72	16.87	14.40	16.62
CaO	10.56	11.08	14.16	8.93	12.75	11.81	12.45
Na_2O	1.11	1.10	0.69	1.18	0.88	1.09	1.36
K_2O	0.010	*b.d.l.*	0.020	0.010	0.010	0.000	0.010
P_2O_5	0.029	0.022	0.000	0.010	0.020	0.025	0.010
L.O.I.	0.00	0.00	0.47	0.060	0.93	0.82	0.49
Total	99.10	99.81	100.01	100.00	99.98	99.23	100.01
Mg-no	*70.5*	*65.1*	*72.5*	*67.8*	*77.8*	*73.8*	*83.2*
CaTs	*42.8*	*44.7*	*46.4*	*39.2*	*41.9*	*46.6*	*48.9*
Qz (wt.%)	*17.9*	*16.7*	*17.3*	*19.4*	*15.3*	*16.5*	*14.3*
Fo (wt.%)	*39.3*	*37.6*	*36.3*	*41.4*	*42.8*	*36.9*	*36.8*
Cs (ppm)	0.79	*b.d.l.*	0.12	0.090	0.17	1.5	0.22
Rb	2.3	0.72	0.95	0.28	0.49	2.8	0.99
Ba	5.9	20	4.7	0.69	6.0	53	12
Th	0.030	0.0031	0.017	0.0035	0.075	0.012	0.034
U	0.0054	0.0020	0.0057	0.056	0.030	0.0052	0.0096
Nb	0.074	0.024	0.097	0.39	0.18	0.23	0.11
Ta	0.036	0.001	0.020	0.030	0.032	0.046	0.037
La	0.72	0.0233	0.039	0.019	0.60	0.56	0.34
Ce	3.0	0.4	0.17	0.054	2.2	1.7	1.1
Pb	0.63	0.47	0.31	0.17	1.1	0.15	0.42
Pr	0.64	0.16	0.040	0.015	0.40	0.28	0.21
Sr	43	25	7.6	4.7	74	65	139
Nd	4.4	1.5	0.32	0.17	2.3	1.8	1.4
Zr	28	15	2.3	5.7	10.0	18	7.7
Hf	1.1	0.63	0.11	0.44	0.42	0.69	0.34
Sm	1.8	0.96	0.22	0.23	0.70	0.90	0.57
Eu	0.71	0.44	0.098	0.13	0.31	0.41	0.34
Gd	3.1	2.0	0.69	1.2	0.93	1.9	0.91
Tb	0.59	0.42	0.17	0.37	0.16	0.39	0.16
Dy	4.5	3.2	1.5	3.6	1.2	3.1	1.1
Y	28	*n.a.*	9.7	26	5.8	19	5.9
Ho	0.98	0.72	0.35	0.93	0.23	0.70	0.23
Er	3.0	2.2	1.2	3.2	0.70	2.3	0.67
Tm	0.45	0.33	0.19	0.53	0.10	0.35	0.093
Yb	3.0	2.2	1.3	3.5	0.65	2.3	0.57
Lu	0.49	0.36	0.24	0.61	0.11	0.39	0.091

n.a.: not analyzed; b.d.l.: below detection limit; L.O.I: Loss on ignition

(1) Sp: Spinel tectonite domain; Ar: Arièǵite domain; Grt-Sp: Garnet-Spinel mylonites.

(2) UTM coordinates zone 30S.

According to their Al_2O_3 content (wt. %, anhydrous), we classify garnet pyroxenites into three groups (Fig. 5.1a), which, as later discussed, have characteristic trace elements and Sr-Nd-Pb-Hf isotopic signatures:

i. *Group A garnet pyroxenites* (samples RO-175, RP7-1, RP7-8, RP7-11, RP7-17 and BB-COR) have elevated Al_2O_3 content ranging from nearly 15 up to 17.5 wt. % (Fig. 5.1a). This group includes the two corundum-bearing garnet pyroxenite samples from the Beni Bousera (BB-COR) and Ronda (RO-175) peridotite massifs (Table 5.1) (Kornprobst *et al.*, 1990; Morishita *et al.*, 2001; Chetouani *et al.*, in press);

ii. *Group B garnet pyroxenites* (samples RO-DIA, RP7-2, RP7-3, BB-DIA and 10BB42-B) have Al_2O_3 < 13.7 wt. % (Fig. 5.1a); these group includes the Ronda (RO-DIA) and Beni Bousera (BB-DIA) garnet pyroxenite samples with graphite-pseudomorphs after diamond (Table 5.1) (Pearson *et al.*, 1989; Davies *et al.*, 1993; El Atrassi *et al.*, 2011);

iii. *Group C garnet pyroxenites* (samples RP7-12 and 10BB60-G) have intermediate Al_2O_3 content around 15 wt. % (Fig. 5.1a) and are common garnet pyroxenites.

Altogether, the MgO content of garnet pyroxenite samples ranges between 9.5 and 17.0 wt. %, and shows covariations with major elements that are similar to those observed in garnet pyroxenites from orogenic peridotites and mantle xenoliths (Hirschmann & Stolper, 1996; Kogiso *et al.*, 2004a; Lambart *et al.*, 2013).

The MgO content of Group A samples (9.5 – 14.5 wt. %) is in the range of contents of low-MgO mantle garnet pyroxenites (Hirschmann & Stolper, 1996; Kogiso *et al.*, 2004a; Lambart *et al.*, 2013). On average, it is lower than those of Group B (12.9 – 17.0 wt. %) and C (> 14.6 wt. %) samples. Altogether, the Al_2O_3 content of garnet pyroxenite samples is in the high-end values for mantle garnet pyroxenites, especially for Group A (Fig. 5.1a). As in other orogenic massifs, the Al_2O_3 content of garnet pyroxenites correlates negatively with MgO (Fig. 5.1a), particularly in Groups A and B samples. The SiO_2 content of garnet pyroxenites is uncorrelated with MgO (Fig. 5.1b), and, on average (47.4 ± 0.8), lies at boundary values between silica-excess (SE) and silica-deficient (SD) mantle garnet pyroxenites (Garrido & Bodinier, 1999; Kogiso & Hirschmann, 2006; Lambart *et al.*, 2016). The CaO abundance of pyroxenite samples is uncorrelated with MgO and is in the middle range of values found in mantle garnet pyroxenites (Hirschmann & Stolper, 1996; Kogiso *et al.*, 2004a; Lambart *et al.*, 2013). The different pyroxenite groups display, on average, distinctly CaO contents (Fig. 5.1c), spanning from high and rather constant values in Group A samples (12.8 – 14.8 wt. %),

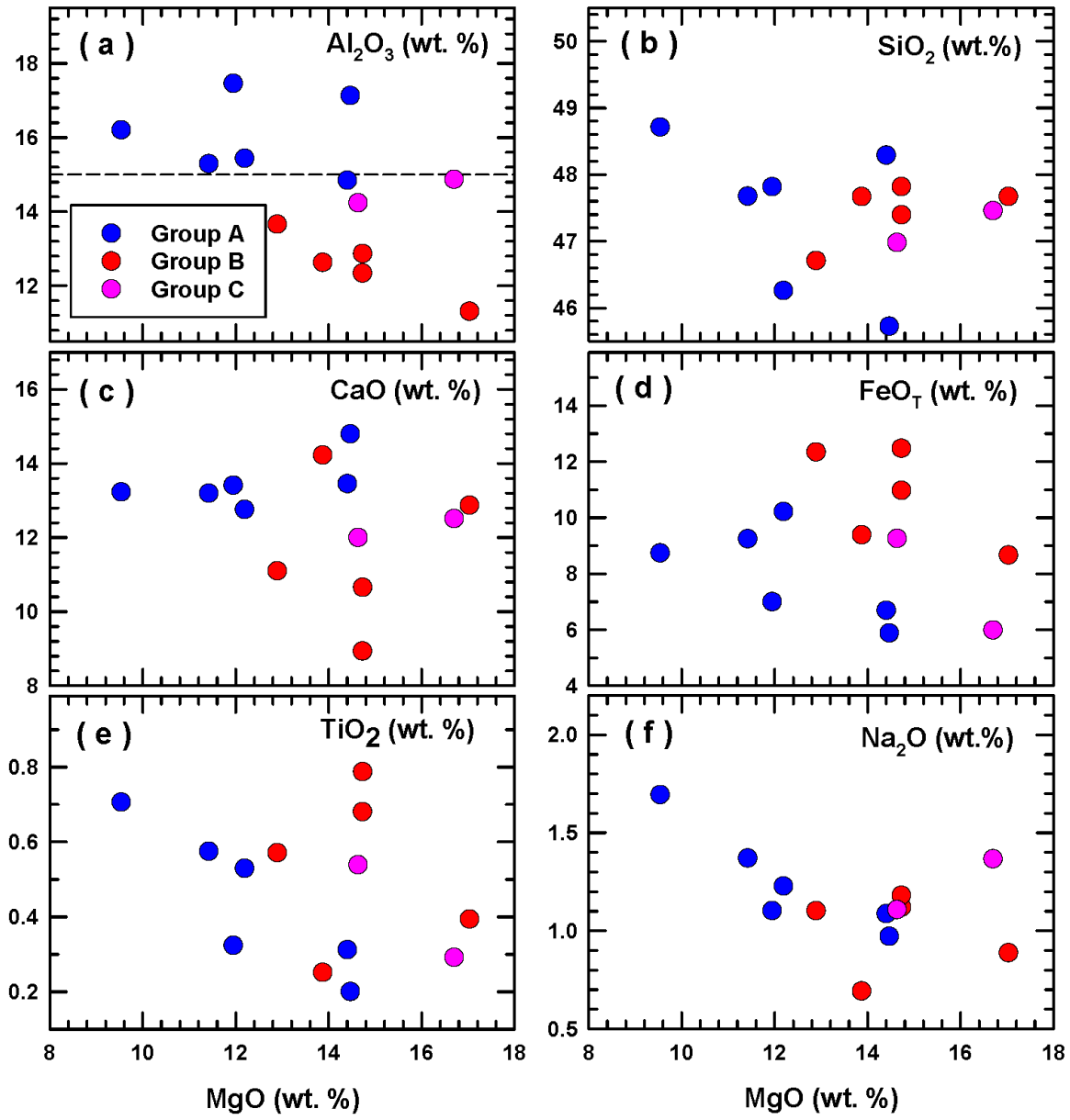

Figure 5.1 *Bulk rock MgO content against (a) Al2O3, (b) SiO2, (c) CaO, (d) FeO, (e) TiO2 and (f) Na2O of garnet pyroxenites from the Ronda and Beni Bousera massifs grouped into Groups A, B and C according to their Al2O3 contents. The short-dashed line in Fig. 5.1 shows an Al2O3 content of 15 wt. %. Data are in wt. % and on anhydrous basis. See text for further details.*

intermediate values in Group C samples (12.0 – 12.5 wt. %), to relatively low and variable values in Group B samples (8.9 – 14.2 wt. %). The FeO_T content of pyroxenite samples is highly variable (5.9 – 12.5 wt. %) and it spans most of the values reported in other mantle garnet pyroxenites. For each pyroxenite group, the FeO_T content correlates negatively with MgO (Fig. 5.1d). The TiO_2 content of pyroxenite samples (0.2 – 0.8 wt. %) is at the lower bound of values reported in other mantle garnet pyroxenites (Hirschmann & Stolper, 1996; Kogiso *et al.*, 2004a; Lambart *et al.*, 2013). In pyroxenite samples with MgO < 14.2 (wt. %), the TiO_2 content is

negatively correlated with MgO (Fig. 5.1e). The Na_2O content of pyroxenite samples altogether varies between 0.7 and 1.7 wt. %, within the low to intermediate values reported in other mantle garnet pyroxenites. As for TiO_2, the Na_2O content is negatively correlated with MgO for pyroxenites with a MgO < 14 (wt. %), a trend that is also observed in compilations of mantle garnet pyroxenites (Hirschmann & Stolper, 1996; Kogiso *et al.*, 2004a; Lambart *et al.*, 2013). Most garnet pyroxenite samples have K_2O contents below the detection limit of the XRF instrumental analysis (Table 5.1).

The Mg-no. of pyroxenite samples is highly variable and ranges from 65.1 to 83.2 (Table 5.1); it tends to be higher in Group C pyroxenite samples (73.8 – 83.2), than in Group A (66.1 – 81.4) and B (65.1 – 77.8); the latter group contains garnet pyroxenite samples with the lowest Mg-no. reported in this study (Hirschmann & Stolper, 1996; Kogiso *et al.*, 2004a; Lambart *et al.*, 2013).

5.3.2 Bulk rock trace elements

Figure 5.2 shows the bulk rock patterns of rare earth elements (REEs) (normalized to chondrite) and trace elements (normalized to Primitive Mantle) for the different groups of garnet pyroxenites.

Most Group A pyroxenites have REE patterns depleted in light (L) REE relative to middle (M) REE, and nearly flat segments for the heavy (H) REE (Ce_N/Sm_N = 0.3 – 0.6; Sm_N/Yb_N = 0.6 – 1.2; N: normalized to chondrites). Exceptions are samples BB-COR, with a "spoon-shaped" pattern (Ce_N/Sm_N = 1.1; Sm_N/Yb_N = 0.8), and RP7-11 that is relatively enriched in LREEs (Nd_N/Yb_N = 1.6) (Fig. 5.2a). These pyroxenites have positive Eu anomalies (Eu_N/Eu^*: 1.2 – 1.6; Eu^*= [(Sm_N + Gd_N)/2]), excluding samples RP7-1 and RP7-17 (Eu_N/Eu^* ~ 1). Group B pyroxenites are depleted in LREE and MREE relative to HREE, and show MORB-like patterns (Ce_N/Sm_N = 0.1 – 0.4; Sm_N/Yb_N = 0.1 – 0.7) —that is remarkably fractionated in samples RP7-3, RO-DIA and BB-DIA— and either lack Eu anomalies (RP7-2, RP7-3; Eu_N/Eu^* ~ 1) or display marked negative Eu anomalies (RO-DIA, BB-DIA; Eu_N/Eu^* = 0.6 – 0.7) (Fig. 5.2b). Sample 10BB42-B has a different relatively flat pattern (Ce_N/Sm_N = 0.8; Sm_N/Yb_N = 1.2) and a positive Eu anomaly (Eu_N/Eu^* = 1.2). Group C pyroxenites are depleted in LREE relatively to MREE (Ce_N/Sm_N = 0.5). Sample 10BB60-G shows a nearly flat HREE pattern (Sm_N/Yb_N = 1.1) and a marked positive Eu anomaly (Eu_N/Eu^* = 1.4), whereas sample RP7-12 has no Eu anomaly (Eu_N/Eu^* = 1) (Fig. 5.2c).

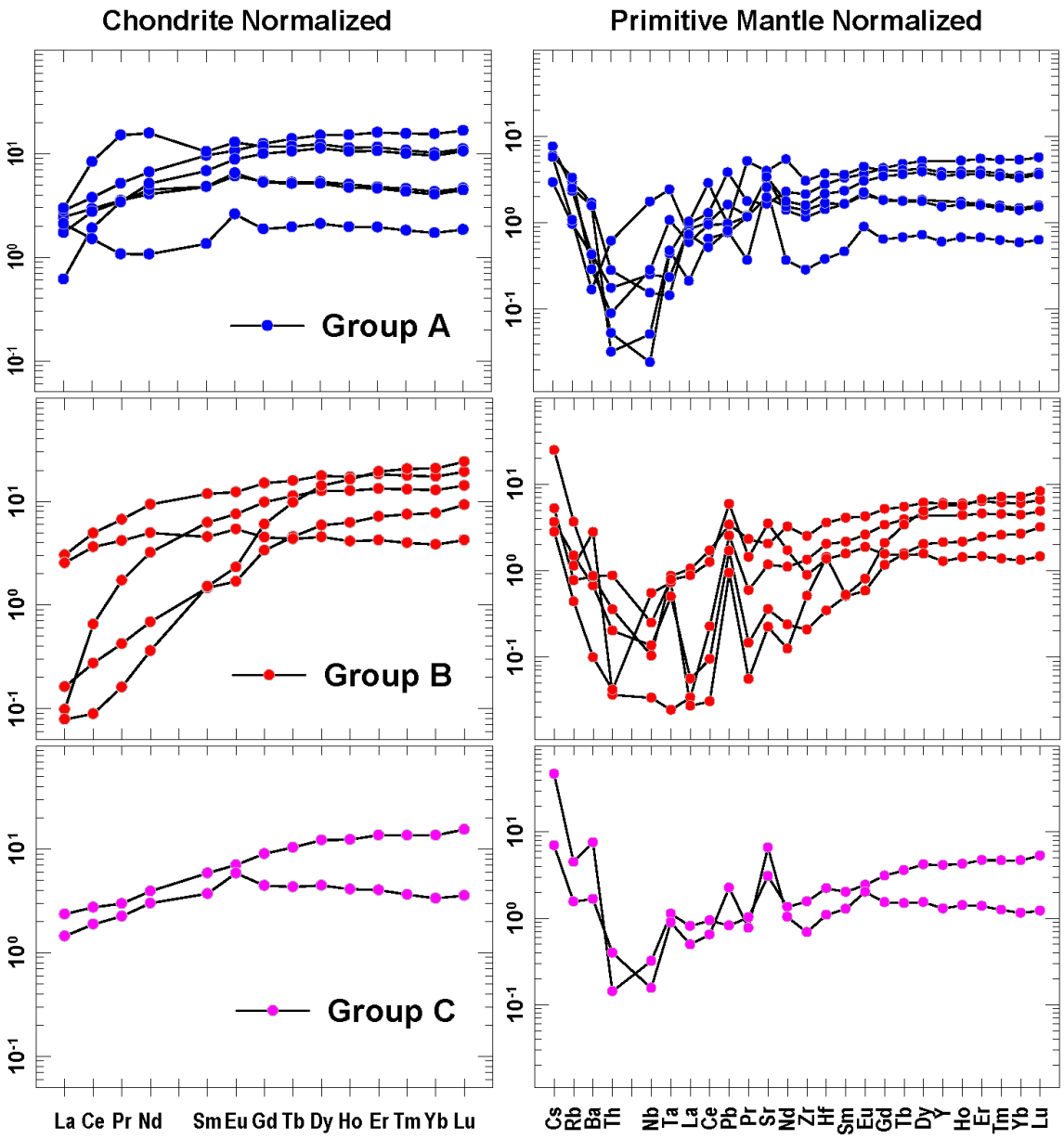

Figure 5.2 *Chondrite-normalized rare earth element patterns (left) and Primitive mantle-normalized trace elements patterns (right) of the Ronda and Beni Bousera Groups A, B and C garnet pyroxenites. Normalizing values after Sun & McDonough (1989).*

Garnet pyroxenite samples of all the groups are variably enriched in Large Ion Lithophile Elements (LILE: Cs, Rb, Ba) and generally show positive anomalies in Pb and Sr (Fig. 5.2). On the other hand, High Field Strength Elements (HFSE: Th, Nb, Zr, and Hf) are generally depleted.

Irrespectively of the pyroxenite group, the TiO_2 contents and some REE contents and ratios are well correlated altogether with Mg-no. (Fig. 5.3). In particular, the Mg-no. of pyroxenites is negatively correlated with TiO_2, which ranges between 0.54 – 0.79 and 0.20 – 0.39 (wt. %) in low and high Mg-no. pyroxenite samples, respectively (Fig. 5.3a). The Yb

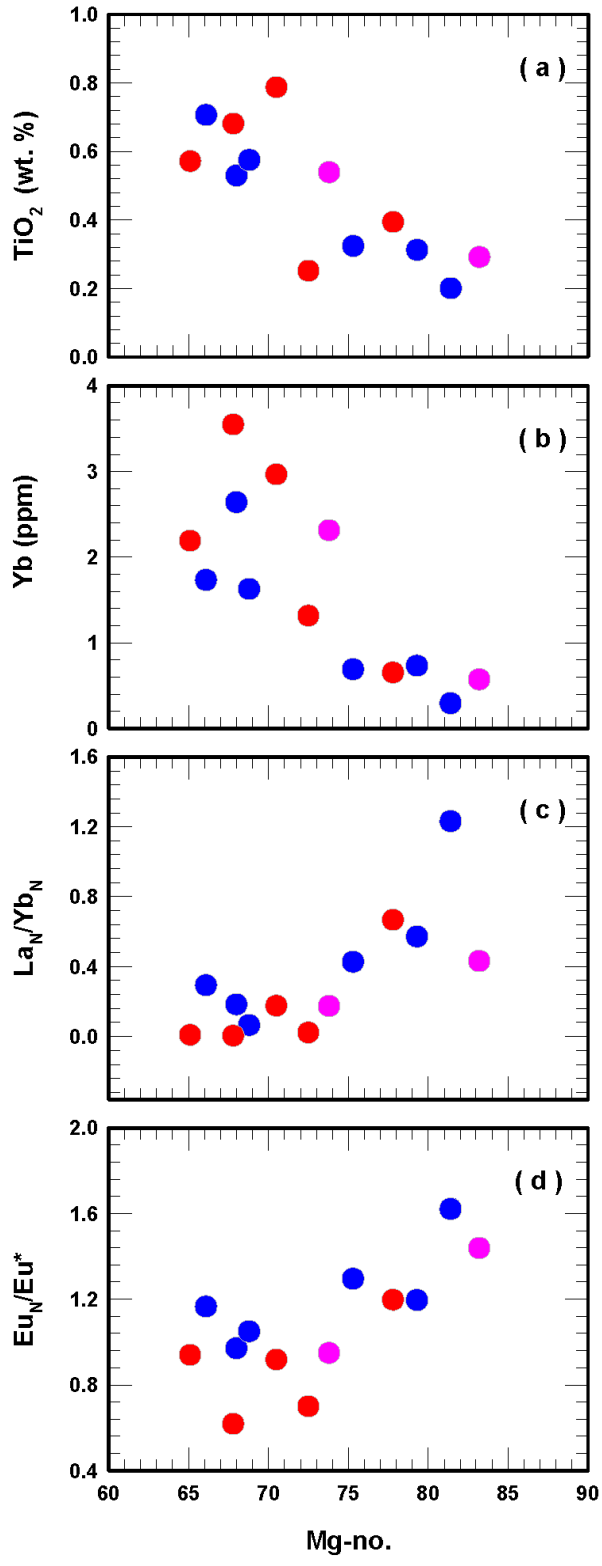

Figure 5.3 *Mg-no. vs (a) TiO_2 (wt. %), (b) Yb (ppm), (c) La_N/Yb_N and (d) Eu_N/Eu^* values of the three groups of garnet pyroxenites from the Ronda and Beni Bousera massifs.*

content of pyroxenite samples is inversely correlated with Mg-no. and ranges from 1.2 – 3.6 to 0.3 – 0.7 ppm in low and high Mg-no. pyroxenite samples, respectively (Fig. 5.3b). The La_N/Yb_N ratio —that portraits the fractionation of LREE relative to HREE— is positively correlated with Mg-no. (Fig. 5.3c), indicating that garnet pyroxenites with highly fractionated REE normalized patterns (Fig. 5.2) are preferentially low Mg-no. garnet pyroxenites. Likewise, the Eu_N/Eu^* ratio correlates positively with Mg-no.; low and high Mg-no. pyroxenites display, respectively, low (0.62 – 0.97) and high (1.20 – 1.62) Eu_N/Eu^* ratios, except for sample RP7-11 that has high Eu_N/Eu^* ratio (1.2) but low Mg-no. (66.1); this correlation indicates that garnet pyroxenite samples with marked positive Eu anomalies are mostly high Mg-no. pyroxenite samples, while those with incipient or negative Eu anomalies are low Mg-no. pyroxenite samples.

5.3.3 Sr-Nd-Pb-Hf radiogenic isotopes

The initial Sr, Nd, Pb and Hf isotopic ratios of garnet pyroxenite samples are provided in Table 5.2, and plots of their aged-corrected Sr, Nd, Pb and Hf isotopic ratios are shown in Fig. 5.4.

Isotopic ratios are corrected to 22 Ma according to Sm-Nd and Lu-Hf absolute ages reported in the literature for Ronda and Beni Bousera garnet pyroxenites (Zindler *et al.*, 1983; Blichert-Toft *et al.*, 1999; Pearson & Nowell, 2004).

The different groups of garnet pyroxenite samples, identified according to their Al_2O_3 content, are characterized by distinct Sr-Nd-Pb-Hf isotopic systematic:

i. Group A garnet pyroxenites have low initial $^{87}Sr/^{86}Sr$ (0.702 – 0.705) and relatively high $^{143}Nd/^{144}Nd$ (0.5130 – 0.5132), $^{206}Pb/^{204}Pb$ (19.099 – 19.504) and $^{176}Hf/^{177}Hf$ (0.2829 – 0.2832) ratios, and highly variable $^{207}Pb/^{204}Pb$ (15.489 – 15.887) and $^{208}Pb/^{204}Pb$ (38.145 – 39.517) ratios.

ii. Group B garnet pyroxenites have relatively high initial $^{87}Sr/^{86}Sr$ (0.704 – 0.711) and low $^{143}Nd/^{144}Nd$ (0.5127 – 0.5130), $^{206}Pb/^{204}Pb$ (18.389 – 18.723) and $^{176}Hf/^{177}Hf$ (0.2826 – 0.2829) ratios. Their $^{207}Pb/^{204}Pb$ (15.566 – 15.674) and $^{208}Pb/^{204}Pb$ (38.018 – 39.057) ratios are more restricted than those of Group A pyroxenites.

iii. Group C pyroxenites are characterized by relatively low initial $^{87}Sr/^{86}Sr$ (0.702 – 0.704) and $^{206}Pb/^{204}Pb$ (18.289 – 18.625), and high $^{143}Nd/^{144}Nd$ (0.5132 – 0.5133) and $^{176}Hf/^{177}Hf$ (0.2830 – 0.2831) ratios. $^{207}Pb/^{204}Pb$ (15.557 – 15.628) and $^{208}Pb/^{204}Pb$ (38.241 – 38.739) in this group are similar to those of Group B.

Group A pyroxenites form an elongated horizontal field in the Sr-Nd isotope diagram (Fig. 5.4a). Their $^{143}Nd/^{144}Nd$ ratios fall within the range of MORB, whereas their $^{87}Sr/^{86}Sr$ extend from depleted MORB-like to more radiogenic compositions (Fig. 5.4a). These pyroxenites show some of the highest Nd and Hf radiogenic isotope ratios among the analyzed samples. They form a positive correlation in the ε_{Nd}– ε_{Hf} diagram and overlap the field of MORB, plotting just below the Hf-Nd mantle array, from a HIMU-type towards a depleted MORB component (Fig. 5.4b). On the other hand, in the Pb isotopic diagrams Group A pyroxenites partially cover the OIB field close to the EMII component (Fig. 5.4c, d). These pyroxenites have relatively high and homogeneous $^{206}Pb/^{204}Pb$ ratios, whereas in terms of $^{207}Pb/^{204}Pb$ and $^{208}Pb/^{204}Pb$ they show a large variability. In particular, sample RP7-11 plots below the Northern Hemisphere Reference Line (NHRL) (Hart, 1988) and below the MORB and OIB fields due to its low $^{207}Pb/^{204}Pb$ and $^{208}Pb/^{204}Pb$, similar to sample RP7-17 in the $^{206}Pb/^{204}Pb$-$^{208}Pb/^{204}Pb$ diagram (Fig. 5.4c, d). On the contrary, sample RO-175 plots well above the NHRL due to its exceptionally high $^{207}Pb/^{204}Pb$ (Fig. 5.4c). In the Pb isotopic diagrams, all Group A samples plot to the right of the 4.45 Ga Geochron (Fig. 5.4c, d).

Table 5.2 Bulk rock present day Sr-Nd-Pb-Hf isotope data of garnet pyroxenites

Sample	Group	$^{87}Sr/^{86}Sr$	$^{143}Nd/^{144}Nd$	$\varepsilon Nd_{(0)}$	$^{176}Hf/^{177}Hf$	$\varepsilon Hf_{(0)}$	$^{206}Pb/^{204}Pb$	$^{207}Pb/^{204}Pb$	$^{208}Pb/^{204}Pb$
RP7-1	A	0.70323 ± 2.3	0.513045 ± 4.5	7.9	0.283093 ± 1.5	11.4	19.101 ± 9.7	15.656 ± 7.8	39.03 ± 2.1
RP7-8	A	0.704014 ± 3.1	0.513264 ± 4.4	12.2	0.283330 ± 1.3	19.7	19.314 ± 5.8	15.679 ± 4.9	39.25 ± 1.2
RP7-11	A	0.703302 ± 3.6	0.513153 ± 3.5	10.0	0.283211 ± 1.5	15.5	19.169 ± 3.0	15.489 ± 2.6	38.147 ± 6.7
RP7-17	A	0.702716 ± 3.6	0.513208 ± 4.5	11.1	0.283203 ± 1.8	15.2	19.229 ± 2.0	15.590 ± 1.2	38.443 ± 3.8
RO175	A	0.704611 ± 3.2	0.513252 ± 5.5	12.0	0.283321 ± 1.6	19.4	19.508 ± 6.2	15.888 ± 5.2	39.52 ± 1.3
BBCOR	A	0.702400 ± 4.4	0.513136 ± 6.7	9.7	*b.d.l.*	*b.d.l.*	19.49 ± 1.0	15.59 ± 7.9	39.36 ± 2.0
RP7-2	B	0.706097 ± 3.0	0.512718 ± 3.4	1.5	0.283057 ± 1.3	10.1	18.603 ± 1.5	15.669 ± 1.3	39.060 ± 3.0
RP7-3	B	0.70471 ± 1.1	0.513004 ± 5.1	7.1	0.282949 ± 1.5	6.2	*b.d.l.*	*b.d.l.*	*b.d.l.*
RODIA	B	0.706378 ± 8.1	0.512959 ± 4.8	6.3	*b.d.l.*	*b.d.l.*	18.727 ± 9.8	15.631 ± 7.4	38.73 ± 1.9
BBDIA	B	0.710629 ± 8.7	0.513135 ± 7.7	9.7	0.283147 ± 1.5	13.3	18.457 ± 9.0	15.569 ± 7.6	38.02 ± 1.9
10BB42B	B	0.704271 ± 2.9	0.512774 ± 5.2	2.6	0.282812 ± 1.5	1.4	18.579 ± 2.0	15.674 ± 3.8	39.039 ± 4.4
RP7-12	C	0.703874 ± 3.4	0.513208 ± 3.6	11.1	0.283183 ± 1.6	14.5	18.633 ± 4.6	15.557 ± 3.9	38.247 ± 9.4
10BB60G	C	0.702315 ± 6.6	0.513324 ± 4.5	13.4	0.283200 ± 2.9	15.1	18.294 ± 2.4	15.629 ± 2.1	38.744 ± 5.3

b.d.l.: below detection limit

Group B pyroxenites form a negative correlation in the Sr-Nd isotope diagram and overlap the compositions of EMII-type OIBs, except for sample BB-DIA that has extremely high initial $^{86}Sr/^{87}Sr$ at a given $^{143}Nd/^{144}Nd$ (Fig. 5.4a). In the $\varepsilon_{Nd} - \varepsilon_{Hf}$ diagram, most of Group B pyroxenites plot below the mantle array forming a positive correlation and encompassing almost the entire range of EMII-type OIBs in ε_{Nd}, but with lower ε_{Hf} values (Fig. 5.4b). Only sample 10BB42-B, with a relatively high ε_{Hf}, plots above the mantle array. Similar to Group A, these samples also show a decoupling between Sr-Nd-Hf and Pb isotopes. The relatively low $^{206}Pb/^{204}Pb$ ratios of Group B pyroxenites are more akin to MORB isotopic compositions than to those of EMII-type OIBs (Fig. 5.4c, d). These samples plot above the NHRL in Pb isotopic diagrams (Fig. 5.4c, d).

Group C pyroxenites partially overlap Group A in Sr, Nd and Hf isotopes, with compositions similar to depleted MORB (Fig. 5.4), whereas in terms of Pb isotopes their

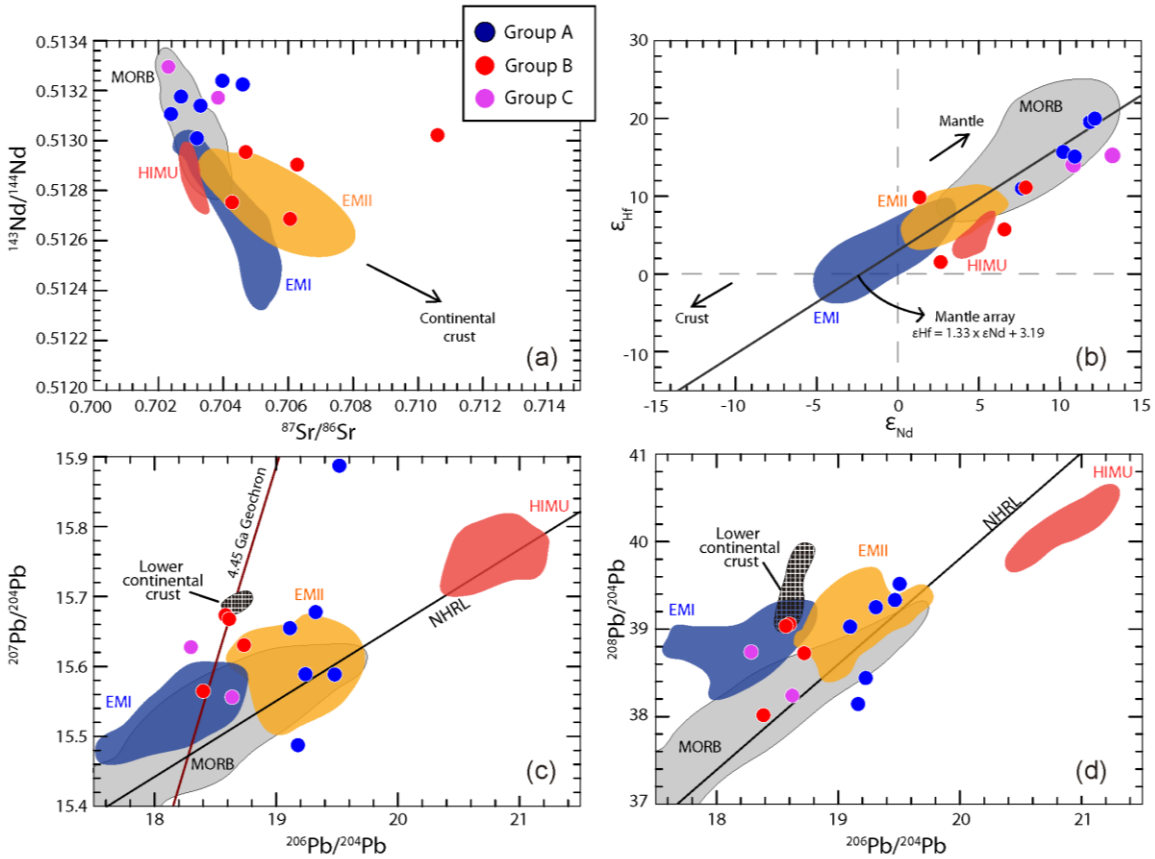

Figure 5.4 *Plots of age corrected (at 22 Ma) Sr-Nd-Pb-Hf isotopic ratios of Groups A, B and C pyroxenites. (a) 87Sr/86Sr vs 143Nd/144Nd; (b) ƐNd vs ƐHf; (c) 206Pb/204Pb vs 207Pb/204Pb: and (d) 206Pb/204Pb vs 208Pb/204Pb. Also shown are the fields of EMI (Tristan da Cunha, Pitcairn and Kerguelen islands, and the Walvis ridge), EMII (Society, Samoa and Marquesas islands) and HIMU (St. Helena and Austral-Cook) basalt components obtained from the GEOROC database (http://georoc.mpch-mainz.gwdg.de; vs. July, 2016). The field of MORB is from PetDB database compilation (vs. July, 2016) of MORB; the 4.45 Ga Geochron and the Northern Hemisphere Reference Line (NHRL) after Hart (1984).*

compositions are comparable to those of Group B, partially overlapping the MORB and EMI-type OIB fields and plotting above the NHRL (Fig. 5.4).

5.4 Discussion

5.4.1 Origin of the isotopic signature of UHP garnet pyroxenites

The Nd and Hf isotopic compositions of Group A pyroxenite samples largely overlap that of MORB (Fig. 5.4) pointing to a provenance from a common mantle reservoir. There is a general agreement that the source of MORB derives from the depleted upper mantle mixed with variable amounts of recycled oceanic crust (e.g., Rehkämper & Hofmann, 1997; Eiler *et al.*, 2000; Workman & Hart, 2005; Hofmann, 2007). The daughter elements of the Sm-Nd and Lu-Hf systems are preferentially partitioned into subduction zone fluids (e.g., Kogiso *et al.*, 1997; Stracke *et al.*, 2003), which results in elevated Lu/Hf and Sm/Nd ratios and long-time integrated initial $^{143}Nd/^{144}Nd$ and $^{176}Hf/^{177}Hf$ ratio in recycled and dehydrated oceanic crust. The high initial $^{143}Nd/^{144}Nd$ and $^{176}Hf/^{177}Hf$ ratios of the majority of Group A samples support their derivation from old, recycled depleted oceanic crust. Because pelagic sediments have lower Sm/Nd and Lu/Hf ratios than oceanic igneous crust (Ben Othman *et al.*, 1989; Plank, 2014), the relatively low Nd and Hf isotope ratios of some Group A samples likely reflect a greater contribution of sediments in their source.

Figure 5.5 shows the isotopic evolution of 0.5 – 3.5 Ga recycled oceanic crust — composed of altered Atlantic MORB and various proportions of pelagic sediments— computed with the quantitative model of Stracke *et al*. (2003) and using the parameters provided in Table 5.3. Recycling of 1.5 – 3.5 Ga old oceanic crust with modest amounts (c. 4 %) of pelagic sediments accounts for the entire Hf and Nd isotopic variability of Group A samples (Fig. 5.5b). Seawater alteration of such old oceanic crust would also explain the variability of $^{87}Sr/^{86}Sr$ at similar $^{143}Nd/^{144}Nd$ values observed in Group A samples (Fig. 5.5a). Subduction processes result in high U/Pb and Th/Pb ratios in the recycled oceanic crust (Kogiso *et al.*, 1997; Kelley *et al.*, 2005) that evolve towards high present-day $^{206}Pb/^{204}Pb$, $^{207}Pb/^{204}Pb$ and $^{208}Pb/^{204}Pb$ ratios (Figs. 5.5c, d). Therefore, recycling of 1.5 – 3.5 Ga old oceanic crust with less than 2% of pelagic sediments would also explain most of the $^{206}Pb/^{204}Pb$ variation of Group A pyroxenites (Fig. 5.5c), although their $^{207}Pb/^{204}Pb$ and $^{208}Pb/^{204}Pb$ variabilities are larger than those predicted by the model (Fig. 5.5c, d). Overall, the Sr-Nd-Pb-Hf isotopic signatures of Group A pyroxenites demonstrate the involvement of ancient recycled oceanic crust with minor

proportions of pelagic sediments in its genesis. However, this model cannot explain the Sr-Nd-Pb-Hf isotopic variability of Group B samples (Fig. 5.5) and would only accounts for some Group B samples if recycled oceanic crust was 2.5 – 3.5 Ga old and contained relatively high amounts (~ 2 – 10%) of pelagic sediments (Fig. 5.5).

As noted above, in the Sr-Nd and ε_{Nd}-ε_{Hf} diagrams, Group B pyroxenites overlap the compositional field of EMII-type OIBs (Fig. 5.4), pointing potentially to a shared isotopic source. The EMII component in OIBs is commonly ascribed to recycled oceanic crust with various amounts of continental terrigenous sediments (e.g., White, 1985; Weaver, 1991; Chauvel *et al.*, 1992) and/or upper and lower continental crust (Willbold & Stracke, 2006, 2010; Stracke, 2012). In the $^{206}Pb/^{204}Pb$-$^{207}Pb/^{204}Pb$ diagram, most Group B samples plot along the 4.45 Ga Geochron (Fig. 5.4c), which is the estimated age of the Earth's core segregation and formation of the bulk silicate Earth (BSE) (Halliday, 2004; Allègre *et al.*, 2008). It seems unlikely, however, that the Pb reservoir of Group B pyroxenites has remained isolated since the formation of the BSE. Alternatively, this trend may be a mixing line between two components isolated at a minimum age of 4.45 Ga (White, 2015). The linear trend of Group B samples in

Table 5.3 Input values used in the modeling of the composition of recycling oceanic crust

Input values	MORB composition[1]	Sediment composition[2]	Mobility coefficients during subduction for basalts[3]	Mobility coefficients during subduction for sediment-fluid alteration [4]
Rb	4.82	57.20	81%	40.1%
Sr	114.8	327.0	41%	38.4%
Hf	1.96	4.06	22%	10.7%
Nd	8.28	27.00	20%	37.1%
Sm	2.75	5.78	13%	33.4%
Lu	0.43	0.41	0%	16.0%
Pb	0.450	19.90	50%	23.6%
Th	0.4	6.91	50%	15.0%
U	0.118	1.68	54%	17.1%
$^{87}Sr/^{86}Sr$	0.70219	0.7173		
$^{143}Nd/^{144}Nd$	0.51330	0.51218		
$^{176}Hf/^{177}Hf$	0.28350	0.2824		
μ ($^{238}U/^{204}Pb$)	8.1			
Ω ($^{232}Th/^{204}Pb$)	31			

1- Average of Atlantic MORB depleted values from the PetDB Expert MORB (Mid-Ocean Ridge Basalt) Compilation;2- All values are from Plank & Langmuir (1998), except for 176Hf/177Hf, which is the preferred value used in Stracke et al., 2003; 3- Mobility estimates for sub-arc basalt alteration are taken from Kogiso et al., (1997) but are modified to account for garnet pyroxenites; 4- Mobility estimates for sediment fluid-alteration during subduction at 700º C are taken from Johnson & Plank (1999)

the $^{206}Pb/^{204}Pb$ – $^{208}Pb/^{204}Pb$ diagram (Fig. 5.4d) may be also due to mixing, in particular between a depleted MORB-like mantle and a component with relatively high $^{207}Pb/^{204}Pb$ and $^{208}Pb/^{204}Pb$ for a given $^{206}Pb/^{204}Pb$. Oceanic basalts, marine sediments, and the upper continental crust plot to the right of the 4.45 Ga Geochron (White, 2015), excluding them from being potential end members. Lower continental crust, on the other hand, plots on both sides of the 4.45 Ga Geochron, making it a potential end-member candidate. Remarkably, in the $^{206}Pb/^{204}Pb$ vs. $^{207}Pb/^{204}Pb$ and $^{206}Pb/^{204}Pb$ vs. $^{208}Pb/^{204}Pb$ diagrams, granulitic gneisses that constitute the lower continental crust overlying the Ronda peridotite (Barich *et al.*, 2014; Varas-Reus *et al.*, in press) —hereafter referred to as Ronda lower crust— lie in the same 4.45 Ga Geochron as Group B pyroxenites, mostly plotting at higher $^{207}Pb/^{204}Pb$ and $^{208}Pb/^{204}Pb$ values (Fig. 5.4c, d). Recycling of a component alike the Ronda lower crust would not only explain the elevated $^{207}Pb/^{204}Pb$ and $^{208}Pb/^{204}Pb$ at relatively low $^{206}Pb/^{204}Pb$ values of Group B samples, but also their relatively high $^{87}Sr/^{86}Sr$ and low $^{143}Nd/^{144}Nd$, $^{176}Hf/^{177}Hf$ and $^{206}Pb/^{204}Pb$ compared to Group A samples (Fig. 5.5).

The isotopic signature of Group C pyroxenites is halfway between that of Groups A and B, which points toward a possible hybrid origin for this group. The Sr-Nd-Hf isotopic similarities between Groups A and C samples indicate that both groups are derived from ancient and depleted recycled oceanic crust (Fig. 5.5). Minor differences in the nature of the recycled component might have resulted in the relatively higher present-day $^{143}Nd/^{144}Nd$ ratios of one Group C sample. On the other hand, their low $^{206}Pb/^{204}Pb$ ratios is more akin to the Pb signature of Group B samples (Fig. 5.4c, d). A possible explanation for the relatively low time-integrated $^{206}Pb/^{204}Pb$ ratios of Group C pyroxenites is that they come from a source alike that of Group A but that was hybridized with a component that lowered its $^{238}U/^{204}Pb$ ratio. This event might have been related to the hybridization of the source of Group A with a Ronda lower continental crust component preponderant in Group B samples.

The results of this investigation support previous studies that account for the isotopic variability of Ronda and Beni Bousera UHP garnet pyroxenites by recycling of ancient oceanic crust and hemipelagic oceanic sediments (Polvé & Allègre, 1980; Pearson *et al.*, 1991; Blichert-Toft *et al.*, 1999; Pearson & Nowell, 2004). However, our results show that such a source only accounts for the Sr-Nd-Pb-Hf signatures of high-Al_2O_3 UHP garnet pyroxenites (Group A).

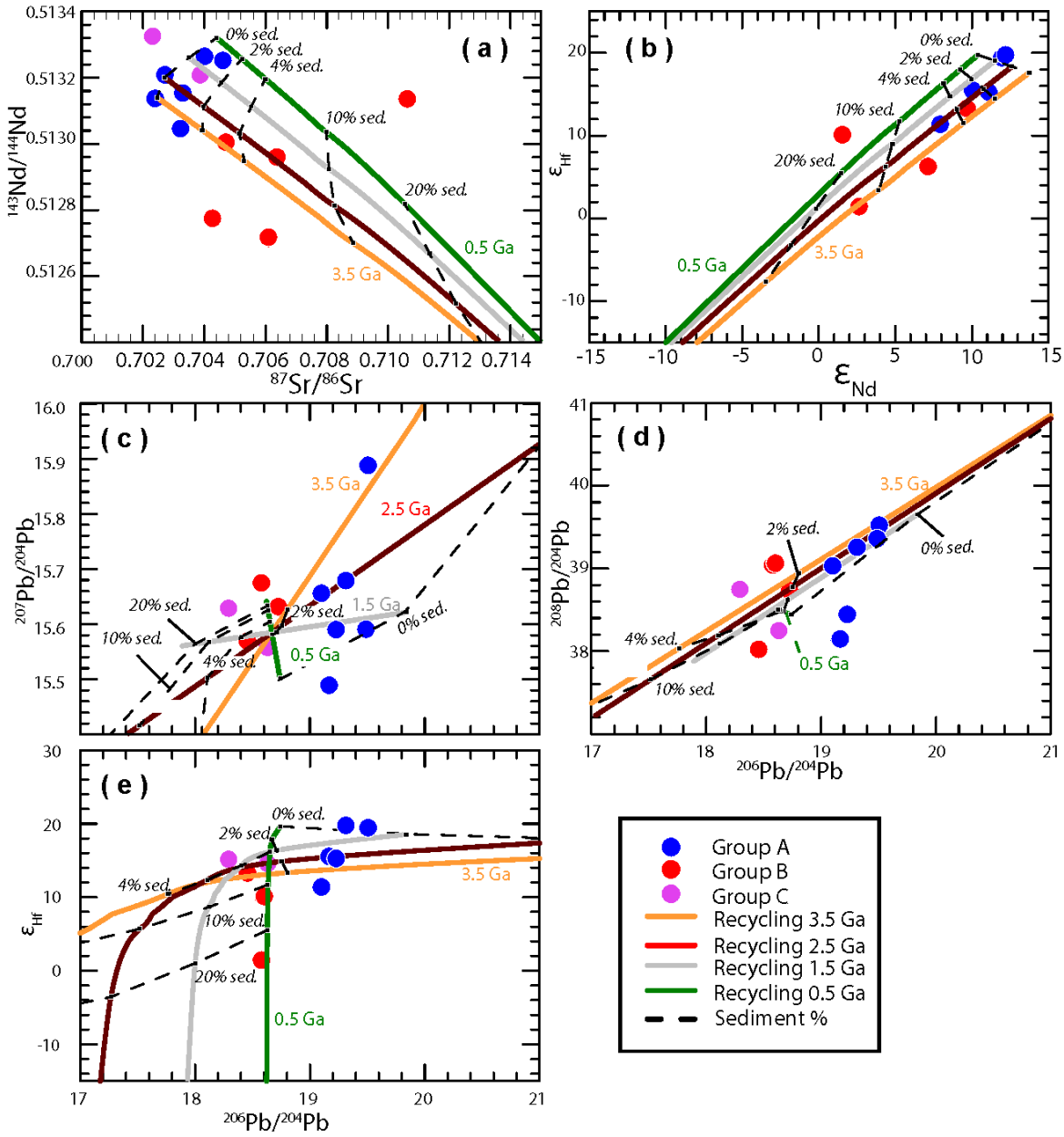

Figure 5.5 *Plots of isotopic ratios showing the calculated present-day isotopic composition of depleted MORB recycled oceanic crust as a function of different recycling ages (0.5 – 3.5 Ga; solid lines) and mixing with various percentage of sediments (dashed lines). Calculations use the quantitative model of Stracke et al. (2003) and the parameters given in Table 5.3. The model assumes a differentiation/source age of the MORB source of 3.5 Ga. The composition of the sediments is that of the global subducted sediments (GLOSS) from Plank & Langmuir (1998). Also shown are the age corrected (22 Ma) Sr-Nd-Pb-Hf isotopic variations of the different groups of garnet pyroxenite samples from the Ronda and Beni Bousera massifs. See text for further details.*

Besides recycled oceanic crust, the Sr–Nd–Pb–Hf isotopic variability of lower Al_2O_3 UHP garnet pyroxenites (Groups B and C) requires the involvement of a lower continental crustal component alike the Ronda lower crust. This result strongly suggests genetic links between the genesis of Group B garnet pyroxenites in the SCLM sampled by the Ronda and Beni Bousera

orogenic peridotites, and the lower continental crust in the same lithospheric section. This link establishes an unprecedented connection between the composition of the continental crust and the generation of mantle pyroxenitic heterogeneities in the Earth's mantle.

5.4.2 Formation of garnet pyroxenite mantle heterogeneities

The isotopic Sr-Nd-Hf-Pb signatures of Ronda and Beni Bousera UHP garnet pyroxenites demonstrate that recycling of oceanic and continental crust played a fundamental role in their genesis. However, this evidence is insufficient to constrain how these lithological heterogeneities were formed in the Earth's mantle. Conversely to the isotopic variability of mantle basalts that portrays the chemical heterogeneity of their mantle sources, the isotopic heterogeneity of mantle garnet pyroxenites may record a wider range of processes. For instance, on the basis of their recycled crustal isotopic and trace element signatures, Beni Bousera and Ronda UHP garnet pyroxenites have been interpreted as straps of subducted oceanic crust in the convecting mantle (Kornprobst *et al.*, 1990; Blichert-Toft *et al.*, 1999; Morishita *et al.*, 2003), or mineral segregates formed via melt-crystal fractionation from melts derived from recycled oceanic crust (Pearson *et al.*, 1991; Davies *et al.*, 1993; Garrido & Bodinier, 1999; Pearson & Nowell, 2004).

Further insights into the genesis of UHP garnet pyroxenites can be gained from phase relations in the condensed CaO-MgO-Al_2O_3-SiO_2 system (Fig. 5.6a, b) (Garrido & Bodinier, 1999; Kogiso *et al.*, 2004a; Lambart *et al.*, 2013). Figure 5.6c displays the compositions of the different groups of garnet pyroxenites recast in the CaO-MgO-Al_2O_3-SiO_2 condensed system (Fig. 5.6a) and plotted in the pseudoternary system forsterite (Fo)–Ca-Tschermak molecule (CaTs)–quartz (Qz) projected from diopside [Di] (Fig. 5.6b) (Table 5.1) (O'Hara, 1968, 1972). At pressures greater than c. 2 – 3 GPa, the garnet–aluminous pyroxene plane —i.e. the En–CaTs–Di plane— is a thermal divide that separates the CMAS system into SE (right side) and SD (left side) bulk compositions (Kogiso *et al.*, 2004b; Lambart *et al.*, 2013, and references therein). When the thermal divide is operative, the primary melts or their derived melts —via crystal fractionation or different degrees of fractional partial melting— are confined to the same side of the divide as the bulk composition of their sources (Ringwood, 1967; Herzberg & O'Hara, 1998; Milholland & Presnall, 1998).

As previously noted (Garrido & Bodinier, 1999; Lambart *et al.*, 2009; Chetouani *et al.*, in press), Ronda and Beni Bousera garnet pyroxenite samples lie either at the SE side or nearly parallel to the En–CaTs thermal divide (Fig. 5.6c). Garnet pyroxenite samples with high CaTs

contents (c. > 50 wt. %; Group A) are commonly SE and plot along the garnet-anorthite (Gt-An) join, while pyroxenites with lower CaTs content (c. < 50 wt. %; Groups B and C) plot on the En-CaTs-Di thermal divide between the garnet-pyrope (Gt-Py) solid solution end members. These compositional trends confined to the SE side indicate that the bulk compositions of their sources were silica-enriched. They also indicate that the garnet-aluminous pyroxene thermal divide was operative during the igneous evolution of these UHP garnet pyroxenites, which hence record garnet-controlled differentiation processes at high-pressures (> 2 – 3 GPa). The compositional trend of UHP garnet pyroxenites from the Ronda and Beni Bousera peridotites contrasts with that of other mantle pyroxenites with recycled oceanic crustal signatures, such as those in the Northern Apennines ophiolites (Fig. 5.6c) (Montanini *et al.*, 2012; Montanini & Tribuzio, 2015; Borghini *et al.*, 2016). These pyroxenites have a greater range of primary bulk compositions mainly encompassing SD sources (Montanini & Tribuzio, 2015).

If UHP garnet pyroxenites derived from the solid-state recycling of oceanic crust (Allègre & Turcotte, 1986), then their average major bulk compositions should be similar to those of their oceanic crustal protoliths. The magmatic oceanic crust is composed of MORB, MORB-like upper crustal gabbros, and lower crustal cumulate gabbros and troctolites with positive Eu anomalies (Coogan, 2007, and references therein). The compositions of MORB and lower arc crustal gabbros are dominated by low-pressure cotectic melts and plot at high Q/Fo ratios towards the Qz apex. These compositional trends are unlike those of Group A pyroxenites (Fig. 5.6c, d) ruling out that they are closed-system derivatives of lower arc crustal gabbros (Gysi *et al.*, 2011) or MORBs. The compositions of oceanic crustal gabbros and troctolites are controlled by low-pressure crystal fractionation of olivine, plagioclase and pyroxene (Coogan, 2007) and, as a result, their compositions plot along the An-Fo-Di plane and the An-Fo tie line (Fig. 5.6d). Along with other Ronda and Beni Bousera SE and high CaTs garnet pyroxenites, Group A samples also plot along the An-Fo join (Fig. 5.6c). This indicates that their bulk composition is somehow controlled by a low-pressure fractionation trend similar to that of lower oceanic crustal cumulates. This observation, along with their isotopic compositions and the elevated Eu_N/Eu^* ratio of some Group A samples (Fig. 5.3d), points to a derivation from recycled oceanic crust (Kornprobst *et al.*, 1990; Garrido & Bodinier, 1999; Morishita *et al.*, 2003). However, the Na_2O contents (0.97 – 1.69 wt. % anhydrous) of Group A samples are significantly lower than those of lower oceanic crust (2.23–3.27 wt. %; Coogan, 2007). It is

hence unlikely that these pyroxenites represent closed-system recycling of oceanic crust (Kornprobst *et al.*, 1990; Morishita *et al.*, 2003). As plagioclase is never —or rarely a minor — a liquidus phase during high-pressure melting of SE bulk compositions (Lambart *et al.*, 2013, and references therein), the elevated Eu_N/Eu^* of some Group A pyroxenites makes it unfeasible that they are high-pressure mineral segregates from melts derived from subducted oceanic crust

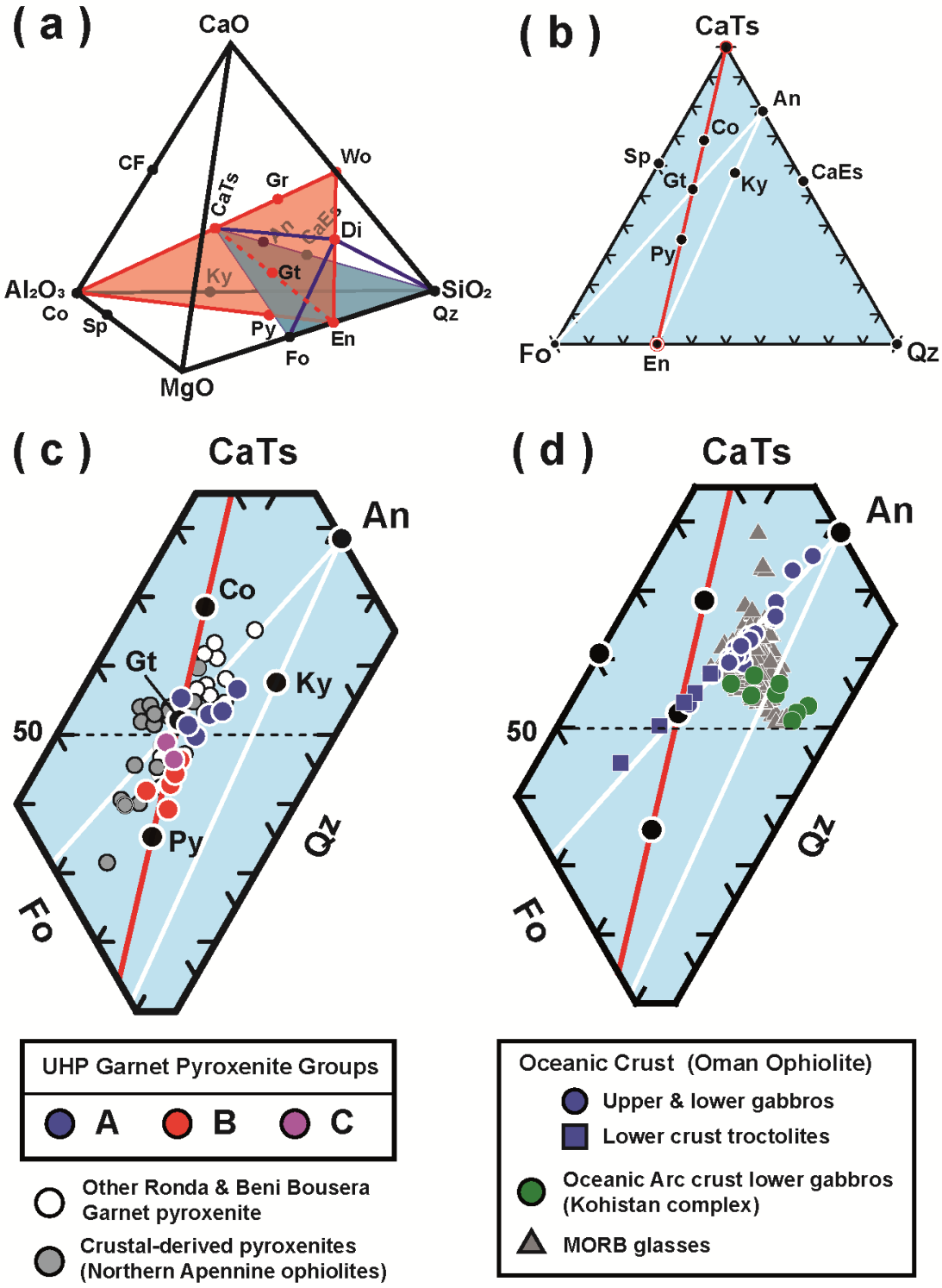

(Pearson *et al.*, 1989, 1993). Elevated Eu_N/Eu^* in Group A samples is most likely a trace element signature inherited from their low-pressure gabbroic protoliths.

Alternatively, Group A pyroxenites may well be residues of low degrees of high-pressure partial melting of recycled oceanic gabbros. Experimental work shows that, at high-pressure (> 2.5 GPa), the residues of low degree partial melting of anhydrous MORB eclogites and oceanic gabbros are mostly garnet pyroxenites (Fig. 5.7) (Pertermann & Hirschmann, 2003; Yaxley & Sobolev, 2007; Lambart *et al.*, 2013; Rosenthal *et al.*, 2014; Lambart *et al.*, 2016). Such garnet pyroxenite restites are Al_2O_3-rich, silica-enriched, and have CaTs contents similar to their protoliths (Fig. 5.7a). Furthermore, the bulk Na_2O contents of such garnet pyroxenite restites are lower than those of their protoliths and, alike for Group A pyroxenites (Fig. 5.1f), are negatively correlated with MgO contents (Pertermann & Hirschmann, 2003). The bulk rock and pyroxene compositions of these plagioclase-free garnet pyroxenite restites also show ghost positive Eu anomalies (Yaxley & Sobolev, 2007), which are similar to those observed in clinopyroxene from crustal-derived mantle pyroxenites (Montanini *et al.*, 2012; Marchesi *et al.*,

Figure 5.6 *(a) CaO-MgO-Al_2O_3-SiO_2 (wt. %.) tetrahedron (modified after Lambart et al., 2013) showing the aluminous pyroxene-garnet plane (red), which constitutes a thermal divide at high pressure (> 2 – 3 GPa). Silica-deficient (SD) and silica-excess (SE) pyroxenites plot on the left and right side of the aluminous pyroxene-garnet plane, respectively (Kogiso et al., 2004a), while bimineralic eclogite plots on this plane (Kogiso & Hirschmann, 2006). Also shown are the Fo-Q-CaTs-Di tetrahedron and the Fo-Q-CaTs plane. In the Fo-Q-CaTs-Di tetrahedron, the critical plane of undersaturation (Di–Fo–An) separates nepheline from hypersthene normative compositions, while the silica saturation plane (En–An–Di) separates hypersthene- and olivine-normative from quartz-normative compositions (Yoder & Tilley, 1962). The CMAS end members shown are: An, anorthite ($CaAl_2Si_2O_8$); CaEs, Ca Eskola's molecule ($Ca_{0.5}X_{0.5}AlSi_2O_6$; where X stands for crystal vacancies) CaTs, Ca Tschermak's molecule ($CaAl_2SiO_6$); CF, high pressure aluminous phase ($CaAl_2O_4$) with a calcium ferrite structure; Co, corundum (Al_2O_3); Di, diopside ($CaMgSi_2O_6$); En, enstatite ($MgSiO_3$); Fo, forsterite (Mg_2SiO_4); Gr, grossular ($Ca_3Al_2Si_3O_{12}$); Ky, kyanite (Al_2SiO_5); Py, pyrope ($Mg_3Al_2Si_3O_{12}$); Qz, quartz or coesite (SiO_2); Sp, spinel ($MgAl_2O_4$); and Wo, wollastonite ($CaSiO_3$). (b) Pseudoternary system (wt. %) Fo–CaTs–Qz (wt. %) projected from Di (wt. %). The dashed red line is the intersection of the aluminous pyroxene-garnet thermal divide in this ternary system. Dark gray solid lines are the An-Fo intersection of the critical plane of undersaturation (Di–Fo–An), and the An-En intersection of the silica saturation plane (En–An–Di) in this ternary system (see Fig. 5.6a, b). Data reduction and projection schemes after O'Hara (1972). (c & d) Portion of the pseudoternary system Fo-CaTs-Qz (slice boundaries: Fo, 0 – 60 wt. %; CaTs, 10 – 85 wt. %; and Qz, 0 – 35 wt. %) projected from diopside Di (wt. %) (Fig. 5.6b) showing: (c) the composition of the different groups of Ronda and Beni Bousera UHP garnet pyroxenites from the present study (symbol as in Fig. 5.1). Also shown are other garnet pyroxenites from the Ronda and Beni Bousera peridotites (open circles) (Suen & Frey, 1987; Garrido & Bodinier, 1999; Morishita et al., 2003), and pyroxenites from N. Apennines ophiolites derived from crustal recycled materials (dark gray circles) (Jenner & O'Neill, 2012; Montanini et al., 2012; Montanini & Tribuzio, 2015); and (d) the compositions of fresh MORB glasses (dark gray triangles) (Jenner & O'Neill, 2012), oceanic crustal gabbros from the upper and lower plutonic crust (blue circles) and lower crustal olivine troctolites (blue squares) from the Oman ophiolite (Garrido et al., 2001), and garnet granulite facies gabbros from the lower arc crustal section of the Kohistan paleo-arc terrane (green circles) (Garrido et al., 2006, 2007; Dhuime et al., 2009; Bosch et al., 2011). See text for further details.*

2013; Montanini & Tribuzio, 2015; Borghini *et al.*, 2016). High-pressure melting of anhydrous MORB-like eclogites and gabbros generates garnet pyroxenite restites (Fig. 5.7a) that plot between their liquidus garnets and clinopyroxenes (Fig. 5.7b), while their hypersthene- or quartz-normative partial melts plot off the thermal divide towards the Qz apex (Fig. 5.7a) (Lambart *et al.*, 2013, and references therein). Near liquidus garnet compositions are rich in Gt-Py components, while liquidus clinopyroxene contains significant amounts of Ca-Tschermak and non-stoichiometric Ca-Eskola components (Fig. 5.7b) (Rosenthal *et al.*, 2014), which explain why such (coesite-lacking) bimineralic garnet pyroxenite restites plot at the SE side of the thermal divide (Fig. 5.7a) (Garrido & Bodinier, 1999; Rosenthal *et al.*, 2014). The compositions of Group A samples, together with those of other Ronda and Beni Bousera SE garnet pyroxenites with CaTs > 50 wt.%, are offset from the An-Fo join defining a trend between experimental liquidus pyroxenes and garnet from partially melted MORB-like eclogite and gabbros (Fig. 5.7b). Furthermore, the compositions of the most SE Group A samples plot close to that of experimental residual eclogite (Fig. 5.7a; yellow crossed circle) (Rosenthal et al., 2014; Res2 initial bulk composition) obtained after high-pressure melting (5 GPa) and c. 15% extraction of siliceous melts from a fertile oceanic crust model composition (Spandler *et al.*, 2008). These observations strongly indicate that Group A garnet pyroxenites are most likely restites formed after high-pressure melting and extraction of moderate fractions of siliceous melts from recycled MORB oceanic crust.

Conversely to Group A samples, in the Fo-Qz-CaTs ternary system the compositions of Group B pyroxenites lie on the thermal divide at CaTs contents < 50 wt. % (Fig. 5.6c). The trend of Group B pyroxenites in this projection shows that their primary compositions were dominated by garnet and aluminous pyroxenes. Group B compositions are unlike those of silica-enriched sources such as MORB-like eclogites, oceanic gabbros and troctolites (Fig. 5.6d), and partial melts or residues of small degrees of partial melting and melt extraction of these sources (Fig. 5.7a). Kogiso & Hirschmann (2006) argued that, during subduction, extraction of silica from recycled altered MORB may form bimineralic eclogite (Fig. 5.7b) —solely composed of garnet and aluminous pyroxenes— that might be the main lithology derived from ancient recycled crust in the mantle sources of basalts. Melting of bimineralic eclogite is eutectic (Kogiso & Hirschmann, 2006) and consequently its melting residues and partial melts plot

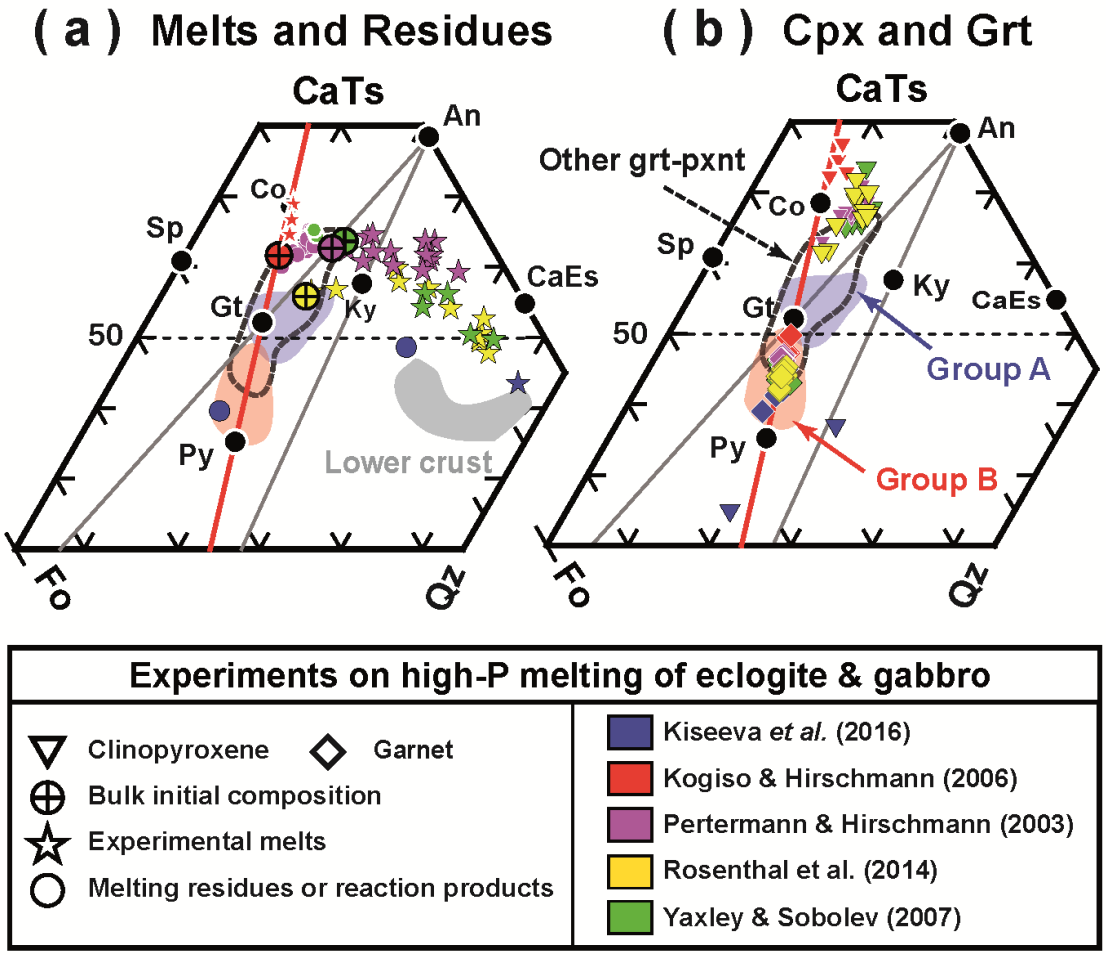

Figure 5.7 *Pseudoternary system Fo-CaTs-Qz (wt. %) (slice boundaries: Fo, 0 – 60 wt. %; CaTs, 20 – 80 wt. %; and Qz, 0 – 80 wt. %) projected from diopside Di (wt. %) (see Fig. 5.6b) showing:(a) melt and residue compositions determined experimentally in high-pressure, partial melting experiments of anhydrous MORB-like eclogite (Pertermann & Hirschmann, 2003), oceanic lower crustal gabbro (Yaxley & Sobolev, 2007), bimineralic eclogite (Kogiso & Hirschmann, 2006), and dry residual eclogite (Rosenthal et al., 2014; melting of the Res2 initial bulk composition). High-pressure sandwich experiments of carbonated, quartz-eclogite and peridotite (Kiseeva et al., 2016) are also shown. The gray field depicts the composition of Ronda lower crustal gneisses (Varas-Reus et al., in press). (b) Compositions of liquidus garnet and clinopyroxene from the same experiments shown in (a). The compositional fields of Group A (blue) and Groups B and C (red), and other Ronda and Beni Bousera garnet pyroxenites, are from Fig. 5.6c. Data reduction and projection schemes after O'Hara (1972). End member compositions as in Fig. 5.6.*

along the thermal divide at CaTs > 50 wt. % (Fig. 5.7a), between the compositions of liquidus garnets and clinopyroxenes (Fig. 5.7b). Group B pyroxenites cannot therefore be derived from bimineralic eclogites of such composition. Likewise, Group B garnet pyroxenites can neither be high-pressure garnet and clinopyroxene segregates from melts of subducted oceanic crust (Pearson *et al.*, 1991, 1993). As shown in the Fo-Qz-CaTs ternary projection (Fig. 5.7), such garnet-clinopyroxene segregates have SE compositions lying between liquidus garnets and

high-Eskola pyroxene (Fig. 5.7b). As for Group A pyroxenites, a high-pressure segregate origin can hardly account for the range of positive to negative Eu anomalies (Fig. 5.3d) observed in Group B pyroxenites.

As noted in previous studies of Ronda and Beni Bousera garnet pyroxenites (Loubet & Allègre, 1982; Pearson *et al.*, 1993; Garrido & Bodinier, 1999), the elevated TiO_2 and Yb contents and low La_N/Yb_N ratios of Group B samples (Fig. 5.3a, b, c) are indicative of these pyroxenites being rutile-bearing, garnet-dominated restites formed after extraction of moderate- to high-fractions of partial melts. Unlike Group A pyroxenites, Group B residual bulk compositions —characterized by CaTs content < 50% and lying on the thermal divide (Fig. 5.6c)— are hardly attainable during partial melting of silica-rich MORB sources (Fig. 5.7a) (Lambart *et al.*, 2013; Rosenthal *et al.*, 2014, and references therein). Therefore, as reflected in their different Sr-Nd-Pb-Hf systematics (Fig. 5.4), the component preponderant in the genesis of Group B pyroxenites likely had a bulk major element composition distinct from that of the MORB source of Group A pyroxenites. In the Fo-Qz-CaTs system, compositions similar to Group B pyroxenites are those of restitic bimineralic garnet pyroxenites formed after variable degrees of high-pressure partial melting and melt extraction from SD lithologies lying at the left side of the thermal divide (Lambart *et al.*, 2013, and references therein). Conversely to most SE sources, partial melts from SD pyroxene-rich bulk compositions are nepheline-normative. Several authors have argued that such melts may play an important role in the genesis of alkaline basalts and, to a lesser extent, MORBs (Hirschmann *et al.*, 2003; Kogiso *et al.*, 2003, 2004a; Lambart *et al.*, 2012, 2013). The origin of such SD lithologies in the mantle is a matter of some debate (Lambart *et al.*, 2013). They might be olivine-rich oceanic cumulates, such as troctolites (Montanini *et al.*, 2012; Montanini & Tribuzio, 2015), or bodies of subducted oceanic crust hybridized with mantle peridotite during stretching and stirring in the convective mantle (Hirschmann *et al.*, 2003; Kogiso *et al.*, 2003, 2004a; Lambart *et al.*, 2012, 2013). Interaction with carbonatite liquids or hybridization of carbonated MORB-like eclogite melts with peridotite may also generate such SD protoliths (Fig. 5.7) (Kiseeva *et al.*, 2016), and would account for the presence of diamond-bearing pyroxenites among Group B samples. Olivine-bearing pyroxene or garnet-rich delaminated lower continental crust may also be SD and the potential source of EM isotopic reservoirs (Tatsumi, 2000), fairly explaining the EM signature of Group B pyroxenites (Fig. 5.4). Whatever the origin of this SD component, it must be emphasized that the major and trace element compositions of Group B pyroxenites are consistent with these rocks being garnet-dominated restites and therefore they cannot simply be

closed-system derivatives of SD protoliths. Furthermore, their marked residual character indicates that, compared to Group A, the SD component in the source of Group B pyroxenites likely promoted a relatively lower solidus temperature and enhanced partial melting. Therefore, Group B pyroxenites may have underwent significantly higher extent of melting than Group A pyroxenites. Finally, in the Fo-Qz-CaTs system, Group C pyroxenites lie on the thermal divide and have intermediate compositions between Groups A and B. As for their Sr-Nd-Pb-Hf isotopic signatures (Fig. 5.4), their major element compositions most likely reflect hybrid sources between Group A and B pyroxenites.

Summing up, in good agreement with their Sr-Nd-Pb-Hf systematics, consideration of partial melting relations in the CMAS system indicates that Ronda and Beni Bousera UHP garnet pyroxenites most likely represent melting residues of straps of recycled MORB and gabbroic oceanic crust mixed with a recycled SD components akin to carbonated eclogite and/or lower continental crust.

5.4.3 A new recipe for the "marble cake" model for the genesis of UHP garnet pyroxenites in orogenic peridotites

The major and trace elements, and isotopic compositions of Ronda and Beni Bousera UHP garnet pyroxenites somewhat lend support to Allègre and Turcotte's "marble cake" hypothesis (Allègre & Turcotte, 1986) for the genesis of these pyroxenites as straps of ancient, recycled oceanic crust intimately mixed with mantle peridotites. The present study reveals, however, that besides this "exotic" component of ancient recycled oceanic crust, the genesis of these mantle pyroxenites requires a previously unnoticed component of recycled lower continental crust. This "native" component is somehow connected to the crustal section of the lithosphere where these UHP garnet pyroxenites now reside in (Fig. 5.4c, d). Several studies have highlighted the importance of continental lower crust foundering beneath continents or incorporated during subduction erosion in creating heterogeneous mantle sources of basalts (Stracke, 2012, and references therein). The present study shows that UHP garnet pyroxenites are potential markers of such contribution.

The geochemistry of these UHP garnet pyroxenites further unveils that the exotic recycled oceanic crust and the native lower continental-like components are intimately mixed in the Earth's mantle at length scales of these pyroxenites layers. The remarkable correlations between CaTs content and some isotopic ratios observed in UHP garnet pyroxenites (Fig. 5.8),

illustrate how intimately mixed these components are. CaTs content is negatively correlated with $^{87}Sr/^{86}Sr_{(i)}$ (Fig. 5.8a) and positively correlated their initial ε_{Nd}, ε_{Hf}, and $^{206}Pb/^{204}Pb$ ratios (Fig. 5.8b, c, d). These correlations imply that the sources of UHP garnet pyroxenites are mixtures of an exotic high-Al_2O_3, SE component, derived from recycled oceanic crust, with low-Al_2O_3, SD sources with a more detritic continental contribution and genetically link to the Ronda lower crust.

It is intriguing how UHP garnet pyroxenites, with such an isotopically diverse composition and sources, become intimately mixed and sampled by the subcontinental lithospheric mantle. The oldest U-Pb ages found in zircons from Ronda UHP garnet pyroxenites (1783 ± 37 Ma; Sánchez-Rodriguez & Gebauer, 2000) and chromitites (1815 ± 9 Ma to 1794 ± 17 Ma; González-Jimenez *et al.*, in press) are in the range of the oldest Re-Os depletion ages of 1.6 – 1.8 Ga in peridotites and their base-metal sulphides (Marchesi *et al.*, 2010; González-Jiménez *et al.*, 2013a, 2013b). In comparison, bulk rock Re-Os model ages of Beni Bousera pyroxenites (~ 1.2 – 1.4 Ga) are younger (Pearson & Nowell, 2004). These ages suggest that the portion of the Earth's mantle sampled by these massifs left the convecting mantle c. 1.2 – 1.8 Ga and became part of the

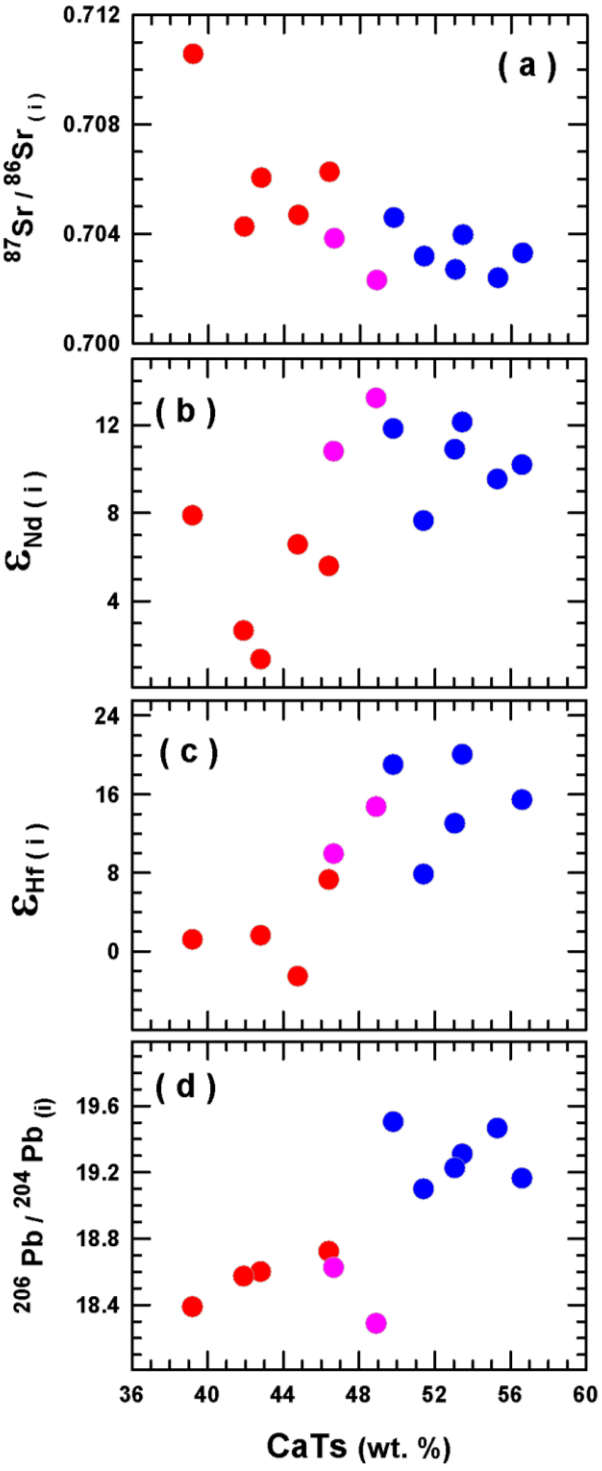

Figure 5.8 *CaTs (wt.%) of the different groups of UHP garnet pyroxenites against their age-corrected (a) $^{87}Sr/^{86}Sr_{(i)}$ ratio, (b) $\varepsilon_{Nd(i)}$, (c) $\varepsilon_{Hf(i)}$, and (d) $^{206}Pb/^{204}Pb$ ratios. Symbols as in Fig. 5.1. See caption of Fig. 5.4 and text for further details.*

depleted lithospheric mantle. The straps of recycled oceanic crust must have then been part of the convective mantle before its incorporation in the SCLM. The characteristic thickness of Ronda and Beni Bousera UHP garnet pyroxenites is in the order of cm to a few meters (Pearson *et al.*, 1993; Garrido & Bodinier, 1999; Frets *et al.*, 2012; Chetouani *et al.*, in press). Subducted crust stretched and thinned by convective stirring in the Earth's mantle typically attains this range of length scales after 1 Gyr (Kogiso *et al.*, 2004b). Interestingly, the predicted ages for the recycled oceanic crustal component of Group A pyroxenites (1.5 – 3.5 Ga; Fig. 5.5), are in agreement with the Nd depletion model ages of the Ronda (~ 1.7 Ga) (Varas-Reus *et al.*, in press) and Beni Bousera lower crust (c. 1.4 – 1.6 Ga) (Pearson & Nowell, 2004, and references therein). Given the eminently restitic composition of Group B pyroxenite sources, it seems feasible that these sources were melted during the adiabatic decompression of convecting mantle and creation of the SCLM and crust.

High-pressure decompression melting of mixed SD and SE lithologies, as those found in UHP garnet pyroxenites, would generate partial melts with compositions ranging from nepheline- to hypersthene- or quartz-normative (Lambart *et al.*, 2013, 2016), and contrasted isotopic signatures. The isotopic signature of recycled continental crust would be preponderant in nepheline-normative melts, and that of recycled oceanic crust in hypersthene- to quartz-normative melts. In addition, these sources would differ in their melt productivity. Experimental works indicate that the main factors controlling their high-pressure solidus, irrespectively of their SE or SD compositions, are the bulk Mg-no. and alkalis content (Lambart *et al.*, 2013, 2016, and references therein). Trace element signatures of an increasingly restitic character in UHP garnet pyroxenites are negatively correlated with Mg-no. (Fig. 5.3b, c), regardless their CaTs and Al_2O_3 contents, and isotopic source components. In good agreement with experimental work, these correlations suggest that low Mg-no. sources were more fertile, underwent higher extent of partial melting and led to their garnet-dominated restitic compositions (Fig. 5.7).

Figure 5.9 shows the temperature of low degree of melting (F = 5%;) —hereafter termed melting temperature— of the different groups of Ronda and Beni Bousera pyroxenites at 3.5 GPa, plotted against different major and trace element parameters of these pyroxenites. Melting temperatures are computed using the semi-empirical Melt-PX model of Lambart *et al.* (2016). Computed temperatures at 4.5, 3.5 and 2.5 GPa are given in Table 5.4. A caveat of this computation is that UHP garnet pyroxenites are restitic in composition; however, it is unlikely

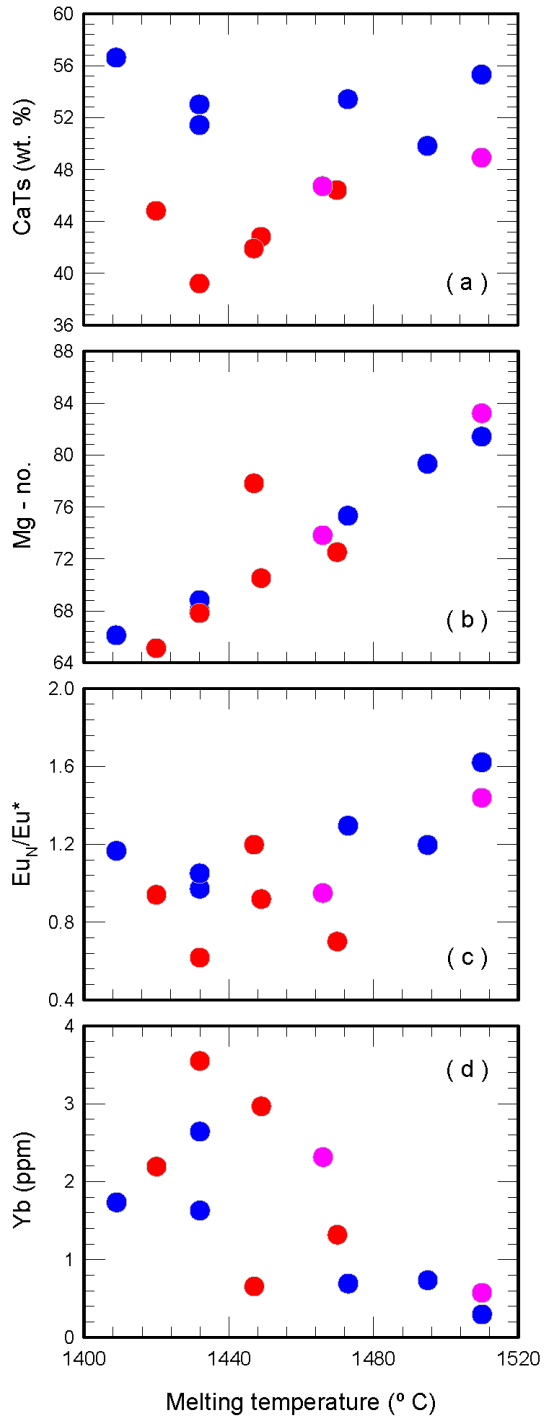

Figure 5.9 *Computed near solidus temperatures (ºC) of partial melting (F = 5 %) at 3.5 GPa for the studied UHP pyroxenite samples from the different groups (see Table 5.4) against the (a) CaTs content (wt. %), (b) Mg-no, (c) Eu_N/Eu^* ratio, and Yb (ppm) content of samples. Near-solidus temperatures and extents of melting as a function of temperature and pressure for mantle pyroxenites are calculated using the Melt-PX semi-empirical model of Lambart et al. (2016). Symbols as in Fig. 5.1. See text for further details.*

that their Mg-no., which is the main factor controlling their liquidus temperature, differ much from that of their sources.

Melting temperatures of pyroxenites are uncorrelated with Ca-Ts content (Fig. 5.9a), and positively correlated with Mg-no. (Fig. 5.9b). Although the correlation of the Mg-no. with melting temperature is inherent to the Melt-PX semi-empirical calibration, it also accounts for the effects of alkalis and other minor elements (Lambart *et al.*, 2016). The lack of correlation of the melting temperature with CaTs emphasizes that their liquidus mostly depend on their Mg-no., regardless of the pyroxenite group. At 3.5 GPa, the melting temperature ranges between c. 1400 and 1510 ºC, from low to high Mg-no. pyroxenites (Fig. 5.9b). Interestingly, the Eu_N/Eu^* of UHP pyroxenites correlates positively with their melting temperatures (Fig. 5.9c). This correlation most likely indicates that the positive Eu anomalies and other trace element signatures of gabbroic cumulate protoliths in high Mg-no. pyroxenites were largely preserved due to relatively higher melting temperatures (Fig. 5.9c). Low Mg-no pyroxenites, on the other hand, had lower liquidus temperatures and their garnet dominated character is demonstrated by the negative correlation of Yb with melting temperatures (Fig. 5.9d).

Table 5.4 Temperatures of 5% melting and cpx-out at different pressures of garnet pyroxenites

Sample	Group	P = 4.5 GPa		P = 3.5 GPa		P = 2.5 GPa	
		T (ºC) F = 5 %	T (ºC) (cpx - out)	T (ºC) F = 5 %	T (ºC) (cpx - out)	T (ºC) F = 5 %	T (ºC) (cpx - out)
RP7-1	A	1,501	1,647	1,432	1,582	1,352	1,489
RP7-8	A	1,554	1,650	1,473	1,585	1,382	1,492
RP7-11	A	1,474	1,640	1,409	1,575	1,334	1,482
RP7-17	A	1,503	1,655	1,432	1,590	1,352	1,497
RO175	A	1,582	1,686	1,495	1,621	1,398	1,528
BBCOR	A	1,599	1,683	1,510	1,618	1,408	1,525
RP7-02	B	1,522	1,656	1,449	1,591	1,449	1,591
RP7-03	B	1,485	1,640	1,420	1,575	1,344	1,482
RODIA	B	1,547	1,702	1,470	1,637	1,381	1,544
BB-DIA	B	1,501	1,636	1,432	1,571	1,352	1,478
10BB42B	B	1,587	1,712	1,447	1,647	1,397	1,554
RP7-12	C	1,544	1,664	1,466	1,599	1,377	1,506
10BB60G	C	1,602	1,684	1,510	1,619	1,407	1,526

6 Sr-Nd-Pb isotopic systematics of crustal rocks from the western Betics (S. Spain): Implications for crustal recycling in the lithospheric mantle beneath the westernmost Mediterranean[1]

6.1 Introduction

Despite numerous detailed metamorphic and tectono-sedimentary studies (e.g., Balanyá *et al.*, 1997; Faccenna *et al.*, 2004; Guerrera *et al.*, 2005; Crespo-Blanc & de Lamotte, 2006; Booth-Rea *et al.*, 2007; Platt *et al.*, 2013; Booth-Rea *et al.*, 2015), the origin and geodynamic evolution of the Flysch sediments and the Betic internal zones (Fig. 6.1a) are open to debate (c.f. Sec. 1.4). In addition, the role of these crustal units in the petrogenesis of the Cenozoic magmatism of the westernmost Mediterranean is uncertain (e.g., Duggen *et al.*, 2008; Marchesi *et al.*, 2012).

Geochemical and isotopic studies of the Betic crustal units may help to assess their relationships with Alpine and older tectono-magmatic processes that built the western Mediterranean region (c.f. Sec. 1.4). Here we present new trace element and Sr-Nd-Pb isotopic data of the Flysch sediments and metamorphic rocks from the internal Betics (western Alpujárride complex). We use these data, in particular Nd model ages, to constrain the provenance and evolution of these crustal units. The Nd model age represents the average crustal residence time of the rock and it is based on the evidence that Sm/Nd ratio is little affected by weathering, erosion, sedimentation, high-grade metamorphism and even partial melting processes, and therefore the time-integrated effects of these processes are generally negligible (Dickin, 2005; White, 2015). However, these ages calculated for detrital sedimentary sequences, as the Flysch sediments from the Betics, have to be considered with caution as they may average inputs from different continental sources. Finally, we also evaluate the influence of the studied crustal rocks on the composition of Cenozoic magmatism by contamination of the subcontinental mantle beneath the western Mediterranean or shallow assimilation. For this

[1] *This chapter has been published in the JCR journal Lithos*

purpose, we test different isotope mixing models of mantle metasomatism and crustal assimilation.

6.2 Sample selection

The lithology and geographical coordinates of the samples collected for the present study are given in Table 6.1. From the Algeciras Flysch unit, we collected ten samples of the Tarifa and the Punta Carnero sections (Fig. 6.1b). In the Tarifa section the sampling covers the Late Cretaceous to Oligocene sequence, whereas the Punta Carnero samples are from the Oligocene sequence (Guerrera *et al.*, 2005). The Algeciras Flysch unit consist of calcareous and siliciclastic turbidites interbedded with marls, pelites, siltstones and, locally, coarse calcareous conglomerates (Guerrera *et al.*, 2005; de Capoa *et al.*, 2014). The selected samples are calcareous and marly-calcareous turbidites, pelites and coarse-grained breccias.

In addition, we sampled metasedimentary rocks from the Jubrique and Blanca units (Fig. 6.1b). From the Jubrique unit, we selected 17 samples of increasing metamorphic grade from phyllites and schists, to porphyroblastic and mylonitic paragneisses. Acosta-Vigil *et al.* (2016), Balanyá *et al.* (1997), Barich *et al.* (2014) and Platt *et al.* (2003) provide a thorough petrological description of the Jubrique metamorphic crustal sequence. Phyllites mainly consist of magnesian chlorite and kyanite, whereas schists have an early assemblage of garnet, staurolite, kyanite, plagioclase and rutile, and a foliation defined by sillimanite and biotite; late andalusite porphyroblasts are common. Porphyroblastic paragneisses are mainly composed of quartz, plagioclase, K-feldspar, Al_2SiO_5 polymorphs, biotite, garnet and cordierite, and porphyroblasts of garnet and K-feldspar. Mylonitic paragneisses have mineralogical and microstructural features similar to porphyroblastic gneisses but they are finer-grained and have higher modal contents of garnet and Al_2SiO_5 polymorphs.

The samples from the Blanca unit are two pelitic migmatites located near the contact with the Ronda peridotite, and four quartz-feldspathic migmatites taken further down section. Acosta-Vigil (1998) and Acosta-Vigil *et al.* (2014) present the petrological, geochemical and geochronological characterization of these samples, including their bulk rock major and trace element analyses. Both migmatite types are composed of quartz, plagioclase, K-feldspar, cordierite, biotite, muscovite, Al_2SiO_5 polymorphs, ilmenite and rare tourmaline.

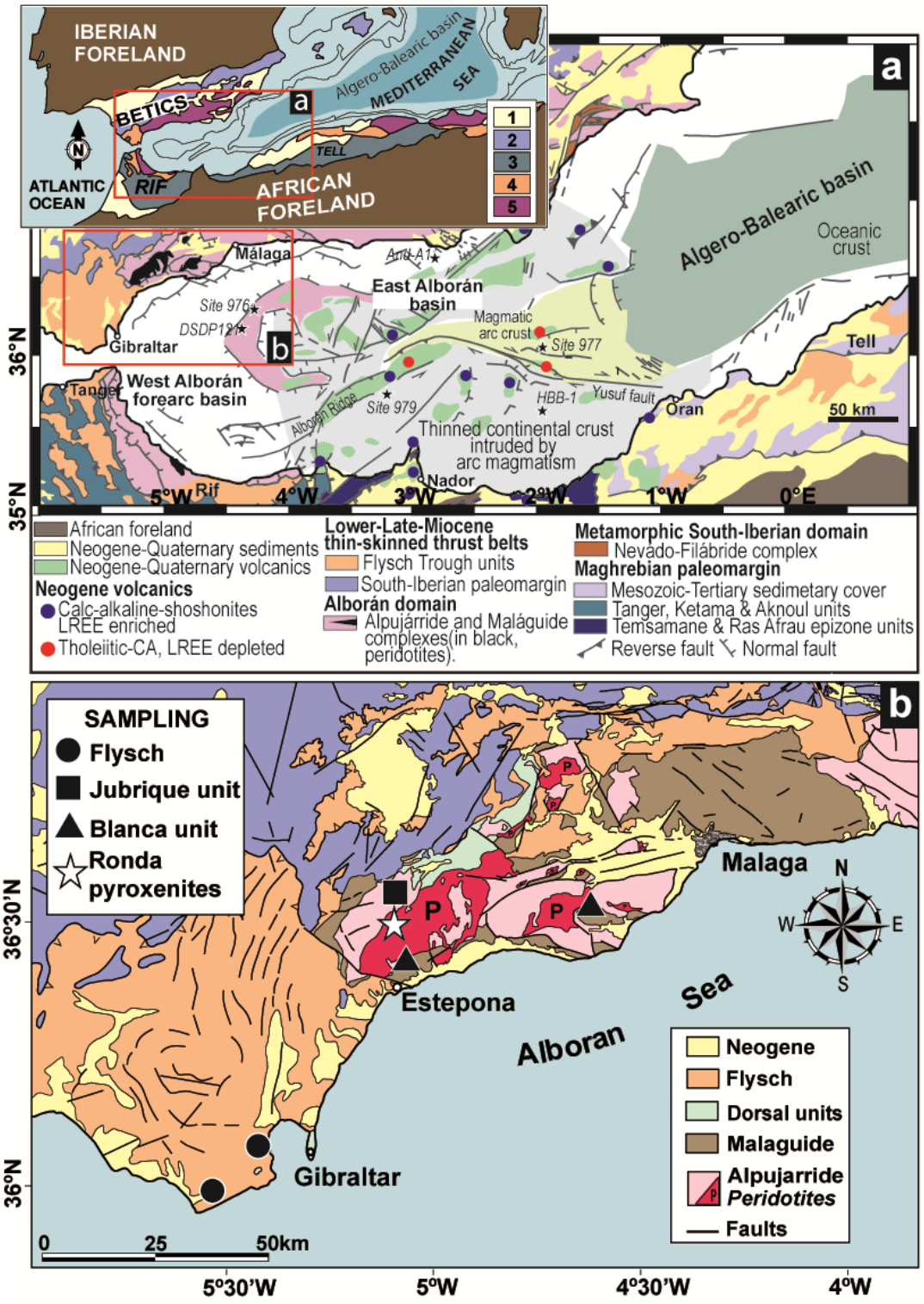

Figure 6.1 *(a) Simplified geological map of the westernmost Mediterranean termination of the circum-Mediterranean Alpine belt (inset) showing the main tectonic domains of the Betic-Rif belt and the areas of oceanic crust, magmatic arc, and thin continental crust in the Alborán basin (modified after Booth-Rea et al., 2007, and references therein). Inset: 1– Neogene sediments; 2– South-Iberian domain; 3– Maghrebian domain; 4–Flysch Trough units; 5– Alborán domain. (b) Simplified geological map of the westernmost Betic belt showing locations of samples (see Table 6.1 for sampling coordinates and sample description). Star indicates the location of Ronda high-Mg pyroxenites studied by Marchesi et al. (2012).*

Table 6.1 Trace element data of the Flysch sediments, and the crustal rocks of Jubrique and Blanca Units

		FLYSCH SEDIMENTS											ALPUJÁRRIDE COMPLEX					
Sample		**FPC1**	**FPC3**	**FPC4**	**FPC6**	**FPC7**	**FPC10**	**FPC12**	**FTA1**	**FTA2**	**FT4-D**	**FTA4-C**	**JU06**	**JU07**	**JU09**	**JU10**	**JU12**	**JU21**
Coordinates	**X**[1]	280125	280125	280125	280161	280161	280167	280167	266786	266786	266786	266786	302118	302118	302118	302118	302118	301786
Coordinates	**Y**[1]	3996511	3996511	3996511	3996349	3996349	3996347	3996347	3989930	3989930	3989930	3989930	4044479	4044479	4044479	4044479	4044479	4044529
Locality		**Flysch Punta Carnero**							**Flysch Tarifa**				**Jubrique unit**					
Rock-type		Grey calcareous sandstone	Red pelite	Grey marble	Green pelite	Red pelite	Coarse-grained sandstone	Fine-grained sandstone	Grey calcareous sandstone	Red pelite	Coarse-grained breccia, detritic part	Coarse-grained breccia, calcareus part	Mylonitic gneiss					
Trace elements (ppm)																		
Rb		4.0	134	19	110	79	33	86	5.9	57	11	9.4	5.9	47	9.7	67	6.8	93
Cs		0.26	9.0	1.0	5.6	3.8	1.0	2.9	0.37	3.7	0.40	0.32	0.16	0.29	0.18	0.43	0.36	0.55
Be		0.38	3.4	0.69	2.2	1.7	1.1	2.2	0.39	1.5	0.38	0.35	1.7	0.85	0.68	0.89	0.91	0.79
Sr		317	128	267	90	171	150	189	193	84	195	235	102	124	76	153	106	126
Ba		18	314	67	399	290	119	614	33	136	37	29	132	617	229	670	258	526
Y		11	34	16	17	20	12	20	10	26	7.0	6.3	39	27	24	26	16	28
Nb		0.94	26	3.8	15	11	5.0	12	1.8	8.3	1.0	1.0	17	14	18	14	20	15
Ta		0.058	2.2	0.27	1.3	0.92	0.52	1.2	0.15	0.80	0.089	0.095	0.93	1.0	1.1	0.88	1.2	1.1
Sn		0.40	4.2	0.88	3.1	2.4	1.7	4.0	0.48	2.1	0.41	0.40	0.89	0.48	0.60	0.68	1.2	1.0
Tl		0.034	0.76	0.13	0.63	0.44	0.20	0.53	0.045	0.45	0.070	0.064	0.089	0.38	0.33	0.41	0.31	0.57
Pb		3.5	23	3.2	7.3	11	8.7	16	3.0	9.0	4.7	4.3	7.7	16	16	20	15	17
U		0.56	2.9	1.0	2.2	2.0	1.3	2.4	0.51	1.3	0.49	0.28	0.65	1.2	0.56	0.81	0.90	1.0
Th		0.82	16	4.1	11	9.8	5.5	9.6	1.3	8.6	0.57	0.53	6.5	16	11	13	7.4	15
La		7.35	57	14	25	27	16	29	9.2	28	6.0	6.0	15	39	31	43	14	42
Ce		11	108	25	52	50	32	55	13	43	8.7	7.9	46	84	69	86	39	89
Pr		1.50	13	3.1	5.8	5.6	3.6	6.6	1.9	6.9	1.1	1.1	3.9	9.2	8.4	10.09	3.9	9.9
Nd		6.44	50	12	23	22	14	25	7.4	27	4.6	4.3	16	35	32	38	16	38
Sm		1.5	9.4	2.8	5.2	4.7	2.9	5.2	1.5	5.8	0.90	0.86	4.3	6.5	6.3	7.6	3.2	7.4
Eu		0.34	2.0	0.63	1.1	1.0	0.61	1.1	0.32	1.2	0.22	0.20	0.86	1.4	0.98	1.7	0.44	1.4
Gd		1.5	7.7	2.6	4.2	4.0	2.6	4.5	1.5	5.2	0.92	0.86	4.9	5.6	5.1	6.0	2.8	6.2
Tb		0.23	1.1	0.41	0.61	0.59	0.38	0.65	0.22	0.76	0.14	0.13	0.95	0.86	0.78	0.88	0.49	0.93
Dy		1.4	6.2	2.4	3.3	3.3	2.1	3.6	1.4	4.3	0.82	0.78	7.1	5.2	4.9	4.8	3.3	5.2
Ho		0.29	1.2	0.51	0.64	0.69	0.42	0.69	0.30	0.88	0.18	0.17	1.6	1.1	1.1	1.0	0.76	1.1
Er		0.73	3.3	1.3	1.6	1.7	1.0	1.8	0.83	2.3	0.47	0.43	4.7	3.0	3.1	2.7	2.2	2.8
Tm		0.100	0.49	0.21	0.25	0.29	0.16	0.26	0.13	0.36	0.075	0.067	0.70	0.47	0.46	0.40	0.37	0.42
Yb		0.62	3.1	1.3	1.7	1.8	1.00	1.7	0.91	2.2	0.41	0.41	4.6	3.0	3.2	2.7	2.4	2.6
Lu		0.088	0.51	0.20	0.28	0.28	0.15	0.26	0.14	0.35	0.063	0.058	0.81	0.50	0.52	0.43	0.39	0.41
$(La/Yb)_N$		8.5	13	7.8	11	11	12	12	7.3	9.1	11	11	2.3	9.2	6.8	11	4.3	12
Eu_N/Eu^*		0.69	0.69	0.70	0.69	0.70	0.67	0.66	0.63	0.68	0.72	0.69	0.58	0.70	0.51	0.75	0.43	0.63
Ce_N/Ce^*		0.77	0.94	0.87	1.0	0.95	0.97	0.93	0.74	0.73	0.76	0.70	1.4	1.0	1.0	0.98	1.3	1.0

[1] *UTM coordinates zone 30S ; (La/Yb)N normalized to chondrite after Sun and McDonough (1989) ;Eu*= [(SmN + GdN)/2]); Ce*= [(LaN + PrN)/2]*

[2] *Data from Acosta-Vigil (1998)*

Table 6.1 (continued)

	ALPUJÁRRIDE COMPLEX																	
Sample	**JU19**	**JU25**	**JU27**	**JU39**	**JU28**	**JU30**	**JU34**	**JU41**	**JU53**	**JU54**	**JU58**	**AC114[2]**	**SBA30[2]**	**AC115-2[2]**	**AC50[2]**	**ISTA16[2]**	**ROA30[2]**
Coordinates X[1]	301806	301700	301664	300428	300332	300333	300307	299104	298320	298493	298961	338229	304826	338355	338455	326636	305818
Coordinates Y[1]	4044503	4044628	4044821	4044385	4045077	4045059	4044634	4044710	4049800	4049573	4049213	4053287	4039211	4053377	4053437	4052743	4037956
Locality	**Jubrique unit**				**Jubrique unit**				**Jubrique unit**			**Blanca Unit**		**Blanca Unit**			
Rock-type	Porphyroblastic gneiss				Schist				Phyllite			Pelitic migmatite		Quartz-feldespatic migmatite			
Trace elements (ppm)																	
Rb	63	73	29	42	42	28	35	30	64	124	42	82	136	212	269	299	239
Cs	0.74	0.57	0.67	1.9	4.9	5.2	4.5	5.1	5.2	7.0	5.3	4.3	7.1	4.0	4.0	22	8.6
Be	1.8	1.1	3.9	1.0	2.4	2.7	3.1	3.3	2.7	3.8	3.3	1.7	3.0	2.0	0.60	2.8	2.9
Sr	202	133	192	123	67	111	107	119	56	143	84	101	114	103	86	103	157
Ba	443	379	139	186	162	169	217	193	193	504	212	464	462	277	238	244	313
Y	32	30	20	19	7.6	4.8	5.0	9.9	14	23	5.3	20	16	12	11	16	17
Nb	12	17	13	12	17	18	20	18	18	18	19	16	17	8.8	13	13	11
Ta	0.77	1.1	0.98	0.92	1.3	1.3	1.3	1.4	1.4	1.5	1.5	1.4	1.3	0.90	0.90	1.9	1.4
Sn	1.8	1.1	1.8	3.2	3.7	4.3	5.2	5.2	4.1	4.8	7.1	0.80	2.2	1.4	0.00	10	8.6
Tl	0.43	0.50	0.27	0.55	0.72	0.682	0.867	0.78	0.74	0.95	0.84	0.50	0.70	1.1	1.0	1.5	1.4
Pb	27.81	13.53	12.93	18.44	19	18	21	29	11	13	24	14	19	34	51	28	30
U	2.0	1.9	1.2	1.4	1.7	1.5	1.7	2.3	1.6	2.7	1.5	1.4	2.0	2.5	2.2	4.7	4.8
Th	8.9	13.83	8.5	9.0	6.9	6.0	8.1	10.0	5.6	9.9	6.0	15	13	11	7.2	10.0	13
La	28.62	39.95	24.32	23.45	18	13	17	23	17	28	14	91	40	25	22	24	28
Ce	58.10	84.83	52.21	56.15	46	36	40	55	45	72	29	91	87	57	47	53	59
Pr	6.5	9.3	5.7	6.0	5.0	3.6	4.5	6.0	4.3	6.5	3.6	9.6	9.5	6.7	5.8	6.3	7.1
Nd	25.34	35.74	22.35	23.58	19	15	18	24	17	25	14	37	35	26	23	24	28
Sm	5.3	7.2	4.4	4.9	3.9	2.9	3.5	4.9	3.7	5.1	2.9	7.2	6.7	6.3	4.3	5.2	6.3
Eu	1.6	1.4	1.1	1.1	0.69	0.482	0.656	0.95	0.68	1.0	0.57	1.2	1.2	0.90	0.61	0.73	1.1
Gd	5.0	6.1	3.7	4.2	2.6	2.1	2.5	3.8	3.2	4.5	2.2	6.2	5.4	5.0	3.2	4.5	6.6
Tb	0.83	0.92	0.57	0.63	0.38	0.281	0.344	0.55	0.50	0.71	0.33	0.73	0.71	0.64	0.44	0.62	0.86
Dy	5.2	5.3	3.2	3.6	1.8	1.3	1.4	2.6	3.1	4.2	1.7	4.0	3.6	2.9	2.0	3.1	3.5
Ho	1.1	1.1	0.68	0.73	0.35	0.24	0.257	0.45	0.65	0.88	0.34	0.84	0.59	0.47	0.31	0.53	0.65
Er	3.1	3.0	1.8	2.0	0.93	0.576	0.573	1.0	1.7	2.3	0.85	2.4	1.3	1.0	0.76	1.3	1.6
Tm	0.49	0.45	0.29	0.31	0.17	0.104	0.096	0.17	0.26	0.35	0.13	0.34	0.19	0.12	0.11	0.18	0.21
Yb	3.1	2.9	1.8	2.0	1.1	0.646	0.603	1.0	1.6	2.2	0.86	2.2	1.1	0.66	0.50	1.1	1.5
Lu	0.50	0.46	0.26	0.28	0.15	0.096	0.080	0.15	0.22	0.29	0.13	0.34	0.17	0.090	0.070	0.16	0.21
$(La/Yb)_N$	6.7	9.8	9.8	8.6	12	15	20	15	7.3	9.2	11	30	25	27	31	16	14
Eu_N/Eu^*	0.92	0.65	0.80	0.70	0.63	0.56	0.64	0.65	0.59	0.64	0.66	0.53	0.58	0.47	0.48	0.45	0.52
Ce_N/Ce^*	1.0	1.0	1.0	1.1	1.2	1.2	1.1	1.1	1.3	1.3	0.99	0.61	1.1	1.1	0.99	1.0	1.0

[1] *UTM coordinates zone 30S ; (La/Yb)N normalized to chondrite after Sun and McDonough (1989) ;Eu*= [(SmN + GdN)/2]); Ce*= [(LaN + PrN)/2]*

[2] *Data from Acosta-Vigil (1998)*

6.3 Results

6.3.1 Trace elements

Trace elements of the Flysch and the Jubrique samples are reported in Table 6.1, together with the trace element data of the Blanca unit reported by Acosta-Vigil (1998).

6.3.1.1 Flysch sediments

The chondrite-normalized Rare Earth Element (REE) patterns of the Flysch sediments are shown in Fig. 6.2a. These patterns are light (L)REE-enriched (La_N/Yb_N = 7 – 13) and show relatively flat heavy (H)REE segments (Ho_N/Yb_N = 0.9 – 1.4), as seen also in Atlantic sediments (Fig. 6.2a) and continental crustal rocks (Ben Othman *et al.*, 1989; Rudnick & Gao, 2003). The Flysch sediments from the two sampled localities have very similar REE patterns, only differing in their absolute abundances. The samples with the lowest REE concentrations are those with high amounts of carbonate component and generally correspond to samples from the Tarifa section (Fig. 6.2a, Table 6.1). All the patterns have strong negative Eu anomalies (Eu_N/Eu^* ~ 0.68; Eu*= [(Sm_N + Gd_N)/2]), and some samples, especially from the Tarifa section, show slight negative Ce anomalies (Ce_N/Ce^* ~ 0.74; Ce*= [(La_N + Pr_N)/2]). The analyzed Flysch sediments are enriched in fluid-mobile, incompatible elements (Rb, U, Pb and ±Th) relative to more compatible REE and High Field Strength Elements (HFSE: Nb, Ta) (Fig. 6.3a), as also described in marine pelagic sediments (Ben Othman *et al.*, 1989).

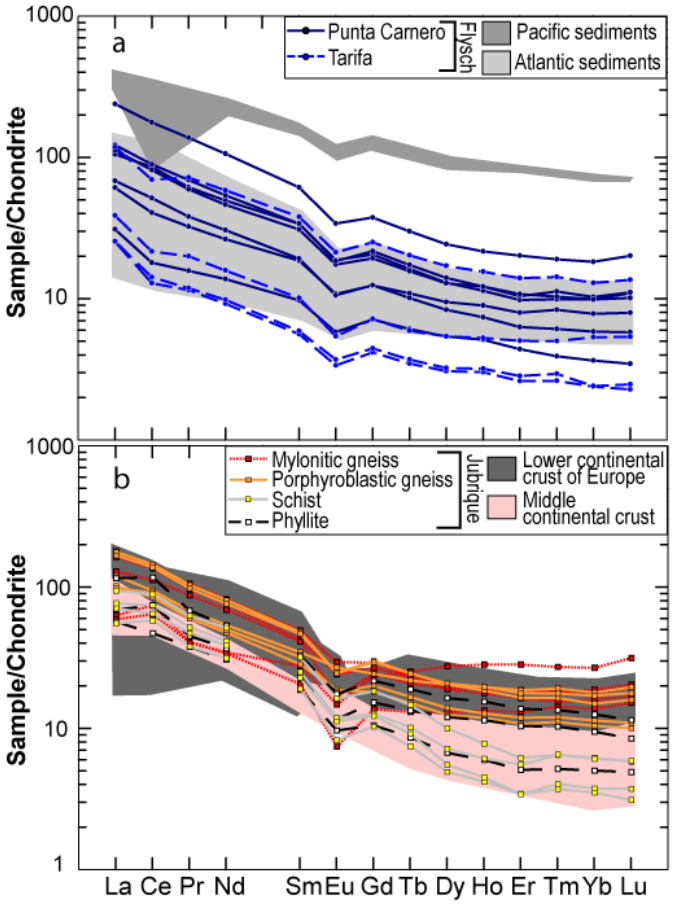

Figure 6.2 *Chondrite-normalized REE patterns (Sun & McDonough, 1989) of (a) Flysch sediments and (b) Jubrique samples.*

6.3.1.2 Metamorphic rocks from the western Alpujárride units

The chondrite-normalized REE patterns of the Jubrique metapelitic rocks are shown in Fig. 6.2b. These samples have REE patterns similar to those of the Flysch sediments, with strong negative Eu anomalies ($Eu_N/Eu^* \sim 0.65$) and relatively flat HREE segments ($Ho_N/Yb_N = 0.9 – 1.3$). Mylonitic gneisses have a wide range of La_N/Yb_N values (2.4 – 11.8), covering the entire array of phyllites and porphyroblastic gneisses ($La_N/Yb_N = 7.4 – 11.3$; $La_N/Yb_N = 6.7 – 9.8$, respectively). The schists have more fractionated REE patterns than the other Jubrique samples ($La_N/Yb_N = 14.7 – 20.1$). Some rocks, in particular the schists and phyllites, show positive Ce anomalies ($Ce_N/Ce^* \sim 1.22$). The REE normalized patterns of the phyllite and schist samples are similar to those of the middle continental crust (Rudnick & Gao, 2003, and references therein), and those of the gneisses overlap with the values of the European lower continental crust (Downes, 1993) (Fig. 6.2b). In most samples, fluid-mobile, incompatible elements, such as Cs, Rb, Ba, Th, U and Pb, are enriched relative to REE and HFSE (Fig. 6.3b).

6.3.2 Sr-Nd-Pb isotopic systematics

The present-day Sr-Nd-Pb isotopic data of the analyzed samples are provided in Table 6.2.

6.3.2.1 Flysch sediments

The present-day Sr-Nd-Pb radiogenic isotope ratios of the Flysch samples are shown in Fig. 6.4. These isotopic compositions overlap with those of marine sediments, supporting a marine pelagic provenance, and are relatively unradiogenic in $^{87}Sr/^{86}Sr$ and radiogenic in $^{206}Pb/^{204}Pb$ ratios.

Based on their $^{87}Sr/^{86}Sr$ and $^{143}Nd/^{144}Nd$ ratios, we distinguish two groups:

a. *Group A* (FTA1, FTA4-D, FTA4-C, FPC1, and FPC4). These samples are characterized by relatively low $^{87}Sr/^{86}Sr$ (0.70796 – 0.70871) and high $^{143}Nd/^{144}Nd$ (0.51211 – 0.51222) ratios (Fig. 6.4a). This group consists of marble, sandstone and breccia from the Late Cretaceous–lower Oligocene Flysch sequence (Table 6.1).
b. *Group B* (FTA2, FPC3, FPC6, FPC7, FPC10, and FPC12). These samples have higher $^{87}Sr/^{86}Sr$ (0.71156 – 0.71667) and slightly lower $^{143}Nd/^{144}Nd$ (0.51207 – 0.51215) ratios than Group A (Fig. 6.4a). This group mainly consists of Oligocene pelite and sandstone (Table 6.1).

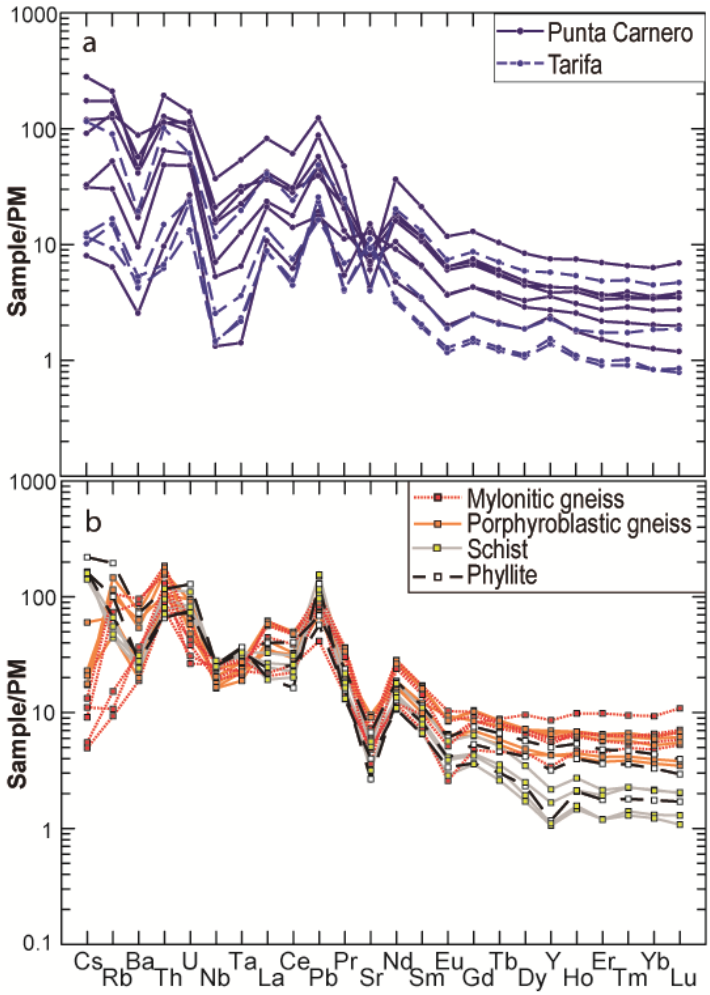

Figure 6.3 *Primitive mantle (PM)-normalized trace elements patterns (Sun & McDonough, 1989) of (a) Flysch sediments and (b) Jubrique samples.*

Henceforth, we will refer to these two groups as Flysch A and B, respectively. The Nd model ages of Flysch A (1.37 – 1.93 Ga) are slightly younger than those of Flysch B (1.53 – 1.91 Ga). The average value of the samples as a whole is 1.7 Ga (Fig. 6.5).

Both groups show a large range of present-day Pb isotopic ratios. The samples of Flysch A generally have lower Pb isotope ratios ($^{206}Pb/^{204}Pb$: 18.756 – 19.104; $^{207}Pb/^{204}Pb$: 15.674 – 15.694, and $^{208}Pb/^{204}Pb$: 38.783 – 39.161) than Flysch B ($^{206}Pb/^{204}Pb$: 18.821 – 19.218; $^{207}Pb/^{204}Pb$: 15.687 – 15.733, and $^{208}Pb/^{204}Pb$: 38.898 – 39.347). All the Flysch samples lie well above the Northern Hemisphere Reference Line (NHRL) of Hart (1984) (Fig. 6.4b, c).

6.3.2.2 Metamorphic rocks from the western Alpujárride units

The present-day Sr, Nd and Pb radiogenic isotope ratios of Jubrique and Blanca samples are shown in Fig. 6.4.

6.3.2.2.1 The Jubrique unit

In general, the present-day isotopic compositions of the Jubrique samples overlap with the field of the European lower continental crust (Fig. 6.4). The Jubrique high-grade (porphyroblastic and mylonitic gneisses) and low-grade metamorphic rocks (schists and phyllites) have rather homogeneous $^{143}Nd/^{144}Nd$ ratios (high-grade rocks: 0.51199 – 0.51210; low-grade rocks: 0.51197 – 0.51206). The $^{87}Sr/^{86}Sr$ ratios of the Jubrique samples are intermediate between those

Table 6.2 Present-day bulk rock Sr-Nd-Pb isotope data

Sample	Classification	$^{87}Sr/^{86}Sr$		$^{143}Nd/^{144}Nd$		Nd T_{DM}	$^{206}Pb/^{204}Pb$		$^{207}Pb/^{204}Pb$		$^{208}Pb/^{204}Pb$	
FPC1	Flysch A	0.707958	± 3	0.512147	± 5	1859	18.7965	± 5	15.6800	± 3	38.913	± 2
FPC1 Dup	Flysch A	*0.707976*	*± 4*	*0.512110*	*± 8*	*1929*	*18.7909*	*± 8*	*15.6742*	*± 6*	*38.886*	*± 1*
FPC4	Flysch A	0.708713	± 5	0.512136	± 5	1871	19.1043	± 6	15.6943	± 6	39.161	± 1
FTA1	Flysch A	0.708040	± 5	0.512130	± 3	1621	19.0025	± 8	15.6910	± 8	39.002	± 2
FT4-D	Flysch A	0.708194	± 4	0.512221	± 4	1368	18.7866	± 4	15.6841	± 3	38.7825	± 8
FTA-4 C	Flysch A	0.708076	± 8	0.512195	± 5	1431	18.7564	± 4	15.6822	± 3	38.8070	± 9
FPC3	Flysch B	0.716672	± 6	0.512071	± 5	1525	18.8866	± 3	15.7015	± 3	39.0791	± 7
FPC6	Flysch B	*b.d.l.*		0.512070	± 2	1909	19.2178	± 5	15.7335	± 4	39.347	± 3
FPC7	Flysch B	0.715765	± 5	0.512101	± 8	1776	18.9678	± 4	15.7110	± 3	39.1482	± 9
FPC10	Flysch B	0.711555	± 4	0.512147	± 3	1558	18.8211	± 3	15.6873	± 3	38.9261	± 7
FPC12	Flysch B	0.713382	± 6	0.512145	± 3	1570	18.8595	± 3	15.6876	± 3	38.9327	± 7
FPC12 Dup	Flysch B	*0.713383*	*± 5*	*0.512132*	*± 3*	*1590*	*18.8321*	*± 6*	*15.6882*	*± 5*	*38.898*	*± 1*
FTA2	Flysch B	0.713787	± 5	0.512108	± 3	1696	18.9406	± 2	15.6904	± 2	39.0898	± 6
JU6	Jubrique HG	0.717041	± 3	0.512059	± 1	2642	18.7089	± 2	15.6913	± 2	39.9364	± 5
JU7	Jubrique HG	0.721702	± #	0.512100	± 4	1446	18.6001	± 6	15.6873	± 5	39.402	± 1
JU9	Jubrique HG	0.722221	± 5	0.512053	± 5	1603	18.5712	± 2	15.6843	± 2	39.2211	± 4
JU10	Jubrique HG	0.721962	± 5	0.512052	± 2	1623	18.5822	± 2	15.6857	± 2	39.2191	± 4
JU12	Jubrique HG	0.722366	± 8	0.512041	± 2	1662	18.6164	± 2	15.6876	± 2	39.4315	± 5
JU19	Jubrique HG	0.721887	± 4	0.512045	± 3	1773	18.5599	± 2	15.6897	± 2	38.9501	± 5
JU21	Jubrique HG	0.723810	± 2	0.512013	± 9	1659	18.5690	± 4	15.6818	± 4	39.0145	± 9
JU25	Jubrique HG	0.724855	± 2	0.511995	± 2	1748	18.7443	± 2	15.7011	± 2	39.2124	± 5
JU27	Jubrique HG	0.722986	± 2	0.512033	± 2	1644	18.6408	± 2	15.6900	± 2	38.9553	± 5
JU39	Jubrique HG	0.727306	± 4	0.512053	± 3	1747	18.7043	± 2	15.6989	± 2	39.0507	± 5
JU39 Dup	Jubrique HG	*0.727336*	*± 4*	*0.512052*	*± 4*	*1747*	*18.7031*	*± 2*	*15.6983*	*± 2*	*39.0474*	*± 4*
JU28	Jubrique LG	0.726853	± 5	0.512039	± 6	1654	18.6913	± 2	15.6988	± 2	39.0907	± 5
JU30	Jubrique LG	0.726657	± 5	0.512019	± 3	1690	18.6726	± 2	15.6983	± 2	39.0888	± 5
JU34	Jubrique LG	0.732282	± 3	0.511970	± 2	1695	18.6387	± 2	15.7083	± 2	39.0850	± 5
JU41	Jubrique LG	0.729042	± #	0.512005	± 2	1748	18.6334	± 2	15.6908	± 2	39.0265	± 4
JU53	Jubrique LG	0.726395	± 6	0.512032	± 2	1809	18.8174	± 2	15.7069	± 2	39.3432	± 4
JU54	Jubrique LG	0.720528	± 3	0.512064	± 5	1651	19.1064	± 1	15.7129	± 1	39.5641	± 3
JU58	Jubrique LG	0.729267	± 3	0.512057	± 2	1648	18.6389	± 2	15.6874	± 1	38.9822	± 4
AC115-2	Blanca A	0.746503	± 7	0.512098	± 15	2071	18.8503	± 4	15.6951	± 2	38.7531	± 6
AC50	Blanca A	0.753573	± 7	0.512093	± 4	1494	18.8783	± 5	15.6939	± 5	38.757	± 1
ISTA16	Blanca A	0.742120	± 5	0.512130	± 3	1711	18.9913	± 5	15.7016	± 5	38.752	± 1
ROA30	Blanca A	0.731056	± 4	0.512077	± 4	1899	18.8617	± 5	15.6967	± 3	38.7857	± 9
AC114	Blanca B	0.729572	± #	0.511988	± 3	1730	18.7556	± 4	15.6996	± 4	39.0310	± 9
SBA30	Blanca B	0.729686	± 3	0.512019	± 7	1583	18.7375	± 4	15.6934	± 3	39.0665	± 9

Italic ratios are duplicates; Nd T_{DM}: Nd depleted mantle model ages; HG: high-grade; LG: low-grade; b.d.l. = below detection limit
The Nd depleted mantle model ages are calculated following DePaolo (1981).

of the Flysch and Blanca samples (Fig. 6.4a). Jubrique high-grade rocks generally have lower $^{87}Sr/^{86}Sr$ ratios (0.71704 – 0.72733) than the low-grade samples (0.72053 – 0.73228).

Except for the phyllite samples that display a relatively large range of $^{206}Pb/^{204}Pb$ ratios (18.639 – 19.106), most of the Jubrique samples have lower $^{206}Pb/^{204}Pb$ ratios than the Flysch

and Blanca samples (Fig. 6.4b, c). The $^{206}Pb/^{204}Pb$ ratios of schist and high-grade samples range

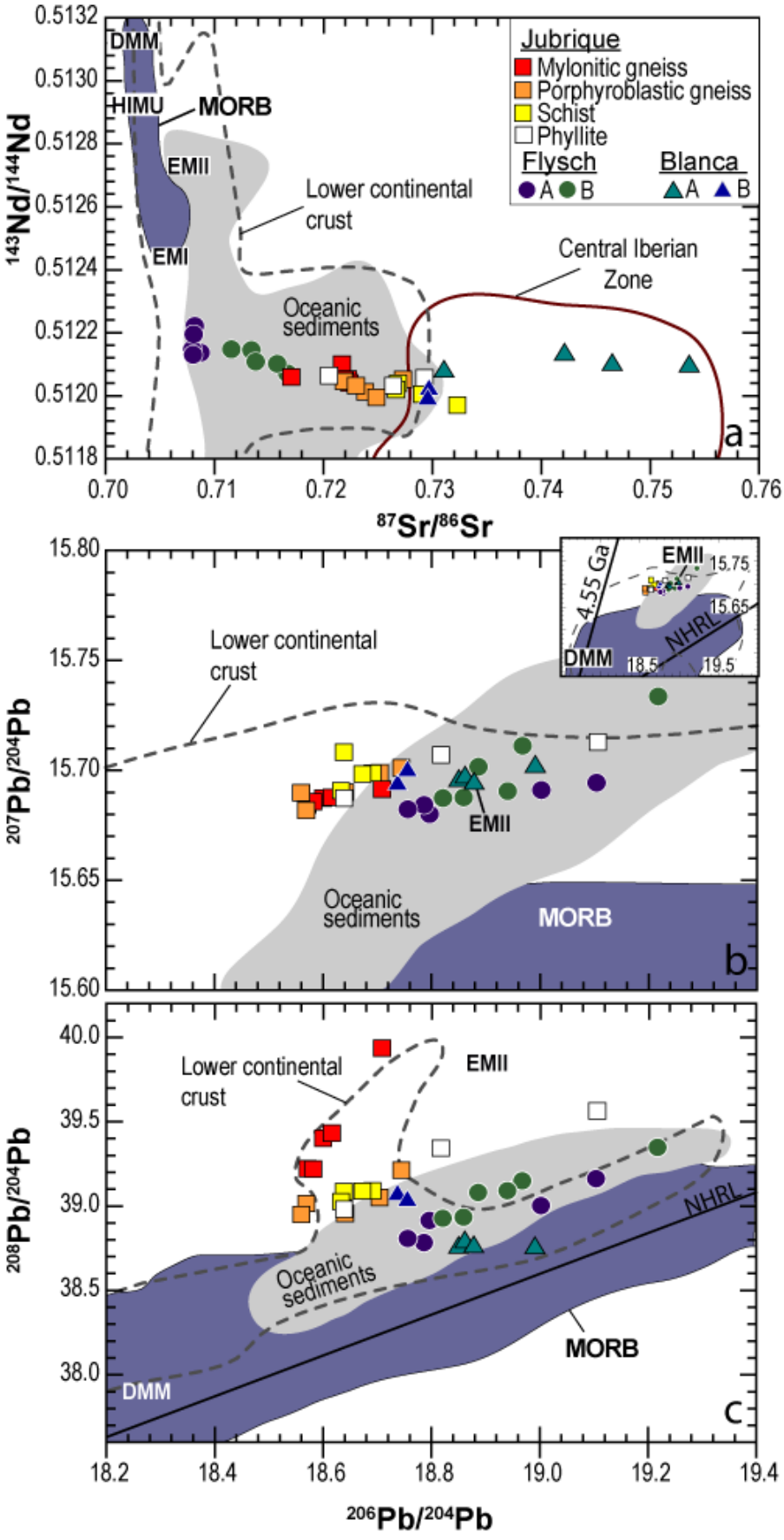

from 18.633 to 18.691, and from 18.560 to 18.744, respectively. The phyllite samples also display a relatively large range of $^{207}Pb/^{204}Pb$ (15.687 – 15.713), compared to the schist (15.691 – 15.710) and high-grade samples (15.682 – 15.701) (Fig. 6.4b). The $^{208}Pb/^{204}Pb$ ratios of the porphyroblastic gneisses and low-grade rocks are very similar (38.950 – 39.212; 38.982 – 39.564, respectively) and, as a whole, follow a trend parallel to that of the Flysch sediments, whereas the mylonitic gneisses differ by higher $^{208}Pb/^{204}Pb$ ratios (39.219 – 39.936) at a given $^{206}Pb/^{204}Pb$ ratio (Fig. 6.4c). As the samples of the Flysch and Blanca units, the Jubrique rocks also plot above the NHRL in the Pb isotope diagrams (Fig. 6.4b, c).

The Nd model ages of the Jubrique rocks are within the range of the Flysch sediments and the Blanca migmatites, with an average value of 1.7 Ga (Fig. 6.5). The mylonitic gneisses have the younger (1.45 Ga) and older (2.64 Ga) Nd model ages among the Jubrique samples, and the Nd model ages of phyllite, schist and porphyroblastic gneiss samples range from 1.65 to 1.81 Ga, 1.65 to 1.75 Ga, and 1.65 to 1.77 Ga, respectively (Table 6.2).

6.3.2.2.2 The Blanca unit

The present-day $^{87}Sr/^{86}Sr$ ratios of the Blanca samples are the highest among the analyzed samples, overlapping the metasedimentary rocks of the Central Iberian Zone, and part of the fields of marine sediments and European lower continental crust (Fig. 6.4a). Based on their present-day Sr-Nd-Pb isotopic compositions, we distinguish two groups:

a. *Group A* (AC-115.2, ISTA16 and AC50; Table 6.2). These samples are quartz-feldspathic migmatites located slightly below the contact with the overlying Ronda peridotites. They have extremely high $^{87}Sr/^{86}Sr$ (0.74212 – 0.75357) and relatively high $^{143}Nd/^{144}Nd$ ratios (0.51209 – 0.51213). Their $^{207}Pb/^{204}Pb$ ratios (15.694 – 15.702) are similar to those of Group B samples, whereas their $^{206}Pb/^{204}Pb$ (18.850 – 18.991) and $^{208}Pb/^{204}Pb$ (38.752 – 38.757) ratios are higher and lower, respectively (Fig. 6.4).
b. *Group B* (SBA30, AC114; Table 6.2). These samples are pelitic migmatites located at

Figure 6.4 *Plots of the present-day (a) $^{87}Sr/^{86}Sr$ vs. $^{143}Nd/^{144}Nd$, (b) $^{206}Pb/^{204}Pb$ vs. $^{207}Pb/^{204}Pb$ and (c) $^{206}Pb/^{204}Pb$ vs. $^{208}Pb/^{204}Pb$ isotopic variations of the Flysch sediments and the Jubrique and Blanca metamorphic rocks. Also shown for comparison are the fields of the oceanic sediments (data from Ben Othman et al., 1989, Hoernle, 1998, Jolly et al., 2006, Revel et al., 1996), the European lower (Downes, 1993, and references therein) and bulk continental crust (Rudnick & Goldstein, 1990), and the Neoproterozoic metasediments from the Central Iberian Zone (Spain) (Villaseca et al., 2014). Also shown are the DMM, EMI, EMII and HIMU mantle components (Salters & Stracke, 2004; Workman & Hart, 2005; Hofmann, 2007), and the field of MORB (GEOROC database, vs. November 2015). The 4.55 Ga geochron and the Northern Hemisphere Reference Line (NHRL) (Hart, 1984) are also shown for reference.*

the contact with the overlying Ronda peridotites. They have lower $^{87}Sr/^{86}Sr$ (0.72957 – 0.72969) and $^{143}Nd/^{144}Nd$ ratios (0.51199 – 0.51202) than Group A. Their $^{206}Pb/^{204}Pb$ and $^{208}Pb/^{204}Pb$ ratios range from 18.738 to 18.756 and from 39.031 to 39.066, respectively, whereas their $^{207}Pb/^{204}Pb$ ratios (15.693 – 15.699) are within the range of the Group A samples (Fig. 6.4). In terms of Sr-Nd-Pb isotopic ratios, they overlap with the Jubrique porphyroblastic gneiss, schist and phyllite samples (Fig. 6.4).

Henceforth, we will refer to these groups as Blanca A and B, respectively. The sample ROA-30 has isotopic compositions intermediate between these groups. We included it in Group A due to its lithological similarity to the other samples of this group (Table 6.2).

The Nd model ages range from 1.49 to 2.07 Ga and 1.58 to 1.73 Ga for Blanca A and B samples, respectively, and the average Nd model age of the unit is 1.7 Ga, coincident with those of the Flysch sediments and the Jubrique rocks (Fig. 6.5).

6.4 Discussion

6.4.1 Provenance of the western Betics crustal units

6.4.1.1 Provenance of the pre-Miocene Algeciras Flysch sediments

The isotopic systematics of the Flysch sediments indicates a temporal shift from a pelagic dominance (Flysch A) to an increase in detrital components (Flysch B). The low Rb/Sr and low present-day $^{87}Sr/^{86}Sr$ ratio of Flysch A (Fig. 6.4a) can be attributed to variable mixtures of detrital and seawater carbonate fractions. Carbonates precipitated from seawater acquire its low $^{87}Sr/^{86}Sr$ (modern seawater $^{87}Sr/^{86}Sr$ ratio = 0.70916) and Rb/Sr ratio, which are fundamentally controlled by mid-ocean ridge hydrothermalism (Elderfield & Schultz, 1996). On the other hand, the Sm/Nd ratio of fine-grained material —such as the pre-Miocene Flysch samples— is slightly affected by sedimentary processes because these elements are effectively transported in the clay fraction and are rather insoluble in seawater. Therefore, their Sm/Nd and Nd model ages should not differ significantly from those of their precursor crystalline rocks (Vervoort *et al.*, 2011).

From the Oligocene onward, the AlKaPeCa and Maghrebian continental margins were uplifted and eroded and their detritus were delivered to the Flysch basin (Thomas *et al.*, 2010) (c.f. Sec. 1.4.4). As documented in sedimentological studies (e.g., Guerrera *et al.*, 2005; Luján *et al.*, 2006), this geodynamic evolution is recorded by an increase of the detrital input in the

Flysch Trough. In the case of the Algeciras Flysch sediments, their Cretaceous–Oligocene (Flysch A) and late Oligocene–early Miocene (Flysch B) detrital components have been ascribed, respectively, to an African and an Alborán upper crust provenance (Guerrera *et al.*, 2005; Crespo-Blanc & de Lamotte, 2006; Luján *et al.*, 2006; Thomas *et al.*, 2010). The range of Nd model ages of the Algeciras Flysch sediments (1.4 to 1.9 Ga; Fig. 6.5) indicates a provenance from a crustal source with an early Mesoproterozoic–late Paleoproterozoic average Nd crustal residence time, or mixtures of older crust with juvenile components. Cenozoic detritus from the westerly African margins of the Alpine Tethys was likely derived from the erosion of the Atlas, Anti-Atlas and Pan-African granitoids (Guerrera *et al.*, 2005; Thomas *et al.*, 2010), which have an average Nd model age of 1 Ga (Bea *et al.*, 2010), or from younger Paleozoic components.

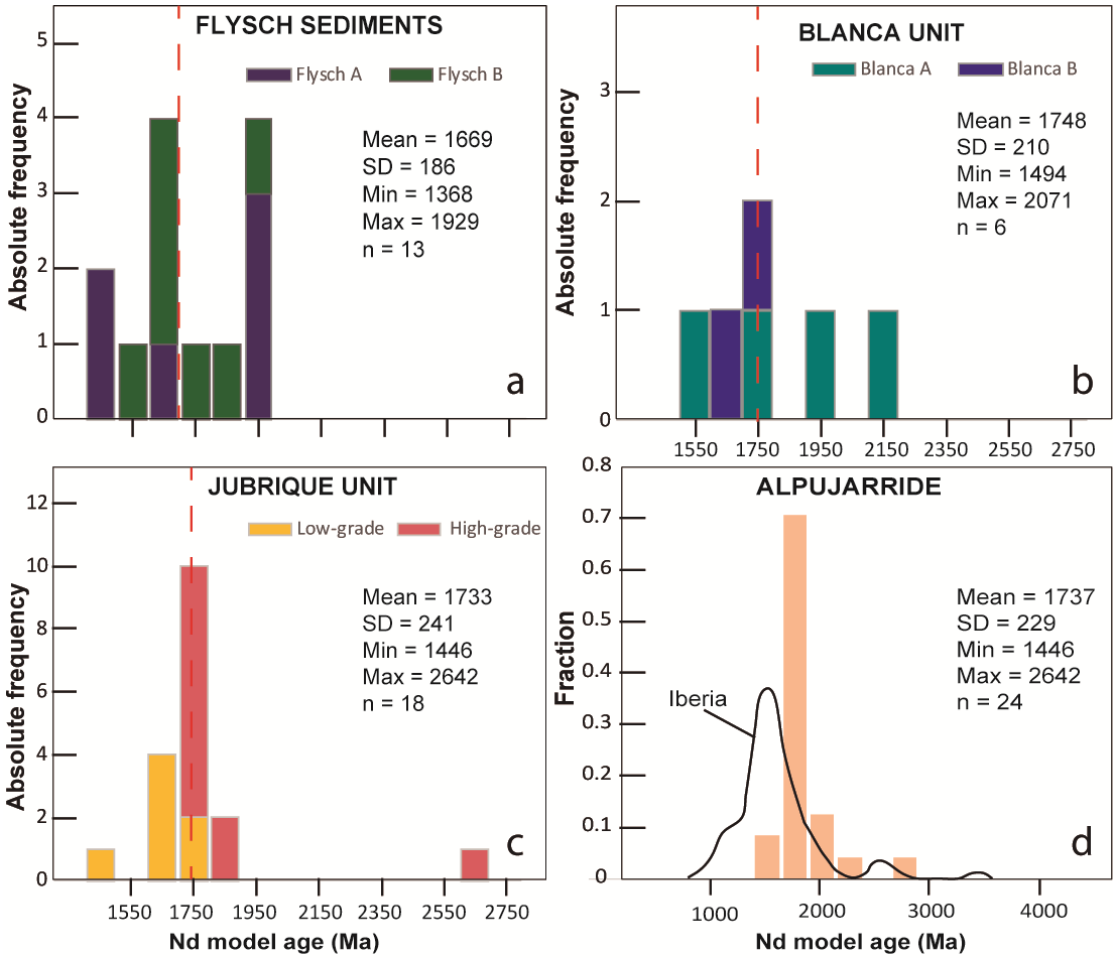

Figure 6.5 *Distribution of the Nd model ages of (a) the pre-Miocene Algeciras Flysch sediments, and the (b) Blanca and (c) Jubrique metamorphic rocks; (d) density distribution of the Nd model ages of the western Alpujárride rocks (Blanca and Jubrique samples) analyzed in this study compared to the Nd model ages density distribution of Central Iberia Zone granitic rocks (solid line) (Bea et al., 2010).*

The average Nd model age of the Flysch sediments (1.7± 0.2 Ga; Fig. 6.5a) is akin to that of the western Alpujárride crustal rocks (1.7± 0.2 Ga; Fig. 6.5c, d). Although these Nd model ages may be affected by contributions from the Neoproterozoic-Paleozoic African margins, the similarity between the Flysch and Alpujárride model ages supports a dominant detrital input from the Alborán domain. However, despite this similarity, some elemental and isotopic signatures of the pre-Miocene Algeciras Flysch sediments cannot be explained by provenance from a western Alpujárride source. The western Alpujárride rocks have higher present-day $^{87}Sr/^{86}Sr$ ratio and markedly different Pb isotopic ratios than those of the Flysch sediments (Fig. 6.4). Although these isotopic differences might be due to post-depositional contamination by relatively low radiogenic Sr from seawater (Elderfield & Schultz, 1996), this contamination would have also increased the U concentration of sediments relative to their crustal sources, but such enrichment is not observed in the Flysch sediments (Table 6.1). Thus, the sources of the pre-Miocene Algeciras Flysch sediments were likely derived from a crust similar to the western Alpujárride rocks, but with a different time-integrated isotopic evolution. Possible sources of this Flysch may be the Maláguide Complex —that formed the Paleozoic-Paleogene uppermost crust of the Alborán domain (Platt *et al.*, 2013)— or a lost realm of the Alborán domain (Martín‐Algarra *et al.*, 2000).

6.4.1.2 Provenance of the westernmost Alpujárride crustal rocks

The provenance of the Alborán domain complexes is key to understand the formation of the Betic-Rif belt (Platt *et al.*, 2013; van Hinsbergen *et al.*, 2014, and references therein). Relative to the Early Cretaceous paleogeography of the westernmost Alpine Tethys, the Alborán domain complexes have been regarded either as part of the African or the Southern Iberian margins, or as pieces of the AlKaPeCa continental domain that was placed along the northern passive margin of the Alpine Tethys (Faccenna *et al.*, 2004; Booth-Rea *et al.*, 2007; Mauffret *et al.*, 2007; Bosch *et al.*, 2011; Vergés & Fernàndez, 2012; Platt *et al.*, 2013; van Hinsbergen *et al.*, 2014). These peri-Alpine Tethyan candidates for the derivation of the Alborán domain are built upon Variscan basements with metasediments that testify their Neoproterozoic peri-Gondwanan origin (Stampfli & Hochard, 2009; Stampfli *et al.*, 2013). This provenance is well preserved in their Nd model ages and U-Pb detrital and inherited zircon ages (Stampfli & Hochard, 2009; Bea *et al.*, 2010; Esteban *et al.*, 2011; Williams *et al.*, 2012; Villaseca *et al.*, 2014).

The Jubrique and Blanca samples yield coincident average Nd model ages of 1.7 Ga, with one Jubrique paragneiss around 2.7 Ga (Fig. 6.5b, c and d), testifying a provenance from Paleoproterozoic or Archean sources with a limited contribution of post-Paleoproterozoic juvenile crustal components. These ages are, in average, older than those of the N. Africa Anti-Atlas granitoids (c. 1.0 Ga; Bea *et al.,* 2010) and those of the Central Iberian Zone (c. 1.5 Ga, with minor population at 2.6-2.7 and 3.5 Ga; Bea *et al.,* 2010) (Fig. 6.5d). On the other hand, the Jubrique and Blanca samples show Nd model ages more akin to the Pan-African granites of the Tuareg Shield (Nd model ages ~1.8–1.9 Ga, and some older values between 2.0 and 2.5 Ga; Bea *et al.,* 2010). This similarity with the Tuareg Shield is in good agreement with the assumed Neoproterozoic paleogeographic position of the Betics-Rif terranes along the northern margin of Gondwana (Stampfli *et al.*, 2013).

Despite the coincident Nd model ages of the Blanca and Jubrique units (Fig. 6.5), their distinct present-day isotopic signatures (Fig. 6.4) imply different sedimentary sources and different time-integrated evolutions. This is also supported by the inherited U-Pb zircon ages of these units. Alpine (~ 15 – 50 Ma) and Variscan (~ 280 – 320 Ma) U-Pb zircon ages are common in the Alpujárride units and are the result of the Alpine tectono-metamorphic reworking of a Variscan metamorphic, metasedimentary and anatectic basement (Platt & Whitehouse, 1999; Zeck & Williams, 2001; Acosta-Vigil *et al.*, 2014). Available U-Pb inherited and detrital zircon ages of the Torrox orthogneisses —a central Alpujárride tectonic unit equivalent to the Jubrique high-grade gneisses— are grouped into four populations: c. 2.7 Ga, 2.2 Ga – 2.0 Ga, 1.1 Ga – 0.9 Ga, and 0.8 Ga – 0.5 Ga (Zeck & Whitehouse, 1999). These ages differ from the U-Pb inherited and detrital zircon ages of the Blanca orthogneisses and metasediments (c. 624 Ma and 2.0 – 2.5 Ga) (Zeck & Whitehouse, 1999; Zeck & Williams, 2001; Esteban *et al.*, 2011).

Petrological studies are also consistent with different tectono-metamorphic evolutions for the Jubrique and Blanca units. The composition of nanogranitoid inclusions in garnet cores of the Jubrique gneisses is in agreement with garnet-present, fluid-absent melting of these rocks in an overthickened crust (P < 1.5 GPa and 800ºC) (Barich *et al.*, 2014; Barich, 2015; Acosta-Vigil *et al.*, 2016). Lu-Hf garnet ages place this event at the latest stages of the Variscan orogeny (c. 300 Ma) (Barich, 2015). In this scenario, lower-crustal melting during Variscan times may explain the high present-day $^{208}Pb/^{204}Pb$ ratios at a given $^{206}Pb/^{204}Pb$ ratio of the Jubrique mylonitic gneisses (Fig. 6.4c) by capture of monazite —a mineral with high Th/Pb ratio (Parrish, 1990)— in peritectic garnet in disequilibrium with their host rock. Anatexis of the

Blanca migmatites underlying the Ronda peridotite also occurred in the latest stages of the Variscan orogeny (~ 280 – 290 Ma) but at HT-LP conditions (T ~ 675 – 750 °C; P ~ 0.30 – 0.35 GPa) (Acosta-Vigil *et al.*, 2014), and it was triggered by delamination in an extensional tectonic setting (Acosta-Vigil *et al.*, 2014; Barich *et al.*, 2014).

Summarizing, these results point to a Neoproterozoic location of the protoliths of the Alpujárride crust in the northern margin of Gondwana. However, the Jubrique and Blanca units experienced contrasting tectonic evolutions in Variscan and pre-Variscan times, implying they have been juxtaposed after the Paleozoic and most likely during the Alpine orogeny.

The Blanca migmatites show distinct isotopic signatures. The Blanca A samples have higher present-day $^{86}Sr/^{87}Sr$ ratios, similar to the Central Iberian Zone metasediments (Villaseca *et al.*, 2014), and higher $^{206}Pb/^{204}Pb$ than Blanca B (Fig. 6.4), indicating a protolith with higher initial Rb/Sr and U/Pb ratios. These features result from the different chemical and mineralogical compositions of the analyzed Blanca samples, with Blanca A (quartz-feldspathic migmatites) akin to granitic compositions (Acosta-Vigil, 1998). Granitic melts have high Rb/Sr and U/Pb ratios (e.g., Rudnick & Gao, 2003), thus evolve towards high $^{86}Sr/^{87}Sr$ and $^{206}Pb/^{204}Pb$ ratios. Platt *et al.* (2013) suggest an affinity of the Blanca unit with the southern margin of Iberia. This affinity seems in agreement with similar Sr-Nd isotopic signatures of Blanca A and the Central Iberian Zone (Fig. 6.4a). However, the older Nd model ages (c. 1.7 Ga) and different U-Pb zircon ages (c. 624 Ma and 2.0 – 2.5 Ga) of the Blanca unit (Zeck & Whitehouse, 1999; Zeck & Williams, 2001; Esteban *et al.*, 2011) compared to the Iberian terranes (Nd model age c.1.5 Ga; U-Pb zircon ages c. 615; Bea *et al.,* 2010) (Fig. 6.5) are not totally consistent with an Iberian origin.

6.4.2 Recycling of the Alborán lower crust in the Ronda peridotite mantle

Discordant dykes of high-Mg pyroxenites have been reported in the Ronda peridotite massif (Fig. 6.1b), specifically in the garnet-spinel mylonite and spinel tectonite domains (Garrido & Bodinier, 1999; Marchesi *et al.*, 2012). These dykes were formed by high-pressure (> 1 GPa) crystallization of high-Mg-no. andesite and/or boninite melts, which commonly witness subduction initiation and/or oceanic accretion in forearc settings (Whattam & Stern, 2011, and references therein). The presence of discordant high-Mg pyroxenite dykes in the Ronda peridotite massif has been associated to a supra-subduction setting for the Alborán mantle before its final intracrustal emplacement in the Miocene (Garrido & Bodinier, 1999; Marchesi *et al.*, 2012; Hidas *et al.*, 2015). Their relatively high radiogenic $^{87}Sr/^{86}Sr$ and unradiogenic

$^{143}Nd/^{144}Nd$ ratios (Marchesi *et al.*, 2012) indicate that the parental melts of these dykes derived from a depleted mantle source metasomatized by fluids/melts of crustal rocks. Marchesi *et al.* (2012) proposed the Flysch sediments as the possible subducted contaminant involved in the genesis of the Ronda high-Mg pyroxenites dykes. The present Sr-Nd-Pb isotopic dataset of the Flysch sediments and the Alborán crustal rocks allows testing this hypothesis.

6.4.2.1 Origin of the subduction component in the Ronda high-Mg pyroxenite dykes

Fig. 6.6 compares the Sr-Nd-Pb isotopic signature of the Ronda high-Mg pyroxenite dykes calculated at 25 Ma —their estimated age of crystallization (Marchesi *et al.*, 2012)— with age-corrected isotopic signatures of the Flysch sediments and the western Alpujárride crustal rocks. Flysch sediments are too low in $^{87}Sr/^{86}Sr$ and too high in $^{206}Pb/^{204}Pb$- $^{207}Pb/^{204}Pb$ ratios to explain the initial isotopic composition of the Ronda high-Mg pyroxenite dykes (Fig. 6.6). Blanca samples can also be excluded as the possible crustal subducted component because of their high $^{206}Pb/^{204}Pb$ ratios. On the other hand, the age-corrected isotopic ratios of the Jubrique mylonitic gneisses (Fig. 6.6) make them suitable sources for the continental subduction component detected in the Ronda high-Mg pyroxenite dykes. The isotopic modeling of a mantle peridotite source metasomatized by fluids/melts derived from dehydration/melting of the Jubrique mylonitic gneisses is shown in Fig. 6.6. For the modeling we take into account the heterogeneous compositions of the Ronda peridotites and the mylonitic gneisses, together with the variability of partition coefficients at different dehydration/melting conditions for metasedimentary rocks (Johnson & Plank, 2000). Our model shows that addition to a Ronda mantle source (or to a deeper asthenospheric mantle isotopically similar to the DMM) of up to 15% of fluids/melts derived from the Jubrique mylonitic gneisses can produce the Sr-Nd-Pb isotopic signature of the Ronda high-Mg pyroxenite dykes (Fig. 6.6). The $^{208}Pb/^{204}Pb$-$^{206}Pb/^{204}Pb$ ratios of the Jubrique mylonitic gneisses are rather unique and rarely observed in crustal rocks (Fig 6.4c; c.f. Sec. 6.4.1.2). Thus, it is unlikely that another crustal source in the Alborán realm or the peri-Tethyan terranes might have produced such specific isotopic signature. In summary, the mantle source of the Ronda high-Mg pyroxenite dykes was most likely a SCLM contaminated by fluids/melts released from the dehydration/melting of lower-crustal rocks akin to the Jubrique mylonitic gneisses. Since the Jubrique mylonitic gneisses represent the Alborán lower crust now exposed above the Ronda peridotite massif (Fig. 6.1), an episode of intra-continental underthrusting in the Alborán realm must have occurred, where

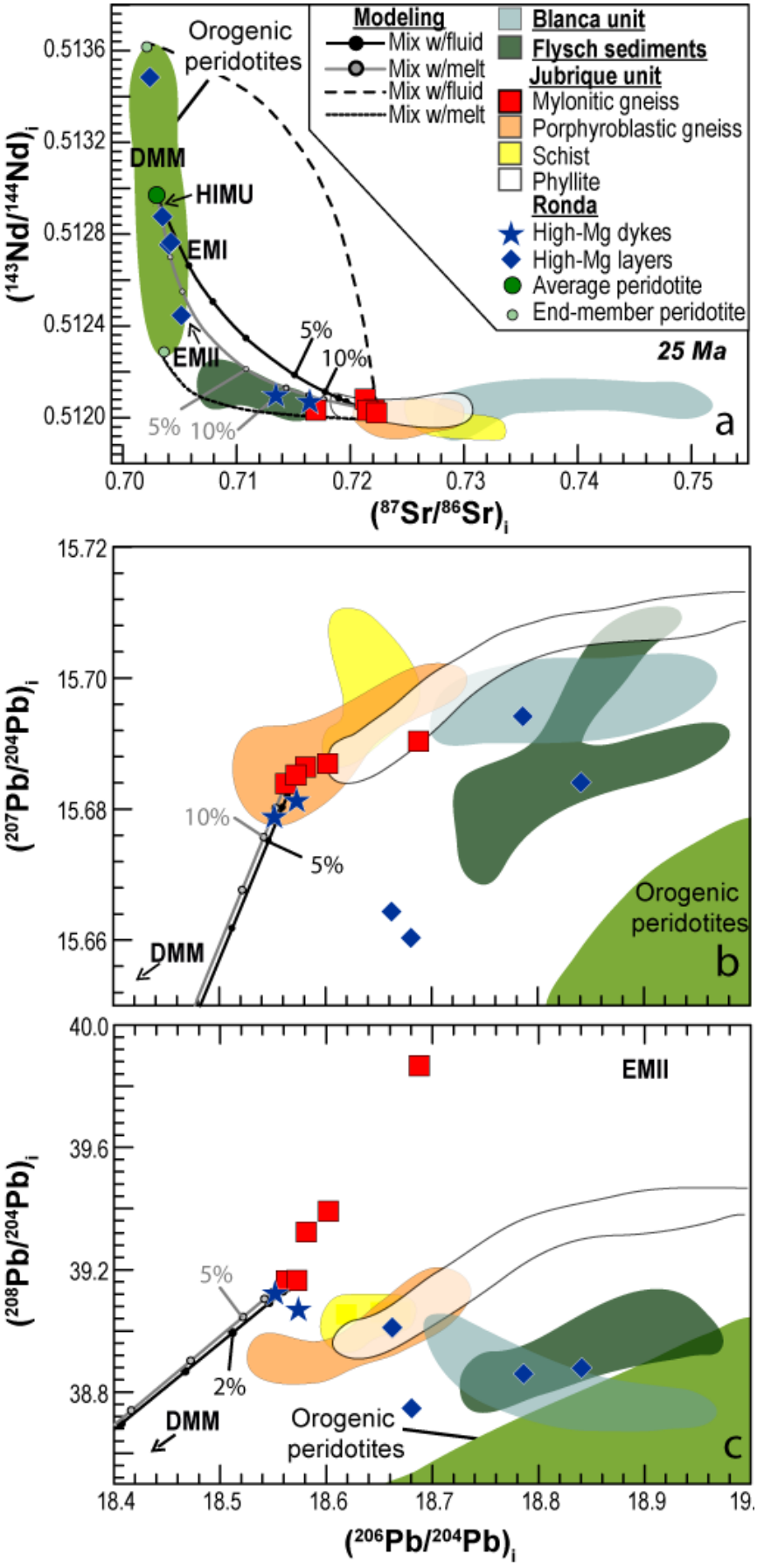
Modeling
Mix w/fluid
Mix w/melt
Mix w/fluid
Mix w/melt
Blanca unit
Flysch sediments
Jubrique unit
Mylonitic gneiss
Porphyroblastic gneiss
Schist
Phyllite
Ronda
High-Mg dykes
High-Mg layers
Average peridotite
End-member peridotite
Orogenic peridotites
DMM
HIMU
EMI
EMII
5%
10%
25 Ma
a
$(^{143}Nd/^{144}Nd)_i$
$(^{87}Sr/^{86}Sr)_i$
$(^{207}Pb/^{204}Pb)_i$
b
$(^{208}Pb/^{204}Pb)_i$
2%
c
$(^{206}Pb/^{204}Pb)_i$

the lower crust subducted below the Ronda SCLM peridotite before its Miocene intracrustal emplacement (Fig. 6.7).

6.4.2.2 Implications for the emplacement of the Ronda peridotite in the western Betics

The orogenic peridotite massifs in the western Mediterranean record a pre-Neogene complex history of crustal recycling and magmatism. Previous studies have proposed either a Mesozoic or Cenozoic age for the late tectono-magmatic evolution and intracrustal emplacement of the Betic-Rif peridotites (Platt *et al.*, 2013; van Hinsbergen *et al.*, 2014, and references therein). Mesozoic uplift and emplacement of peridotites in a passive margin extensional setting seems to be in good agreement with the Jurassic extensional event that pervasively affected the AlKaPeCa continental domain during the opening of the Piemonte-Ligurian ocean, and it is consistent with the U-Pb Jurassic ages of zircons in Ronda garnet pyroxenites (Sánchez-Rodriguez & Gebauer, 2000; van Hinsbergen *et al.*, 2014, and references therein). However, a passive margin setting is at odds with the ultra-HP origin of garnet pyroxenites (Davies *et al.*, 1993) —implying their formation in an overthickened mantle lithosphere— and their isotopic composition that reflects a subduction component derived from pelagic sediments (Pearson & Nowell, 2004). Emplacement in the Jurassic neither accounts for the late Oligocene to Miocene ages recorded in zircon rims (U-Pb) and garnets (Lu-Hf) of garnet pyroxenites from the Betic-Rif peridotites (Sánchez-Rodriguez & Gebauer, 2000; Pearson & Nowell, 2004), the pervasive Miocene resetting of U-Pb zircon ages in the crustal sections overlying and underlying the peridotites (Zeck & Williams, 2001; Platt *et al.*, 2013; Acosta-Vigil *et al.*, 2014), and the suprasubduction signature of the high-Mg pyroxenite and tholeiitic gabbro dykes cutting the Ronda peridotites (Marchesi *et al.*, 2012; Hidas *et al.*, 2015). These data are more consistent

Figure 6.6 *Plots of the age corrected (25 Ma) (a) $^{87}Sr/^{86}Sr$ vs $^{143}Nd/^{144}Nd$, (b) $^{206}Pb/^{204}Pb$ vs $^{207}Pb/^{204}Pb$ and (c) $^{206}Pb/^{204}Pb$ vs $^{208}Pb/^{204}Pb$ variations of the Flysch sediments, and the Jubrique and Blanca metamorphic rocks. Isotopic compositions of orogenic peridotites (Bodinier & Godard, 2014, and references therein) and Ronda high-Mg pyroxenites layers and dykes (Marchesi et al., 2012) are also shown. Solid lines model the mixing between an average Ronda peridotite (Lenoir et al., 2001) and a fluid (black line) or melt (grey line) released from Jubrique mylonitic gneisses at 700° and 900° C, respectively (partition coefficients from Johnson & Plank, 2000). The modeled mantle source has the average isotopic composition of orogenic peridotites (Reisberg, 1988; Reisberg et al., 1989). Labels indicate the percentages of fluid/melt contribution. Dashed lines in (a) represent mixing between Ronda peridotites —with end-member isotopic signatures from Reisberg et al. (1989) and Sr-Nd concentrations from Lenoir et al. (2001)— and fluid/melt derived from Jubrique mylonitic gneisses of extreme compositions, encompassing the whole variability of partition coefficients between fluid/melt and metasediments (Johnson & Plank, 2000) (modeling parameters are given in Table 6.3). Inset in (b) defines the enlarged area in the $^{206}Pb/^{204}Pb$-$^{207}Pb/^{204}Pb$ diagram.*

with a suprasubduction setting for the Cenozoic evolution of the westernmost Alborán domain (Fig. 1.11) (Royden, 1993; Faccenna *et al.*, 2004; Booth-Rea *et al.*, 2005) and the Ronda peridotite in the westernmost Mediterranean (Fig. 6.7).

Garrido *et al*. (2011) proposed that southward to westward retreat of the African slab during the Oligocene-early Miocene accounts for the intense back-arc lithosphere extension (Royden, 1993; Faccenna *et al*., 2004; Booth-Rea *et al*., 2007) and the development of the Ronda peridotite extensional shear zone, coeval with extreme thinning of the Alborán overlying crust (Fig. 6.7). Hidas *et al*. (2013) proposed that inversion of this back-arc basin in the late Oligocene-early Miocene resulted in km-scale folding and shearing of the attenuated Ronda SCLM peridotite (Fig. 6.7b; c.f. Sec. 1.4.4). These events led to a subduction initiation that ended in the earliest Miocene intracrustal emplacement of the massif into the Alborán wedge

Table 6.3 Parameters of mixing models for high-Mg pyroxenites

Solid line models	**Average peridotite source**[a]	**Fluid source (JU10)**	**Melt source (JU9)**	**D metasediment/ fluid (700 °C)**[b]	**D metasediment/ melt (900 °C)**[b]
Sr (ppm)	4.7	153	76	0.91	1.2
Nd (ppm)	0.27	38.5	32.5	1.4	1.5
Pb (ppm)	0.081	19.8	16.0	0.94	1.3
$^{87}Sr/^{86}Sr_{(25\ Ma)}$	0.70298	0.72151	0.72209		
$^{143}Nd/^{144}Nd_{(25\ Ma)}$	0.51297	0.51203	0.51203		
$^{206}Pb/^{204}Pb_{(25\ Ma)}$	18.1893	18.5722	18.5626		
$^{207}Pb/^{204}Pb_{(25\ Ma)}$	15.5366	15.6852	15.6839		
$^{208}Pb/^{204}Pb_{(25\ Ma)}$	38.080	39.1645	39.1640		
Lower dashed line model	**Peridotite source (RX31)**[c]		**Melt source (JU21)**		**D metasediment/ melt (900 °C)**[b]
Sr (ppm)	4.1		126		1.2
Nd (ppm)	0.11		38.0		1.5
$^{87}Sr/^{86}Sr_{(25\ Ma)}$[d]	0.70344		0.72305		
$^{143}Nd/^{144}Nd_{(25\ Ma)}$[d]	0.51228		0.51199		
Upper dashed line model	**Peridotite source (RX42)**[c]	**Fluid source (JU12)**		**D metasediment/ fluid (650 °C)**[b]	
Sr (ppm)	1.9	106		0.42	
Nd (ppm)	0.17	15.9		3.6	
$^{87}Sr/^{86}Sr_{(25\ Ma)}$[d]	0.70208	0.72230			
$^{143}Nd/^{144}Nd_{(25\ Ma)}$[d]	0.51363	0.51202			

[a] *Average Sr-Nd-Pb of peridotites from the Ronda massif (Lenoir et al., 2001) and average isotopic composition of orogenic peridotites (Bodinier & Godard, 2014, and references therein).* [b] *Johnson and Plank (1999).* [c] *Lenoir et al. (2001).* [d] *Reisberg et al. (1989)*

(Fig. 6.7b). Folding of the SCLM (Hidas *et al*., 2013) may explain how lower crustal units currently overlying the Ronda massif (i.e., Jubrique mylonitic gneisses), could have underthrusted the peridotites (Fig. 6.7b). Doin & Henry (2001) suggested that during subduction initiation, the SCLM accommodates convergence by bending and the upper lithosphere indents at the level of its weakest layer, leading to decoupling of the lower continental crust, which is then subducted below the mantle. In this context, the age-corrected (25 Ma) isotopic signatures of the Jubrique lower-crustal rocks (Fig. 6.6) show that Ronda high-Mg pyroxenite dykes can be accounted for by flux melting of hot, attenuated back-arc mantle induced by fluids/melts from the underthrusted Alpujárride lower crust (Fig. 6.7b, stage B1). As shown by numerical models (Jammes & Huismans, 2012), upon subsequent inversion of extension, the exhumed SCLM and upper crustal levels are incorporated into the fold-thrust belt. Hence, as subduction progressed in the westernmost Mediterranean, the thinned SCLM could be emplaced over the foreland (Fig. 6.7b, stage B2).

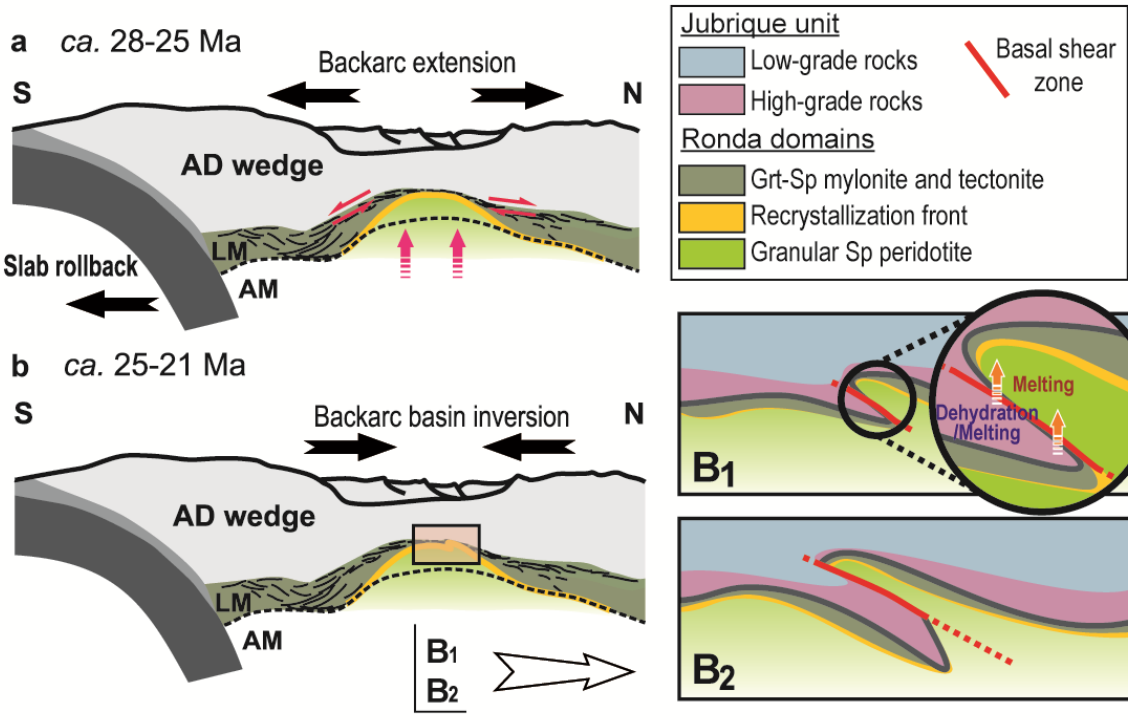

Figure 6.7 *(a) North–south cross-section for the late Oligocene back-arc extension referring to partial melting at the base of the lithosphere induced by asthenospheric upwelling. AM: asthenospheric mantle; LM: lithospheric mantle. (b) Proposed scenario in a north–south cross-section for the late Oligocene–early Miocene back-arc basin inversion that led to km-scale folding, shown in detail in B1 and B2 (area outlined). B1: Subduction initiation of the lower crust followed by dehydration/melting of the crustal slab, and subsequent melting of the contaminated subcontinental mantle. B2: emplacement of the SCLM into the crust. The Ronda structural domains are from Lenoir et al. (2001).*

6.4.3 Involvement of the Alpujárride crustal rocks and Flysch sediments in the Neogene volcanism of the Alborán Sea region

The Neogene construction and tectono-magmatic evolution of the Alborán Sea basin was associated with tholeiitic to calc-alkaline volcanism (Turner *et al.*, 1999; Duggen *et al.*, 2004; Gill *et al.*, 2004; Duggen *et al.*, 2008). LREE-depleted tholeiitic and LREE-enriched calc-alkaline volcanism occurred in the central part and along the continental margins of the Alborán Sea basin, respectively (Fig. 6.1a) (Duggen *et al.*, 2008). LREE-depleted tholeiitic volcanism has been intepreted by Duggen *et al.* (2008) as the result of high degrees of partial melting of a depleted mantle source triggered by the influx of hydrous fluids released from subducted oceanic lithosphere, and the LREE-enriched calc-alkaline volcanism as the result of lower degrees of mantle partial melting and/or crustal assimilation of the Alborán metamorphic basement. These authors modeled the role of subducted sediments and assimilation of the Alborán metamorphic basement using a limited isotopic dataset of drilled Alborán Sea basement rocks (Soto & Platt, 1999) and the average global subducted sediments (GLOSS). The new Sr-Nd-Pb isotopic dataset of the Alborán continental crust and the Flysch sediments presented in this study allows us to test in more detail the involvement of these sources in the genesis of the Neogene volcanism in the Alborán region.

6.4.3.1 Source of the Sr-Nd-Pb crustal signature of Neogene volcanism in the Alborán Sea basin

To assess the role of the Alborán continental crust and the Flysch sediments in crustal assimilation and source enrichment in the Neogene Alborán Sea volcanism, we compared published isotopic data of these volcanic rocks (Duggen *et al.*, 2004; Gill *et al.*, 2004; Duggen *et al.*, 2008) with the compositions of our samples. Data were corrected at 10 Ma, which is the average age of volcanism in this area (e.g., Turner *et al.*, 1999; Duggen *et al.*, 2004; Gill *et al.*, 2004) (Figs. 6.8 & 6.9).

Duggen *et al.* (2008) proposed that addition of < 1% of hydrous fluids derived from the GLOSS to a MORB source may explain the isotopic signature of the LREE-depleted tholeiitic lavas. Our isotopic modeling rules out this hypothesis because it leads to $^{206}Pb/^{204}Pb$ ratios much greater than those of the LREE-depleted lavas (not shown). From the Eocene to Burdigalian times, the Flysch sediments were deposited in a foredeep basin of the Alpine Tethys (Guerrera *et al.*, 2005; Crespo-Blanc & de Lamotte, 2006; Luján *et al.*, 2006) (c.f. Sec. 1.4.4); hence the Flysch sediments are potential candidates to account for the subducted sediment signature

observed in the mantle source of the Neogene Alborán lavas. Fig. 6.8 illustrates the results of an isotopic mixing model where melting of a mantle source metasomatized by the addition of < 2% of fluids/melts from Flysch B sediments explains the Sr-Nd-Pb isotopic signatures of the LREE-depleted volcanism (for additional information on the modeling see figure caption). In agreement with Duggen *et al.* (2008), the present modeling also excludes assimilation of western Alpujárride crustal rocks for the LREE-depleted lavas.

Based on their Sr-Nd isotopic signature, Duggen *et al.* (2008) further classified the LREE-enriched lavas into two groups, which will be referred here as Group I and II. Group I shows higher $^{143}Nd/^{144}Nd$ (> 0.5224) and lower $^{87}Sr/^{86}Sr$ (< 0.710) ratios than Group II (Fig. 6.8a). In addition, the compilation of available Pb isotopic data (Duggen *et al.*, 2004; Gill *et al.*, 2004) shows that Group I lavas have generally lower $^{206}Pb/^{204}Pb$ (< 18.83) ratios than Group II (Fig. 6.8b, c). The Sr-Nd isotopic signature of Group I and Group II lavas can be explained by addition of 2 – 5% and 20 – 50% of fluid/melt, respectively, from Flysch B sediments to a DMM source (Fig. 6.8a).

The high percentages of fluids/melts required to explain the Sr-Nd isotopic signature of the Group II lavas are highly unlikely, thus another process and/or a different mantle source must be involved. To account for the Sr-Nd signature of the Group II lavas, Duggen *et al.* (2008) proposed crustal contamination of either a LREE-depleted or a LREE-enriched parental magma. To test these hypotheses, we modeled in Fig. 6.9 different scenarios of crustal assimilation of Jubrique rocks, which are similar to the continental basement of the Alborán Sea basin (Soto & Platt, 1999). Blanca samples were excluded because their extremely radiogenic present-day Sr ratios preclude them as a potential crustal contaminant (Fig. 6.4a). Assuming lavas with a mantle source similar to those of the LREE-depleted or Group I LREE-enriched lavas (a DMM metasomatized by different amounts of fluids/melts from Flysch B; Fig. 6.8), assimilation of relatively high amounts (~ 15 – 40%) of the Alpujárride basement rocks might account for the Sr-Nd isotopic signature of Group II lavas (Fig. 6.9a); however, these models do not explain their high $^{206}Pb/^{204}Pb$ ratios (Fig. 6.9b, c). Alternatively, Group II lavas may derive from a DMM source metasomatized by older Flysch A sediments and assimilation of the Alborán crustal basement. This scenario is only feasible if assimilation involved crustal rocks similar to the Jubrique upper crust phyllites (Fig. 6.9). This model nicely accounts for the linear trends of Group II lavas in the Pb isotopic diagrams (Fig. 6.9b, c).

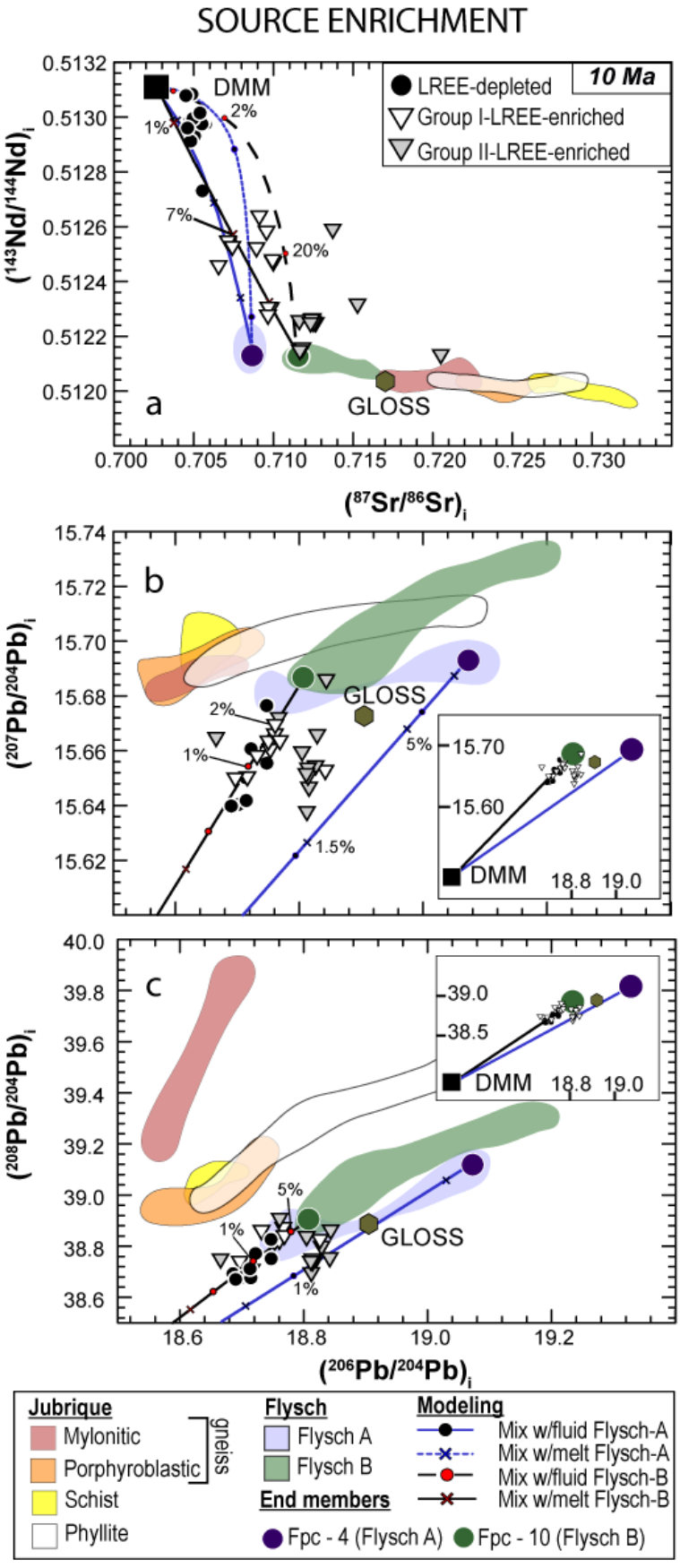
SOURCE ENRICHMENT
LREE-depleted
Group I-LREE-enriched
Group II-LREE-enriched
10 Ma
DMM
2%
1%
7%
20%
GLOSS
a
$(^{143}Nd/^{144}Nd)_i$
$(^{87}Sr/^{86}Sr)_i$
b
$(^{207}Pb/^{204}Pb)_i$
5%
1.5%
c
$(^{208}Pb/^{204}Pb)_i$
$(^{206}Pb/^{204}Pb)_i$
Jubrique
Mylonitic
Porphyroblastic
Schist
Phyllite
gneiss
Flysch
Flysch A
Flysch B
End members
Fpc - 4 (Flysch A)
Fpc - 10 (Flysch B)
Modeling
Mix w/fluid Flysch-A
Mix w/melt Flysch-A
Mix w/fluid Flysch-B
Mix w/melt Flysch-B

6.4.3.2 Origin of the Neogene volcanism in the Alborán region by eastward subduction of the Paleo-Tethys

Geophysical images of the upper mantle beneath the westernmost Mediterranean confirm the role of slab rollback and tearing of the continental margins in the Neogene evolution of the Alborán Sea basin and the Betic-Rif belt (Wortel & Spakman, 2001; Mancilla *et al.*, 2015; Villaseñor *et al.*, 2015). Fig. 6.10 illustrates the current structure of the Alborán Sea basin. Subducted oceanic —still attached to the surface along the Gibraltar Arc– and extended continental lithospheres occur beneath the Alborán Sea basin, coeval with tearing of the slab at the South Iberian and Maghrebian continental margins. Slab-tearing initiated in the east and propagated to the west, accompanying the westward slab rollback and possibly producing lower crustal edge delamination under the eastern Betics (Mancilla *et al.*, 2015). Marine magnetotelluric studies have revealed the presence of two conductive features above the subducted oceanic crust that indicate the presence of fluids released by the subducting slab and/or a small amount of partial melt in the upper mantle (Garcia *et al.*, 2015) (Fig. 6.10). The upper mantle structure during the Neogene volcanism may have changed due to the c. 200 – 700 km westward rollback migration of the Alborán Sea basin between the late Burdigalian to late Tortonian (~ 16 to 8.5 Ma) (Faccenna *et al.*, 2004; Balanyá *et al.*, 2007; Booth-Rea *et al.*, 2007). We propose that the easternmost conductive feature is a remnant of water-present —and likely decompression— melting of the mantle wedge contaminated by subducted Flysch B sediments, which generated the LREE-depleted tholeiitic lavas that crop in a triangular area in the central and eastern Alborán basin (e.g., Duggen *et al.*, 2008). The top of this triangular area in the center of the Alborán basin coincides with the transition from the foredeep thicker crust in the western Alborán basin to thinner arc-like crust in the east Alborán basin (Fig. 6.10). The absence of assimilation of the Alborán Sea continental basement in the Sr-Nd-Pb isotopic

Figure 6.8 *Plots of the age corrected 10 Ma (a) $^{143}Nd/^{144}Nd$ vs. $^{87}Sr/^{86}Sr$, (b) $^{206}Pb/^{204}Pb$ vs. $^{207}Pb/^{204}Pb$ and (c) $^{206}Pb/^{204}Pb$ vs. $^{208}Pb/^{204}Pb$ variations of LREE-depleted and LREE-enriched lavas of the Alborán Sea Basin (Duggen et al., 2004; Gill et al., 2004; Duggen et al., 2008), Flysch sediments, and crustal rocks from the Jubrique unit. Solid and dashed lines are the result of modeling a DMM source (Salters & Stracke, 2004; Workman & Hart, 2005) enrichment by a melt or a fluid released from Flysch A (blue line) and Flysch B sediments (black line) at 900 °C and 700 °C, respectively (partition coefficients from Johnson and Plank, 2000). Partition coefficients were selected on the basis that Sr/Nd ratio of the fluids are 50 times higher than for the bulk melt (e.g., Duggen et al., 2008). Labels indicate the percentages of fluid/melt contribution. As end members we selected the FPC4 and FPC10 samples as representative of the Flysch A and Flysch B sediments, respectively. Also shown for comparison is the average global subducting sediment (GLOSS) from Plank and Langmuir (1998). Geochemical modeling parameters are given in Table 6.4. Inset in (b) and (c) defines the enlarged area in the $^{207-206}Pb/^{204}Pb$ and $^{208-206}Pb/^{204}Pb$ diagrams, respectively.*

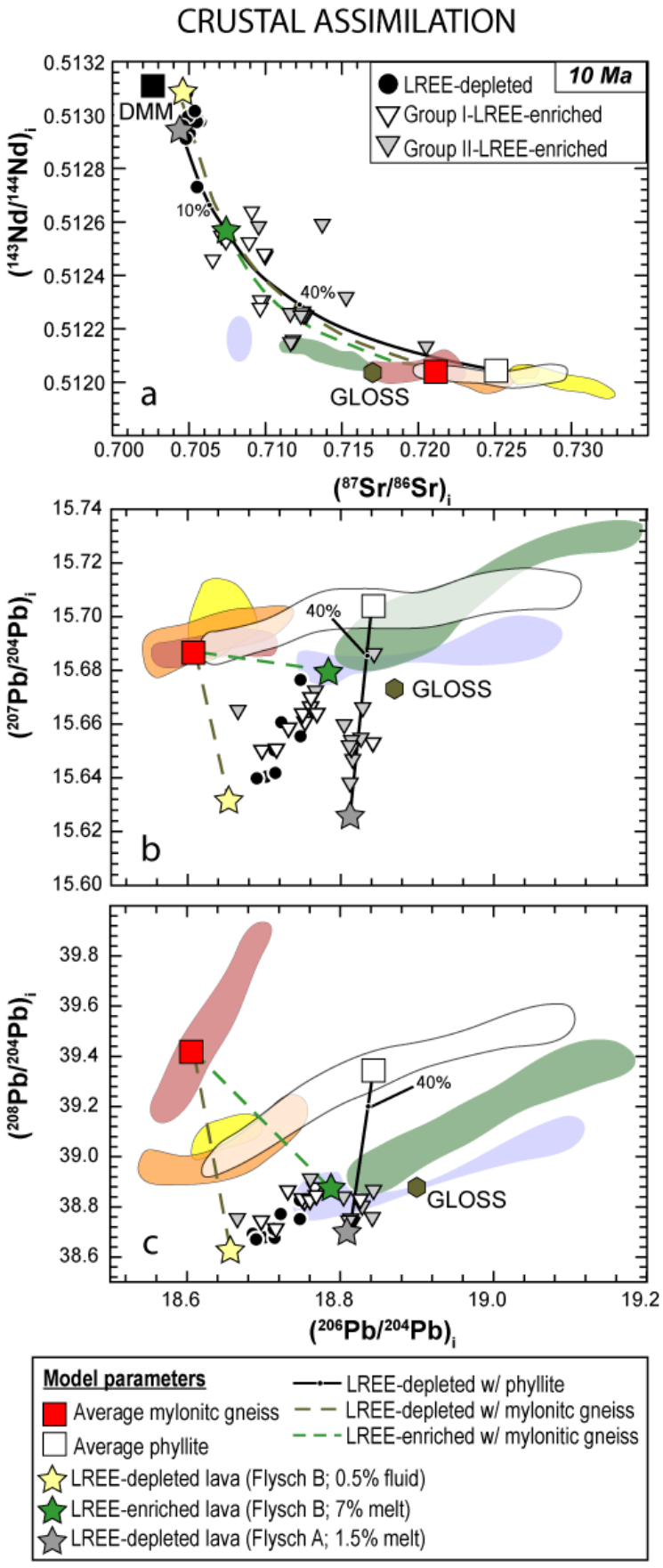
CRUSTAL ASSIMILATION
10 Ma
LREE-depleted
Group I-LREE-enriched
Group II-LREE-enriched
DMM
10%
40%
GLOSS
a
$(^{143}Nd/^{144}Nd)_i$
$(^{87}Sr/^{86}Sr)_i$
b
$(^{207}Pb/^{204}Pb)_i$
c
$(^{208}Pb/^{204}Pb)_i$
$(^{206}Pb/^{204}Pb)_i$
Model parameters
Average mylonitc gneiss
Average phyllite
LREE-depleted lava (Flysch B; 0.5% fluid)
LREE-enriched lava (Flysch B; 7% melt)
LREE-depleted lava (Flysch A; 1.5% melt)
LREE-depleted w/ phyllite
LREE-depleted w/ mylonitc gneiss
LREE-enriched w/ mylonitic gneiss

Table 6.4 Parameters for source enrichement for Alboran Sea basin lavas

Source enrichment parameters	**DMM**[a]	**Fluid (dashed blue line) and melt (solid blue line) source FPC4 (Flysch A)**	**Fluid (dashed blak line) and melt (solid black line) source FPC10 (Flysch B)**	**D metasediment/ fluid (700 °C)**[b]	**D metasediment/ melt (900 °C)**[b]
Sr (ppm)	7.7	267	150	0.42	1.2
Nd (ppm)	0.58	12.3	14.3	3.6	1.5
Pb (ppm)	0.018	3.2	8.7	0.94	1.3
$^{87}Sr/^{86}Sr_{(10\ Ma)}$	0.702627	0.708684	0.711464		
$^{143}Nd/^{144}Nd_{(10\ Ma)}$	0.513114	0.512127	0.512139		
$^{206}Pb/^{204}Pb_{(10\ Ma)}$	18.2579	19.0734	18.8068		
$^{207}Pb/^{204}Pb_{(10\ Ma)}$	15.4852	15.6928	15.6866		
$^{208}Pb/^{204}Pb_{(10\ Ma)}$	37.8860	39.1194	38.9055		

[a] *Sr-Nd-Pb concentrations and isotopic composition of DMM from Workman & Hart, 2005 and Salters & Stracke, 2004.* [b] *Johnson and Plank (1999).*

Figure 6.9 *Plots of the age-corrected 10 Ma (a) $^{143}Nd/^{144}Nd$ vs. $^{87}Sr/^{86}Sr$, (b) $^{206}Pb/^{204}Pb$ vs. $^{207}Pb/^{204}Pb$ and (c) $^{206}Pb/^{204}Pb$ vs. $^{208}Pb/^{204}Pb$ variations of LREE-depleted and LREE-enriched lavas of the Alborán Sea Basin (Duggen et al., 2004; Gill et al., 2004; Duggen et al., 2008), Flysch sediments, and crustal rocks from Jubrique unit. The solid black line models the contamination of a LREE-depleted A lava caused by assimilation of a crustal component similar to the average Jubrique phyllites, whereas dashed lines model crustal contamination of a LREE-depleted B (dark-yellow line) lava and a LREE-enriched lava (green line) by a crustal component similar to the average Jubrique mylonitic gneisses. Crustal assimilation was modeled using the excel program of Ersoy & Helvacı (2010). Labels indicate the percentages of crustal assimilation. Geochemical modeling end members are: the LREE-depleted A lava (gray star) with the trace element composition of sample ALB-01 from Duggen et al. (2008), and the isotope composition of a DMM enriched by 1.5% of melt derived from Flysch A (this study); the LREE-depleted B (yellow star) and LREE-enriched lavas (green star), which are modeled isotopically as the DMM enriched by 0.5% of fluid and 7% of melt, respectively, derived from Flysch B (see Fig. 6.8), and with trace elements from samples AlB-01 and 7519 from Duggen et al. (2008), respectively. Fields as in Fig. 6.7. Geochemical modeling parameters are given in Table 6.5.*

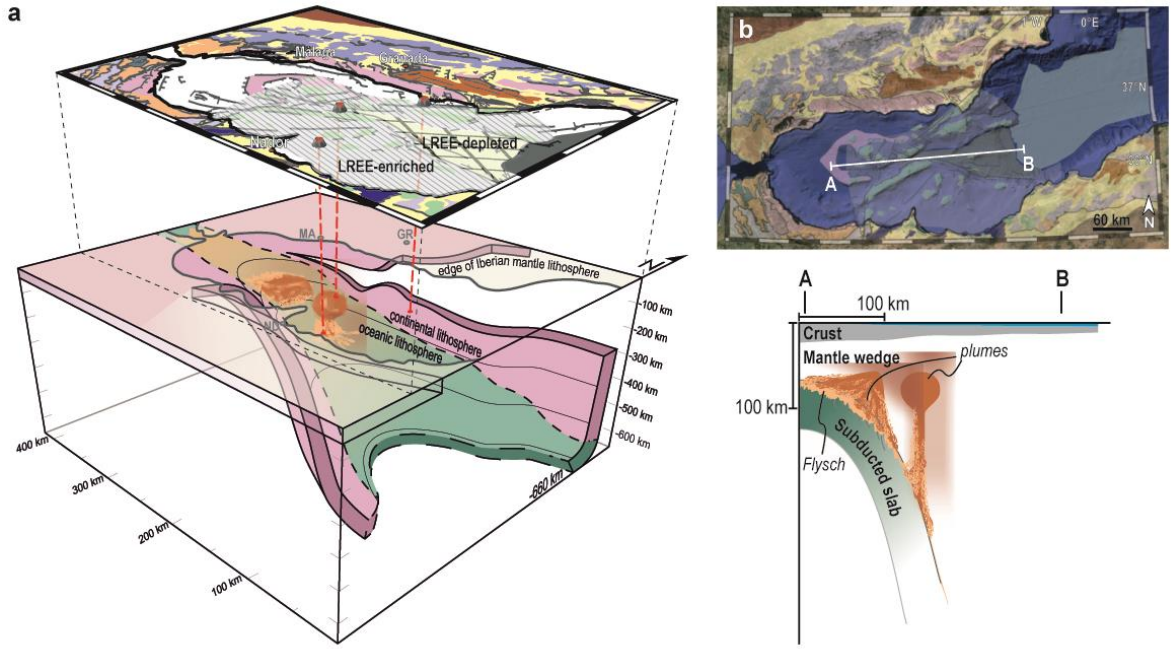

Figure 6.10 *(a) Conceptual 3D model of the Western Mediterranean. See text for more details. MA: Malaga; GR: Granada, and ND: Nador. (b) E-W cross-section that shows the structure of the mantle wedge beneath the Alborán Sea basin. Geological map is modified after Booth-Rea et al. (2007), the LREE-enriched and LREE-depleted areas are taken from Duggen et al. (2008), and the cartoon of the low resistivity areas are estimated based on magnetotelluric marine studies (Garcia et al., 2015). Satellite image from Google Earth Professional ™.*

signature of the LREE-depleted tholeiitic lavas (Fig. 6.9) implies that most of the crust in the eastern Alborán basin was newly accreted by this tholeiitic magmatism. On the other hand, the Sr-Nd-Pb isotopic signature of the LREE-enriched lavas (Figs. 6.8 & 6.9) located at the margins of the Alborán Sea basin suggests a mantle source metasomatized by variable Flysch sediments (Flysch A and B) and, in Group II LREE-enriched lavas, assimilation of the upper Alborán continental crust. The lack of Alborán lower crust involvement in the genesis of the LREE-enriched lavas (Fig. 6.9) supports a possible lower-crustal delamination of the South Iberian margin under the southeastern Betics and the northern margin of the Eastern Alborán basin. This is also supported by the upper-crustal nature of the subducted South Iberian domain rocks, now exhumed by extensional detachments in the core of the Betics (Booth-Rea *et al.*, 2015; Mancilla *et al.*, 2015).

Table 6.5 Parameters of crustal contamination for Alborán Sea basin lavas

Solid line model	**LREE-depleted A lava (isotopes: DMM + 1.5% melt from Flysch A; trace elements of sample ALB-1 from Duggen et al. 2008)**	**Average Jubrique phyllites (black line)**	
Sr (ppm)	104	94	
Nd (ppm)	4.7	19	
Pb (ppm)	2.9	16	
$^{87}Sr/^{86}Sr_{(10\ Ma)}$	0.704453	0.725054	
$^{143}Nd/^{144}Nd_{(10\ Ma)}$	0.512935	0.512043	
$^{206}Pb/^{204}Pb_{(10\ Ma)}$	18.813	18.8402	
$^{207}Pb/^{204}Pb_{(10\ Ma)}$	15.626	15.7017	
$^{208}Pb/^{204}Pb_{(10\ Ma)}$	38.725	39.2793	
Dashed line models	**LREE-depleted B lava (isotopes: DMM + 0.5% fluid from Flysch B; trace elements of sample ALB-1 from Duggen et al. 2008)**	**LREE-enriched B lava (isotopes: DMM + 7% melt from Flysch B; trace elements of sample 7519 from Duggen et al. 2008)**	**Average Jubrique Mylonitic gneisses**
Sr (ppm)	104	298	150
Nd (ppm)	4.7	15	28
Pb (ppm)	2.9	3.5	18
$^{87}Sr/^{86}Sr_{(10\ Ma)}$	0.704305	0.707444	0.720970
$^{143}Nd/^{144}Nd_{(10\ Ma)}$	0.513082	0.512569	0.512053
$^{206}Pb/^{204}Pb_{(10\ Ma)}$	18.6542	18.7881	18.6099
$^{207}Pb/^{204}Pb_{(10\ Ma)}$	15.6306	15.6797	15.6870
$^{208}Pb/^{204}Pb_{(10\ Ma)}$	38.6221	38.8708	39.4181

Part III

Conclusions

7 Conclusions

The main objective of this thesis is to shed new light on the role of melt-rock reaction processes and recycling of oceanic and continental crustal material in creating chemical heterogeneities in the Earth's mantle. To achieve this objective, we carried out a detailed geochemical study of mantle rocks exposed in orogenic peridotites from the Betic-Rif Cordillera in the westernmost Mediterranean and their allied crustal rocks. Two processes responsible for the development of geochemical heterogeneities in the Earth's upper mantle are addressed in this thesis: (i) the formation of secondary lherzolites by melt-rock reaction processes, and (ii) the genesis of ultra-high pressure (UHP) garnet pyroxenites and its implications for crustal recycling into the Earth's mantle. Furthermore, (iii) to investigate the role of crustal recycling into the Earth's mantle on the isotopic signature of subduction magmatism, this thesis explores to what extent subduction of Betic crustal rocks (western Alpujárride complex and pre-Miocene Flysch Trough units) was involved in the geochemical signature of magmatism occurring in subcontinental lithospheric mantle (SCLM) peridotites of the Ronda massif, and in the Miocene Alborán Sea basin volcanism.

In Ch. 4 of this thesis, we investigate the role of melt-rock reaction processes in the generation of secondary lherzolites in the SCLM. This study shows that peridotites from the four tectono-metamorphic domains of the Beni Bousera orogenic massif (garnet-spinel mylonite, Ariègite, Ariègite-Seiland and Seiland domains) have overlapping bulk rock and mineral compositions and show covariation trends between major and minor elements classically interpreted as due to partial melting. In this scenario, the composition of most harzburgites can be explained by melt extraction up to 30% at pressures < 3 GPa, and cryptic metasomatism as evidenced in the clinopyroxene trace element budgets. On the other hand, a more detailed inspection of geochemical variations in lherzolites reveals that they are generally inconsistent with melting models in the spinel and garnet peridotite facies. Major elements in bulk rock and minerals, and trace elements in clinopyroxene indicate that garnet-spinel mylonite lherzolites were largely affected by tectonic mixing and subsolidus re-

equilibration with garnet pyroxenites, which obscured the record of primary igneous processes. Lherzolites in the rest of the massif mostly show the compositional imprints of two types of melt-rock reaction between evolved melts and a depleted peridotite protolith (Mg-no. ~ 91, olivine ~ 70%, clinopyroxene/orthopyroxene = 0.4). Groups I and II lherzolites, which are distributed in all the domains, were produced by clinopyroxene and orthopyroxene precipitation and olivine dissolution at melt/rock ratios < 0.75, and mass ratio between crystallized minerals and infiltrated melt (*R*) ranging from 0.13 to 1.20. Group III lherzolites, which mostly crop out in the Ariègite-Seiland and Seiland domains, resulted from orthopyroxene dissolution and crystallization of clinopyroxene and olivine at melt/rock ratios ≤ 1 and $R = 0.2 – 0.3$. The relatively homogeneous distribution of Groups I and II lherzolites in the whole massif supports the occurrence of a widespread refertilization event prior to the differentiation of the Beni Bousera mantle section into four petro-structural domains. On the other hand, the predominance of Group III lherzolites in the Ariègite-Seiland and Seiland domains supports that these rocks were formed by later refertilization reactions associated with the development of the tectono-metamorphic domains. The late genesis of Group III lherzolites suggests that their protolith may have been a previously refertilized Group I lherzolite.

Despite robust isotopic evidence for the presence of recycled crustal lithologies in the Earth's mantle, the nature, mechanisms, length scales and extent to which different recycled crustal components are mixed in the mantle are still not fully understood. UHP garnet pyroxenites in orogenic peridotite massifs have isotopic compositional variations similar to the recycled oceanic crustal component commonly observed in oceanic basalts. These pyroxenites hence provide an exceptional opportunity to investigate *in situ* the nature and scale of the Earth's mantle compositional heterogeneities. The second aim of this thesis was to constrain the genesis of UHP garnet pyroxenites and their bearings on crustal recycling into the Earth's mantle. To achieve this objective, we performed an integrated geochemical study of UHP garnet pyroxenites from the Ronda and Beni Bousera peridotite massifs presented in Ch. 5. This investigation encompasses, in the same sample, bulk rock major and trace elements, as well as Sr-Nd-Pb-Hf isotopic analyses. According to their Al_2O_3 content, we classify UHP garnet pyroxenites into three groups that have diverse trace elements and Sr-Nd-Pb-Hf isotopic signatures. *Group A pyroxenites* (Al_2O_3: 15 – 17.5 wt. %) mostly have REE

patterns depleted in LREE relative to MREE, nearly flat segments for HREE, and elevated Eu_N/Eu^* ratios (1 – 1.2). They are characterized by low initial $^{87}Sr/^{86}Sr$, relatively high $^{143}Nd/^{144}Nd$, $^{206}Pb/^{204}Pb$ and $^{176}Hf/^{177}Hf$ ratios, and highly variable $^{207}Pb/^{204}Pb$ and $^{208}Pb/^{204}Pb$ ratios. *Group B pyroxenites* (Al_2O_3 < 13.7 wt. %) are depleted in LREE and MREE relative to HREE, show MORB-like patterns, and moderate to elevated Eu_N/Eu^* ratios (0.6 – 1.2). Their isotopic signature is characterized by relatively high initial $^{87}Sr/^{86}Sr$ and low $^{143}Nd/^{144}Nd$, $^{206}Pb/^{204}Pb$ and $^{176}Hf/^{177}Hf$ ratios. *Group C pyroxenites* (Al_2O_3 ~ 15 wt. %) are depleted in LREE relatively to MREE, and have moderate to elevated Eu_N/Eu^* ratios (1– 1.4). They display relatively low initial $^{87}Sr/^{86}Sr$ and $^{206}Pb/^{204}Pb$ ratios, high $^{143}Nd/^{144}Nd$ and $^{176}Hf/^{177}Hf$ ratios, and $^{207}Pb/^{204}Pb$ and $^{208}Pb/^{204}Pb$ ratios similar to Group B pyroxenites.

The major and trace element, and isotopic compositions of Ronda and Beni Bousera UHP garnet pyroxenites lend support to the marble cake hypothesis whereby these pyroxenites represent straps of ancient, recycled oceanic crust intimately mixed with mantle peridotites by mantle convection processes. The present study reveals, however, that besides this exotic component of ancient recycled oceanic crust, the genesis of these pyroxenites requires a previously unnoticed component of recycled lower continental crust. The latter is akin to the lower crustal section of the lithosphere where these UHP garnet pyroxenites now reside in. This result strongly suggests a genetic link between the source of Group B garnet pyroxenites, and the lower continental crust of the same lithospheric section than the pyroxenites. The results of this study hence provide a new recipe for the marble cake hypothesis for the genesis of UHP garnet pyroxenites in orogenic peridotites. Furthermore, it establishes an unprecedented connection between the composition of the continental crust and the generation of Earth's mantle heterogeneities.

Finally, the geochemical study of the Betic crustal rocks presented in this thesis (Ch. 6) has allowed us to draw important conclusions about their evolution and role in the genesis of Cenozoic magmatism in the westernmost Mediterranean. The isotopic signature and Nd model ages of the pre-Miocene Algeciras Flysch reveal an increasing detrital input from the Alborán crust to the sedimentary basin in the late Oligocene. The Jubrique and Blanca metamorphic rocks in the western Alpujárride complex have an average Nd model age of ~ 1.7 Ga, which indicates derivation from Paleoproterozoic crustal sources and a limited contribution of younger crustal components. Such as old Nd model ages are different from

those of the Central Iberian Zone and are similar to those of the Tuareg shield, which is in good agreement with the Neoproterozoic paleogeographic position of the Betic-Rif-Kabylides terranes along the northern margin of Gondwana. Despite these similar Nd model ages, the distinct isotopic signatures of the Jubrique and Blanca units entail different sources and contrasted Variscan and pre-Variscan tectono-magmatic evolutions, suggesting that these crustal units were juxtaposed after Paleozoic times.

The crustal component in the mantle source of the late Oligocene high-Mg pyroxenite dykes in the Ronda peridotites derived from continental crustal rocks similar to the Jubrique mylonitic gneisses. Since these gneisses represent the Alborán lower crust now exposed on top of the Ronda peridotite massif, this result reveals an episode of intra-continental subduction of the lower crust beneath the Ronda peridotites before their Miocene intracrustal emplacement. The isotopic signature of the Neogene LREE-depleted tholeiitic and LREE-enriched calc-alkaline volcanism in the Alborán Sea basin may be explained by enrichment of the mantle source through dehydration/melting of the subducted pre-Miocene Algeciras Flysch sediments. Only the isotopic compositions of some LREE-enriched calc-alkaline lavas indicate assimilation of the Alpujárride upper crust, implying that most of the crust of the central Alborán Sea basin was newly accreted by tholeiitic magmatism, and a possible lower crustal delamination occurred at the continental margins of the Alborán Sea basin.

Part IV

References

References

Ackerman, L., Mahlen, N., JelÍnek, E., Medaris, G., Ulrych, J., Strnad, L. & Mihaljevic, M. (2007). Geochemistry and evolution of subcontinental lithospheric mantle in central Europe: Evidence from peridotite enoliths of the Kozákov volcano, Czech Republic. *Journal of Petrology* **48**, 2235-2260.

Acosta-Vigil, A. (1998). Estudio de los fenómenos de fusión cortical y generación de granitoides asociados a las peridotitas de Ronda. Unpublished PhD Thesis: Universidad de Granada, 305.

Acosta-Vigil, A., Barich, A., Bartoli, O., Garrido, C. J., Cesare, B., Remusat, L., Poli, S. & Raepsaet, C. (2016). The composition of nanogranitoids in migmatites overlying the Ronda peridotites (Betic Cordillera, S Spain): the anatectic history of a polymetamorphic basement. *Contributions to Mineralogy and Petrology* **171**, 1-31.

Acosta-Vigil, A., Rubatto, D., Bartoli, O., Cesare, B., Meli, S., Pedrera, A., Azor, A. & Tajčmanová, L. (2014). Age of anatexis in the crustal footwall of the Ronda peridotites, S Spain. *Lithos* **210–211**, 147-167.

Afiri, A., Gueydan, F., Pitra, P., Essaifi, A. & Précigout, J. (2011). Oligo-Miocene exhumation of the Beni-Bousera peridotite through a lithosphere-scale extensional shear zone. *Geodinamica Acta* **24**, 49-60.

Allègre, C. J., Manhès, G. & Göpel, C. (2008). The major differentiation of the Earth at ~ 4.45 Ga. *Earth and Planetary Science Letters* **267**, 386-398.

Allègre, C. J. & Turcotte, D. L. (1986). Implications of a two-component marble-cake mantle. *Nature* **323**, 123-127.

Anderson, D. L. (1995). Lithosphere, asthenosphere, and perisphere. *Reviews of Geophysics* **33**, 125-149.

Arai, S. (1994). Characterization of spinel peridotites by olivine-spinel compositional relationships: Review and interpretation. *Chemical Geology* **113**, 191-204.

Arndt, N. T. & Goldstein, S. L. (1989). An open boundary between lower continental crust and mantle: its role in crust formation and crustal recycling. *Tectonophysics* **161**, 201-212.

Azañon, J. M., Crespo-Blanc, A. & García-Dueñas, V. (1997). Continental collision, crustal thinning and nappe forming during the pre-Miocene evolution of the Alpujarride Complex (Alboran Domain, Betics). *Journal of Structural Geology* **19**, 1055-1071.

Balanyá, J. C., Crespo-Blanc, A., Díaz Azpiroz, M., Expósito, I. & Luján, M. (2007). Structural trend line pattern and strain partitioning around the Gibraltar Arc accretionary wedge: Insights as to the mode of orogenic arc building. *Tectonics* **26**, 10.1029/2005tc001932.

Balanyá, J. C., García Dueñas, V., Azañon, J. M. & Sánchez Gómez, M. (1997). Alternating contractional and extensional events in the Alpujarride Nappes of the Alboran domain (Betics, Gibraltar arc). *Tectonics* **16**, 226-238.

Barich, A. (2015). Unravelling the anatectic history of the lower continental crust through the petrology of melt inclusions and Lu-Hf garnet geochronology: a case study from the western Alpujárrides (Betic Cordillera, Spain). Unpublished Ph. D. Thesis: Universidad de Granada.

Barich, A., Acosta-Vigil, A., Garrido, C. J., Cesare, B., Tajčmanová, L. & Bartoli, O. (2014). Microstructures and petrology of melt inclusions in the anatectic sequence of Jubrique (Betic Cordillera, S Spain): Implications for crustal anatexis. *Lithos* **206–207**, 303-320.

Bea, F., Montero, P., Talavera, C., Abu Anbar, M., Scarrow, J. H., Molina, J. F. & Moreno, J. A. (2010). The palaeogeographic position of Central Iberia in Gondwana during the Ordovician: evidence from zircon chronology and Nd isotopes. *Terra Nova* **22**, 341-346.

Becker, H. (1996a). Geochemistry of garnet peridotite massifs from lower Austria and the composition of deep lithosphere beneath a Palaeozoic convergent plate margin. *Chemical Geology* **134**, 49-65.

Becker, H. (1996b). Crustal trace element and isotopic signatures in garnet pyroxenites from garnet peridotite massifs from lower Austria. *Journal of Petrology* **37**, 785-810.

Bédard, J. H. (2006). A catalytic delamination-driven model for coupled genesis of Archaean crust and sub-continental lithospheric mantle. *Geochimica et Cosmochimica Acta* **70**, 1188-1214.

Ben Othman, D., White, W. M. & Patchett, J. (1989). The geochemistry of marine sediments, island arc magma genesis, and crust-mantle recycling. *Earth and Planetary Science Letters* **94**, 1-21.

Beyer, E., Griffin, W. L. & O'Reilly, S. Y. (2006). Transformation of Archaean lithospheric mantle by refertilization: Evidence from exposed peridotites in the Western Gneiss Region, Norway. *Journal of Petrology* **47**, 1611-1636.

Bina, C. R. & Helffrich, G. (2014). Geophysical Constraints on Mantle Composition. In: Turekian, K. & Heinrich, H. (eds.) *Treatise on Geochemistry (Second Edition)*. Oxford: Elsevier, 41-65.

Blichert-Toft, J. & Albarède, F. (1997). The Lu-Hf isotope geochemistry of chondrites and the evolution of the mantle-crust system. *Earth and Planetary Science Letters* **148**, 243-258.

Blichert-Toft, J., Albarède, F. & Kornprobst, J. (1999). Lu-Hf Isotope systematics of garnet pyroxenites from Beni Bousera, Morocco: implications for basalt origin. *Science* **283**, 1303-1306.

Blichert-Toft, J., Chauvel, C. & Albarède, F. (1997). Separation of Hf and Lu for high-precision isotope analysis of rock samples by magnetic sector-multiple collector ICP-MS. *Contributions to Mineralogy and Petrology* **127**, 248-260.

Bodinier, J.-L., Menzies, M. A., Shimizu, N., Frey, F. A. & McPherson, E. (2004). Silicate, hydrous and carbonate metasomatism at Lherz, France: Contemporaneous derivatives of silicate melt–harzburgite reaction. *Journal of Petrology* **45**, 299-320.

Bodinier, J. L. (1988). Geochemistry and petrogenesis of the Lanzo peridotite body, western Alps. *Tectonophysics* **149**, 67-88.

Bodinier, J. L., Garrido, C. J., Chanefo, I., Bruguier, O. & Gervilla, F. (2008). Origin of pyroxenite-peridotite veined mantle by refertilization reactions: Evidence from the Ronda peridotite (Southern Spain). *Journal of Petrology* **49**, 999-1025.

Bodinier, J. L. & Godard, M. (2014). Orogenic, Ophiolitic, and Abyssal Peridotites. In: Turekian, K. & Heinrich, H. (eds.) *Treatise on Geochemistry (Second Edition)*. Oxford: Elsevier, 103-167.

Bodinier, J. L., Vasseur, G., Vernières, J., Dupuy, C. & Fabriès, J. (1990). Mechanisms of mantle metasomatism: Geochemical evidence from the Lherz orogenic peridotite. *Journal of Petrology* **31 (3)**, 597-628.

Booth-Rea, G., Azañón, J. M., Martínez-Martínez, J. M., Vidal, O. & García-Dueñas, V. (2005). Contrasting structural and P-T evolution of tectonic units in the southeastern Betics: Key for understanding the exhumation of the Alboran Domain HP/LT crustal rocks (western Mediterranean). *Tectonics* **24**, 10.1029/2004tc001640.

Booth-Rea, G., Martínez-Martínez, J. M. & Giaconia, F. (2015). Continental subduction, intracrustal shortening, and coeval upper-crustal extension: P-T evolution of subducted south Iberian paleomargin metapelites (Betics, SE Spain). *Tectonophysics* **663**, 122-139.

Booth-Rea, G., Ranero, C. R., Martínez-Martínez, J. M. & Grevemeyer, I. (2007). Crustal types and Tertiary tectonic evolution of the Alborán sea, western Mediterranean. *Geochemistry Geophysics Geosystems* **8**, Q10005.

Borghini, G., Rampone, E., Zanetti, A., Class, C., Cipriani, A., Hofmann, A. W. & Goldstein, S. L. (2016). Pyroxenite layers in the northern Apennines' upper mantle (Italy)—Generation by pyroxenite melting and melt Infiltration. *Journal of Petrology* **57**, 625-653.

Bosch, D., Blichert-Toft, J., Moynier, F., Nelson, B. K., Telouk, P., Gillot, P.-Y. & Albarède, F. (2008). Pb, Hf and Nd isotope compositions of the two Réunion volcanoes (Indian Ocean): A tale of two small-scale mantle "blobs"? *Earth and Planetary Science Letters* **265**, 748-765.

Bosch, D., Garrido, C. J., Bruguier, O., Dhuime, B., Bodinier, J.-L., Padron-Navarta, J. A. & Galland, B. (2011). Building an island-arc crustal section: Time constraints from a LA-ICP-MS zircon study. *Earth and Planetary Science Letters* **309**, 268-279.

Bouybaouene, M., Michard, A. & Goffé, B. (1998). High-pressure granulites on top of the Beni Bousera peridotites, Rif belt, Morocco: a record of an ancient thickened crust in the Alboran domain. *Bulletin Société Géologique France* **169**, 153-162.

Bruguier, O., Hammor, D., Bosch, D. & Caby, R. (2009). Miocene incorporation of peridotite into the Hercynian basement of the Maghrebides (Edough massif, NE Algeria): Implications for the geodynamic evolution of the Western Mediterranean. *Chemical Geology* **261**, 172-184.

Canil, D. (2004). Mildly incompatible elements in peridotites and the origins of mantle lithosphere. *Lithos* **77**, 375-393.

Coogan, L. A. (2007). The Lower Oceanic Crust. In: Rudnick, R. (ed.) *Treatise on Geochemistry: The Crust*: Elsevier Science.

Crespo-Blanc, A., Balanyá, J. C., Expósito, I., Luján, M. & Suades, E. (2012). Crescent-like large-scale structures in the external zones of the western Gibraltar Arc (Betic–Rif orogenic wedge). *Journal of the Geological Society* **169**, 667-679.

Crespo-Blanc, A. & Frizon de Lamotte, D. F. (2006). Structural evolution of the external zones derived from the Flysch trough and the South Iberian and Maghrebian paleomargins around the Gibraltar arc: a comparative study. *Bulletin Société Géologique France* **177**, 267-282.

Chalouan, A. & Michard, A. (2004). The Alpine Rif Belt (Morocco): A case of mountain building in a subduction-subduction-transform fault triple junction. *Pure Applied Geophysics* **161**, 489-519.

Chauvel, C. & Blichert-Toft, J. (2001). A hafnium isotope and trace element perspective on melting of the depleted mantle. *Earth and Planetary Science Letters* **190**, 137-151.

Chauvel, C., Hofmann, A. W. & Vidal, P. (1992). HIMU-EM: The French Polynesian connection. *Earth and Planetary Science Letters* **110**, 99-119.

Chetouani, K., Bodinier, J.-L., Garrido, C. J., Marchesi, C., Amri, I. & Targuisti, K. (in press). Spatial variability of pyroxenite layers in the Beni Bousera orogenic peridotite (Morocco) and implications for their origin. *Comptes Rendus Geoscience*, 10.1016/j.crte.2016.1006.1001.

Davies, G. F. (1998). Topography: a robust constraint on mantle fluxes. *Chemical Geology* **145**, 479-489.

Davies, G. F. (2002). Stirring geochemistry in mantle convection models with stiff plates and slabs. *Geochimica et Cosmochimica Acta* **66**, 3125-3142.

Davies, G. F. (2011). Dynamical geochemistry of the mantle. *Solid Earth* **2**, 159-189.

Davies, G. R., Nixon, P. H., Pearson, D. G. & Obata, M. (1993). Tectonic implications of graphitized diamonds from the Ronda, peridotite massif, southern Spain. *Geology* **21**, 471-474.

de Capoa, P., D'errico, M., Di Staso, A., Morabito, S., Perrone, V. & Perrota, S. (2014). Biostratigraphic and petrographic study of the Oligocene-lower Miocene successions of the external oceanic units in the Apennines and Sicilian Maghrebides. *Revista de la Sociedad Geológica de España* **27**, 151-174.

DePaolo, D. J. (1981). Trace element and isotopic effects of combined wall rock assimilation and fractional crystallization. *Earth and Planetary Science Letters* **53**, 189-202.

Dhuime, B., Bosch, D., Garrido, C. J., Bodinier, J.-L., Bruguier, O., Hussain, S. S. & Dawood, H. (2009). Geochemical architecture of the lower- to middle-crustal section of a paleo-island arc (Kohistan complex, Jijal-Kamila area, Northern Pakistan): Implications for the evolution of an oceanic subduction zone. *Journal of Petrology* **50**, 531-569.

Dickin, A. P. (2005). *Radiogenic Isotope Geology*: Cambridge University Press.

Doin, M.-P. & Henry, P. (2001). Subduction initiation and continental crust recycling: the roles of rheology and eclogitization. *Tectonophysics* **342**, 163-191.

Downes, H. (1993). The nature of the lower continental crust of Europe: petrological and geochemical evidence from xenoliths. *Physics of the Earth and Planetary Interiors* **79**, 195-218.

Downes, H. (2001). Formation and modification of the shallow sub-continental lithospheric mantle: a review of geochemical evidence from ultramafic xenolith suites and tectonically emplaced ultramafic massifs of western and central Europe. *Journal of Petrology* **42**, 233-250.

Downes, H. (2007). Origin and significance of spinel and garnet pyroxenites in the shallow lithospheric mantle: Ultramafic massifs in orogenic belts in Western Europe and NW Africa. *Lithos* **99**, 1-24.

Duggen, S., Hoernle, K., Klügel, A., Geldmacher, J., Thirlwall, M., Hauff, F., Lowry, D. & Oates, N. (2008). Geochemical zonation of the Miocene Alborán Basin volcanism (westernmost Mediterranean): geodynamic implications. *Contributions to Mineralogy and Petrology* **156**, 577-593.

Duggen, S., Hoernle, K., Van den Bogaard, P. & Harris, C. (2004). Magmatic evolution of the Alboran region: The role of subduction in forming the western Mediterranean and causing the Messinian Salinity Crisis. *Earth and Planetary Science Letters* **218**, 91-108.

Durand-Delga, M., Rossi, P., Olivier, P. & Puglisi, D. (2000). Situation structurale et nature ophiolitique de roches basiques jurassiques associées aux flyschs maghrébins du Rif (Maroc) et de Sicile (Italie). *Comptes Rendus de l'Académie des Sciences - Series IIA - Earth and Planetary Science* **331**, 29-38.

Eiler, J. M., Schiano, P., Kitchen, N. & Stolper, E. M. (2000). Oxygen-isotope evidence for recycled crust in the sources of mid-ocean-ridge basalts. *Nature* **403**, 530-534.

Eisele, J., Sharma, M., Galer, S. J. G., Blichert-Toft, J., Devey, C. W. & Hofmann, A. W. (2002). The role of sediment recycling in EM-1 inferred from Os, Pb, Hf, Nd, Sr isotope and trace element systematics of the Pitcairn hotspot. *Earth and Planetary Science Letters* **196**, 197-212.

El Atrassi, F., Brunet, F., Bouybaouene, M., Chopin, C. & Chazot, G. (2011). Melting textures and microdiamonds preserved in graphite pseudomorphs from the Beni Bousera peridotite massif, Morocco. *European Journal of Mineralogy* **23**, 157-168.

El Atrassi, F., Brunet, F., Chazot, G., Bouybaouene, M. & Chopin, C. (2013). Metamorphic and magmatic overprint of garnet pyroxenites from the Beni Bousera massif (northern Morocco): Petrography, mineral chemistry and thermobarometry. *Lithos* **179**, 231-248.

Elderfield, H. & Schultz, A. (1996). Mid-Ocean Ridge hydrothermal fluxes and the chemical composition of the ocean. *Annual Review of Earth and Planetary Sciences* **24**, 191-224.

Ersoy, Y. & Helvacı, C. (2010). FC–AFC–FCA and mixing modeler: A Microsoft® Excel© spreadsheet program for modeling geochemical differentiation of magma by crystal fractionation, crustal assimilation and mixing. *Computers & Geosciences* **36**, 383-390.

Esteban, J. J., Cuevas, J., Tubía, J. M., Sergeev, S. & Larionov, A. (2011a). A revised Aquitanian age for the emplacement of the Ronda peridotites (Betic Cordilleras, southern Spain). *Geological Magazine* **148**, 183-187.

Esteban, J. J., Tubía, J. M., Cuevas, J., Vegas, N., Sergeev, S. & Larionov, A. (2011b). Peri-Gondwanan provenance of pre-Triassic metamorphic sequences in the western Alpujarride nappes (Betic Cordillera, southern Spain). *Gondwana Research* **20**, 443-449.

Fabriès, J. & Conquéré, F. (1983). Spinel-lherzolites and associated garnet pyroxenites of bestiac (Ariège, France). *Bulletin de Mineralogie* **106**, 781-803.

Faccenna, C., Piromallo, C., Crespo-Blanc, A., Jolivet, L. & Rossetti, F. (2004). Lateral slab deformation and the origin of the western Mediterranean arcs. *Tectonics* **23**.

Fernandez, L., Bosch, D., Bruguier, O., Hammor, D., Caby, R., Monié, P., Arnaud, N., Toubal, A., Galland, B. & Douchet, C. (2016). Permo-Carboniferous and early Miocene geological evolution of the internal zones of the Maghrebides – New insights on the western Mediterranean evolution. *Journal of Geodynamics* **96**, 146-173.

Frets, E., Tommasi, A., Garrido, C. J., Padrón-Navarta, J. A., Amri, I. & Targuisti, K. (2012). Deformation processes and rheology of pyroxenites under lithospheric mantle conditions. *Journal of Structural Geology* **39**, 138-157.

Frets, E. C., Tommasi, A., Garrido, C. J., Vauchez, A., Mainprice, D., Targuisti, K. & Amri, I. (2014). The Beni Bousera peridotite (Rif Belt, Morocco): an oblique-slip low-angle shear zone thinning the subcontinental mantle lithosphere. *Journal of Petrology* **55**, 283-313.

Gao, S., Liu, X., Yuan, H., Hattendorf, B., Günther, D., Chen, L. & Hu, S. (2002). Determination of forty-two major and trace elements in USGS and NIST SRM glasses by Laser Ablation-Inductively Coupled Plasma-Mass Spectrometry. *Geostandards Newsletter* **26**, 181-196.

Garcia, X., Seille, H., Elsenbeck, J., Evans, R. L., Jegen, M., Hoelz, S., Ledo, J., Lovatini, A., Marti, A., Marcuello, A., Queralt, P., Ungarelli, C. & Ranero, C. R. (2015). Structure of the mantle beneath the Alboran Basin from magnetotelluric soundings. *Geochemistry Geophysics Geosystems* **16**, 4261-4274.

Garrido, C. J., Bodinier, J.-L., Burg, J.-P., Zeilinger, G., Hussain, S. S., Dawood, H., Chaudhry, M. N. & Gervilla, F. (2006). Petrogenesis of mafic garnet granulite in the lower crust of the Kohistan paleo-arc Complex (Northern Pakistan): Implications for intra-crustal differentiation of island arcs and generation of continental crust. *Journal of Petrology* **47**, 1873-1914.

Garrido, C. J. & Bodinier, J. L. (1999). Diversity of mafic rocks in the Ronda peridotite: Evidence for pervasive melt-rock reaction during heating of subcontinental lithosphere by upwelling asthenosphere. *Journal of Petrology* **40**, 729-754.

Garrido, C. J., Bodinier, J. L., Dhuime, B., Bosch, D., Chanefo, I., Bruguier, O., Hussain, S. S., Dawood, H. & Burg, J. P. (2007). Origin of the island arc Moho transition zone via melt-rock reaction and its implications for intracrustal differentiation of island arcs: Evidence from the Jijal complex (Kohistan complex, northern Pakistan). *Geology* **35**, 683-686.

Garrido, C. J., Gueydan, F., Booth-Rea, G., Précigout, J., Hidas, K., Padrón-Navarta, J. A. & Marchesi, C. (2011). Garnet lherzolite and garnet-spinel mylonite in the Ronda peridotite: Vestiges of Oligocene backarc mantle lithospheric extension in the western Mediterranean. *Geology* **39**, 927-930.

Garrido, C. J., Kelemen, P. B. & Hirth, G. (2001). Variation of cooling rate with depth in lower crust formed at an oceanic spreading ridge: plagioclase crystal size distributions in gabbros from the Oman ophiolite. *Geochemistry Geophysics Geosystems* **2**, 10.1029/2000gc000136.

Gill, R. C. O., Aparicio, A., El Azzouzi, M., Hernandez, J., Thirlwall, M. F., Bourgois, J. & Marriner, G. F. (2004). Depleted arc volcanism in the Alboran Sea and shoshonitic volcanism in Morocco: geochemical and isotopic constraints on Neogene tectonic processes. *Lithos* **78**, 363-388.

Godard, M., Jousselin, D. & Bodinier, J. L. (2000). Relationships between geochemistry and structure beneath a palaeo-spreading centre: A study of the mantle section in the Oman ophiolite. *Earth and Planetary Science Letters* **180**, 133-148.

Goffé, B., Azañón, J. M., Bouybaouene, M. L. & Jullien, M. (1996). Metamorphic cookeite in Alpine metapelites from Rif, northern Morocco, and the Betic Chain, southern Spain. *European Journal of Mineralogy* **8**, 335-348.

González-Jiménez, J. M., Marchesi, C., Griffin, W. L., Gutiérrez-Narbona, R., Lorand, J.-P., O'Reilly, S. Y., Garrido, C. J., Gervilla, F., Pearson, N. J. & Hidas, K. (2013a). Transfer of Os isotopic signatures from peridotite to chromitite in the subcontinental mantle: Insights from in situ analysis of platinum-group and base-metal minerals (Ojén peridotite massif, southern Spain). *Lithos* **164–167**, 74-85.

González-Jiménez, J. M., Villaseca, C., Griffin, W. L., Belousova, E., Konc, Z., Ancochea, E., O'Reilly, S. Y., Pearson, N. J., Garrido, C. J. & Gervilla, F. (2013b). The architecture of the European-Mediterranean lithosphere: A synthesis of the Re-Os evidence. *Geology* **41**, 547-550.

Govindaraju, K. (1994). 1994 compilation of working values and sample description for 383 geostandards. *Geostandards Newsletter* **18**, 1-158.

Grand, S. P., van der Hilst, R. D. & Widiyantoro, S. (1997). High resolution global tomography: a snapshot of convection in the Earth. *Geological Society of America Today* **7**.

Guerrera, F., Martín-Martín, M., Perrone, V. & Tramontana, M. (2005). Tectono-sedimentary evolution of the southern branch of the Western Tethys (Maghrebian Flysch Basin and Lucanian Ocean): consequences for Western Mediterranean geodynamics. *Terra Nova* **17**, 358-367.

Gysi, A. P., Jagoutz, O., Schmidt, M. W. & Targuisti, K. (2011). Petrogenesis of pyroxenites and melt infiltrations in the ultramafic complex of Beni Bousera, northern Morocco. *Journal of Petrology* **52**, 1679-1735.

Halliday, A. N. (2004). Mixing, volatile loss and compositional change during impact-driven accretion of the Earth. *Nature* **427**, 505-509.

Hanan, B. B. & Graham, D. W. (1996). Lead and Helium isotope evidence from oceanic basalts for a common deep source of mantle plumes. *Science* **272**, 991-995.

Hart, S. R. (1984). A large-scale isotope anomaly in the Southern Hemisphere mantle. *Nature* **309**, 753-757.

Hart, S. R. (1988). Heterogeneous mantle domains: signatures, genesis and mixing chronologies. *Earth and Planetary Science Letters* **90**, 273-296.

Hart, S. R., Hauri, E. H., Oschmann, L. A. & Whitehead, J. A. (1992). Mantle plumes and entrainment: isotopic evidence. *Science* **256**, 517-520.

Hauri, E. H. & Hart, S. R. (1993). ReOs isotope systematics of HIMU and EMII oceanic island basalts from the south Pacific Ocean. *Earth and Planetary Science Letters* **114**, 353-371.

Helffrich, G. R. & Wood, B. J. (2001). The Earth's mantle. *Nature* **412**, 501-507.

Herzberg, C. (2004). Geodynamic information in peridotite petrology. *Journal of Petrology* **45**, 2507-2530.

Herzberg, C. & O'Hara, M. J. (1998). Phase equilibrium constraints on the origin of basalts, picrites, and komatiites. *Earth Science Reviews* **44**, 39-79.

Hidas, K., Booth-Rea, G., Garrido, C. J., Martínez-Martínez, J. M., Padrón-Navarta, J. A., Konc, Z., Giaconia, F., Frets, E. & Marchesi, C. (2013a). Backarc basin inversion and subcontinental mantle emplacement in the crust: kilometre-scale folding and shearing at the base of the proto-Alborán lithospheric mantle (Betic Cordillera, southern Spain). *Journal of the Geological Society* **170**, 47-55.

Hidas, K., Garrido, C. J., Tommasi, A., Padrón-Navarta, J. A., Thielmann, M., Konc, Z., Frets, E. & Marchesi, C. (2013b). Strain localization in pyroxenite by reaction-enhanced softening in the shallow subcontinental lithospheric mantle. *Journal of Petrology* **54**, 1997-2031.

Hidas, K., Varas-Reus, M. I., Garrido, C. J., Marchesi, C., Acosta-Vigil, A., Padrón-Navarta, J. A., Targuisti, K. & Konc, Z. (2015). Hyperextension of continental to oceanic-like lithosphere: The record of late gabbros in the shallow subcontinental lithospheric mantle of the westernmost Mediterranean. *Tectonophysics* **650**, 65-79.

Hirschmann, M. M., Kogiso, T., Baker, M. B. & Stolper, E. M. (2003). Alkalic magmas generated by partial melting of garnet pyroxenite. *Geology* **31**, 481-484.

Hirschmann, M. M. & Stolper, E. M. (1996). A possible role for garnet pyroxenite in the origin of the "garnet signature" in MORB. *Contributions to Mineralogy and Petrology* **124**, 185-208.

Hoernle, K. (1998). Geochemistry of Jurassic oceanic crust beneath Gran Canaria (Canary Islands): Implications for crustal recycling and assimilation. *Journal of Petrology* **39**, 859-880.

Hofmann, A. W. (1988). Chemical differentiation of the Earth: the relationship between mantle, continental crust, and oceanic crust. *Earth and Planetary Science Letters* **90**, 297-314.

Hofmann, A. W. (1997). Mantle geochemistry: the message from oceanic volcanism. *Nature* **385**, 219-229.

Hofmann, A. W. (2007). Sampling Mantle Heterogeneity through Oceanic Basalts: Isotopes and Trace Elements. In: Turekian, K. & Holland, H. D. (eds.) *Treatise on Geochemistry*. Oxford: Pergamon, 1-44.

Hofmann, A. W. (2014). Sampling Mantle Heterogeneity through Oceanic Basalts: Isotopes and Trace Elements. In: Turekian, K. K. & Holland, H. D. (eds.) *Treatise on Geochemistry (Second Edition)*. Oxford: Elsevier, 67-101.

Hofmann, A. W. & White, W. M. (1982). Mantle plumes from ancient oceanic crust. *Earth and Planetary Science Letters* **57**, 421-436.

Ionov, D., Chanefo, I. & Bodinier, J.-L. (2005). Origin of Fe-rich lherzolites and wehrlites from Tok, SE Siberia by reactive melt percolation in refractory mantle peridotites. *Contributions to Mineralogy and Petrology* **150**, 335-353.

Ionov, D. A., Savoyant, L. & Dupuy, C. (1992). Application of the ICP - MS technique to trace element analysis of peridotites and their minerals. *Geostandards Newsletter* **16**, 311-315.

Iwamori, H. & Nakamura, H. (2015). Isotopic heterogeneity of oceanic, arc and continental basalts and its implications for mantle dynamics. *Gondwana Research* **27**, 1131-1152.

Jammes, S. & Huismans, R. S. (2012). Structural styles of mountain building: Controls of lithospheric rheologic stratification and extensional inheritance. *Journal of Geophysical Research: Solid Earth* **117**, B10403.

Janots, E., Negro, F., Brunet, F., Goffé, B., Engi, M. & Bouybaouène, M. L. (2006). Evolution of the REE mineralogy in HP–LT metapelites of the Sebtide complex, Rif, Morocco: Monazite stability and geochronology. *Lithos* **87**, 214-234.

Jenner, F. E. & O'Neill, H. S. C. (2012). Analysis of 60 elements in 616 ocean floor basaltic glasses. *Geochemistry, Geophysics, Geosystems* **13**, 10.1029/2011gc004009.

Jochum, K. P., Weis, U., Schwager, B., Stoll, B., Wilson, S. A., Haug, G. H., Andreae, M. O. & Enzweiler, J. (2016). Reference values following ISO guidelines for frequently requested rock reference materials. *Geostandards and Geoanalytical Research* **40**, 333-350.

Johnson, M. C. & Plank, T. (2000). Dehydration and melting experiments constrain the fate of subducted sediments. *Geochemistry, Geophysics, Geosystems* **1**, 10.1029/1999gc000014.

Jolly, W. T., Lidiak, E. G. & Dickin, A. P. (2006). Cretaceous to Mid-Eocene pelagic sediment budget in Puerto Rico and the Virgin Islands (northeast Antilles Island arc) *Geologica Acta* **14**, 35-62.

Kay, R. W. & Mahlburg Kay, S. (1993). Delamination and delamination magmatism. *Tectonophysics* **219**, 177-189.

Kelley, K. A., Plank, T., Farr, L., Ludden, J. & Staudigel, H. (2005). Subduction cycling of U, Th, and Pb. *Earth and Planetary Science Letters* **234**, 369-383.

Kiseeva, E. S., Wood, B. J., Ghosh, S. & Stachel, T. (2016). The pyroxenite-diamond connection. *Geochemical Perspectives Letters* **2**, 1-9.

Kogiso, T. & Hirschmann, M. M. (2006). Partial melting experiments of bimineralic eclogite and the role of recycled mafic oceanic crust in the genesis of ocean island basalts. *Earth and Planetary Science Letters* **249**, 188-199.

Kogiso, T., Hirschmann, M. M. & Frost, D. J. (2003). High-pressure partial melting of garnet pyroxenite: possible mafic lithologies in the source of ocean island basalts. *Earth and Planetary Science Letters* **216**, 603-617.

Kogiso, T., Hirschmann, M. M. & Pertermann, M. (2004a). High-pressure partial melting of mafic lithologies in the mantle. *Journal of Petrology* **45**, 2407-2422.

Kogiso, T., Hirschmann, M. M. & Reiners, P. W. (2004b). Length scales of mantle heterogeneities and their relationship to ocean island basalt geochemistry. *Geochimica et Cosmochimica Acta* **68**, 345-360.

Kogiso, T., Tatsumi, Y. & Nakano, S. (1997). Trace element transport during dehydration processes in the subducted oceanic crust: 1. Experiments and implications for the origin of ocean island basalts. *Earth and Planetary Science Letters* **148**, 193-205.

Kornprobst, J. (1969). Le massif ultrabasique des Beni Bouchera (Rif Interne, Maroc): Etude des péridotites de haute température et de haute pression, et des pyroxénolites, à grenat ou sans grenat, qui leur sont associées. *Contributions to Mineralogy and Petrology* **23**, 283-322.

Kornprobst, J., Piboule, M., Roden, M. & Tabit, A. (1990). Corundum-bearing garnet clinopyroxenites at Beni Bousera (Morocco): Original plagioclase-rich gabbros recrystallized at depth within the mantle? *Journal of Petrology* **31**, 717-745.

Lambart, S., Baker, M. B. & Stolper, E. M. (2016). The role of pyroxenite in basalt genesis: Melt-PX, a melting parameterization for mantle pyroxenites between 0.9 and 5 GPa. *Journal of Geophysical Research: Solid Earth*, 10.1002/2015JB012762.

Lambart, S., Laporte, D., Provost, A. & Schiano, P. (2012). Fate of pyroxenite-derived melts in the peridotitic mantle: Thermodynamic and experimental constraints. *Journal of Petrology* **53**, 451-476.

Lambart, S., Laporte, D. & Schiano, P. (2009). An experimental study of pyroxenite partial melts at 1 and 1.5 GPa: Implications for the major-element composition of Mid-Ocean Ridge Basalts. *Earth and Planetary Science Letters* **288**, 335-347.

Lambart, S., Laporte, D. & Schiano, P. (2013). Markers of the pyroxenite contribution in the major-element compositions of oceanic basalts: Review of the experimental constraints. *Lithos* **160**, 14-36.

Le Roux, V., Bodinier, J. L., Alard, O., O'Reilly, S. Y. & Griffin, W. L. (2009). Isotopic decoupling during porous melt flow: A case-study in the Lherz peridotite. *Earth and Planetary Science Letters* **279**, 76-85.

Le Roux, V., Bodinier, J. L., Tommasi, A., Alard, O., Dautria, J. M., Vauchez, A. & Riches, A. J. V. (2007). The Lherz spinel lherzolite: Refertilized rather than pristine mantle. *Earth and Planetary Science Letters* **259**, 599-612.

Le Roux, V., Tommasi, A. & Vauchez, A. (2008). Feedback between melt percolation and deformation in an exhumed lithosphere–asthenosphere boundary. *Earth and Planetary Science Letters* **274**, 401-413.

Leblanc, M. & Temagoult, A. (1989). Chromite pods in a lherzolite massif (Collo, Algeria) - Evidence of oceanic-type mantle rocks along the west Mediterranean Alpine belt. *Lithos* **23**, 153-162.

Lenoir, X., Garrido, C., Bodinier, J. L., Dautria, J. M. & Gervilla, F. (2001). The recrystallization front of the Ronda peridotite: Evidence for melting and thermal erosion of subcontinental lithospheric mantle beneath the Alboran Basin. *Journal of Petrology* **42**, 141-158.

Lonergan, L. & White, N. (1997). Origin of the Betic-Rif mountain belt. *Tectonics* **16**, 504-522.

Loomis, T. P. (1975). Tertiary mantle diapirism, orogeny, and plate tectonics east of the Strait of Gibraltar. *American Journal of Science* **275**, 1-30.

Loubet, M. & Allègre, C. J. (1982). Trace elements in orogenic lherzolites reveal the complex history of the upper mantle. *Nature* **298**, 809-814.

Luján, M., Crespo-Blanc, A. & Balanyá, J. C. (2006). The Flysch Trough thrust imbricate (Betic Cordillera): A key element of the Gibraltar Arc orogenic wedge. *Tectonics* **25**.

Lustrino, M. (2005). How the delamination and detachment of lower crust can influence basaltic magmatism. *Earth-Science Reviews* **72**, 21-38.

Mancilla, F. d. L., Booth-Rea, G., Stich, D., Pérez-Peña, J. V., Morales, J., Azañón, J. M., Martin, R. & Giaconia, F. (2015). Slab rupture and delamination under the Betics and Rif constrained from receiver functions. *Tectonophysics* **663**, 225-237.

Marchesi, C., Dale, C. W., Garrido, C. J., Pearson, D. G., Bosch, D., Bodinier, J.-L., Gervilla, F. & Hidas, K. (2014). Fractionation of highly siderophile elements in refertilized mantle: Implications for the Os isotope composition of basalts. *Earth and Planetary Science Letters* **400**, 33-44.

Marchesi, C., Garrido, C. J., Bosch, D., Bodinier, J.-L., Gervilla, F. & Hidas, K. (2013). Mantle refertilization by melts of crustal-derived garnet pyroxenite: Evidence from the Ronda peridotite massif, southern Spain. *Earth and Planetary Science Letters* **362**, 66-75.

Marchesi, C., Garrido, C. J., Bosch, D., Bodinier, J.-L., Hidas, K., Padrón-Navarta, J. A. & Gervilla, F. (2012). A late Oligocene suprasubduction setting in the Westernmost Mediterranean revealed by intrusive pyroxenite dikes in the Ronda peridotite (Southern Spain). *The Journal of Geology* **120**, 237-247.

Marchesi, C., Griffin, W. L., Garrido, C. J., Bodinier, J.-L. & Pearson, N. J. (2010). Persistence of mantle lithospheric Re-Os signature during asthenospherization of the subcontinental lithospheric mantle: insights from in situ isotopic analysis of sulfides from the Ronda peridotite (Southern Spain). *Contributions to Mineralogy and Petrology* **159**, 315-330.

Martín-Algarra, A. (1987). Evolución geológica alpina del contacto entre las zonas internas y las zonas externas de la cordillera Bética: sector central y occidental. Unpublished Ph.D. Thesis: Universidad de Granada.

Martín‐Algarra, A., Messina, A., Perrone, V., Russo, S., Maate, A. & Martín‐Martín, M. (2000). A lost realm in the internal domains of the Betic‐Rif orogen (Spain and Morocco): Evidence from conglomerates and consequences for Alpine geodynamic evolution. *The Journal of Geology* **108**, 447-467.

Mauffret, A., Ammar, A., Gorini, C. & Jabour, H. (2007). The Alboran Sea (Western Mediterranean) revisited with a view from the Moroccan Margin. *Terra Nova* **19**, 195-203.

McDonough, W. F. & Frey, F. A. (1989). Rare earth elements in upper mantle rocks. *Reviews in Mineralogy and Geochemistry* **21**, 100-145.

McDonough, W. F. & Sun, S. s. (1995). The composition of the Earth. *Chemical Geology* **120**, 223-253.

McKenzie, D. & O'Nions, R. K. (1983). Mantle reservoirs and ocean island basalts. *Nature* **301**, 229-231.

Menzies, M. A. & Dupuy, C. (1991). Orogenic Massifs: Protolith, Process and Provenance. *Journal of Petrology* **2.1**, 1-16.

Michard, A., Chalouan, A., Montigny, R. & Ouazzani-Touhami, M. (1983). (The inner Rif metamorphic nappes, Sebtids, Morocco, a piece of a Pennic type, Alpine pile of nappes, including the upper mantle). *Comptes Rendus des Seances-Academie des Sciences, Serie II* **296**, 1337-1340.

Michard, A., Goffe, B., Bouybaouene, M. L. & Saddiqi, O. (1997). Late Hercynian-Mesozoic thinning in the Alboran domain: metamorphic data from the northern Rif, Morocco. *Terra Nova* **9**, 171-174.

Michard, A., Negro, F., Saddiqi, O., Bouybaouene, M. L., Chalouan, A., Montigny, R. & Goffé, B. (2006). Pressure–temperature–time constraints on the Maghrebide mountain building: evidence from the Rif–Betic transect (Morocco, Spain), Algerian correlations, and geodynamic implications. *Comptes Rendus Geoscience* **338**, 92-114.

Milholland, C. S. & Presnall, D. C. (1998). Liquidus phase relations in the CaO-MgO-Al_2O_3-SiO_2 system at 3.0 GPa: The aluminous pyroxene thermal divide and high-pressure fractionation of picritic and komatiitic magmas. *Journal of Petrology* **39**, 3-27.

Montanini, A. & Tribuzio, R. (2015). Evolution of recycled crust within the mantle: Constraints from the garnet pyroxenites of the External Ligurian ophiolites (northern Apennines, Italy). *Geology* **43**, 911-914.

Montanini, A., Tribuzio, R. & Thirlwall, M. (2012). Garnet clinopyroxenite layers from the mantle sequences of the Northern Apennine ophiolites (Italy): Evidence for recycling of crustal material. *Earth and Planetary Science Letters* **351-352**, 171-181.

Morishita, T., Arai, S. & Gervilla, F. (2001). High-pressure aluminous mafic rocks from the Ronda peridotite massif, southern Spain: significance of sapphirine- and corundum-bearing mineral assemblages. *Lithos* **57**, 143-161.

Morishita, T., Arai, S., Gervilla, F. & Green, D. H. (2003). Closed-sytem geochemical recycling of crustal materials in alpine-type peridotite. *Geochimica et Cosmochimica Acta* **67**, 303-310.

Müntener, O., Pettke, T., Desmurs, L., Meier, M. & Schaltegger, U. (2004). Refertilization of mantle peridotite in embryonic ocean basins: trace element and Nd isotopic evidence and implications for crust–mantle relationships. *Earth and Planetary Science Letters* **221**, 293-308.

Negro, F., Beyssac, O., Goffé, B., Saddiqi, O. & Bouybaouene, M. L. (2006). Thermal structure of the Alboran Domain in the Rif (northern Morocco) and the Western Betics (southern Spain). Constraints from Raman spectroscopy of carbonaceous material. *Journal of Metamorphic Geology* **24**, 309-327.

Niu, Y. (2004). Bulk-rock major and trace element compositions of abyssal peridotites: Implications for mantle melting, melt extraction and post-melting processes beneath mid-ocean ridges. *Journal of Petrology* **45**, 2423-2458.

O'Hara, M. J. (1968). The bearing of phase equilibria studies in synthetic and natural systems on the origin and evolution of basic and ultrabasic rocks. *Earth Science Reviews* **4**, 69-133.

O'Hara, M. J. (1972). Data reduction and projection schemes for complex compositions. *Progress in Experimental Petrology*. Edinburgh: N.E.R.C., 103-106.

Obata, M. (1980). The Ronda peridotite: Garnet-, spinel-, and plagioclase-lherzolite facies and the P-T trajectories of a high-temperature mantle intrusion. *Journal of Petrology* **21**, 533-572.

Parrish, R. R. (1990). U–Pb dating of monazite and its application to geological problems. *Canadian Journal of Earth Sciences* **27**, 1431-1450.

Paton, C., Hellstrom, J., Paul, B., Woodhead, J. & Hergt, J. (2011). Iolite: Freeware for the visualisation and processing of mass spectrometric data. *Journal of Analytical Atomic Spectrometry* **26**, 2508-2518.

Pearce, N. J. G., Perkins, W. T., Westgate, J. A., Gorton, M. P., Jackson, S. E., Neal, C. R. & Chenery, S. P. (1997). A compilation of new and published major and trace element data for NIST SRM 610 and NIST SRM 612 glass reference materials. *Geostandards Newsletter* **21**, 115-144.

Pearson, D. G., Canil, D. & Shirey, S. B. (2014). Mantle Samples Included in Volcanic Rocks: Xenoliths and Diamonds. In: Turekian, K. K. & Holland, H. D. (eds.) *Treatise on Geochemistry (Second Edition)*. Oxford: Elsevier, 169-253.

Pearson, D. G., Davies, G. R. & Nixon, P. H. (1993). Geochemical constraints on the petrogenesis of diamond facies pyroxenites from the Beni Bousera peridotite massif, North Morocco. *Journal of Petrology* **34**, 125-172.

Pearson, D. G., Davies, G. R., Nixon, P. H., Greenwood, P. B. & Mattey, D. P. (1991). Oxygen isotope evidence for the origin of pyroxenites in the Beni Bousera peridotite massif, North Morocco: derivation from subducted oceanic lithosphere. *Earth and Planetary Science Letters* **102**, 289-301.

Pearson, D. G., Davies, G. R., Nixon, P. H. & Milledge, H. J. (1989). Graphitized diamonds from a peridotite massif in Morocco and implications for anomalous diamond occurrences. *Nature* **338**, 60-62.

Pearson, D. G. & Nowell, M. (2004). Re-Os and Lu-Hf isotope constraints on the origin and age of pyroxenites from the Beni Bousera peridotite massif: Implications for mixed peridotite-pyroxenite mantle sources. *Journal of Petrology* **45 (2)**, 439-455.

Pertermann, M. & Hirschmann, M. M. (2003). Anhydrous partial melting experiments on MORB-like eclogite: Phase relations, phase compositions and mineral–melt partitioning of major elements at 2–3 GPa. *Journal of Petrology* **44**, 2173-2201.

Pin, C., Briot, D., Bassin, C. & Poitrasson, F. (1994). Concomitant separation of strontium and samarium-neodymium for isotopic analysis in silicate samples, based on specific extraction chromatography. *Analytica Chimica Acta* **298**, 209-217.

Plank, T. (2014). The Chemical Composition of Subducting Sediments. In: Turekian, K. K. & Holland, H. D. (eds.) *Treatise on Geochemistry (Second Edition)*. Oxford: Elsevier, 607-629.

Plank, T. & Langmuir, C. H. (1998). The chemical composition of subducting sediment and its consequences for the crust and mantle. *Chemical Geology* **145**, 325-394.

Platt, J. P., Anczkiewicz, R., Soto, J.-I., Kelley, S. P. & Thirlwall, M. (2006). Early Miocene continental subduction and rapid exhumation in the western Mediterranean. *Geology* **34**, 981-984.

Platt, J. P., Argles, T. W., Carter, A., Kelley, S. P., Whitehouse, M. J. & Lonergan, L. (2003). Exhumation of the Ronda peridotite and its crustal envelope: constraints from thermal modelling of a P–T–time array. *Journal of the Geological Society* **160**, 655-676.

Platt, J. P., Behr, W. M., Johanesen, K. & Williams, J. R. (2013). The Betic-Rif arc and Its orogenic hinterland: A review. *Annual Review of Earth and Planetary Sciences* **41**, 313-357.

Platt, J. P., Kelley, S. P., Carter, A. & Orozco, M. (2005). Timing of tectonic events in the Alpujarride Complex, Betic Cordillera, southern Spain. *Journal of the Geological Society* **162**, 451-462.

Platt, J. P. & Whitehouse, M. J. (1999). Early Miocene high-temperature metamorphism and rapid exhumation in the Betic Cordillera (Spain): evidence from U–Pb zircon ages. *Earth and Planetary Science Letters* **171**, 591-605.

Polvé, M. & Allègre, C. J. (1980). Orogenic lherzolite complexes studied by ^{87}Rb-^{87}Sr: A clue to understand the mantle convection processes? *Earth and Planetary Science Letters* **51**, 71-93.

Precigout, J., Gueydan, F., Gapais, D., Garrido, C. J. & Essaifi, A. (2007). Strain localisation in the subcontinental mantle - a ductile alternative to the brittle mantle. *Tectonophysics* **445**, 318-336.

Rampone, E., Romairone, A. & Hofmann, A. W. (2004). Contrasting bulk and mineral chemistry in depleted mantle peridotites: evidence for reactive porous flow. *Earth and Planetary Science Letters* **218**, 491-506.

Rehkämper, M. & Hofmann, A. W. (1997). Recycled ocean crust and sediment in Indian Ocean MORB. *Earth and Planetary Science Letters* **147**, 93-106.

Reisberg, L., Zindler, A. & Jagoutz, E. (1989). Further Sr and Nd isotopic results from peridotites of the Ronda Ultramafic Complex. *Earth and Planetary Science Letters* **96**, 161-180.

Reisberg, L. C. (1988). Isotopic and Geochemical Systematics of the Ronda Ultramafic Complex of southern Spain. *Unpublished Ph.D. Thesis*: University of Columbia, 248.

Reisberg, L. C., Allègre, C. J. & Luck, J.-M. (1991). The Re-Os systematics of the Ronda Ultramafic Complex of southern Spain. *Earth and Planetary Science Letters* **105**, 196-213.

Reuber, I., Michard, A., Chalouan, A., Juteau, T. & Jermoumi, B. (1982). Structure and emplacement of the Alpine-type peridotites from Beni Bousera, Rif, Morocco: A polyphase tectonic interpretation. *Tectonophysics* **82**, 231-251.

Revel, M., Sinko, J. A., Grousset, F. E. & Biscaye, P. E. (1996). Sr and Nd isotopes as tracers of North Atlantic lithic particles: Paleoclimatic implications. *Paleoceanography* **11**, 95-113.

Ringwood, A. E. (1967). The pyroxene-garnet transformation in the earth's mantle. *Earth and Planetary Science Letters* **2**, 255-263.

Rosenthal, A., Yaxley, G. M., Green, D. H., Hermann, J., Kovács, I. & Spandler, C. (2014). Continuous eclogite melting and variable refertilisation in upwelling heterogeneous mantle. *Scientific Reports* **4**, 6099.

Rossetti, F., Theye, T., Lucci, F., Bouybaouene, M. L., Dini, A., Gerdes, A., Phillips, D. & Cozzupoli, D. (2010). Timing and modes of granite magmatism in the core of the Alboran Domain, Rif chain, northern Morocco: Implications for the Alpine evolution of the western Mediterranean. *Tectonics* **29**, 10.1029/2009tc002487.

Royden, L. H. (1993). The tectonic expression slab pull at continental convergent boundaries. *Tectonics* **12**, 303-325.

Rudnick, R. L. & Gao, S. (2003). Composition of the Continental Crust. In: Turekian, K. & Holland, H. D. (eds.) *Treatise on Geochemistry*. Oxford: Pergamon, 1-64.

Rudnick, R. L. & Goldstein, S. L. (1990). The Pb isotopic compositions of lower crustal xenoliths and the evolution of lower crustal Pb. *Earth and Planetary Science Letters* **98**, 192-207.

Rudnick, R. L., McDonough, W. F. & Chappell, B. W. (1993). Carbonatite metasomatism in the northern Tanzanian mantle: Petrographic and geochemical characteristics. *Earth and Planetary Science Letters* **114**, 463-475.

Saddiqi, O., Reuber, I. & Michard, A. (1988). Sur la tectonique de dénudation du manteau infracontinental dans les Beni Bousera, Rif septentrional, Maroc. *Comptes rendus de l'Académie des sciences. Série 2, Sciences de la Terre* **307**, 657-662.

Salters, V. J. M. & Stracke, A. (2004). Composition of the depleted mantle. *Geochemistry, Geophysics, Geosystems* **5**, Q05B07. 10.1029/2003gc000597.

Sánchez-Rodriguez, L. & Gebauer, D. (2000). Mesozoic formation of pyroxenites and gabbros in the Ronda area (southern Spain), followed by Early Miocene subduction metamorphism and emplacement into the middle crust: U-Pb sensitive high-resolution ion microprobe dating of zircon. *Tectonophysics* **316**, 19-44.

Santos, J. F., Schärer, U., Gil Ibarguchi, J. I. & Girardeau, J. (2002). Genesis of pyroxenite-rich peridotite at Cabo Ortegal (NW Spain): Geochemical and Pb–Sr–Nd isotope data. *Journal of Petrology* **43**, 17-43.

Schubert, G., Turcotte, D. L. & Olson, P. (2001). *Mantle convection in the Earth and planets*: Cambridge University Press.

Schubert, W. (1977). Reaktionen im alpinotypen Peridotitmassiv von Ronda (Spanien) und seinen partiellen Schmelzprodukten. *Contributions to Mineralogy and Petrology* **62**, 205-220.

Soto, J. I. & Platt, J. P. (1999). Petrological and structural evolution of high-grade metamorphic rocks from the floor of the Alboran Sea basin, western Mediterranean. *Journal of Petrology* **40**, 21-60.

Soustelle, V., Tommasi, A., Bodinier, J. L., Garrido, C. J. & Vauchez, A. (2009). Deformation and reactive melt transport in the mantle lithosphere above a large-scale partial melting domain: the Ronda Peridotite massif, Southern Spain. *Journal of Petrology* **50**, 1235-1266.

Stampfli, G. M. & Hochard, C. (2009). Plate tectonics of the Alpine realm. *Geological Society, London, Special Publications* **327**, 89-111.

Stampfli, G. M., Hochard, C., Verard, C., Wilhem, C. & von Raumer, J. (2013). The formation of Pangea. *Tectonophysics* **593**, 1-19.

Stracke, A. (2012). Earth's heterogeneous mantle: A product of convection-driven interaction between crust and mantle. *Chemical Geology* **330–331**, 274-299.

Stracke, A., Bizimis, M. & Salters, V. J. M. (2003). Recycling oceanic crust: Quantitative constraints. *Geochemistry, Geophysics, Geosystems* **4**, 10.1029/2001GC000223.

Stracke, A., Hofmann, A. W. & Hart, S. R. (2005). FOZO, HIMU, and the rest of the mantle zoo. *Geochemistry, Geophysics, Geosystems* **6**, 10.1029/2004GC000824.

Streckeisen, A. (1976). To each plutonic rock its proper name. *Earth-Science Reviews* **12**, 1-33.

Suen, C. J. & Frey, F. A. (1987). Origins of the mafic and ultramafic rocks in the Ronda peridotite. *Earth and Planetary Science Letters* **85**, 183-202.

Sun, S.-s. & McDonough, W. F. (1989). Chemical and isotopic systematics of oceanic basalts: implications for mantle composition and processes. *Geological Society London, Special Publications* **42**, 313-345.

Svojtka, M., Ackerman, L., Medaris, L. G., Hegner, E., Valley, J. W., Hirajima, T., Jelínek, E. & Hrstka, T. (2016). Petrological, geochemical and Sr–Nd–O isotopic constraints on the origin of garnet and spinel pyroxenites from the Moldanubian zone of the Bohemian massif. *Journal of Petrology* **57**, 897-920.

Tabit, A., Kornprobst, J. & Woodland, A. B. (1997). Les péridotites à grenat du massif des Béni Bousera (Maroc): mélanges tectoniques et interdiffusion du fer et du magnésium. *Comptes Rendus de l'Académie des Sciences - Séries IIA - Earth and Planetary Science* **325**, 665-670.

Tackley, P. J. (2000). Mantle convection and plate tectonics: Toward an integrated physical and chemical theory. *Science* **288**, 2002-2007.

Targuisti, K. (1994). Petrología y geoquímica de los macizos ultramáficos de Ojén (Andalucía) y de Beni Bousera (Rif Septentrional, Marruecos). Unpublished Ph.D. Thesis, Universidad de Granada.

Tatsumi, Y. (2000). Continental Crust Formation by Crustal Delamination and Complimentary Accumulation of the Enriched Mantle Component in the Mantle. *Geochemistry Geophysics Geosystems* **1**, 2000GC000094.

Thirlwall, M. F. (2002). Multicollector ICP-MS analysis of Pb isotopes using a ^{207}Pb-^{204}Pb double spike demonstrates up to 400 ppm/amu systematic errors in Tl-normalization. *Chemical Geology* **184**, 255-279.

Thomas, M. F. H., Bodin, S., Redfern, J. & Irving, D. H. B. (2010). A constrained African craton source for the Cenozoic Numidian Flysch: Implications for the palaeogeography of the western Mediterranean basin. *Earth-Science Reviews* **101**, 1-23.

Tubía, J. M., Cuevas, J. & Gil Ibarguchi, J. I. (1997). Sequential development of the metamorphic aureole beneath the Ronda peridotites and its bearing on the tectonic evolution of the Betic Cordillera. *Tectonophysics* **279**, 227-252.

Turner, S. P., Platt, J. P., George, R. M. M., Kelley, S. P., Pearson, D. G. & Nowell, G. M. (1999). Magmatism associated with orogenic collapse of the Betic–Alboran domain, SE Spain. *Journal of Petrology* **40**, 1011-1036.

Van Achterberg, E., Ryan, C. G., Jackson, S. E. & Griffin, W. L. (2001). Data reduction software for LA-ICP-MS. In: Sylvester, P. (ed.) *Laser ablation ICP-MS in the earth sciences*: Mineralogical Association of Canada, 239 - 243.

Van der Wal, D. & Bodinier, J. L. (1996). Origin of the recrystallisation front in the Ronda peridotite by km-scale pervasive porous melt flow. *Contributions to Mineralogy and Petrology* **122**, 387-405.

Van der Wal, D. & Vissers, R. L. M. (1993). Uplift and emplacement of upper mantle rocks in the western Mediterranean. *Geology* **21**, 1119-1122.

Van der Wal, D. & Vissers, R. L. M. (1996). Structural Petrology of the Ronda Peridotite, SW Spain: Deformation History. *Journal of Petrology* **37**, 23-43.

van Hinsbergen, D. J. J., Vissers, R. L. M. & Spakman, W. (2014). Origin and consequences of western Mediterranean subduction, rollback, and slab segmentation. *Tectonics* **33**, 2013TC003349.

van Keken, P. E., Ballentine, C. J. & Hauri, E. H. (2014). Convective Mixing in the Earth's Mantle. In: Turekian, K. K. & Holland, H. D. (eds.) *Treatise on Geochemistry (Second Edition)*. Oxford: Elsevier, 509-525.

Varas-Reus, M. I., Garrido, C. J., Marchesi, C., Bosch, D., Acosta-Vigil, A., Hidas, K., Barich, A. & Booth-Rea, G. (in press). Sr-Nd-Pb isotopic systematics of crustal rocks from the western Betics (S. Spain): Implications for crustal recycling in the lithospheric mantle beneath the westernmost Mediterranean. *Lithos*, 10.1016/j.lithos.2016.1010.1003.

Vauchez, A. & Garrido, C. J. (2001). Seismic properties of an asthenospherized lithospheric mantle: constraints from lattice preferred orientations in peridotite from the Ronda massif. *Earth and Planetary Science Letters* **192**, 235-249.

Vergés, J. & Fernàndez, M. (2012). Tethys–Atlantic interaction along the Iberia–Africa plate boundary: The Betic–Rif orogenic system. *Tectonophysics* **579**, 144-172.

Vernières, J., Godard, M. & Bodinier, J.-L. (1997). A plate model for the simulation of trace element fractionation during partial melting and magma transport in the Earth's upper mantle. *Journal of Geophysical Research: Solid Earth* **102**, 24771-24784.

Vervoort, J. D., Plank, T. & Prytulak, J. (2011). The Hf–Nd isotopic composition of marine sediments. *Geochimica et Cosmochimica Acta* **75**, 5903-5926.

Villaseca, C., Merino, E., Oyarzun, R., Orejana, D., Pérez-Soba, C. & Chicharro, E. (2014). Contrasting chemical and isotopic signatures from Neoproterozoic metasedimentary rocks in the Central Iberian Zone (Spain) of pre-Variscan Europe: Implications for terrane analysis and Early Ordovician magmatic belts. *Precambrian Research* **245**, 131-145.

Villaseñor, A., Chevrot, S., Harnafi, M., Gallart, J., Pazos, A., Serrano, I., Cordoba, D., Pulgar, J. A. & Ibarra, P. (2015). Subduction and volcanism in the Iberia-North Africa collision zone from tomographic images of the upper mantle. *Tectonophysics* **663**, 238-249.

Walter, M. J. (1998). Melting of garnet peridotite and the origin of komatiite and depleted lithosphere. *Journal of Petrology* **39**, 29-60.

Walter, M. J. (2014). Melt Extraction and Compositional Variability in Mantle Lithosphere. In: Turekian, K. & Holland, H. D. (eds.) *Treatise on Geochemistry (Second Edition)*. Oxford: Elsevier, 393-419.

Weaver, B. L. (1991). The origin of ocean island basalt end-member compositions: trace element and isotopic constraints. *Earth and Planetary Science Letters* **104**, 381-397.

Whattam, S. & Stern, R. (2011). The 'subduction initiation rule': a key for linking ophiolites, intra-oceanic forearcs, and subduction initiation. *Contributions to Mineralogy and Petrology* **162**, 1031-1045.

White, W. M. (1985). Sources of oceanic basalts: Radiogenic isotopic evidence. *Geology* **13**, 115-118.

White, W. M. (2015). *Isotope Geochemistry*: John Wiley & Sons.

White, W. M., Albarède, F. & Télouk, P. (2000). High-precision analysis of Pb isotope ratios by multi-collector ICP-MS. *Chemical Geology* **167**, 257-270.

Willbold, M. & Stracke, A. (2006). Trace element composition of mantle end-members: Implications for recycling of oceanic and upper and lower continental crust. *Geochemistry, Geophysics, Geosystems* **7**, 10.1029/2005GC001005.

Willbold, M. & Stracke, A. (2010). Formation of enriched mantle components by recycling of upper and lower continental crust. *Chemical Geology* **276**, 188-197.

Williams, I. S., Fiannacca, P., Cirrincione, R. & Pezzino, A. (2012). Peri-Gondwanan origin and early geodynamic history of NE Sicily: A zircon tale from the basement of the Peloritani Mountains. *Gondwana Research* **22**, 855-865.

Part V

Appendixes

Appendix A

Bulk rock major and minor transition elements of the Beni Bousera peridotites

Appendix A Analyses of bulk rock major and minor transition elements in the Beni Bousera peridotite massif

Domains	*ARIEGITE*																			
Lithology	**Harzburgite**								**Lherzolite**											
Sample	**BB032**	**BB035C**	**BB035D**	**BB108**	**BB111**	**BB112A**	**BB181**	**BB188**	**BB004**	**BB026**	**BB029B-B**	**BB030**	**BB035A**	**BB036**	**BB095**	**BB096**	**BB097**	**BB098**	**BB099**	**BB100**
Groups of lherzolites	N/A	N/A	N/A	N/A	N/A	N/A	N/A	N/A	I	III	II	II	I	II	III	I	II	I	I	I
Clinopyroxene	5	4	2	5	3	5	4	3	6	9	15	14	6	14	14	6	14	6	8	9
Olivine	80	73	82	87	83	72	80	83	78	72	56	54	72	48	71	62	52	80	69	66
Orthopyroxene	15	23	15	8	14	24	15	14	16	19	29	31	21	37	14	32	33	13	23	25
Garnet	0.0	0.0	0.0	0.0	0.0	0.0	0.0	0.0	0.0	0.0	0.0	0.0	0.0	0.0	0.0	0.0	0.0	0.0	0.0	0.0
Spinel	0.4	0.1	0.6	0.6	0.2	0.0	0.5	0.1	0.4	0.0	0.9	1.0	0.1	0.1	0.8	0.0	0.2	0.7	0.3	0.3
UTM E	330145	330275	330275	327055	327495	327489	326303	325761	327408	329866	329899	329941	330275	330684	326128	326192	326354	326496	326527	326548
UTM N	3901142	3901333	3901333	3908734	3906096	3906086	3908333	3908102	3907716	3901073	3900853	3901050	3901333	3901307	3904636	3904635	3904684	3904706	3904712	3904762
Bulk rock data (wt%)																				
SiO_2	42.87	43.12	41.36	39.07	41.85	40.97	42.40	42.21	41.73	42.11	44.37	44.69	43.62	44.76	43.13	40.33	44.18	41.41	42.36	43.54
Al_2O_3	1.12	1.25	0.49	1.05	0.65	1.27	1.10	0.50	1.81	2.09	4.12	3.88	1.44	4.06	3.45	1.48	3.50	2.00	2.48	2.49
Fe_2O_3	8.71	9.09	8.36	7.80	8.71	8.30	8.30	8.38	8.31	8.58	9.78	9.09	8.11	8.70	8.96	8.14	8.70	8.60	8.25	7.86
MnO	0.14	0.13	0.13	0.13	0.14	0.13	0.12	0.12	0.13	0.13	0.14	0.14	0.13	0.14	0.14	0.13	0.15	0.13	0.14	0.13
MgO	43.24	41.89	43.84	40.68	44.68	40.85	42.13	42.19	41.69	40.95	36.27	36.73	42.02	37.45	37.95	41.37	38.06	39.98	39.83	39.96
CaO	1.13	1.03	0.47	0.68	0.65	1.01	0.94	0.57	1.50	1.96	3.42	3.23	1.35	3.20	2.97	1.36	3.02	1.58	2.13	1.82
Na_2O	*b.d.l.*	*b.d.l.*	*b.d.l.*	*b.d.l.*	*b.d.l.*	*b.d.l.*	0.00	0.00	*b.d.l.*	*b.d.l.*	0.03	*b.d.l.*	*b.d.l.*	0.03	0.08	*b.d.l.*	*b.d.l.*	*b.d.l.*	*b.d.l.*	0.02
K_2O	*b.d.l.*	*b.d.l.*	*b.d.l.*	*b.d.l.*	*b.d.l.*	*b.d.l.*	0.01	0.01	*b.d.l.*	*b.d.l.*	*b.d.l.*	*b.d.l.*	*b.d.l.*	*b.d.l.*	*b.d.l.*	*b.d.l.*	*b.d.l.*	*b.d.l.*	*b.d.l.*	0.01
P_2O_5	0.01	0.01	0.01	0.01	0.01	0.02	0.00	0.00	0.01	0.01	0.02	0.02	0.01	0.02	0.02	0.01	0.01	0.01	0.01	0.01
LOI	2.72	2.43	4.45	11.08	3.98	7.40	5.12	6.31	4.04	4.26	1.23	1.57	2.97	1.09	3.16	7.57	2.54	6.52	5.38	4.90
Total	99.9	99.0	99.1	100.5	100.7	100.0	100.2	100.3	99.3	100.1	99.6	99.5	99.7	99.7	100.0	100.4	100.3	100.3	100.6	100.8
Mg-no.	90.8	90.1	91.2	91.2	91.1	90.7	91.0	90.9	90.9	90.4	88.0	88.9	91.1	89.5	89.4	91.0	89.7	90.2	90.5	91.0
(ppm)																				
V	34.40	34.00	15.70	20.60	21.40	32.20	28.40	*n.a.*	41.20	45.60	89.50	86.60	33.00	86.70	80.00	33.30	82.80	35.20	49.50	39.80
Cr	2449	2535	2522	2096	1790	2255	2874	1900	2303	2370	2245	1970	2380	2327	2362	2302	2284	2176	2609	2603
Ni	2212	2225	2262	2055	2298	2025	2093	2299	2113	1987	1866	1926	2162	1888	1881	2057	1908	2016	1989	1958

b.d.l.: below detection limit; n.a.: not analized

Appendix A (continued)

Domains	*ARIEGITE*																			
Lithology	**Lherzolite**																			
Sample	**BB101**	**BB104**	**BB105**	**BB106A**	**BB107**	**BB109**	**BB110**	**BB114A**	**BB126**	**BB127**	**BB128**	**BB129**	**BB131**	**BB132**	**BB143**	**BB144A**	**BB144B**	**BB145**	**BB146**	**BB182**
Groups of lherzolites	II	I	II	I	I	I	II	II	I	I	I	I	I	I	I	II	II	II	I	I
Clinopyroxene	12	6	15	6	10	6	13	13	9	7	10	11	13	7	10	14	14	14	11	6
Olivine	53	61	55	80	65	76	52	54	65	67	64	60	61	64	62	53	53	50	62	76
Orthopyroxene	34	33	30	13	25	18	35	33	25	26	26	29	26	28	28	32	32	36	26	17
Garnet	0.0	0.0	0.0	0.0	0.0	0.0	0.0	0.0	0.0	0.0	0.0	0.0	0.0	0.0	0.0	0.0	0.0	0.0	0.0	0.0
Spinel	0.2	0.0	0.3	0.4	0.3	0.3	0.2	0.3	0.3	0.1	0.3	0.1	0.1	0.8	0.3	0.4	0.4	0.4	0.3	0.5
UTM E	326663	328631	328418	328423	326565	327119	326895	327508	327155	327238	327259	327228	327217	327119	326567	326558	326558	326556	326397	326287
UTM N	3904814	3908118	3908218	3908245	3908666	3908705	3908767	3905914	3903470	3903320	3903345	3903404	3903521	3903671	3908689	3908709	3908709	3908613	3907931	3908305
Bulk rock data (wt%)																				
SiO_2	43.27	40.43	41.05	39.74	42.11	40.34	42.20	43.91	44.15	43.65	43.01	43.65	44.17	44.35	42.55	43.87	43.99	43.31	42.54	43.21
Al_2O_3	3.37	2.34	3.53	2.07	2.71	1.67	3.74	3.40	2.51	1.84	2.76	3.06	3.16	2.22	3.05	3.65	4.03	3.65	2.66	1.37
Fe_2O_3	8.75	7.77	8.23	8.35	8.29	7.96	8.59	9.38	8.30	8.03	8.69	8.85	8.92	8.75	8.51	8.94	9.07	8.65	8.24	8.38
MnO	0.14	0.13	0.14	0.14	0.13	0.13	0.14	0.14	0.13	0.13	0.14	0.14	0.14	0.13	0.12	0.14	0.14	0.14	0.12	0.13
MgO	38.29	37.83	34.37	38.40	38.88	38.68	35.53	38.05	40.37	40.63	39.08	38.89	38.87	41.87	38.59	37.09	36.49	36.86	38.46	42.09
CaO	2.74	1.31	2.88	1.44	2.21	1.14	2.84	2.89	2.12	1.70	2.41	2.49	2.66	1.76	2.51	3.05	3.07	3.01	2.35	1.13
Na_2O	*b.d.l.*	*b.d.l.*	*b.d.l.*	*b.d.l.*	*b.d.l.*	*b.d.l.*	*b.d.l.*	0.21	0.12	0.03	0.17	0.20	0.23	0.12	0.18	0.26	0.28	0.24	0.12	0.03
K_2O	*b.d.l.*	*b.d.l.*	*b.d.l.*	*b.d.l.*	*b.d.l.*	*b.d.l.*	*b.d.l.*	0.00	0.00	0.00	0.01	0.01	0.01	0.01	0.01	0.00	0.01	0.01	0.00	0.00
P_2O_5	0.01	0.01	0.02	0.01	0.01	0.02	0.02	0.01	0.01	0.01	0.01	0.01	0.01	0.01	0.01	0.01	0.01	0.01	0.00	0.00
LOI	3.28	10.42	8.80	10.37	5.11	10.61	7.16	1.87	2.22	4.03	3.70	2.59	1.65	0.64	4.44	2.85	2.75	4.02	5.61	3.67
Total	100.0	100.3	99.2	100.6	99.5	100.7	100.4	100.0	100.0	100.1	100.1	100.1	100.0	100.0	100.2	100.1	100.1	100.1	100.3	100.1
Mg-no.	89.7	90.6	89.2	90.1	90.3	90.6	89.1	88.9	90.6	90.9	89.9	89.7	89.6	90.5	90.0	89.2	88.9	89.4	90.3	90.9
(ppm)																				
V	66.90	48.10	74.40	46.10	50.00	36.20	25.40	67.50	55.70	43.60	56.50	61.10	66.60	48.60	60.40	74.40	81.80	73.10	54.30	34.50
Cr	2444	2425	2147	1533	2319	2250	2091	2066	2527	2786	2349	2257	2377	2499	2355	2204	2266	2186	2339	2457
Ni	1913	1873	1625	1870	1961	1885	2038	1859	2058	2051	1974	1991	1964	2159	1952	1889	1824	1863	1943	2140

b.d.l.: below detection limit; n.a.: not analized

Appendix A (continued)

Domains	*ARIEGITE*												*ARIEGITE-SEILAND*							
Lithology	**Lherzolite**												**Harzburgite**							
Sample	**BB183**	**BB184**	**BB185**	**BB186**	**BB187**	**BB190**	**BB191**	**BB192**	**BB203**	**BB235**	**BB236**	**BB240**	**BB069**	**BB070**	**BB071**	**BB076A**	**BB115**	**BB117A**	**BB134A**	**BB259**
Groups of lherzolites	III	II	III	II	II	I	III	I	II	I	III	II	N/A	N/A	N/A	N/A	N/A	N/A	N/A	N/A
Clinopyroxene	12	13	8	12	12	13	8	5	13	6	8	14	3	5	5	3	1	1	4	3
Olivine	74	51	72	52	53	62	85	70	53	66	72	52	76	86	76	82	86	84	83	82
Orthopyroxene	14	36	19	35	35	26	6	25	34	28	19	33	21	9	20	16	13	15	13	14
Garnet	0.0	0.0	0.0	0.0	0.0	0.0	0.0	0.0	0.0	0.0	0.0	0.0	0.0	0.0	0.0	0.0	0.0	0.0	0.0	0.0
Spinel	0.2	0.4	0.8	0.4	0.4	0.2	1.1	0.0	0.3	0.1	0.7	0.3	0.0	0.4	0.0	0.0	0.0	0.0	0.7	0.3
UTM E	326248	326135	326094	325990	325772	325690	325654	325624	328911	332056	331861	327400	327706	327594	327594	327564	327146	327130	327206	329988
UTM N	3908294	3908176	3908139	3908016	3908080	3908160	3908164	3908181	3902317	3897544	3897911	3902683	3906212	3906168	3906168	3905953	3905079	3905030	3903780	3903571
Bulk rock data (wt%)																				
SiO_2	43.2	44.3	43.8	43.9	44.6	42.9	41.3	40.7	42.1	42.4	43.4	44.0	42.5	42.1	41.5	40.7	39.7	41.2	42.7	40.9
Al_2O_3	3.0	3.3	2.1	3.3	3.2	2.8	2.0	1.3	3.3	1.5	2.1	3.6	0.8	1.0	1.1	0.6	0.5	0.6	1.0	1.2
Fe_2O_3	8.9	8.8	8.4	8.9	9.1	8.4	8.1	8.6	8.2	8.5	8.6	9.1	8.2	8.5	8.3	8.4	7.7	8.1	8.8	7.8
MnO	0.1	0.1	0.1	0.1	0.1	0.1	0.1	0.1	0.1	0.1	0.1	0.1	0.1	0.1	0.1	0.1	0.1	0.1	0.1	0.1
MgO	39.1	38.3	40.2	37.7	38.0	37.8	39.9	40.9	35.7	41.4	40.8	38.1	44.0	43.4	42.4	44.7	42.7	43.3	44.2	41.3
CaO	2.5	2.8	1.8	2.7	2.7	2.5	1.7	1.2	2.7	1.4	1.9	3.1	0.7	1.0	1.1	0.6	0.3	0.3	0.8	1.0
Na_2O	0.2	0.2	0.1	0.2	0.2	0.2	0.0	0.0	0.2	0.0	0.1	0.2	*b.d.l.*	*b.d.l.*	*b.d.l.*	*b.d.l.*	0.0	0.0	0.0	0.0
K_2O	0.0	0.0	0.0	0.0	0.0	0.0	0.0	0.0	0.0	0.0	0.0	0.0	*b.d.l.*	*b.d.l.*	*b.d.l.*	*b.d.l.*	0.0	0.0	0.0	0.0
P_2O_5	0.0	0.0	0.0	0.0	0.0	0.0	0.0	0.0	0.0	0.0	0.0	0.0	0.0	0.0	0.0	0.0	0.0	0.0	0.0	0.0
LOI	2.8	1.9	3.4	3.1	1.8	5.3	7.2	7.4	8.1	4.8	2.9	1.7	3.1	3.1	4.9	4.4	9.6	6.5	2.3	8.1
Total	100.1	100.0	100.1	100.1	100.0	100.2	100.4	100.4	100.6	100.2	100.1	100.0	99.4	99.2	99.4	99.4	100.8	100.4	100.0	100.6
Mg-no.	89.8	89.6	90.5	89.3	89.3	89.9	90.7	90.4	89.7	90.6	90.4	89.3	91.4	91.0	91.0	91.4	91.7	91.3	90.9	91.3
(ppm)																				
V	60.80	70.20	43.00	61.30	75.60	52.80	40.20	30.80	74.90	42.00	47.70	77.10	18.60	30.10	33.00	*n.a.*	*n.a.*	*n.a.*	26.60	29.50
Cr	2331	2396	2479	2128	2358	2513	2422	2325	2400	2517	2612	2285	2581	2480	2604	1903	2111	2144	2870	2678
Ni	1996	1974	2030	1975	1928	1984	1991	2105	1814	2139	2037	1920	2219	2193	2172	2279	2086	2157	2224	2087

b.d.l.: below detection limit; n.a.: not analized

Appendix A (continued)

Domains	*ARIEGITE-SEILAND*																			
Lithology	**Lherzolite**																			
Sample	**BB072**	**BB074**	**BB076C**	**BB077**	**BB078**	**BB079**	**BB080B**	**BB102**	**BB103B**	**BB130**	**BB133**	**BB163**	**BB204**	**BB205**	**BB207**	**BB209**	**BB211**	**BB216**	**BB229A**	**BB254**
Groups of lherzolites	I	I	III	I	III	III	I	III	I	I	I	III	III	II	III	I	III	III	II	III
Clinopyroxene	5	8	9	8	9	11	8	8	9	9	5	16	13	16	8	8	11	9	14	11
Olivine	73	68	74	67	79	71	67	82	67	64	68	70	75	46	71	58	79	75	54	72
Orthopyroxene	21	23	15	24	11	17	24	9	24	26	27	14	11	38	20	33	9	16	33	16
Garnet	0.0	0.0	0.0	0.0	0.0	0.0	0.0	0.0	0.0	0.0	0.0	0.0	0.0	0.0	0.0	0.0	0.0	0.0	0.0	0.0
Spinel	0.0	0.4	1.2	0.3	0.8	0.7	0.3	1.0	0.3	0.3	0.0	0.7	1.0	0.2	0.5	0.8	0.9	0.6	0.1	0.5
UTM E	327543	327522	327564	327245	327245	327231	327231	326724	327211	327295	327181	331024	328905	328910	329012	329093	329138	329369	327934	329947
UTM N	3906181	3906107	3905953	3905256	3905256	3905071	3905071	3904828	3904978	3903510	3903744	3903333	3902332	3902394	3902621	3902674	3902872	3903106	3906760	3903967
Bulk rock data (wt%)																				
SiO_2	42.62	41.54	43.13	42.06	42.26	42.45	43.21	42.58	42.70	43.22	43.67	44.84	41.98	42.15	43.09	42.04	42.82	44.10	42.70	42.82
Al_2O_3	1.24	2.16	3.13	2.37	2.36	2.90	2.25	2.01	2.29	2.56	1.46	3.94	3.40	4.12	2.36	3.21	2.33	2.32	3.34	2.73
Fe_2O_3	8.83	8.91	9.64	8.32	7.85	8.47	8.59	8.32	8.39	8.66	8.57	9.17	8.45	8.91	8.21	8.50	8.55	8.77	8.49	8.54
MnO	0.14	0.14	0.14	0.13	0.13	0.14	0.13	0.13	0.14	0.13	0.13	0.14	0.13	0.13	0.12	0.13	0.13	0.13	0.13	0.13
MgO	43.36	39.47	38.06	39.09	39.74	39.05	40.85	41.19	40.81	40.24	42.49	36.08	36.04	34.61	39.50	37.24	40.29	40.72	37.08	39.14
CaO	1.16	1.91	2.72	2.03	1.84	2.46	1.89	1.69	2.06	2.17	1.27	3.26	2.98	3.38	2.02	1.80	2.10	1.97	2.85	2.39
Na_2O	*b.d.l.*	*b.d.l.*	*b.d.l.*	*b.d.l.*	*b.d.l.*	*b.d.l.*	*b.d.l.*	*b.d.l.*	*b.d.l.*	0.16	0.01	0.27	0.23	0.29	0.09	0.13	0.12	0.13	0.22	0.14
K_2O	*b.d.l.*	*b.d.l.*	*b.d.l.*	*b.d.l.*	*b.d.l.*	*b.d.l.*	*b.d.l.*	*b.d.l.*	*b.d.l.*	0.01	0.00	0.00	0.01	0.01	0.00	0.01	0.01	0.01	0.00	0.00
P_2O_5	0.01	0.01	0.02	0.01	0.01	0.02	0.01	0.01	0.01	0.01	0.00	0.01	0.01	0.01	0.01	0.01	0.01	0.01	0.01	0.00
LOI	1.56	5.51	2.40	5.23	4.75	3.65	2.27	4.76	4.30	2.76	2.36	2.11	7.00	6.50	4.68	7.19	3.63	1.72	5.25	4.10
Total	99.0	99.8	99.4	99.4	99.1	99.2	99.3	100.7	100.7	100.1	100.1	100.0	100.4	100.4	100.2	100.4	100.1	100.0	100.2	100.1
Mg-no.	90.7	89.8	88.7	90.3	90.9	90.1	90.4	90.8	90.6	90.2	90.8	88.6	89.4	88.5	90.5	89.7	90.3	90.2	89.6	90.1
(ppm)																				
V	36.30	54.90	70.60	48.50	48.00	60.20	51.80	42.90	55.90	53.80	37.50	80.90	65.70	93.20	56.70	73.60	47.40	58.10	65.30	55.40
Cr	2539	1975	2291	2099	2549	2526	2299	2379	2426	2350	2442	2133	2227	2132	2360	2301	2376	2544	2275	2458
Ni	2234	1982	1909	1936	1986	1964	2096	2063	2028	2047	2161	1965	1832	1742	2010	1809	2053	2082	1869	1966

b.d.l.: below detection limit; n.a.: not analized

Appendix A (continued)

Domains	*ARIEGITE-SEILAND*		*GRT-SP MYLONITES*																
Lithology	**Lherzolite**		**Harzburgite**					**Lherzolite**											
Sample	**BB256**	**BB275**	**BB088A**	**BB088C**	**BB093A**	**BB093B**	**BB125A**	**BB001**	**BB002**	**BB003**	**BB005**	**BB006**	**BB009**	**BB022A**	**BB022B**	**BB023**	**BB024**	**BB083**	**BB084**
Groups of lherzolites	III	II	N/A	N/A	N/A	N/A	N/A	N/A	N/A	N/A	N/A	N/A	N/A	N/A	N/A	N/A	N/A	N/A	N/A
Clinopyroxene	8	13	0	0	3	3	4	14	9	12	16	11	15	15	8	8	14	16	14
Olivine	83	51	66	80	83	83	82	71	68	64	48	64	46	48	70	76	47	65	59
Orthopyroxene	9	35	25	15	14	13	13	11	22	24	36	24	39	38	22	16	38	18	26
Garnet	0.0	0.0	0.0	0.0	0.0	0.0	0.0	3.6	0.0	0.0	0.0	0.3	0.0	0.0	0.0	0.0	0.0	1.5	0.0
Spinel	0.4	0.4	0.3	0.5	0.4	0.7	0.8	0.9	0.1	0.0	0.1	0.1	0.1	0.1	0.3	0.4	0.0	0.5	0.6
UTM E	329969	329176	325976	325976	326057	326057	327605	324754	324769	324727	328999	329096	329620	332109	332109	332039	331999	325674	325819
UTM N	3903696	3902392	3904448	3904448	3904591	3904591	3902345	3910128	3910124	3910165	3901421	3901021	3900818	3897033	3897033	3897044	3897091	3904914	3904610
Bulk rock data (wt%)																			
SiO_2	41.65	43.89	42.07	41.62	40.76	40.84	41.43	41.56	40.78	40.89	43.60	42.73	44.11	42.58	41.65	41.75	42.03	42.55	42.80
Al_2O_3	1.95	3.42	2.54	1.20	0.85	0.96	0.95	2.94	2.42	2.72	4.52	3.20	3.79	3.30	2.02	1.38	3.49	3.76	3.41
Fe_2O_3	8.76	9.24	8.34	8.11	8.45	8.31	8.17	8.38	7.98	8.02	8.23	8.47	8.55	8.36	8.04	8.20	8.71	8.75	8.63
MnO	0.12	0.13	0.14	0.13	0.13	0.13	0.12	0.14	0.13	0.13	0.13	0.14	0.14	0.13	0.13	0.13	0.14	0.14	0.14
MgO	39.35	33.60	39.92	42.09	43.87	42.96	42.20	37.31	38.54	37.19	33.29	37.76	36.91	37.48	40.59	37.66	35.31	36.62	37.96
CaO	1.69	2.78	2.15	1.09	0.70	0.74	0.77	2.49	2.03	2.32	3.33	2.85	3.06	3.12	1.70	1.58	3.16	3.01	2.97
Na_2O	0.10	0.25	*b.d.l.*	*b.d.l.*	*b.d.l.*	*b.d.l.*	0.01	0.46	*b.d.l.*	*b.d.l.*	0.33	*b.d.l.*	*b.d.l.*	*b.d.l.*	*b.d.l.*	*b.d.l.*	*b.d.l.*	*b.d.l.*	*b.d.l.*
K_2O	0.00	0.01	0.04	*b.d.l.*	*b.d.l.*	*b.d.l.*	0.00	0.02	*b.d.l.*	*b.d.l.*	0.10	*b.d.l.*	*b.d.l.*	*b.d.l.*	*b.d.l.*	*b.d.l.*	*b.d.l.*	*b.d.l.*	*b.d.l.*
P_2O_5	0.01	0.01	0.02	0.01	0.01	0.01	0.00	0.02	0.02	0.01	0.02	0.01	0.01	0.01	0.01	0.01	0.02	0.02	0.02
LOI	6.35	6.85	3.96	5.06	5.73	6.52	6.65	7.44	8.38	7.15	5.56	3.80	2.94	4.52	5.63	9.02	7.56	4.15	3.39
Total	100.4	100.4	99.2	99.3	100.5	100.5	100.4	100.9	100.4	98.7	99.3	99.2	99.6	99.6	99.8	99.7	100.6	99.2	99.4
Mg-no.	89.9	87.8	90.5	91.1	91.2	91.1	91.1	89.8	90.6	90.2	88.9	89.8	89.5	89.9	90.9	90.1	88.9	89.3	89.7
(ppm)																			
V	55.10	63.70	52.70	25.30	18.30	26.90	26.10	63.90	48.30	61.40	80.40	66.40	70.80	64.00	42.40	38.40	79.90	77.00	78.60
Cr	2239	2197	2354	2318	2354	3136	2401	2190	2273	2183	2230	2255	2321	2331	2411	1990	2316	2257	2178
Ni	1977	2062	1999	2166	2245	2164	2136	1826	1878	1837	1636	1888	1914	1844	1987	2096	1838	1838	1885

b.d.l.: below detection limit; n.a.: not analized

Appendix A (continued)

Domains	*GRT-SP MYLONITES*																			
Lithology	**Lherzolite**																			
Sample	**BB085**	**BB087**	**BB088B**	**BB090**	**BB091**	**BB120**	**BB122**	**BB123**	**BB124**	**BB165**	**BB166**	**BB167**	**BB169**	**BB171**	**BB173**	**BB193**	**BB194**	**BB195**	**BB196**	**BB197A**
Groups of lherzolites	N/A	N/A	N/A	N/A	N/A	N/A	N/A	N/A	N/A	N/A	N/A	N/A	N/A	N/A	N/A	N/A	N/A	N/A	N/A	N/A
Clinopyroxene	12	8	11	14	13	14	9	14	11	9	13	11	8	20	5	13	10	9	6	11
Olivine	71	74	78	57	58	53	67	49	62	74	51	60	61	65	67	54	61	65	64	61
Orthopyroxene	15	15	10	28	28	33	24	37	27	16	36	29	31	14	27	33	29	26	30	28
Garnet	0.9	0.0	0.0	0.0	0.0	0.0	0.0	0.0	0.0	0.0	0.0	0.0	0.0	1.7	0.0	0.0	0.0	0.0	0.0	0.0
Spinel	1.1	2.9	0.8	0.5	0.6	0.3	0.3	0.3	0.2	1.1	0.4	0.1	0.0	0.5	0.0	0.4	0.1	0.1	0.0	0.1
UTM E	325918	325990	325976	326046	326041	327425	327496	327528	327581	328688	328707	328656	328762	328800	328865	325521	325411	325448	325431	325397
UTM N	3904335	3904408	3904448	3904548	3904564	3902551	3902553	3902512	3902480	3901576	3901602	3901589	3901994	3902043	3902241	3908250	3908265	3908258	3908266	3908293
Bulk rock data (wt%)																				
SiO_2	41.60	42.62	43.00	43.05	43.91	44.69	43.29	44.66	44.29	42.51	42.38	41.89	41.30	41.80	40.15	43.82	44.29	41.56	41.88	43.41
Al_2O_3	3.03	3.03	2.57	3.56	3.52	3.70	2.19	4.05	2.85	2.55	3.33	3.20	2.55	4.97	1.38	3.25	3.11	2.02	1.74	2.93
Fe_2O_3	8.29	8.59	8.39	8.73	8.93	8.97	8.45	9.06	8.68	8.47	8.26	8.44	8.24	8.40	7.93	8.96	8.61	8.37	8.11	8.76
MnO	0.14	0.14	0.13	0.14	0.14	0.14	0.13	0.14	0.13	0.12	0.13	0.12	0.12	0.13	0.12	0.14	0.14	0.12	0.12	0.13
MgO	37.11	38.75	40.07	38.08	38.67	37.45	40.68	36.79	38.95	37.71	35.29	33.72	38.06	34.06	40.28	36.54	37.74	39.31	39.08	35.47
CaO	2.50	2.55	2.17	2.89	2.89	3.04	1.87	3.11	2.41	2.10	2.73	2.08	2.02	3.90	1.14	2.89	2.49	1.90	1.56	2.28
Na_2O	*b.d.l.*	*b.d.l.*	0.17	*b.d.l.*	*b.d.l.*	0.28	0.09	0.26	0.16	0.13	0.13	0.18	0.11	0.29	0.04	0.24	0.19	0.05	0.03	0.18
K_2O	*b.d.l.*	*b.d.l.*	0.02	*b.d.l.*	*b.d.l.*	0.01	0.01	0.00	0.01	0.01	0.01	0.03	0.01	0.01	0.00	0.01	0.01	0.01	0.00	0.01
P_2O_5	0.02	0.02	0.02	0.01	0.01	0.01	0.01	0.01	0.01	0.01	0.01	0.01	0.01	0.01	0.01	0.01	0.01	0.01	0.00	0.01
LOI	6.54	3.40	2.95	3.05	1.40	1.51	3.26	1.73	2.44	6.62	8.14	11.16	7.99	6.59	9.65	4.03	3.34	6.94	7.92	7.10
Total	99.4	99.2	99.6	99.6	99.6	100.0	100.1	100.0	100.0	100.4	100.5	101.0	100.5	100.4	100.8	100.1	100.1	100.4	100.5	100.4
Mg-no.	89.9	89.9	90.5	89.6	89.6	89.2	90.5	89.0	89.9	89.8	89.4	88.8	90.2	88.9	91.0	89.0	89.7	90.3	90.5	88.9
(ppm)																				
V	63.80	56.50	49.80	73.20	66.40	80.00	49.70	79.60	54.70	51.00	50.20	81.10	50.60	71.80	32.40	65.50	65.30	56.30	41.50	58.10
Cr	2254	2328	2374	2379	2164	2331	2600	2319	2336	2305	2429	2237	2222	2411	2279	2160	2437	2302	2471	2269
Ni	1866	1935	2030	1890	1958	1932	2055	1836	2024	1957	1887	1806	1898	1666	2026	1914	1981	1971	2029	2095

b.d.l.: below detection limit; n.a.: not analized

Appendix A (continued)

Domains	*GRT-SP MYLONITES*									*SEILAND*										
Lithology	**Lherzolite**									**Harzburgite**										
Sample	**BB199**	**BB201**	**BB202**	**BB233**	**BB234**	**BB237**	**BB238**	**BB239**	**BB241**	**BB014**	**BB019**	**BB039**	**BB048**	**BB050A**	**BB050B**	**BB054**	**BB065**	**BB135**	**BB138**	**BB142A**
Groups of lherzolites	N/A	N/A	N/A	N/A	N/A	N/A	N/A	N/A	N/A	N/A	N/A	N/A	N/A	N/A	N/A	N/A	N/A	N/A	N/A	N/A
Clinopyroxene	6	10	9	13	15	6	5	14	9	3	2	2	4	2	4	2	2	1	4	2
Olivine	70	76	62	54	51	66	72	53	71	81	80	79	82	85	81	83	81	81	85	85
Orthopyroxene	24	14	29	33	34	28	23	33	19	15	17	18	14	12	14	14	17	18	10	13
Garnet	0.0	0.1	0.0	0.0	0.0	0.0	0.0	0.0	0.0	0.0	0.0	0.0	0.0	0.0	0.0	0.0	0.0	0.0	0.0	0.0
Spinel	0.1	0.7	0.2	0.3	0.2	0.1	0.0	0.3	0.7	0.1	0.4	0.1	0.4	0.3	0.5	0.4	0.1	0.1	0.4	0.2
UTM E	325326	325308	328742	332013	332014	327444	327477	327428	327392	330478	330216	329893	332276	332198	332198	331953	327732	331975	331590	331258
UTM N	3908359	3908403	3901553	3897252	3897353	3902557	3902587	3902655	3902713	3905284	3904771	3904515	3903836	3903825	3903825	3903580	3906406	3903592	3903253	3903052
Bulk rock data (wt%)																				
SiO_2	42.42	42.63	41.58	43.86	43.76	41.27	41.75	44.04	43.98	40.98	40.60	42.39	41.69	38.12	39.53	41.46	40.46	41.47	42.18	40.98
Al_2O_3	1.59	2.24	2.19	3.41	3.63	1.72	1.21	3.56	2.39	1.12	1.38	1.10	1.19	1.02	1.17	0.89	0.88	0.91	1.06	0.78
Fe_2O_3	8.22	8.66	8.20	8.94	8.84	8.34	8.68	9.06	8.51	8.41	8.37	8.55	9.65	9.03	9.03	8.58	8.41	8.72	8.77	8.62
MnO	0.12	0.13	0.12	0.14	0.14	0.12	0.13	0.14	0.13	0.13	0.13	0.13	0.14	0.13	0.14	0.13	0.13	0.12	0.12	0.12
MgO	38.73	36.31	38.41	37.98	37.31	40.99	42.33	37.98	40.69	41.90	41.54	43.19	43.03	42.77	43.06	43.66	43.35	43.68	42.99	43.60
CaO	1.30	2.02	1.84	2.88	3.09	1.54	1.25	3.01	2.23	0.99	0.96	0.85	0.92	1.05	0.86	0.48	0.47	0.45	0.78	0.41
Na_2O	0.06	0.06	0.08	0.20	0.25	0.02	0.05	0.25	0.11	*b.d.l.*	*b.d.l.*	*b.d.l.*	*b.d.l.*	*b.d.l.*	*b.d.l.*	*b.d.l.*	*b.d.l.*	0.00	0.00	0.00
K_2O	0.01	0.01	0.01	0.01	0.01	0.00	0.00	0.00	0.01	*b.d.l.*	*b.d.l.*	*b.d.l.*	*b.d.l.*	*b.d.l.*	*b.d.l.*	*b.d.l.*	0.01	0.00	0.00	0.01
P_2O_5	0.01	0.01	0.01	0.01	0.01	0.00	0.00	0.01	0.01	0.01	0.01	0.01	0.01	0.01	0.01	0.01	0.01	0.01	0.01	0.00
LOI	7.98	8.48	7.96	2.42	2.82	6.22	4.71	1.77	1.84	6.45	6.08	3.04	3.06	7.95	6.10	4.54	6.10	4.75	4.14	5.70
Total	100.5	100.6	100.5	100.0	100.1	100.3	100.2	100.0	100.0	100.0	99.3	99.3	99.7	100.1	99.9	99.8	99.9	100.2	100.2	100.3
Mg-no.	90.3	89.3	90.3	89.4	89.3	90.7	90.6	89.3	90.5	90.8	90.8	90.9	89.8	90.4	90.4	91.0	91.1	90.9	90.7	90.9
(ppm)																				
V	32.30	49.00	55.10	68.70	76.20	37.80	28.70	72.10	56.40	22.10	32.50	24.10	24.50	*n.a.*	15.50	20.80	15.00	18.70	25.10	17.10
Cr	1949	2364	2486	2267	2316	2438	2561	2190	2687	2097	1390	2039	1828	2652	2553	2069	1525	1712	2232	2249
Ni	2176	2064	1931	1936	1874	2025	2132	1945	2046	2107	2082	2184	2112	2172	2180	2185	2232	2253	2214	2240

b.d.l.: below detection limit; n.a.: not analized

Appendix A (continued)

Domains	*SEILAND*																		
Lithology	**Harzburgite**														**Lherzolite**				
Sample	**BB149**	**BB154**	**BB157**	**BB179B**	**BB213**	**BB214A**	**BB221**	**BB226**	**BB230**	**BB232**	**BB253**	**BB267**	**BB270**	**BB272**	**BB010**	**BB011**	**BB012**	**BB013**	**BB015A**	**BB015B**
Groups of lherzolites	N/A	N/A	N/A	N/A	N/A	N/A	N/A	N/A	N/A	N/A	N/A	N/A	N/A	N/A	I	I	I	I	I	III
Clinopyroxene	2	2	4	3	4	1	2	4	4	4	4	1	5	4	13	10	10	10	7	8
Olivine	82	83	72	83	82	80	81	77	79	81	71	81	81	71	64	64	66	66	78	73
Orthopyroxene	16	15	24	13	14	18	17	19	17	14	24	18	13	25	24	25	23	23	15	19
Garnet	0.0	0.0	0.0	0.0	0.0	0.0	0.0	0.0	0.0	0.0	0.0	0.0	0.0	0.0	0.0	0.0	0.0	0.0	0.0	0.0
Spinel	0.1	0.1	0.0	0.5	0.7	0.4	0.1	0.4	0.1	0.4	0.9	0.2	0.7	0.1	0.1	0.9	0.9	1.0	0.4	0.6
UTM E	329875	331392	331283	329397	329239	329292	334524	334089	330643	332976	330281	333390	329921	329294	327931	330688	330688	330579	330508	330508
UTM N	3904483	3903259	3903282	3903651	3902905	3902984	3899525	3900007	3905829	3903895	3904063	3900340	3902976	3902444	3906525	3905527	3905527	3905463	3905274	3905274
Bulk rock data (wt%)																				
SiO_2	40.75	41.75	43.08	39.55	43.28	43.86	42.49	42.17	39.74	39.48	41.45	41.48	43.42	41.62	42.00	41.57	41.46	41.06	39.97	40.69
Al_2O_3	1.00	0.69	1.21	1.01	0.94	0.77	0.55	1.32	1.42	1.02	1.56	0.88	1.52	1.42	3.01	2.71	2.82	3.00	1.60	2.13
Fe_2O_3	8.71	9.09	8.59	8.97	8.83	8.60	8.41	8.44	9.12	9.36	8.73	8.63	8.73	8.44	8.54	8.35	8.01	7.75	8.08	7.98
MnO	0.12	0.12	0.12	0.12	0.13	0.13	0.12	0.12	0.13	0.10	0.12	0.13	0.13	0.11	0.14	0.14	0.13	0.12	0.13	0.13
MgO	44.00	43.44	40.46	43.62	44.22	45.53	40.12	40.18	39.96	37.25	41.82	40.02	42.04	41.73	38.27	37.99	38.29	38.17	39.92	38.71
CaO	0.51	0.48	1.01	0.67	0.94	0.61	0.43	0.99	0.84	0.61	1.01	0.58	1.24	1.19	2.54	2.33	2.46	2.09	1.32	1.85
Na_2O	0.00	0.00	0.05	0.00	0.00	0.00	0.00	0.07	0.04	0.00	0.04	0.00	0.01	0.05	*b.d.l.*	*b.d.l.*	*b.d.l.*	*b.d.l.*	*b.d.l.*	*b.d.l.*
K_2O	0.01	0.01	0.01	0.01	0.00	0.00	0.01	0.01	0.01	0.01	0.00	0.00	0.00	0.00	*b.d.l.*	*b.d.l.*	*b.d.l.*	*b.d.l.*	*b.d.l.*	*b.d.l.*
P_2O_5	0.01	0.01	0.01	0.01	0.01	0.01	0.01	0.01	0.01	0.01	0.01	0.01	0.01	0.01	0.02	0.01	0.02	0.01	0.01	0.01
LOI	4.98	4.50	5.62	6.28	1.58	0.40	8.40	7.01	9.33	13.49	5.38	8.88	2.87	5.61	4.77	6.57	6.76	6.73	8.99	8.32
Total	100.2	100.2	100.3	100.3	100.0	100.0	100.6	100.4	100.8	101.5	100.2	100.7	100.1	100.3	99.5	99.8	100.1	99.2	100.1	99.9
Mg-no.	90.9	90.5	90.3	90.6	90.9	91.3	90.4	90.4	89.7	88.8	90.5	90.2	90.5	90.8	89.9	90.0	90.5	90.7	90.7	90.6
(ppm)																				
V	28.70	*n.a.*	30.40	17.40	27.90	28.10	17.20	26.90	34.40	29.40	29.00	23.60	29.40	31.40	60.10	55.30	54.70	47.70	35.90	41.40
Cr	1573	1673	2259	2312	2234	2444	2311	2164	1453	1705	1905	2049	2946	2130	2109	1951	2174	2965	2607	2196
Ni	2219	2380	2107	2424	2324	2369	2306	2179	1980	2184	2158	2309	2153	2165	1893	1896	1869	1885	1971	1936

b.d.l.: below detection limit; n.a.: not analized

Appendix A (continued)

Domains	*SEILAND*																			
Lithology	**Lherzolite**																			
Sample	**BB017**	**BB021**	**BB041**	**BB042**	**BB043**	**BB044**	**BB045**	**BB046**	**BB047**	**BB049**	**BB051**	**BB052**	**BB053**	**BB055**	**BB056**	**BB057**	**BB058**	**BB059A**	**BB059B**	**BB059C**
Groups of lherzolites	III	II	III	III	I	III	I	I	I	III	I	III	I	III	III	II	II	III	II	III
Clinopyroxene	8	15	9	12	7	12	13	7	12	8	6	13	10	11	11	14	13	12	13	12
Olivine	85	46	74	73	76	82	61	72	63	72	75	70	67	74	77	47	50	73	48	76
Orthopyroxene	6	39	16	15	17	6	26	22	25	21	19	17	22	15	11	39	37	14	39	11
Garnet	0.0	0.0	0.0	0.0	0.0	0.0	0.0	0.0	0.0	0.0	0.0	0.0	0.0	0.0	0.0	0.0	0.0	0.0	0.0	0.0
Spinel	0.7	0.1	1.2	0.8	0.3	0.0	1.0	0.0	0.1	0.3	0.1	1.3	1.3	0.2	0.3	0.0	0.0	1.0	0.0	1.0
UTM E	330126	333873	329632	329632	329457	332381	332350	332330	332271	332259	332168	332139	332004	331804	328599	328107	328050	328050	328050	328050
UTM N	3904714	3898027	3904244	3904244	3904049	3904157	3904112	3904124	3903962	3903842	3903838	3903804	3903582	3903468	3907351	3906719	3906763	3906763	3906763	3906763
Bulk rock data (wt%)																				
SiO_2	40.64	44.00	42.66	43.92	40.58	41.46	41.84	42.72	43.56	43.61	42.35	43.89	43.83	42.69	41.61	42.88	42.41	41.80	41.37	42.96
Al_2O_3	1.49	3.83	2.62	3.14	1.79	2.45	3.28	1.94	2.96	1.87	1.43	3.00	2.91	2.80	2.50	3.60	2.79	3.28	3.59	3.59
Fe_2O_3	8.65	8.65	8.43	8.64	8.46	8.91	8.54	8.47	8.79	8.28	8.50	8.70	8.63	8.46	8.11	8.71	8.56	8.67	8.33	8.70
MnO	0.14	0.14	0.13	0.14	0.14	0.14	0.14	0.13	0.14	0.13	0.13	0.14	0.14	0.14	0.13	0.14	0.14	0.14	0.14	0.14
MgO	42.85	36.54	40.21	39.53	39.95	38.33	37.86	41.09	38.50	41.23	42.35	39.55	39.83	39.46	38.79	37.48	38.51	37.76	35.20	37.67
CaO	0.99	3.21	2.41	2.61	1.59	2.12	2.62	1.59	2.51	1.70	1.36	2.56	2.48	2.36	2.26	3.03	2.79	2.55	2.77	2.86
Na_2O	*b.d.l.*	*b.d.l.*	*b.d.l.*	*b.d.l.*	*b.d.l.*	*b.d.l.*	*b.d.l.*	*b.d.l.*	*b.d.l.*	*b.d.l.*	*b.d.l.*	*b.d.l.*	*b.d.l.*	*b.d.l.*	*b.d.l.*	*b.d.l.*	*b.d.l.*	*b.d.l.*	*b.d.l.*	*b.d.l.*
K_2O	*b.d.l.*	*b.d.l.*	*b.d.l.*	*b.d.l.*	*b.d.l.*	*b.d.l.*	*b.d.l.*	*b.d.l.*	0.01	*b.d.l.*	*b.d.l.*	*b.d.l.*	*b.d.l.*	*b.d.l.*	*b.d.l.*	*b.d.l.*	*b.d.l.*	*b.d.l.*	*b.d.l.*	*b.d.l.*
P_2O_5	0.01	0.02	0.01	0.01	0.01	0.02	0.02	0.01	0.01	0.01	0.01	0.01	0.01	0.01	0.01	0.02	0.01	0.02	0.01	0.01
LOI	5.05	3.06	2.53	1.44	6.77	5.84	5.28	3.60	2.51	2.84	3.75	1.32	1.76	3.50	6.30	3.21	4.27	5.10	8.16	3.14
Total	99.9	99.6	99.1	99.6	99.4	99.4	99.7	99.6	99.1	99.7	99.9	99.3	99.7	99.5	99.8	99.2	99.6	99.4	99.7	99.2
Mg-no.	90.8	89.3	90.4	90.1	90.4	89.5	89.8	90.6	89.7	90.8	90.8	90.0	90.2	90.2	90.5	89.5	89.9	89.6	89.3	89.6
(ppm)																				
V	26.90	85.40	54.10	64.80	35.00	54.80	62.90	40.40	61.70	48.00	34.30	68.00	62.80	57.00	58.70	73.30	60.20	69.60	70.00	67.60
Cr	1443	2248	2739	2416	1811	1852	1899	2394	2205	2548	1902	2416	2461	2245	2112	2158	2487	2267	2412	2228
Ni	2145	1823	2008	1964	1975	1926	1850	2048	2096	2000	2128	1982	1994	1963	1901	1852	1968	1886	1751	1889

b.d.l.: below detection limit; n.a.: not analized

Appendix A (continued)

Domains	*SEILAND*																			
Lithology	**Lherzolite**																			
Sample	**BB060**	**BB061**	**BB062**	**BB063A**	**BB063B**	**BB064**	**BB067B**	**BB116**	**BB118B**	**BB118C**	**BB136**	**BB139**	**BB140B**	**BB141**	**BB147**	**BB148**	**BB150**	**BB151**	**BB152**	**BB153**
Groups of lherzolites	I	I	III	III	II	II	I	I	II	II	I	I	I	I	I	I	I	I	I	I
Clinopyroxene	9	11	13	14	14	14	7	5	19	18	5	9	5	9	9	9	10	5	6	11
Olivine	69	63	69	72	58	58	70	68	42	47	71	67	60	69	68	69	63	70	67	60
Orthopyroxene	21	26	17	13	27	27	22	27	39	34	23	23	35	22	22	21	27	24	27	29
Garnet	0.0	0.0	0.0	0.0	0.0	0.0	0.0	0.0	0.0	0.0	0.0	0.0	0.0	0.0	0.0	0.0	0.0	0.0	0.0	0.0
Spinel	1.1	0.1	0.8	1.0	0.6	0.7	0.4	0.0	0.5	0.9	0.2	0.9	0.0	0.8	0.8	0.8	0.3	0.4	0.1	0.3
UTM E	327985	327945	327920	327801	327801	327687	327686	327160	327102	327102	331971	331530	331524	331306	330069	329954	329792	329724	329625	331460
UTM N	3906690	3906682	3906584	3906435	3906435	3906431	3906237	3905019	3905052	3905052	3903577	3903195	3903186	3903057	3904577	3904557	3904428	3904341	3904245	3903238
Bulk rock data (wt%)																				
SiO_2	42.30	43.17	41.81	43.27	41.06	41.98	42.15	42.54	44.55	44.60	43.09	43.80	43.14	43.81	42.10	43.34	43.62	40.99	43.51	44.57
Al_2O_3	2.45	2.91	3.14	3.49	3.32	3.40	1.93	1.23	4.44	4.20	1.53	2.30	2.13	2.38	2.40	2.17	2.78	1.51	1.97	2.91
Fe_2O_3	8.51	9.13	8.20	8.34	8.45	8.55	9.15	8.08	9.24	9.18	8.50	8.69	9.06	8.46	8.45	9.08	8.42	8.75	8.39	8.28
MnO	0.14	0.14	0.13	0.14	0.14	0.14	0.14	0.12	0.15	0.14	0.12	0.13	0.14	0.13	0.12	0.13	0.12	0.13	0.13	0.13
MgO	38.81	38.45	36.92	37.22	36.71	36.70	39.25	41.70	34.99	35.07	41.18	40.40	41.00	40.15	39.16	40.72	38.79	40.85	41.42	38.52
CaO	2.04	2.48	2.69	3.07	2.76	2.95	1.86	1.27	3.94	3.78	1.38	2.11	1.38	2.02	2.00	1.87	2.24	1.37	1.51	2.52
Na_2O	*b.d.l.*	*b.d.l.*	*b.d.l.*	*b.d.l.*	*b.d.l.*	*b.d.l.*	*b.d.l.*	0.00	0.31	0.30	0.04	0.14	0.07	0.11	0.13	0.14	0.15	0.06	0.06	0.16
K_2O	0.03	*b.d.l.*	*b.d.l.*	*b.d.l.*	*b.d.l.*	0.01	*b.d.l.*	0.01	0.00	0.00	0.00	0.01	0.01	0.01	0.00	0.00	0.00	0.02	0.01	0.01
P_2O_5	0.01	0.01	0.02	0.01	0.02	0.02	0.01	0.01	0.01	0.01	0.01	0.01	0.01	0.01	0.01	0.01	0.01	0.01	0.01	0.01
LOI	5.07	2.77	6.01	3.54	6.90	5.12	4.53	5.15	2.17	2.53	4.21	2.34	3.02	2.87	5.84	2.49	3.87	6.60	2.96	2.83
Total	99.4	99.2	99.1	99.3	99.5	99.0	99.1	100.2	100.0	100.1	100.2	100.0	100.1	100.1	100.3	100.1	100.1	100.4	100.1	100.1
Mg-no.	90.0	89.3	89.9	89.9	89.6	89.5	89.5	91.1	88.3	88.3	90.6	90.2	90.0	90.4	90.2	89.9	90.1	90.3	90.7	90.2
(ppm)																				
V	49.70	65.20	60.00	71.50	68.10	73.60	50.90	26.10	96.40	87.10	41.40	49.30	40.60	52.20	58.00	42.70	56.90	35.70	41.00	57.80
Cr	1939	2103	2224	2158	2110	2225	2160	2579	2573	2601	2411	2699	1537	2197	2662	2684	2284	1789	2274	2717
Ni	1900	1946	1786	1845	1820	1822	1939	2086	1766	1772	2090	2086	2096	2054	2036	2100	1859	2053	2080	1989

b.d.l.: below detection limit; n.a.: not analized

Appendix A (continued)

Domains	*SEILAND*																			
Lithology	**Lherzolite**																			
Sample	**BB156**	**BB158A**	**BB159**	**BB160**	**BB162**	**BB174**	**BB175**	**BB176**	**BB178**	**BB179A**	**BB180**	**BB210**	**BB212**	**BB214B**	**BB218**	**BB219**	**BB224**	**BB225**	**BB231**	**BB244**
Groups of lherzolites	I	II	III	II	II	I	II	I	III	III	III	II	I	II	II	II	II	II	III	III
Clinopyroxene	9	15	16	14	14	5	15	7	8	8	14	16	8	18	13	14	15	15	12	16
Olivine	68	50	67	50	54	82	46	71	73	72	73	47	59	52	51	52	52	58	71	73
Orthopyroxene	22	35	15	36	32	13	39	21	18	19	11	37	32	30	36	33	32	27	17	10
Garnet	0.0	0.0	0.0	0.0	0.0	0.0	0.0	0.0	0.0	0.0	0.0	0.0	0.0	0.0	0.0	0.0	0.0	0.0	0.0	0.0
Spinel	0.8	0.4	1.2	0.4	0.6	0.6	0.1	0.2	0.8	0.8	1.2	0.2	0.8	0.5	0.3	0.3	0.8	0.1	0.6	1.0
UTM E	331342	331237	331134	331096	331080	329408	329339	329328	329397	329397	329425	329706	329105	329320	329415	329414	334287	334230	330512	333715
UTM N	3903252	3903306	3903297	3903316	3903288	3903952	3903833	3903799	3903651	3903651	3903484	3903304	3902781	3903063	3903199	3903270	3899795	3899858	3905799	3900132
Bulk rock data (wt%)																				
SiO_2	43.24	43.57	44.46	44.00	44.86	41.81	44.29	40.28	41.82	42.04	43.44	43.74	43.87	45.38	43.44	43.80	43.93	43.01	41.48	43.36
Al_2O_3	2.49	3.81	3.85	3.56	3.73	1.11	3.84	2.05	1.72	2.00	3.69	3.74	2.87	4.69	3.66	3.80	3.92	3.60	3.26	4.20
Fe_2O_3	8.47	9.02	9.29	9.21	8.60	8.54	8.75	8.19	7.94	8.12	8.72	8.45	8.62	8.99	9.04	8.80	8.76	8.76	8.03	9.18
MnO	0.13	0.14	0.14	0.14	0.14	0.13	0.14	0.12	0.12	0.12	0.14	0.13	0.13	0.14	0.13	0.13	0.14	0.13	0.13	0.14
MgO	39.44	36.74	37.05	36.23	36.87	41.96	36.93	39.28	40.47	40.74	36.74	35.96	39.33	35.81	35.73	35.52	36.37	36.37	36.23	35.88
CaO	2.01	3.33	3.36	3.00	3.15	0.89	3.31	1.80	1.68	1.88	3.04	3.41	2.44	3.83	2.81	3.03	3.30	3.17	2.55	3.42
Na_2O	0.13	0.26	0.29	0.25	0.24	0.00	0.25	0.07	0.06	0.07	0.20	0.27	0.17	0.34	0.23	0.24	0.26	0.25	0.12	0.26
K_2O	0.01	0.01	0.00	0.00	0.01	0.01	0.01	0.00	0.01	0.01	0.01	0.00	0.00	0.00	0.01	0.02	0.01	0.02	0.00	0.01
P_2O_5	0.01	0.01	0.01	0.01	0.01	0.01	0.01	0.01	0.00	0.00	0.01	0.01	0.01	0.02	0.01	0.01	0.01	0.01	0.00	0.01
LOI	4.08	2.99	1.34	3.50	2.23	5.44	2.30	8.73	6.43	5.12	3.94	4.22	2.45	0.55	4.94	4.62	3.18	4.65	8.72	3.43
Total	100.1	100.1	100.0	100.1	100.0	100.0	100.0	100.6	100.3	100.2	100.1	100.2	100.1	100.0	100.2	100.2	100.1	100.2	100.6	100.1
Mg-no.	90.2	89.0	88.8	88.6	89.5	90.7	89.3	90.5	91.0	90.9	89.3	89.4	90.0	88.8	88.7	88.9	89.2	89.2	90.0	88.6
(ppm)																				
V	52.70	78.90	77.90	70.50	83.80	28.50	77.00	35.80	36.70	40.20	70.10	80.00	62.10	99.10	67.30	82.60	82.00	69.00	61.10	75.80
Cr	2354	1880	2193	2011	2508	2496	2496	2061	2845	3062	2327	2471	2333	2313	2270	2283	2352	2094	2252	2106
Ni	2055	1926	1919	2056	2193	2131	1852	2026	1982	2043	1902	1789	2011	1831	1919	1851	1827	1844	1799	1781

b.d.l.: below detection limit; n.a.: not analized

Appendix A (continued)

Domains	*SEILAND*																		
Lithology	**Lherzolite**																		
Sample	**BB245**	**BB246A**	**BB246B**	**BB247**	**BB249**	**BB250**	**BB251**	**BB252**	**BB258**	**BB260**	**BB261A**	**BB262**	**BB264**	**BB265**	**BB266**	**BB269**	**BB271**	**BB273**	**BB274**
Groups of lherzolites	I	III	I	III	I	III	III	I	II	III	I	III	III	I	I	I	I	II	II
Clinopyroxene	6	10	5	10	6	9	9	5	15	12	10	11	9	13	10	5	10	13	14
Olivine	64	77	72	69	79	73	70	72	43	75	67	68	71	65	60	69	64	54	50
Orthopyroxene	30	13	23	20	14	17	20	22	42	12	23	20	20	22	29	26	26	33	35
Garnet	0.0	0.0	0.0	0.0	0.0	0.0	0.0	0.0	0.0	0.0	0.0	0.0	0.0	0.0	0.0	0.0	0.0	0.0	0.0
Spinel	0.1	0.6	0.1	0.8	0.9	0.7	0.9	0.8	0.2	0.9	0.1	0.7	0.8	0.5	0.1	0.1	0.1	0.3	0.3
UTM E	333635	333565	333565	333490	330872	330706	330347	330404	330064	329790	329790	333316	333287	333127	333068	329889	329603	329278	329286
UTM N	3900124	3900098	3900098	3900157	3904751	3904552	3904375	3904175	3903694	3903244	3903244	3900281	3900321	3900356	3900390	3903041	3902837	3902404	3902329
Bulk rock data (wt%)																			
SiO_2	44.25	43.14	41.69	42.67	41.15	41.49	41.55	41.29	43.25	42.18	40.96	45.25	44.31	45.12	43.55	43.99	43.50	44.12	43.33
Al_2O_3	1.85	2.26	1.73	2.48	1.94	2.26	2.41	1.99	4.08	3.23	2.44	3.31	2.11	3.13	2.70	1.72	2.46	3.43	3.74
Fe_2O_3	8.18	9.03	9.36	8.75	8.42	8.24	8.10	8.40	8.57	8.21	8.29	8.35	8.23	8.56	9.20	8.57	8.32	8.92	8.55
MnO	0.12	0.14	0.13	0.13	0.12	0.12	0.12	0.12	0.13	0.12	0.12	0.13	0.13	0.14	0.14	0.12	0.12	0.14	0.13
MgO	38.93	40.09	40.77	39.49	39.70	39.25	38.44	39.95	35.55	37.04	37.96	38.87	40.60	37.54	38.73	39.70	37.94	37.40	36.43
CaO	1.36	1.77	1.19	2.26	1.54	1.93	1.96	1.51	3.17	2.63	2.06	2.65	1.79	2.60	2.23	1.06	1.94	2.81	3.06
Na_2O	0.04	0.12	0.05	0.10	0.09	0.07	0.10	0.08	0.25	0.16	0.11	0.17	0.09	0.19	0.13	0.08	0.11	0.23	0.24
K_2O	0.01	0.01	0.01	0.00	0.00	0.01	0.01	0.01	0.01	0.01	0.01	0.00	0.01	0.02	0.01	0.01	0.01	0.00	0.01
P_2O_5	0.01	0.01	0.01	0.01	0.01	0.01	0.01	0.01	0.01	0.01	0.01	0.01	0.01	0.01	0.01	0.02	0.01	0.01	0.01
LOI	5.41	3.41	5.18	4.13	7.35	6.88	7.64	6.88	4.98	6.59	8.47	1.12	2.67	2.60	3.27	4.74	5.71	2.83	4.46
Total	100.2	100.1	100.2	100.2	100.5	100.4	100.5	100.4	100.2	100.4	100.6	100.0	100.0	100.0	100.1	100.2	100.3	100.1	100.2
Mg-no.	90.4	89.8	89.6	90.0	90.3	90.4	90.4	90.4	89.2	90.0	90.1	90.2	90.7	89.7	89.3	90.2	90.0	89.3	89.4
(ppm)																			
V	34.80	47.20	34.30	51.60	31.00	45.30	43.60	33.50	77.20	68.70	48.50	78.20	45.60	60.70	61.60	48.00	42.60	67.50	77.90
Cr	2210	1770	1527	2499	1942	2018	2358	1795	2283	2352	2506	2704	3200	2361	2271	2115	2449	2276	2313
Ni	2069	2006	2083	2014	2067	2006	1958	2011	1807	1847	1930	1878	2053	1973	2283	2174	2078	1959	1825

b.d.l.: below detection limit; n.a.: not analized

Appendix B

Trace element abundances in clinopyroxene and other mineral data from the Beni Bousera peridotites

Appendix B Trace element abundances in clinopyroxene and other mineral data

Domains	*GRT-SP MYLONITES*												*ARIEGITE*									
Lithology	**Lherzolite**												**Harzburgite**				**Lherzolite**					
Sample	**BB006**		**BB083**		**BB088B**		**BB165**		**BB171**		**BB201**		**BB201**		**BB201**		**BB035D**		**BB108**		**BB026**		**BB095**		**BB098**		**BB143**		**BB183**	
Mineral	**CPX**		**CPX**		**CPX**		**CPX**		**CPX**		**CPX1**		**CPX2**		**CPX3**		**CPX**		**CPX**		**CPX**		**CPX**		**CPX**		**CPX**	
Groups of lherzolites	**N/A**		**N/A**		**N/A**		**N/A**		**N/A**		**N/A**		**N/A**		**N/A**		**N/A**		**N/A**		**III**		**III**		**I**		**I**		**III**	
nº analyses	**4**		**4**		**5**		**3**		**2**		**3**		**1**		**1**		**5**		**5**		**1**		**5**		**4**		**8**		**5**	
Cs	0.006	(3)	0.003	(4)	0.005	(5)	0.001	(2)	0.001	(6)	*b.d.l.*		0.002		0.005		0.001	(1)	0.000	(2)	0.002		0.007	(2)	0.001	(7)	0.002	(7)	0.001	(9)
Rb	0.025	(6)	*b.d.l.*		0.012	(1)	0.006	(2)	*b.d.l.*		*b.d.l.*		0.003		0.002		0.003	(3)	0.004	(1)	0.008		0.036	(1)	0.007	(1)	0.006	(2)	0.015	(2)
Ba	*b.d.l.*		0.014	(3)	0.007	(1)	*b.d.l.*		*b.d.l.*		0.30	(0)	0.066		0.040		0.020	(1)	0.003	(6)	0.41		0.038	(5)	0.002	(2)	0.020	(6)	0.019	(3)
Th	0.033	(5)	0.036	(5)	0.033	(3)	0.020	(3)	0.017	(9)	0.017	(1)	0.027		0.021		0.016	(4)	0.11	(2)	0.002		0.049	(8)	0.019	(3)	0.046	(8)	0.033	(5)
U	0.011	(9)	0.016	(1)	0.013	(1)	0.009	(7)	0.006	(4)	0.006	(2)	0.006		0.005		0.005	(1)	0.031	(4)	0.000		0.013	(2)	0.011	(2)	0.017	(3)	0.013	(1)
Nb	0.28	(5)	0.16	(4)	0.029	(7)	0.19	(2)	0.017	(1)	0.19	(3)	0.30		0.30		0.23	(2)	0.30	(5)	0.029		0.44	(5)	0.098	(4)	0.41	(1)	0.29	(7)
Ta	0.055	(1)	0.070	(1)	0.004	(1)	0.025	(8)	0.004	(7)	0.033	(9)	0.031		0.018		0.050	(4)	0.039	(6)	0.001		0.044	(4)	0.017	(2)	0.064	(7)	0.042	(3)
La	1.46	(3)	1.61	(1)	0.57	(3)	0.88	(2)	0.82	(8)	0.24	(7)	0.28		0.22		1.60	(8)	1.25	(5)	0.026		0.44	(8)	1.42	(6)	2.05	(9)	1.06	(4)
Ce	5.25	(1)	5.97	(3)	2.03	(1)	3.35	(1)	3.66	(7)	0.45	(2)	0.55		0.34		5.42	(2)	4.06	(2)	0.091		2.51	(3)	6.86	(2)	9.49	(4)	3.65	(9)
Pb	0.15	(1)	0.22	(2)	0.088	(7)	0.13	(1)	0.041	(9)	*b.d.l.*		0.018		0.12		0.043	(3)	0.063	(2)	0.011		0.057	(6)	0.065	(2)	0.066	(8)	0.033	(4)
Pr	0.93	(2)	1.10	(5)	0.41	(2)	0.64	(3)	0.78	(2)	0.061	(6)	0.063		0.035		0.81	(3)	0.75	(3)	0.021		0.49	(9)	1.31	(3)	1.98	(7)	0.71	(4)
Sr	81.1	(6)	90.2	(5)	41.7	(1)	65.5	(4)	53.0	(3)	7.32	(2)	8.51		4.39		43.9	(2)	73.2	(4)	1.47		30.4	(3)	79.3	(5)	124	(6)	69.8	(3)
Nd	5.41	(1)	6.47	(3)	2.72	(1)	3.87	(1)	5.00	(1)	0.35	(3)	0.28		0.17		3.55	(5)	4.70	(2)	0.20		2.95	(6)	7.02	(2)	9.60	(4)	4.52	(6)
Zr	28.5	(5)	31.1	(1)	20.1	(1)	25.2	(1)	32.6	(1)	1.09	(8)	0.11		0.32		11.1	(1)	37.1	(2)	0.84		12.8	(6)	30.4	(2)	35.4	(1)	35.2	(2)
Hf	1.14	(3)	1.43	(5)	0.75	(6)	0.92	(4)	1.44	(6)	0.063	(3)	0.021		0.032		0.28	(4)	1.29	(8)	0.064		0.64	(1)	1.03	(1)	0.86	(2)	1.22	(1)
Sm	1.80	(3)	2.19	(9)	1.39	(1)	1.54	(4)	1.97	(8)	0.20	(3)	0.15		0.16		0.69	(3)	1.98	(9)	0.25		1.37	(2)	2.11	(4)	2.05	(8)	1.89	(3)
Eu	0.62	(1)	0.78	(4)	0.60	(3)	0.65	(7)	0.74	(2)	0.092	(1)	0.067		0.063		0.21	(2)	0.79	(3)	0.13		0.60	(7)	0.77	(1)	0.75	(3)	0.75	(1)
Gd	1.92	(2)	2.42	(2)	2.52	(1)	2.35	(1)	2.28	(4)	0.43	(4)	0.28		0.27		0.73	(5)	2.84	(2)	0.73		2.24	(7)	2.54	(2)	2.50	(8)	2.93	(2)
Ti	4443	(1)	4516	(400)	2485	(100)	3002	(20)	4378	(200)	750	(100)	621		652		326	(30)	3597	(100)	889		2742	(200)	3437	(200)	3472	(90)	3518.0	(50)
Tb	0.28	(3)	0.33	(2)	0.49	(2)	0.44	(6)	0.32	(1)	0.084	(1)	0.046		0.043		0.11	(6)	0.60	(3)	0.18		0.45	(2)	0.43	(3)	0.46	(2)	0.59	(3)
Dy	1.58	(2)	1.79	(2)	3.87	(2)	3.20	(3)	1.57	(3)	0.63	(1)	0.26		0.25		0.68	(5)	4.44	(3)	1.63		3.33	(1)	2.94	(3)	3.31	(2)	4.40	(3)
Y	5.40	(9)	5.44	(4)	20.7	(1)	15.5	(3)	4.53	(8)	2.95	(6)	0.82		0.77		3.49	(3)	23.5	(1)	10.4		17.0	(8)	13.6	(1)	18.1	(8)	23.3	(2)
Ho	0.25	(7)	0.26	(2)	0.85	(5)	0.70	(1)	0.22	(2)	0.12	(2)	0.033		0.034		0.14	(8)	0.97	(6)	0.41		0.74	(3)	0.58	(2)	0.72	(3)	0.95	(7)
Er	0.49	(1)	0.51	(7)	2.55	(2)	1.97	(4)	0.39	(0)	0.31	(5)	0.066		0.070		0.36	(2)	2.80	(29	1.33		2.12	(1)	1.63	(5)	2.16	(8)	2.79	(2)
Tm	0.057	(1)	0.051	(7)	0.37	(2)	0.29	(5)	0.041	(2)	0.045	(1)	0.008		0.008		0.05	(5)	0.41	(2)	0.20		0.32	(2)	0.23	(8)	0.31	(1)	0.40	(3)
Yb	0.31	(9)	0.23	(5)	2.42	(2)	1.83	(2)	0.18	(7)	0.24	(5)	0.037		0.033		0.35	(2)	2.52	(1)	1.39		2.00	(1)	1.49	(5)	1.99	(6)	2.53	(2)
Lu	0.047	(4)	0.019	(6)	0.36	(2)	0.27	(3)	0.020	(4)	0.037	(7)	0.006		0.004		0.05	(3)	0.39	(2)	0.20		0.30	(2)	0.22	(7)	0.28	(1)	0.39	(3)
Other mineral data																														
Mg-no. Cpx	89.7		89.7		91.1		91.0		88.6		92.8		92.8		92.8		*n.a.*		90.6		92.3		91.0		91.0		*n.a.*		90.7	
Mg-no. Opx	89.3		89.5		90.2		90.1		89.3		90.4		90.4		90.4		*n.a.*		89.7		90.2		89.4		90.2		*n.a.*		89.8	
Fo Ol	88.8		88.9		90.0		*n.a.*		88.8		89.8		89.8		89.8		*n.a.*		89.4		*n.a.*		88.9		89.9		*n.a.*		89.5	
Cr-no. Sp	21.6		20.3		14.8		12.8		16.2		20.3		20.3		20.3		*n.a.*		10.2		14.0		11.7		18.4		*n.a.*		11.3	

n, number of analyses; 1σ standard deviation in parentheses refers to the last digit; n.a., not analized.

Appendix B (continued)

Domains	*ARIEGITE*						*ARIEGITE-SEILAND*																	
Lithology	**Lherzolite**						**Harzburgite**						**Lherzolite**											
Sample	**BB184**		**BB187**		**BB191**		**BB070**		**BB076A**		**BB259**		**BB078**		**BB079**		**BB102**		**BB130**		**BB204**		**BB205**		**BB207**		**BB211**		**BB211**	**BB211**
Mineral	**CPX**		**CPX**		**CPX**		**CPX**		**CPX**		**CPX**		**CPX**		**CPX**		**CPX**		**CPX**		**CPX**		**CPX**		**CPX**		**CPX1**		**CPX2**	**CPX3**
Groups of lherzolites	**II**		**II**		**III**		**N/A**		**N/A**		**N/A**		**III**		**III**		**III**		**I**		**III**		**II**		**III**		**III**		**III**	**III**
nº analyses	**7**		**3**		**5**		**4**		**5**		**5**		**5**		**5**		**5**		**6**		**6**		**5**		**6**		**3**		**1**	**1**
Cs	*b.d.l.*		0.001	(1)	0.001	(1)	0.011	(5)	0.004	(1)	0.004	(4)	0.005	(4)	0.005	(7)	0.002	(6)	0.019	(2)	0.016	(9)	0.076	(1)	0.017	(8)	*b.d.l.*		0.10	0.76
Rb	0.016	(4)	0.005	(1)	*b.d.l.*		*b.d.l.*		0.0143	(5)	*b.d.l.*		0.028	(5)	0.11	(3)	0.003	(3)	0.008	(1)	0.008	(2)	0.010	(2)	0.027	(4)	*b.d.l.*		0.015	0.033
Ba	*b.d.l.*		*b.d.l.*		0.032	(3)	0.005	(1)	0.009	(1)	0.006	(9)	0.13	(3)	0.072	(2)	0.004	(8)	0.23	(6)	0.003	(4)	0.040	(5)	0.11	(1)	0.17	(0)	0.043	0.002
Th	0.035	(6)	0.15	(4)	0.057	(1)	0.027	(3)	0.061	(8)	0.057	(2)	0.067	(5)	0.026	(1)	0.014	(3)	0.032	(4)	0.009	(1)	0.082	(2)	0.038	(7)	0.020	(2)	0.050	0.017
U	0.013	(3)	0.019	(3)	0.017	(1)	0.025	(7)	0.011	(2)	0.034	(4)	0.051	(6)	0.008	(2)	0.006	(3)	0.015	(3)	0.004	(5)	0.038	(7)	0.011	(1)	0.011	(3)	0.014	0.15
Nb	0.43	(9)	0.24	(4)	0.67	(7)	0.32	(8)	0.100	(3)	0.84	(1)	0.43	(3)	0.18	(4)	0.16	(2)	0.25	(3)	0.036	(5)	0.20	(5)	0.045	(1)	0.21	(6)	0.17	0.20
Ta	0.040	(5)	0.040	(8)	0.074	(6)	0.047	(4)	0.030	(3)	0.15	(1)	0.048	(3)	0.027	(4)	0.018	(1)	0.021	(5)	0.010	(2)	0.042	(6)	0.006	(2)	0.031	(7)	0.035	0.034
La	1.04	(3)	5.45	(7)	1.01	(3)	1.28	(9)	1.29	(4)	2.42	(8)	1.04	(3)	0.98	(4)	0.51	(2)	1.56	(1)	0.79	(3)	1.60	(2)	0.54	(3)	0.69	(4)	0.67	0.71
Ce	3.51	(1)	13.6	(1)	2.57	(6)	4.05	(3)	4.4	(1)	10.2	(4)	3.19	(1)	3.57	(5)	1.97	(1)	5.86	(3)	3.45	(1)	5.98	(5)	1.27	(1)	2.56	(4)	2.47	2.53
Pb	0.026	(4)	0.14	(1)	0.031	(5)	0.21	(6)	0.094	(1)	0.058	(5)	0.039	(6)	0.034	(1)	0.49	(5)	0.039	(1)	0.098	(6)	0.41	(1)	0.086	(2)	0.037	(6)	1.19	2.76
Pr	0.63	(1)	1.79	(1)	0.39	(1)	0.65	(4)	0.75	(1)	2.18	(7)	0.61	(2)	0.69	(8)	0.39	(2)	1.06	(8)	0.72	(2)	1.11	(9)	0.15	(1)	0.48	(5)	0.45	0.48
Sr	71.6	(2)	67.9	(1)	19.8	(3)	62.7	(5)	65.7	(1)	157	(3)	57.2	(5)	63.9	(2)	37.1	(7)	82.5	(6)	64.2	(3)	88.4	(20)	12.9	(4)	50.7	(1)	50.1	52.0
Nd	4.06	(1)	7.18	(8)	2.10	(5)	3.33	(2)	4.3	(2)	13.8	(3)	3.82	(2)	4.19	(3)	2.39	(9)	6.54	(4)	4.5	(1)	6.79	(6)	0.73	(4)	2.79	(3)	2.71	2.75
Zr	33.1	(1)	23.5	(3)	4.11	(2)	17.6	(1)	26.8	(5)	38.7	(8)	22.3	(2)	25.2	(6)	14.4	(1)	38.9	(2)	29.2	(7)	49.9	(3)	1.20	(6)	10.5	(3)	13.3	10.7
Hf	1.00	(7)	0.61	(5)	0.27	(1)	0.53	(3)	0.97	(5)	1.17	(3)	0.83	(1)	0.84	(3)	0.56	(5)	1.21	(5)	1.01	(6)	1.41	(1)	0.11	(9)	0.43	(3)	0.45	0.40
Sm	1.77	(8)	1.53	(1)	0.83	(3)	1.03	(8)	1.70	(7)	4.38	(2)	1.58	(6)	1.67	(6)	1.05	(5)	2.27	(8)	1.86	(4)	2.54	(2)	0.41	(2)	1.09	(8)	1.07	1.09
Eu	0.70	(2)	0.53	(2)	0.35	(1)	0.38	(1)	0.72	(4)	1.40	(4)	0.64	(2)	0.71	(1)	0.47	(2)	0.82	(6)	0.79	(1)	0.97	(8)	0.21	(1)	0.47	(1)	0.45	0.47
Gd	2.65	(7)	2.05	(6)	1.61	(7)	1.24	(6)	2.7	(1)	3.78	(2)	2.40	(1)	2.52	(1)	1.74	(7)	2.83	(3)	2.92	(4)	3.41	(3)	1.03	(6)	1.67	(1)	1.59	1.67
Ti	3526	(300)	2488	(30)	1532	(80)	937	(40)	3651	(70)	1620	(40)	2471	(100)	2623	(200)	1692	(90)	3254	(300)	3512	(80)	5920	(200)	1030	(40)	1835	(50)	1941	1916
Tb	0.49	(2)	0.39	(2)	0.35	(7)	0.21	(9)	0.50	(3)	0.48	(1)	0.46	(1)	0.51	(1)	0.36	(1)	0.50	(2)	0.55	(8)	0.58	(5)	0.24	(1)	0.33	(6)	0.33	0.33
Dy	3.63	(9)	2.97	(2)	2.86	(6)	1.38	(3)	3.80	(2)	2.69	(1)	3.46	(9)	3.66	(2)	2.79	(1)	3.55	(2)	4.05	(4)	3.94	(4)	2.07	(9)	2.52	(2)	2.42	2.55
Y	19.8	(5)	17.0	(3)	15.7	(6)	6.21	(2)	19.2	(6)	10.8	(3)	17.8	(3)	20.2	(5)	14.6	(3)	19.4	(1)	19.5	(3)	19.6	(2)	11.8	(5)	12.7	(6)	12.9	13.3
Ho	0.79	(3)	0.69	(2)	0.67	(2)	0.28	(1)	0.81	(3)	0.49	(2)	0.75	(2)	0.83	(2)	0.65	(2)	0.76	(4)	0.89	(1)	0.79	(8)	0.50	(2)	0.59	(6)	0.57	0.59
Er	2.30	(7)	2.07	(1)	2.02	(8)	0.79	(3)	2.37	(4)	1.29	(4)	2.21	(3)	2.39	(1)	1.89	(7)	2.20	(8)	2.57	(4)	2.14	(2)	1.53	(7)	1.74	(3)	1.71	1.76
Tm	0.33	(1)	0.31	(8)	0.32	(6)	0.12	(4)	0.35	(2)	0.17	(7)	0.32	(9)	0.36	(7)	0.28	(9)	0.31	(1)	0.38	(5)	0.30	(4)	0.24	(8)	0.26	(8)	0.26	0.27
Yb	2.09	(7)	2.00	(5)	2.00	(7)	0.77	(2)	2.25	(2)	1.04	(4)	2.02	(5)	2.26	(1)	1.83	(6)	2.00	(1)	2.42	(3)	1.89	(2)	1.58	(9)	1.68	(3)	1.67	1.73
Lu	0.30	(1)	0.31	(1)	0.31	(1)	0.12	(6)	0.32	(1)	0.16	(9)	0.30	(8)	0.34	(1)	0.28	(1)	0.28	(8)	0.37	(6)	0.27	(3)	0.24	(1)	0.25	(3)	0.25	0.26
Other mineral data																														
Mg-no. Cpx	*n.a.*		90.7		92.3		92.7		*n.a.*		92.8		*n.a.*		90.7		91.9		*n.a.*		90.0		*n.a.*		90.6		91.3		91.3	91.3
Mg-no. Opx	*n.a.*		89.7		90.5		90.7		*n.a.*		91.2		90.4		89.9		90.6		*n.a.*		89.8		*n.a.*		90.4		90.1		90.1	90.1
Fo Ol	*n.a.*		89.5		90.2		90.4		*n.a.*		91.1		90.1		89.7		90.4		*n.a.*		89.3		*n.a.*		89.5		90.1		90.1	90.1
Cr-no. Sp	*n.a.*		15.2		14.6		32.8		*n.a.*		29.6		15.4		11.3		15.5		*n.a.*		11.1		*n.a.*		14.2		14.8		14.8	14.8

n, number of analyses; 1σ standard deviation in parentheses refers to the last digit; n.a., not analized.

Appendix B (continued)

Domains	*ARIEGITE-SEILAND*								*SEILAND*																	
Lithology	**Lherzolite**								**Harzburgite**																	**Lherzolite**
Sample	**BB216**		**BB229A**		**BB254**		**BB256**		**BB014**		**BB019**		**BB039**		**BB050A**		**BB138**		**BB142A**		**BB214A**		**BB270**		**BB272**		**BB017**	
Mineral	**CPX**		**CPX**		**CPX**		**CPX**		**CPX**		**CPX**		**CPX**		**CPX**		**CPX**		**CPX**		**CPX**		**CPX**		**CPX**		**CPX**	
Groups of lherzolites	**III**		**II**		**III**		**III**		**N/A**		**N/A**		**N/A**		**N/A**		**N/A**		**N/A**		**N/A**		**N/A**		**N/A**		**III**	
nº analyses	**5**		**6**		**5**		**5**		**5**		**3**		**6**		**5**		**5**		**5**		**4**		**6**		**2**		**6**	
Cs	0.002	(6)	0.006	(1)	0.005	(1)	0.005	(3)	0.001	(9)	*b.d.l.*		0.001	(7)	0.004	(2)	0.001	(7)	0.003	(8)	0.001	(3)	0.004	(3)	0.002	(2)	0.019	(6)
Rb	0.006	(1)	0.018	(5)	0.023	(5)	0.029	(9)	0.006	(1)	*b.d.l.*		0.030	(8)	0.007	(4)	0.007	(2)	*b.d.l.*	*b.d.l.*	0.005	(2)	0.008	(1)	0.009	(1)	*b.d.l.*	
Ba	0.001	(4)	0.007	(2)	0.022	(7)	0.076	(2)	0.046	(5)	0.027	(3)	0.088	(2)	0.007	(6)	0.064	(8)	0.065	(2)	0.003	(1)	0.087	(5)	0.021	(5)	0.054	(1)
Th	0.051	(9)	0.015	(3)	0.029	(6)	0.008	(2)	0.18	(2)	0.047	(1)	0.064	(5)	0.035	(1)	0.054	(3)	0.076	(1)	0.040	(4)	0.032	(3)	0.20	(7)	0.19	(2)
U	0.019	(2)	0.004	(8)	0.011	(2)	0.004	(9)	0.041	(1)	0.010	(1)	0.020	(4)	0.010	(2)	0.020	(1)	0.023	(2)	0.016	(1)	0.009	(2)	0.054	(7)	0.030	(4)
Nb	0.38	(9)	0.072	(2)	0.17	(4)	0.18	(4)	0.85	(7)	0.17	(4)	0.36	(7)	0.16	(4)	0.59	(9)	0.39	(5)	0.32	(5)	0.38	(4)	0.041	(4)	0.19	(5)
Ta	0.071	(4)	0.021	(4)	0.027	(7)	0.13	(2)	0.082	(2)	0.046	(3)	0.058	(3)	0.041	(6)	0.069	(8)	0.040	(5)	0.045	(4)	0.029	(4)	*b.d.l.*		0.023	(2)
La	2.15	(6)	1.08	(6)	1.01	(6)	2.48	(5)	1.25	(3)	1.10	(5)	0.91	(3)	1.24	(6)	1.46	(4)	1.56	(1)	1.68	(7)	1.18	(2)	1.89	(1)	1.38	(7)
Ce	6.56	(1)	3.75	(1)	3.56	(1)	14.6	(2)	3.61	(9)	4.69	(2)	2.87	(9)	4.65	(3)	4.54	(2)	4.96	(3)	6.03	(2)	2.43	(8)	5.33	(4)	3.94	(2)
Pb	0.048	(1)	0.068	(2)	0.040	(1)	0.043	(1)	0.037	(5)	0.017	(2)	0.017	(2)	0.042	(1)	0.79	(8)	0.12	(3)	0.036	(5)	0.024	(6)	0.56	(7)	0.036	(1)
Pr	0.96	(2)	0.63	(2)	0.67	(2)	3.22	(3)	0.60	(2)	0.96	(4)	0.49	(1)	0.85	(4)	0.78	(3)	0.79	(8)	1.06	(4)	0.29	(1)	0.79	(6)	0.63	(3)
Sr	72.4	(3)	102	(6)	66.5	(4)	231	(10)	42.5	(1)	58.0	(3)	43.1	(1)	131	(6)	66.0	(3)	75.9	(4)	90.3	(3)	21.4	(2)	39.8	(3)	58.0	(1)
Nd	4.63	(1)	3.67	(1)	4.17	(1)	20.2	(3)	3.29	(8)	5.76	(2)	2.67	(9)	4.83	(3)	4.35	(1)	4.29	(3)	6.10	(2)	1.35	(5)	3.70	(2)	3.50	(2)
Zr	15.1	(2)	26.7	(2)	26.2	(2)	90.4	(3)	10.8	(4)	50.7	(8)	15.0	(5)	22.2	(9)	29.8	(2)	14.1	(1)	42.8	(2)	3.82	(2)	18.5	(1)	17.5	(3)
Hf	0.55	(2)	0.82	(6)	0.95	(9)	3.05	(2)	0.28	(2)	1.78	(2)	0.47	(3)	0.77	(3)	0.86	(7)	0.69	(6)	1.22	(5)	0.17	(1)	0.65	(5)	0.64	(2)
Sm	1.41	(3)	1.59	(7)	1.68	(6)	6.79	(9)	1.06	(2)	2.23	(4)	0.93	(4)	1.46	(6)	1.38	(5)	1.26	(1)	2.35	(1)	0.45	(2)	1.03	(4)	1.40	(6)
Eu	0.55	(1)	0.66	(3)	0.71	(3)	2.42	(4)	0.38	(1)	0.88	(3)	0.37	(1)	0.62	(3)	0.48	(1)	0.46	(2)	0.93	(3)	0.18	(1)	0.38	(2)	0.60	(3)
Gd	1.94	(4)	2.45	(1)	2.55	(2)	7.30	(3)	1.22	(4)	3.08	(8)	1.21	(3)	1.80	(1)	1.63	(3)	1.42	(6)	3.18	(2)	0.74	(6)	1.38	(1)	2.22	(1)
Ti	2066	(30)	3516	(1)	3139	(200)	13298	(300)	927	(40)	4819	(60)	1336	(80)	2351	(70)	1623	(200)	2043	(100)	5170	(70)	1402	(100)	1335	(70)	2081	(30)
Tb	0.36	(9)	0.46	(3)	0.47	(3)	1.00	(3)	0.19	(3)	0.55	(1)	0.21	(3)	0.30	(1)	0.27	(7)	0.21	(1)	0.58	(3)	0.14	(8)	0.28	(3)	0.44	(2)
Dy	2.50	(4)	3.40	(2)	3.50	(3)	5.53	(3)	1.14	(3)	3.67	(5)	1.43	(3)	2.03	(1)	1.73	(6)	1.33	(6)	4.22	(2)	1.12	(3)	2.10	(2)	3.22	(1)
Y	12.1	(3)	18.5	(1)	17.2	(2)	19.6	(7)	4.84	(1)	16.4	(4)	6.70	(1)	9.30	(4)	8.59	(4)	5.43	(1)	22.8	(1)	6.69	(1)	11.5	(6)	15.9	(6)
Ho	0.55	(1)	0.74	(4)	0.75	(6)	0.90	(3)	0.22	(8)	0.75	(6)	0.30	(7)	0.42	(8)	0.34	(5)	0.25	(1)	0.91	(6)	0.25	(2)	0.47	(5)	0.72	(3)
Er	1.55	(4)	2.18	(1)	2.14	(2)	2.17	(9)	0.57	(1)	2.00	(1)	0.84	(2)	1.15	(5)	0.91	(5)	0.66	(3)	2.62	(2)	0.74	(5)	1.42	(2)	2.07	(9)
Tm	0.23	(4)	0.32	(2)	0.30	(3)	0.27	(1)	0.08	(3)	0.28	(3)	0.13	(2)	0.16	(5)	0.13	(4)	0.088	(4)	0.38	(2)	0.11	(7)	0.21	(1)	0.31	(2)
Yb	1.44	(4)	2.06	(1)	2.03	(2)	1.67	(8)	0.54	(2)	1.73	(1)	0.82	(2)	1.04	(5)	0.78	(3)	0.60	(3)	2.47	(1)	0.77	(5)	1.34	(2)	1.94	(1)
Lu	0.22	(7)	0.29	(2)	0.27	(2)	0.23	(8)	0.08	(3)	0.24	(4)	0.13	(3)	0.16	(1)	0.12	(3)	0.095	(5)	0.35	(2)	0.11	(2)	0.20	(2)	0.29	(1)
Other mineral data																												
Mg-no. Cpx	90.6		*n.a.*		90.9		90.2		92.1		91.0		92.1		91.3		92.3		92.2		93.3		92.6		*n.a.*		91.2	
Mg-no. Opx	90.2		*n.a.*		90.3		89.8		90.6		90.4		90.9		*n.a.*		90.7		91.2		90.4		90.7		90.7		90.4	
Fo Ol	90.1		*n.a.*		90.2		89.6		90.3		90.2		90.5		90.2		90.4		90.7		91.2		90.4		90.6		90.3	
Cr-no. Sp	20.4		*n.a.*		13.2		22.9		31.2		22.0		27.7		30.7		34.6		39.5		42.4		28.6		24.0		14.2	

n, number of analyses; 1σ standard deviation in parentheses refers to the last digit; n.a., not analized.

Appendix B (continued)

Domains	*SEILAND*																							
Lithology	**Lherzolite**																							
Sample	**BB041**		**BB042**		**BB044**		**BB052**		**BB055**		**BB056**		**BB057**		**BB059C**		**BB061**		**BB062**		**BB063A**		**BB064**		**BB159**		**BB174**	
Mineral	**CPX**		**CPX**		**CPX**		**CPX**		**CPX**		**CPX**		**CPX**		**CPX**		**CPX**		**CPX**		**CPX**		**CPX**		**CPX**		**CPX**	
Groups of lherzolites	**III**		**III**		**III**		**III**		**III**		**III**		**II**		**III**		**I**		**III**		**III**		**II**		**III**		**I**	
nº analyses	**5**		**5**		**4**		**5**		**5**		**5**		**6**		**5**		**5**		**5**		**5**		**6**		**5**		**6**	
Cs	0.007	(1)	*b.d.l.*		0.005	(3)	0.005	(2)	0.005	(3)	0.005	(6)	*b.d.l.*		0.001	(8)	0.001	(6)	0.009	(2)	0.007	(2)	0.036	(1)	0.005	(1)	0.003	(9)
Rb	0.036	(4)	0.008	(1)	0.014	(5)	0.007	(5)	0.030	(1)	0.023	(3)	0.17	(3)	0.016	(5)	0.014	(4)	0.024	(6)	0.067	(4)	0.25	(4)	0.015	(3)	0.021	(4)
Ba	0.033	(3)	0.16	(5)	0.14	(3)	0.007	(1)	0.096	(5)	0.049	(2)	*b.d.l.*		0.002	(2)	0.024	(2)	0.069	(2)	0.091	(7)	0.58	(5)	0.013	(2)	0.048	(1)
Th	0.034	(5)	0.021	(2)	0.027	(1)	0.043	(6)	0.027	(5)	0.040	(4)	0.12	(3)	0.013	(2)	0.019	(2)	0.013	(2)	0.012	(1)	0.011	(2)	0.030	(5)	0.10	(2)
U	0.013	(1)	0.018	(1)	0.010	(2)	0.016	(2)	0.008	(2)	0.014	(1)	0.046	(1)	0.006	(6)	0.003	(4)	0.004	(2)	0.51	(5)	0.005	(1)	0.011	(2)	0.036	(4)
Nb	0.23	(5)	0.15	(3)	0.22	(4)	0.29	(8)	0.13	(3)	0.24	(4)	0.56	(8)	0.058	(7)	0.063	(1)	0.057	(2)	0.069	(1)	0.089	(3)	0.17	(5)	1.11	(2)
Ta	0.033	(3)	0.022	(2)	0.036	(2)	0.047	(5)	0.020	(3)	0.039	(4)	0.091	(1)	0.014	(2)	0.009	(1)	0.009	(1)	0.012	(1)	0.014	(2)	0.029	(6)	0.15	(1)
La	0.71	(2)	0.86	(2)	1.55	(4)	1.92	(1)	1.07	(4)	1.28	(3)	11.6	(4)	0.95	(4)	0.83	(2)	0.82	(2)	1.00	(3)	0.98	(6)	1.48	(8)	1.67	(7)
Ce	2.52	(9)	3.37	(8)	5.75	(3)	6.20	(3)	3.96	(1)	4.51	(9)	42.9	(9)	3.86	(2)	2.67	(1)	3.58	(9)	4.09	(1)	3.87	(2)	5.56	(2)	5.21	(3)
Pb	0.14	(2)	0.040	(1)	0.035	(9)	0.020	(3)	0.030	(9)	0.027	(5)	0.37	(8)	0.019	(4)	0.022	(5)	0.027	(4)	0.021	(1)	0.043	(1)	0.035	(6)	0.017	(2)
Pr	0.48	(2)	0.66	(1)	1.08	(5)	0.95	(5)	0.73	(1)	0.78	(2)	8.35	(3)	0.77	(3)	0.52	(2)	0.76	(2)	0.80	(2)	0.76	(5)	1.05	(4)	0.91	(5)
Sr	38.8	(7)	62.7	(2)	86.3	(6)	78.0	(2)	87.8	(5)	53.2	(1)	497	(20)	71.3	(3)	88.2	(2)	83.4	(1)	74.5	(2)	69.8	(1)	82.0	(2)	68.5	(4)
Nd	3.00	(1)	3.97	(4)	6.50	(1)	4.83	(3)	4.33	(1)	4.36	(1)	55.8	(2)	4.68	(2)	3.51	(7)	4.71	(1)	4.85	(1)	4.70	(3)	6.38	(3)	5.18	(2)
Zr	16.3	(1)	24.7	(6)	41.3	(2)	26.5	(1)	25.4	(9)	29.2	(2)	441	(10)	31.5	(9)	28.2	(2)	28.2	(1)	31.2	(1)	36.6	(6)	38.3	(3)	32.4	(2)
Hf	0.68	(6)	0.89	(3)	1.46	(1)	1.00	(5)	0.88	(4)	1.04	(8)	13.2	(7)	1.11	(5)	0.88	(1)	0.99	(6)	1.11	(4)	1.10	(2)	1.32	(1)	0.96	(7)
Sm	1.35	(6)	1.62	(3)	2.33	(7)	1.62	(8)	1.63	(7)	1.66	(5)	23.2	(1)	1.89	(7)	1.64	(5)	1.84	(4)	1.91	(4)	1.91	(2)	2.39	(1)	1.75	(8)
Eu	0.59	(2)	0.70	(6)	0.87	(4)	0.68	(3)	0.69	(3)	0.68	(2)	10.0	(2)	0.81	(3)	0.66	(2)	0.76	(1)	0.80	(2)	0.78	(4)	0.93	(3)	0.61	(3)
Gd	2.21	(1)	2.51	(6)	3.24	(2)	2.57	(2)	2.48	(6)	2.63	(2)	32.4	(5)	2.91	(1)	2.40	(1)	2.73	(7)	2.81	(6)	2.71	(3)	3.22	(3)	2.09	(1)
Ti	2192	(100)	3032	(100)	4457	(200)	3248	(100)	2838	(300)	2992	(100)	35178	(2000)	3670	(80)	3881	(400)	3257	(70)	3821	(100)	4507	(500)	4348	(100)	2557	(100)
Tb	0.45	(2)	0.49	(1)	0.57	(3)	0.48	(2)	0.50	(8)	0.52	(2)	6.34	(2)	0.56	(2)	0.51	(3)	0.52	(1)	0.53	(1)	0.48	(7)	0.61	(5)	0.32	(1)
Dy	3.32	(2)	3.53	(9)	4.18	(2)	3.70	(2)	3.61	(1)	3.89	(3)	45.0	(2)	4.05	(1)	3.80	(2)	3.76	(8)	3.79	(8)	3.59	(5)	4.47	(4)	2.10	(8)
Y	16.4	(9)	17.3	(8)	20.4	(1)	19.0	(2)	19.2	(2)	19.0	(1)	259	(9)	19.3	(6)	21.6	(1)	17.9	(7)	18.1	(4)	18.5	(2)	21.0	(2)	9.93	(4)
Ho	0.74	(5)	0.78	(2)	0.88	(5)	0.80	(6)	0.82	(1)	0.86	(6)	9.64	(4)	0.89	(2)	0.82	(5)	0.81	(2)	0.82	(2)	0.76	(1)	0.96	(9)	0.40	(2)
Er	2.15	(2)	2.19	(1)	2.55	(2)	2.40	(1)	2.37	(1)	2.49	(2)	27.0	(6)	2.52	(9)	2.33	(1)	2.30	(8)	2.32	(6)	2.19	(3)	2.52	(2)	1.03	(5)
Tm	0.32	(2)	0.33	(1)	0.36	(3)	0.34	(3)	0.36	(1)	0.36	(3)	3.85	(1)	0.37	(1)	0.34	(2)	0.34	(1)	0.34	(1)	0.32	(3)	0.37	(2)	0.13	(5)
Yb	2.02	(1)	2.04	(9)	2.26	(1)	2.17	(1)	2.13	(1)	2.24	(1)	26.0	(1)	2.35	(7)	2.20	(1)	2.13	(9)	2.14	(5)	2.07	(2)	2.42	(2)	0.83	(3)
Lu	0.30	(2)	0.31	(2)	0.33	(3)	0.31	(3)	0.33	(8)	0.33	(3)	3.68	(1)	0.35	(1)	0.31	(2)	0.32	(1)	0.32	(1)	0.28	(3)	0.34	(2)	0.11	(6)
Other mineral data																												
Mg-no. Cpx	91.5		90.5		89.5		91.0		91.5		90.8		*n.a.*		*n.a.*		*n.a.*		89.8		*n.a.*		*n.a.*		89.4		*n.a.*	
Mg-no. Opx	90.3		89.7		89.3		90.0		90.3		89.9		*n.a.*		*n.a.*		*n.a.*		89.4		*n.a.*		*n.a.*		88.8		*n.a.*	
Fo Ol	90.1		89.6		89.2		89.9		89.9		89.8		*n.a.*		*n.a.*		*n.a.*		89.4		*n.a.*		*n.a.*		88.6		*n.a.*	
Cr-no. Sp	14.1		10.1		12.5		12.1		12.9		12.9		*n.a.*		*n.a.*		*n.a.*		11.1		*n.a.*		*n.a.*		8.13		*n.a.*	

n, number of analyses; 1σ standard deviation in parentheses refers to the last digit; n.a., not analized.

Appendix B (continued)

Domains	*SEILAND*																													
Lithology	**Lherzolite**																													
Sample	**BB178**		**BB180**		**BB212**		**BB214B**		**BB224**		**BB225**		**BB231**		**BB244**		**BB246A**		**BB249**		**BB252**		**BB258**		**BB260**		**BB262**		**BB266**	
Mineral	**CPX**		**CPX**		**CPX**		**CPX**		**CPX**		**CPX**		**CPX**		**CPX**		**CPX**		**CPX**		**CPX**		**CPX**		**CPX**		**CPX**		**CPX**	
Groups of lherzolites	**III**		**III**		**I**		**II**		**II**		**II**		**III**		**III**		**III**		**I**		**I**		**II**		**III**		**III**		**I**	
nº analyses	**3**		**5**		**8**		**6**		**8**		**7**		**5**		**5**		**5**		**5**		**5**		**5**		**5**		**5**		**6**	
Cs	*b.d.l.*		0.037	(3)	0.001	(1)	0.001	(3)	0.019	(6)	0.006	(2)	0.049	(1)	0.027	(4)	0.004	(1)	0.005	(1)	0.005	(2)	0.002	(7)	0.004	(3)	0.003	(6)	0.002	(9)
Rb	0.024	(9)	0.084	(2)	0.004	(1)	0.005	(2)	0.016	(5)	0.025	(2)	0.025	(7)	*b.d.l.*		*b.d.l.*		0.018	(4)	*b.d.l.*		0.015	(3)	0.045	(1)	0.035	(7)	0.015	(4)
Ba	0.076	(0)	0.016	(1)	0.007	(2)	0.003	(1)	0.044	(1)	0.17	(6)	0.068	(1)	0.054	(4)	0.30	(6)	*b.d.l.*		*b.d.l.*		0.016	(2)	0.070	(4)	0.083	(2)	0.017	(1)
Th	0.086	(2)	0.035	(4)	0.014	(2)	0.040	(4)	0.013	(3)	0.022	(6)	0.030	(4)	0.034	(6)	0.029	(7)	0.034	(5)	0.033	(6)	0.031	(8)	0.026	(2)	0.029	(5)	0.034	(5)
U	0.021	(5)	0.015	(3)	0.004	(6)	0.016	(1)	0.005	(1)	0.008	(2)	0.012	(1)	0.009	(1)	0.006	(1)	0.012	(9)	0.011	(2)	0.014	(1)	0.009	(1)	0.008	(2)	0.008	(1)
Nb	0.70	(3)	0.21	(5)	0.14	(3)	0.32	(5)	0.15	(4)	0.19	(6)	0.27	(5)	0.25	(2)	0.20	(7)	0.32	(2)	0.21	(1)	0.24	(6)	0.12	(3)	0.30	(3)	0.30	(1)
Ta	0.064	(1)	0.038	(1)	0.013	(2)	0.045	(4)	0.018	(2)	0.027	(5)	0.037	(3)	0.028	(2)	0.022	(5)	0.035	(6)	0.032	(5)	0.034	(7)	0.023	(4)	0.020	(2)	0.031	(5)
La	1.04	(2)	1.87	(5)	0.57	(3)	1.68	(7)	0.96	(5)	0.90	(2)	0.73	(1)	1.02	(1)	0.24	(2)	0.98	(5)	1.08	(5)	1.66	(5)	1.19	(5)	0.33	(2)	0.70	(1)
Ce	2.89	(5)	6.84	(2)	2.43	(8)	6.03	(2)	3.79	(2)	3.50	(7)	2.00	(3)	3.62	(1)	0.96	(6)	3.39	(1)	3.90	(2)	5.83	(2)	4.39	(1)	1.02	(6)	2.29	(3)
Pb	0.063	(2)	0.18	(5)	0.013	(1)	0.036	(5)	0.034	(1)	0.048	(3)	0.021	(6)	0.019	(4)	0.014	(3)	0.035	(1)	0.035	(2)	0.038	(9)	0.049	(1)	0.007	(1)	0.025	(9)
Pr	0.44	(5)	1.18	(4)	0.51	(2)	1.06	(4)	0.75	(3)	0.68	(1)	0.35	(6)	0.65	(1)	0.27	(2)	0.65	(1)	0.71	(3)	0.99	(4)	0.85	(2)	0.25	(2)	0.44	(3)
Sr	31.8	(2)	85.8	(7)	52.3	(2)	90.3	(3)	78.2	(3)	70.4	(10)	31.4	(9)	84.1	(1)	20.3	(1)	59.8	(3)	69.6	(4)	86.3	(4)	74.0	(3)	22.4	(5)	42.5	(8)
Nd	2.28	(2)	6.35	(2)	3.41	(2)	6.10	(2)	4.88	(2)	4.39	(9)	2.31	(4)	4.06	(7)	2.27	(1)	4.07	(1)	4.34	(2)	5.80	(1)	5.29	(1)	2.07	(1)	2.74	(7)
Zr	8.80	(6)	34.4	(2)	25.1	(1)	42.8	(2)	39.1	(1)	39.4	(6)	12.9	(4)	30.4	(2)	12.5	(7)	26.5	(2)	25.9	(2)	36.8	(2)	33.0	(1)	14.1	(7)	13.5	(1)
Hf	0.28	(2)	1.25	(8)	0.77	(3)	1.22	(5)	1.18	(4)	1.22	(3)	0.60	(4)	1.14	(1)	0.67	(5)	0.97	(9)	0.90	(9)	1.04	(8)	1.24	(4)	0.67	(5)	0.48	(6)
Sm	0.92	(1)	2.17	(7)	1.56	(1)	2.35	(1)	1.98	(9)	1.86	(3)	1.27	(5)	1.71	(3)	1.26	(7)	1.66	(8)	1.71	(5)	2.17	(3)	2.08	(6)	1.23	(7)	1.07	(3)
Eu	0.35	(5)	0.88	(3)	0.65	(3)	0.93	(3)	0.80	(3)	0.75	(1)	0.53	(1)	0.74	(1)	0.51	(3)	0.66	(1)	0.73	(2)	0.86	(2)	0.86	(2)	0.53	(2)	0.43	(1)
Gd	1.29	(1)	3.02	(5)	2.39	(2)	3.18	(2)	2.93	(1)	2.78	(3)	2.29	(8)	2.37	(2)	2.19	(1)	2.52	(6)	2.49	(8)	2.82	(7)	3.03	(1)	2.28	(8)	1.51	(1)
Ti	1045	(40)	3944	(200)	2933	(200)	5170	(7)	4341	(200)	4277	(200)	2323	(90)	3919	(100)	2405	(100)	2881	(100)	2931	(70)	4426	(90)	3701	(70)	2298	(200)	2244	(90)
Tb	0.24	(4)	0.56	(1)	0.44	(3)	0.58	(3)	0.53	(2)	0.51	(3)	0.48	(9)	0.54	(4)	0.44	(2)	0.46	(2)	0.46	(2)	0.50	(2)	0.59	(2)	0.49	(9)	0.30	(2)
Dy	1.77	(2)	3.99	(8)	3.26	(2)	4.22	(2)	3.90	(1)	3.94	(2)	3.86	(7)	3.93	(3)	3.30	(8)	3.38	(1)	3.40	(2)	3.70	(9)	4.39	(1)	3.81	(6)	2.30	(2)
Y	9.43	(5)	18.9	(5)	18.2	(1)	22.8	(1)	21.0	(5)	21.8	(2)	21.3	(4)	20.7	(2)	16.5	(4)	16.9	(7)	17.0	(8)	20.0	(1)	21.7	(7)	19.9	(5)	13.1	(1)
Ho	0.41	(5)	0.86	(2)	0.71	(5)	0.91	(6)	0.84	(3)	0.87	(8)	0.87	(7)	0.86	(8)	0.72	(1)	0.72	(4)	0.73	(4)	0.78	(2)	0.94	(3)	0.86	(3)	0.50	(4)
Er	1.25	(4)	2.40	(7)	2.11	(1)	2.62	(2)	2.44	(8)	2.61	(4)	2.61	(3)	2.66	(7)	2.12	(6)	2.13	(9)	2.11	(1)	2.31	(1)	2.72	(1)	2.54	(8)	1.48	(1)
Tm	0.19	(7)	0.36	(7)	0.30	(2)	0.38	(2)	0.35	(1)	0.41	(1)	0.39	(1)	0.35	(3)	0.32	(1)	0.30	(1)	0.30	(1)	0.34	(2)	0.38	(1)	0.37	(1)	0.22	(2)
Yb	1.34	(6)	2.24	(8)	1.99	(1)	2.47	(1)	2.26	(7)	2.38	(2)	2.53	(9)	2.18	(2)	1.96	(5)	1.86	(9)	1.94	(9)	2.24	(2)	2.48	(8)	2.33	(6)	1.49	(1)
Lu	0.18	(2)	0.33	(1)	0.28	(3)	0.35	(2)	0.32	(9)	0.34	(2)	0.37	(1)	0.33	(3)	0.29	(9)	0.27	(9)	0.27	(3)	0.32	(4)	0.36	(8)	0.35	(1)	0.21	(2)
Other mineral data																														
Mg-no. Cpx	*n.a.*		90.9		*n.a.*		*n.a.*		*n.a.*		*n.a.*		90.8		89.7		91.0		91.3		91.0				90.9		91.7		*n.a.*	
Mg-no. Opx	*n.a.*		89.5		*n.a.*		*n.a.*		*n.a.*		*n.a.*		89.8		88.6		89.8		90.1		90.4		*n.a.*		90.1		90.3		*n.a.*	
Fo Ol	*n.a.*		89.2		*n.a.*		*n.a.*		*n.a.*		*n.a.*		89.7		88.2		89.5		90.1		90.3		*n.a.*		89.9		89.9		*n.a.*	
Cr-no. Sp	*n.a.*		9.28		*n.a.*		*n.a.*		*n.a.*		*n.a.*		9.63		7.44		14.3		14.2		12.4		*n.a.*		11.1		12.4		*n.a.*	

n, number of analyses; 1σ standard deviation in parentheses refers to the last digit; n.a., not analized.




Understanding the mechanisms and processes responsible for mantle heterogeneities is crucial for improving our knowledge about the composition and differentiation of the Earth at different scales. Orogenic peridotite massifs provide an exceptional opportunity to investigate *in situ* the nature and scale of compositional mantle heterogeneities. This Ph.D. thesis aims to shed new light on the role of melt-rock reaction processes and recycling of oceanic and continental crustal material in creating chemical heterogeneities in the mantle. To achieve this objective, this thesis presents a detailed elemental and Sr-Nd-Pb-Hf isotopic study of mantle rocks exposed in orogenic peridotites from the Betic-Rif Cordillera in the westernmost Mediterranean, as well as of the crustal section spatially-associated with the Ronda massif (western Alpujárride complex and pre-Miocene Flysch Trough units of the Betic Cordillera). Two processes for the development of geochemical heterogeneities in the Earth's upper mantle are addressed using this dataset: (i) the formation of secondary lherzolites by melt-rock reaction processes, and (ii) the genesis of ultra-high pressure garnet pyroxenites and its implications for crustal recycling into the Earth's mantle. This thesis explores (iii) to what extent Betic crustal rocks were involved in the geochemical signature of magmatism observed in the subcontinental lithospheric mantle (SCLM), and in the Miocene Alborán Sea basin volcanism. The westernmost Mediterranean records an Alpine history of subduction and slab roll-back that resulted in the creation of the Alborán Sea basin. Mantle rocks and their allied crustal rocks in the Betic-Rif belt hence provide a unique natural laboratory for studying large scale recycling of crustal components in the SCLM.

Some of the questions addressed in this work are: *What is the main cause of the generally fertile compositions of SCLM peridotites? How recycled oceanic and continental crust gets intimately mixed in the mantle sampled by orogenic peridotite massifs? Are crustal components recorded in the composition of magmatic rocks "exotic" — i.e., incorporated by subduction in the convective mantle before the formation of the SCLM mantle — or genetically related to the lithospheric section associated with orogenic peridotites?*

CSIC
Consejo Superior de Investigaciones Científicas
IACT
Instituto Andaluz de Ciencias de la Tierra
Research Group on
Petrology, Geochemistry and Geochronology
Thesis Memoir nº 6
ugr Universidad de Granada